Receiver Technology for Radio Astronomy and Deep Space Communications

Alexander Pollak

Christ Church

University of Oxford

A thesis submitted for the degree of

Doctor of Philosophy

Trinity 2018

If people sat outside and
looked at the stars each night,
I'll bet they'd live a lot
differently.

— CALVIN & HOBBES

Acknowledgements

The time that I spent in Oxford has been one of the best experiences of my life. This was greatly influenced by John and Rupert. It was truly a pleasure to spend this time with you guys, especially going to so many guest nights at your college, which most of the time ended by us playing table football. I cherish the hours spent playing Rocket League way past midnight.

I would like to thank all the people who supported me throughout this DPhil In particular, I would like to thank Rik, Mike and Joe Tacon for all the work they have done helping me building this receiver.

I also would like to thank Bob Watkins for designing the mechanical layout of the cryostat, John Harris for donating a server to my project, which he just pulled out of the Physics IT rack and handed to me, and Ricardo Chiello for organising an iTPM somewhere from Italy... I assume it fell of a truck or whatever the Italian equivalent is!

A big thanks goes to Boon, Jamie, Sumedh and Ian for the marvelous support and for so many helpful and interesting discussions we had in nearly all the pubs in Oxford.

I also would like to thank Ashling, Leanne and Lara for their amazing help and support with all the admin related issues, without you this would not have been possible.

I would also like to thank Luke, Griffin, Sumedh, and Ian for proofreading chapters of my thesis.

Finally, I would like thank my supervisors Mike Jones and Christian Holler as well as Angela Taylor, who though technically was not an official supervisor, was always there for me when I needed any help. Thank you for your continuous support and guidance. At this point I would also like to thank you all for the freedom you gave me and trust you had in me, which allowed me to work independently on this project.

With the last words in this acknowledgement I want to thank my parents who always believed in me and supported me my entire life. I hope I have given back at least some of what you have given me.

Abstract

This thesis presents the design and development of a complete receiver system for a conversion project, which replaces the commercial receiver of a telecommunication antenna with a cryogenically cooled radio astronomy receiver. Part of the project is to explore the synergy between radio astronomy and deep-space communications, which share many technical requirements, but also have technical conflicts. Therefore, this thesis attempts to solve some of these technological issues and provides a design for a receiver system, where radio astronomy and communication applications can successfully share the same hardware and infrastructure.

The receiver system employs a FPGA-based digital signal processing backend, which enables the instrument to be used in three different operational modes, single-dish observation, interferometer observation, and deep-space communication.

The architecture of the receiver system includes a novel technical solution to stabilise gain drift when used in single-dish observation mode. Two stabilisation methods are discussed in detail, and their performance is verified by measurements. The white-noise stabilisation approach uses a modulated reference noise signal and the continuous-wave stabilisation approach uses a narrowband reference signal to track the change in amplification. Both stabilisation methods showed excellent performance and are implemented to stabilise the gain drift of the receiver system.

A number of analogue signal components were specially designed for the receiver system in order to meet the requirements of the conversion project. One of these components is the compact quad-ridged orthomode transducer, which provides the transmission between the feed horn and the coaxial cables. Its design uses a novel approach to reduce significantly the transition length, while retaining a wide operational bandwidth.

Finally we present the design of the complete receiver system, which includes the development work and verification of the components that were built for this project.

Statement of Originality

I declare that this thesis was written by myself and that the work contained within this thesis is my own except where explicitly stated otherwise. The work in this thesis has not been submitted for any other degree or professional qualification. Parts of this work have been published in [Pollak et. al., IEEE AWP].

Alexander Pollak

May 2018

Contents

List of Figures

Chapter 1

Introduction

1.1 Conversion of Telecommunication Antennas into Radio Telescopes

The technical development in the telecommunication industry is leading to an increase in data transmitted through undersea fibre optic cables. As a result of this increase, less and less data is transmitted via satellite communications. In addition, improvements in noise performance of satcom systems means that the same link budget can be achieved using smaller antennas. These trends make large telecommunication antennas that were built in the 1960s and 1970s redundant. A significant number of those antennas were built to the standards defined for communication antennas by Intelsat, which at that time specified for an antenna with the highest rating a diameter of around 30 meters [1]. Although these antennas are no longer of interest for the commercial satcoms industry, they are useful for radio astronomy and deep space communication, where large collecting areas are still important. The radio astronomy community world-wide has recognized the opportunity to convert those redundant telecommunication antennas into radio telescopes. A few examples of such conversion projects are: the Warkworth 30 m antenna in New Zealand [2], the Ceduna 30 m antenna in Australia [3], the Yamaguchi 32 m antenna in Japan [4], the Sicaya 32 m antenna in Peru [5], and the Nkutunse 32 m antenna in Ghana [6]. Joining

the list of conversion projects is the Goonhilly Earth Station, which is providing two antennas to the radio astronomy community. The receiver system presented in this thesis will be part of the 29-m GHY-3 antenna conversion project.

1.2 Goonhilly Earth Station

The Goonhilly Earth Station, is located on the Lizard Peninsula in Cornwall, UK (lat = 50.0504 N, lon = 5.1835 W). Its antennas were used to receive the first-ever transatlantic television broadcast via the Telstar satellite in July 1962.

As a result of the decrease in satellite communications, British Telecommunications Plc (BT) decided in 2008 to close down Goonhilly as an Earth Station and dismantle most of its parabolic antennas. At this time Goonhilly Earth Station Ltd. (GES) was founded with the plan to revitalise Goonhilly as a leading deep-space communication station.

In January 2014 GES Limited took ownership of the site and established a collaboration with a number of universities across the UK. The Consortium of Universities for Goonhilly Astronomy (CUGA) [7] has the aim to use the existing infrastructure at Goonhilly for research and training purposes. As part of this collaboration GES agreed to provide two of its three large antennas (> 25 m) to the consortium, while the consortium agreed to provide two radio astronomy receiver systems, out of which one should include the capability to be used as a downlink antenna for the deep-space network (DSN). The 25-m GHY-1 antenna will be provided with an L-band receiver based on a spare receiver for the Jodrell Bank mk II antenna, which is of very similar design. The 29-m GHY-3 antenna will be provided with a C-band receiver that is subject to this thesis.

1.2.1 Synergy between Radio Astronomy and Deep-Space Communication

Satellite communication antennas and radio astronomy telescopes usually have different hardware requirements. Where astronomy receivers are designed to be low-noise and able to detect faint astronomical sources, communication receivers are generally less sensitive because the communication signals are much stronger. This statement is true for most communication applications with earth orbit spacecraft. However for deep-space communication, where the spacecraft is not located within the Earth's orbit, the requirement on the sensitivity and stability of the antenna and receiver system becomes similar to the requirements for radio astronomy instruments. Therefore, deep-space communications share many technical requirements with radio astronomy, such as a low-noise receiver, large collecting area, precise time standard, and advanced digital signal processing hardware.

The common requirements in hardware opens up an opportunity where radio astronomy and deep-space communication can successfully share infrastructure and facilities, as demonstrated by the Canberra Deep Space Communication Complex in Australia [8].

1.3 Goonhilly Receiver Overview

The GHY-3 receiver system is a cryogenically cooled dual polarisation radio receiver with an operational frequency band of $4.0 - 8.5\,\text{GHz}$. The receiver system is designed to match the existing infrastructure of the GHY-3 antenna, which was built for satellite communications in the late 1960s. A simplified schematic of the receiver system is shown in Figure 1.1. The receiver system can be separated into three main sections. The Antenna includes the existing optics of GHY-3 dish and the feed horn which is especially designed to match the properties of the dish optics. The Cryostat includes the cryogenically cooled front-end components such as the orthomode transducer and low noise amplifiers. The Room Temperature Signal Conditioning includes all ana-

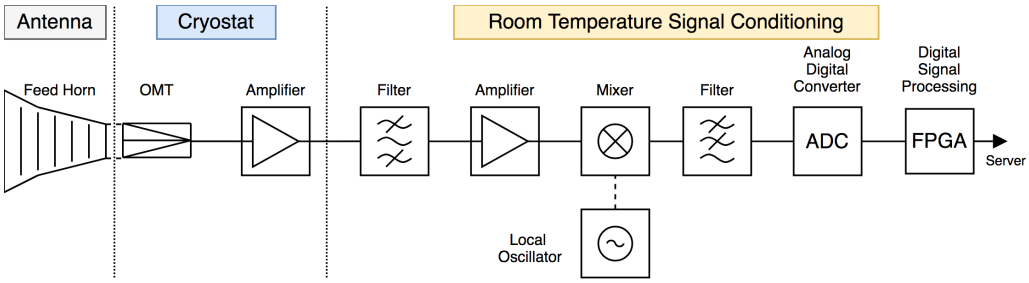

Figure 1.1: A schematic diagram of the components of the GHY-3 receiver.

logue signal components as well as the digital signal processing hardware and data acquisition.

1.4 Antenna Applications

The conversion of the antenna will enable it to be used for a variety of different applications, which include two astronomical observation modes as well as one communication mode. For astronomical observations the antenna can be used in single-dish mode, where the antenna acts as an independent telescope, or it can be used in interferometer mode, where the antenna operates as part of a telescope array to perform aperture synthesis. In the following sections we briefly describe the different operation modes and their applications.

1.4.1 Single-Dish Observation

In single-dish observation mode, GHY-3 can be used for a number of different observations, including: galactic mapping to compliment the C-BASS project [9], 5 GHz continuum observations of micro-quasars, transients, H and C recombination lines [2], pulsar observations, and fast radio burst (FRB) surveys.

In case of pulsar observations the large fractional bandwidth of the GHY-3 telescope would allow us to study the long term pulse profile, which enables us to see the effect of profile changes [10]. Although pulsars detected at C-band are generally weak, a pulsar survey in regions with high electron density would be a reasonable application [11].

In case of FRB surveys there have been bright FRBs detected by ASKAP and UTMOST [12],[13], which imply that even with a smaller collecting area GHY-3 should still be able to detect bright FRBs. In addition to that, the first repeating FRB has been detected by the Green Bank Telescope at C-band [14].

1.4.2 Interferometer Observation

There are two main applications planned for the GHY-3 antenna when used in interferometer mode. The first application is to integrate the antenna after its first light into the UK's e-MERLIN interferometer network [15]. The second application that has been considered after the successful integration into eMERLIN is to implement the antenna into the European VLBI network [16].

1.4.2.1 e-MERLIN

e-MERLIN is the UK's interferometer network for high resolution radio astronomy observations, operated by the University of Manchester at the Jodrell Bank Observatory [15]. The current interferometer in operation consists of seven telescopes around the UK, with a maximum baseline of approximately 217 km. The location of the currently integrated antennas are marked in white on the map shown in Figure 1.2 and the location of the to be included antennas at Goonhilly is marked in yellow. The improvement in performance achieved by the integration of Goonhilly is discussed in [17], which also includes a simulation of the uv-coverage of the e-MERLIN interferometer array with and without the antennas at Goonhilly. The result of a full Earth-rotation for four source declinations is shown in Figure 1.3. The plots show an increase in resolution and improved visibility sampling of the interferometric array.

The increase in maximum baseline to 441 km gained by the integration of Goonhilly enables the instrument to study the complex dynamics of massive star formation at the centimetre wavelengths with sufficient resolution to probe both inflating molecular and outflowing ionized gas. This goes hand-in-hand with high-frequency observations from the Atacama Large Millimeter Array (ALMA), which provides sensitivity

Figure 1.2: Map of the UK, showing the location of the existing e-MERLIN antennas (marked in white). The location of the planned integration of the Goonhilly antennas is marked in yellow. The image has been taken with the approval of the author from [17].

to molecular gas at a similar resolution for objects at observations of a distance of 3 kpc [17].

1.4.2.2 Very Long Baseline Interferometry (VLBI)

Currently the European VLBI Network uses e-MERLIN to resolve large-scale structures, however the overlap in baselines between both networks in their current configuration is marginal. The overlap can be improved by integrating Goonhilly in both instruments, which will increase the western extent of the baseline and also increases the uv-coverage [17].

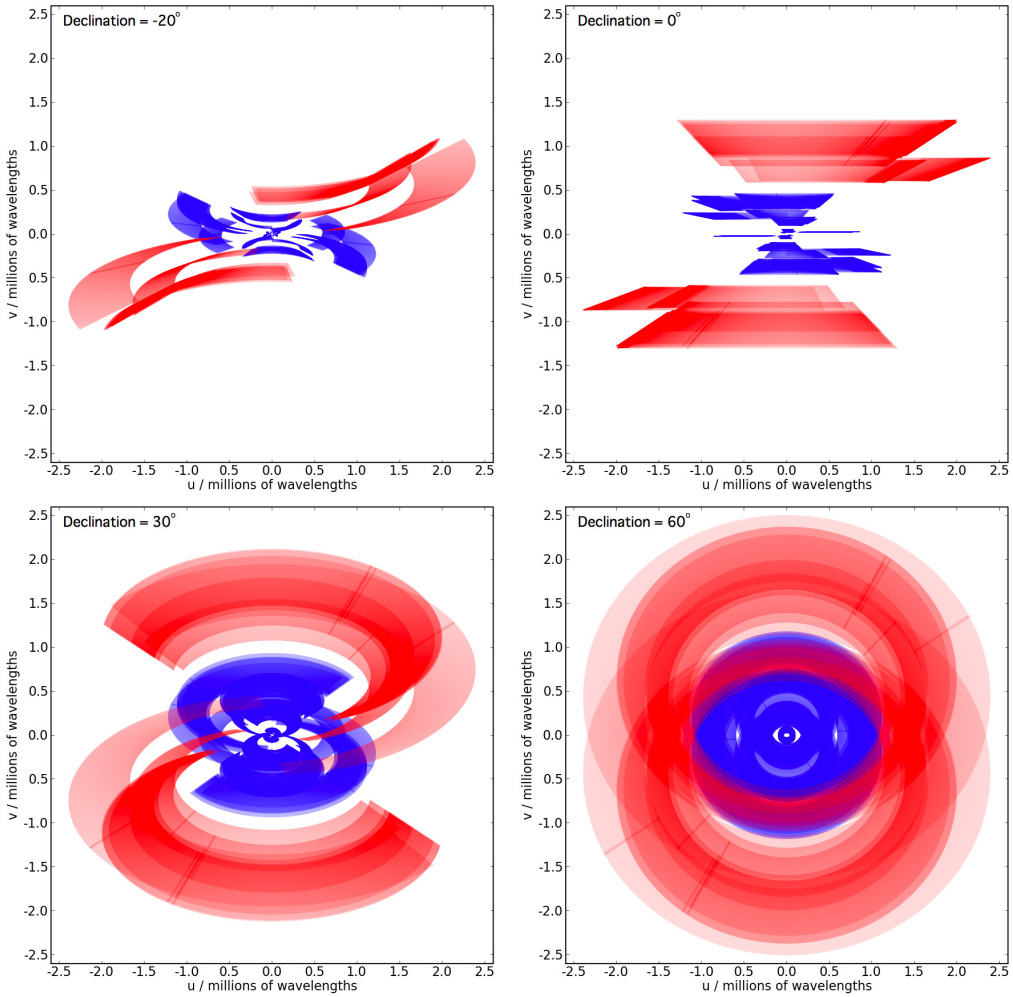

Figure 1.3: Full *uv*-coverage plots of the e-MERLIN interferometric array for four source declinations as indicated on each panel. The additional baselines provided by the Goonhilly station are shown in red. The image has been taken and modified with the approval of the author from [17].

1.4.3 Deep-Space Communication

Deep-space communication has very specific requirements, which are different from communication requirements for earth-orbiting spacecraft. Some of the requirements are due to the greater distance and different orbit of the spacecraft, which can lead to a significant relative velocity between the receiving antenna and the transmitting spacecraft. Hence, one of the requirements includes the ability to accurately determine the spacecraft's position and relative velocity (ranging). This requirement goes together with the ability of the receiver system to correct for the doppler shift in

frequency when receiving a signal of a spacecraft with a known position and relative velocity. Another requirement has to do with the fact that the antenna beam can include multiple spacecrafts and the receiver system must be able to differentiate between the signals.

The European Space Agency (ESA) has a demand for deep-space communication antennas to support future and ongoing missions such as ExoMars [18], Solar Orbiter [19], and EUCLID [20]. To support those spacecraft the receiver system needs to operate at the deep-space network (DSN) downlink frequency at X-Band (8.4 GHz) and support various demodulation schemes.

The implementation of the DSN modem capabilities can be done by either connecting a certified DSN modem to the analogue output of the receiver system, or by implementing the demodulation scheme into the FPGA-based digital signal processing which is part of the receiver system.

Any deep-space communication antenna which provides services for institutions such as ESA or NASA must go through a certification process, which might require for the instrument to use a certified modem such as the Telemetry Telecommand and Control Processor (TTCP) (developed by BAE Systems in the UK).

1.5 FPGAs in Astronomical Signal Processing

Field Programmable Gate Arrays (FPGAs) were invented by Xilinx in 1984, since then the market and applications for FPGAs has increased continuously [21]. Nowadays there are two major manufacturers producing FPGAs, Xilinx and Altera; the latter is owned by Intel.

This section describes the basic principles of FPGAs and their benefits which makes them a unique tool in digital signal processing (DSP).

1.5.1 Introduction

FPGAs are reprogrammable integrated circuits, in contrast to non-reprogrammable integrated circuits like application-specific integrated circuits (ASICs). Generally

speaking, FPGAs consist of three main parts; programmable interconnections, input and output drivers, and logic blocks. The latter usually includes a number of configurable logic blocks and fixed function blocks such as memory and multipliers. A simple schematic of an FPGA is shown in Figure 1.4. The functions that are executed on the FPGA is described in its firmware file. This file contains a compiled bitstream describing the interconnections between logic blocks, memory allocation, input and output configurations, and a number of other parameters.

There are two established description languages for FPGA firmware design, Very High Speed Integrated Circuit Hardware Description Language (VHDL) and Verilog. Both languages are low-level and describe the desired behaviour of the digital circuit, which means that the designer requires sophisticated knowledge in order to imple-

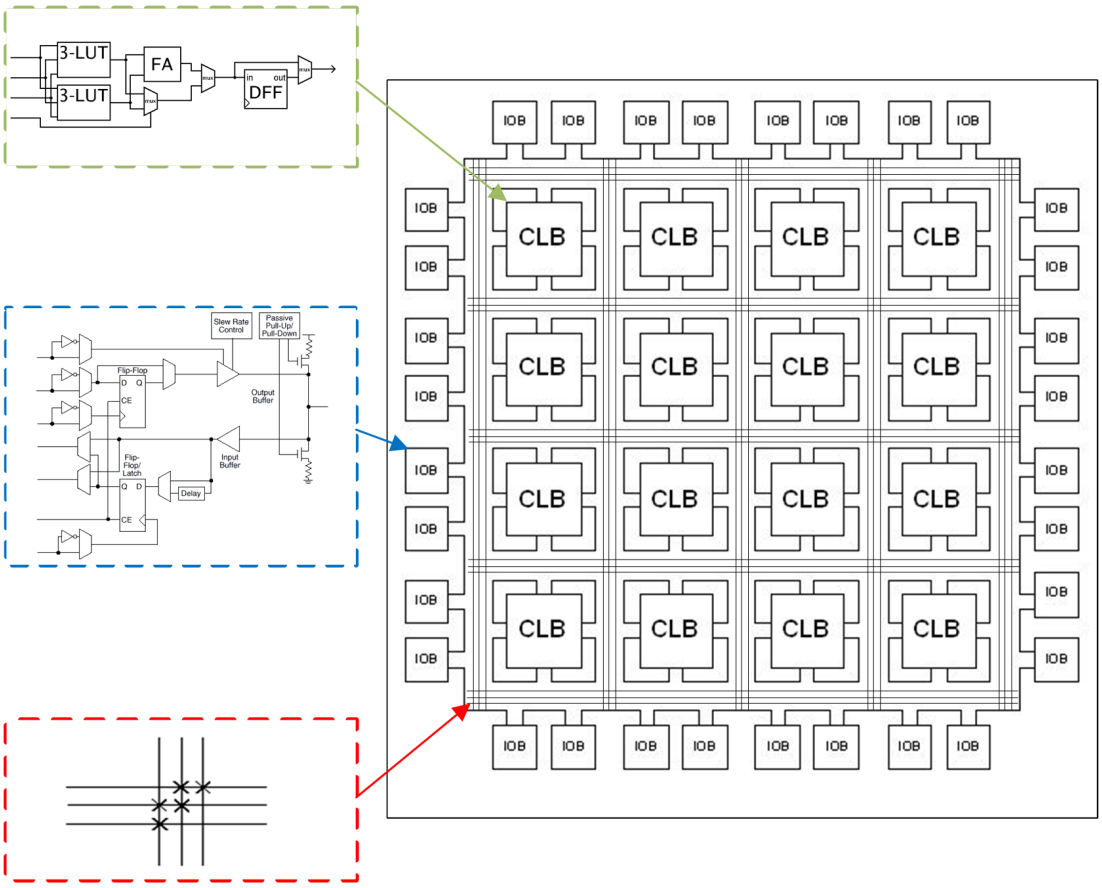

Figure 1.4: A schematic diagram of the main components of an FPGA. The configurable logic blocks (CLB), the input/output blocks (IOB), and the programable interconnections are shown in green, blue, and red, respectively.

ment high-level functions such as Fast Fourier Transforms or similar. However, there are high-level design tools available for some time now, which allow the designer to describe the desired behaviour using graphical blocks [22] or even the C programming language [23], making the use of FPGAs even easier. These tools take the high-level design and convert it into VHDL code, which then is compiled into the firmware bitstream. The process of compiling the VHDL code into the firmware bitstream takes a number of steps and is done by using the compiler that is provided by the chip manufacturer, in case of Xilinx and Altera, Vivado and Quartus, respectively. Each software includes the version-specific FPGA hardware layout of the manufacturer, which allows the designer to compile their VHDL code to a specific hardware platform. At this point we are not going into detail on how the compilation process works, but it is important to know that the software simulates the implemented design and provides feedback on any constraints such as maximum clock frequency of the FPGA.

1.5.2 Current Instruments using FPGAs

FPGAs have a number of advantages which makes them the preferred tool for radio astronomical digital signal processing.

The first advantage of an FPGA is its architecture, which allows it to implement highly parallelized algorithms, hence processing high rates of data in real time, up to several tens of Gbps, where a single FPGA can perform the equivalent of several Tera Floating Point Operations per Second (TFLOPS). This is especially important for radio astronomy, where the amount of digitized data is too large to be stored on hard disks without being reduced beforehand. Some examples of the operations which are performed in realtime are digital filters, Fast Fourier Transforms, cross-correlations, etc.

The second advantage is the cost efficiency when compared with ASICs. FPGAs are mass produced and therefore relatively cheap compared with the costs that are required to manufacture a customised ASIC that has a small production volume.

The third advantage is the flexibility which an FPGA provides. It allows the user to implement different firmware designs suited to the required application. In the

case of the GHY-3 receiver the FPGA-based digital signal processing allows us to implement the three different operational modes, single-dish observation, interferometer observation, or deep-space communication downlink, using a single hardware system.

All these and other unique features make FPGA-based digital signal processing ideal for radio astronomy instruments. A list of some current instruments which employ FPGA-based digital signal processing is shown in Table 1.1. This list shows the variety of instruments that all use FPGA-based hardware, from single-dish instruments to antenna arrays and even for optical applications in the case of DARKNESS. A more detailed list of instruments using FPGA-based signal processing hardware is presented in [29]. However, note that this publication restricts itself to one hardware platform.

Table 1.1: Example list of instruments using FPGA-based digital signal processing.

Instrument	Year	Describtion
KAT7	2010	SKA prototype consisting of 7 antennas with two polarisations [24].
C-BASS South	2013	C-Band All Sky Survey, utilizing a 7.6 m telescope at the South African MeerKAT site [9].
VEGAS	2014	Versatile spectrometer for the Green Bank Telescope, providing up to 10 GHz bandwidth [25].
AVN-Ghana	2016	The AVN Ghana telescope implements a spectrometer with a 400 MHz bandwidth [6].
DARKNESS	2016	MKID readout system using FPGA-based signal processing with a bandwidth of 2 GHz. [26].
AAVS1	2017	SKA-low prototype consisting of 400 dual-pol antennas [27].
MeerKAT	2018	MeerKAT consists of 64 dual-pol antennas with a possible bandwidth of more than 800 MHz. [28]

1.5.3 Future trends for FPGAs

The development of FPGA technology is mainly driven by the demands of the industry in particular for the next generation mobile phone network 5G and large data centres.

Hence, there are two areas in which the current development improves the performance of FPGAs. The first area increases the memory performance with respect to its bandwidth. There are currently two white papers from Xilinx and Altera approaching this area [30, 31]. These papers quote that the requirement in memory bandwidth over the last 10 years has increased significantly, but the increase in memory bandwidth has not met the demands. For most applications this means that in order to provide high memory bandwidth one must increase the number of memory modules, which effectively increases the overall bandwidth. However, this method has the disadvantage that large numbers of ultra-high-speed serial transceivers must be allocated to connect the memory modules to the FPGA.

The developed solution that solves this issue uses silicon stacking technology, which allows the manufacturer to place dynamic random-access memory (DRAM) modules next to the FPGA logic within the same package, as illustrated in Figure 1.5. According to Xilinx, this technique increases the memory bandwidth by a factor of ten compared to the standard DDR-4 memory technology.

The second area that improves the performance of FPGAs focuses on the analogue-to-digital (ADC) and digital-to-analogue (DAC) conversion of signals. Traditionally analogue signals are digitised by high speed ADCs which are connected to the FPGA via a high speed serial links such as JESD204B or via the general i/o pins of the

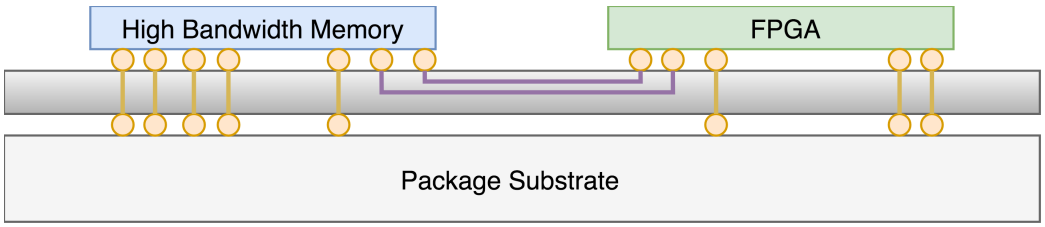

Figure 1.5: Chip-on-Wafer-on Substrate (CoWoS) schematic assembly of an FPGA and a memory module within the same package. The connections from the memory module to the FPGA are routed through the silicon sub layer. The components are interconnected by so called micro-bumps [32].

FPGA. However, the transceivers required to interconnect the FPGA with the ADCs or DACs draw a substantial amount power as well as add constraints on the signal routing in the printed circuit board (PCB).

Xilinx presents in a white paper [33] the radio-frequency (RF) sampling approach, which includes a number of high speed ADCs and DACs within the same package as the FPGA. Such chips that combine several devices on a single substrate are referred to system on chip (SoC). A schematic comparing the conventional architecture of a FPGA-based digitiser with the architecture that integrates the ADCs within the same package as the FPGA is shown in Figure 1.6. This integration reduces the complexity in digital signal processing hardware design. The increase in sample frequency that can be achieved by this integration enables for some applications the direct sampling of the RF signal, thereby reducing the number of analogue components required in order to frequency convert the signal to a lower rate before it can be digitised. This development is especially useful for radio astronomy applications, which require high sampling rates. For example, the Xilinx Zynq UltraScale+ RFSoC employs a version with sixteen 2 Giga samples per second (Gsps) ADCs resulting in a total bandwidth of 16 GHz. This FPGA would be able to digitise and process twice the bandwidth of the GHY-3 antenna.

Future developments in FPGA hardware will favour radio astronomy applications, providing even better capabilities than we have today.

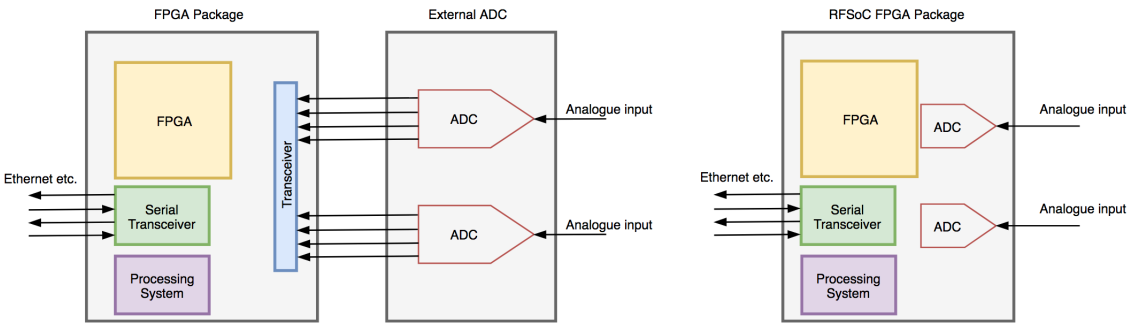

Figure 1.6: Comparison between the conventional and the integrated FPGA-based signal processing. The left-hand side shows the setup using external ADCs which are connected to the FPGA via high speed serial links. The right-hand side shows the next generation layout, which includes the ADCs or DACs within the same package as the FPGA.

1.6 Receiver System Requirements

The requirements for the GHY-3 receiver system are derived by its planned applications: single-dish observation mode, interferometer observation mode, and deep-space communication mode.

The latter two applications define the operational bandwidth of the telescope. For the integration into the eMERLIN interferometer, the receiver must cover the frequency range from $4.0 - 8.0\,\mathrm{GHz}$, which covers the C-Band part of eMERLIN. For it to be used in deep-space communication mode, the receiver must cover the DSN downlink frequency range $8.4 - 8.5\,\mathrm{GHz}$. Hence, the total operational bandwidth of the receiver system is 4.0 to 8.5 GHz.

The single-dish operational mode defines the desired stability of the receiver system with respect to its gain drift. This causes the requirement for the receiver system to include a means to stabilise its gain drifts over an observation period. For the implementation of a suitable stabilisation method we must analyse and compare the performance of several methods and choose the most suitable implementation for the GHY-3 receiver system.

Finally, the receiver system must be integrated within the existing infrastructure of the GHY-3 antenna. This puts constraints on the mechanical size of the receiver system, as well as defining the characteristics of the feed horn which illuminates the existing antenna optics.

The next section will provide an outline of this thesis, describing the sections in which we address the requirements and present the design of the receiver system fulfilling the requirements.

1.7 Thesis Layout

This thesis presents my work towards the GHY-3 antenna conversion project. My work focused on the design and development of the radio astronomy receiver system which replaces the existing communication receiver.

In Chapters 2 to 4 I describe the work I have done to integrate the new receiver system into the existing infrastructure of the GHY-3 antenna. The integration process starts in Chapter 2 with an analysis of the existing antenna optics. In Chapter 3 I present my design of the GHY-3 orthomode transducer which acts as the interface between the feed horn and the cryogenically cooled front-end electronics of the receiver system. In Chapter 4 I present my design of the GHY-3 corrugated ring-loaded feed horn. The feed horn design process uses parameters from both previous chapters to match the optical configuration of the antenna with the waveguide diameter of the orthomode transducer, which is integrated in the cryogenically cooled part of the receiver system.

In Chapter 5 I discuss the theory of gain stabilisation for coherent radio receivers. To do this I provide a short introduction into radio receivers, followed by a comparison between different stabilisation approaches. At the end of this chapter I discuss two stabilisation approaches in detail, which I considered for implementation in the GHY-3 receiver system.

Chapter 6 follows up on the two stabilisation approaches which I explained in the previous chapter and presents the experimental verification. This includes a description of the laboratory setup and the digital signal processing firmware implemented on the FPGA-based signal processing hardware. At the end of this chapter I present the measured performance of both stabilisation approaches with a short comparison of their advantages and disadvantages.

In Chapter 7 I present the complete receiver system for the GHY-3 antenna. I start with the system overview which is then followed by the design and development of a number of analogue signal components that I developed especially for this receiver system. After that I present the design and development of the temperature

stabilised module platform that houses all room temperature analogue signal components. In the final part of this chapter I present the FPGA-based digital signal processing hardware and firmware which implements the different operational modes of the antenna.

Finally, in Chapter 8 I present my conclusions along with an outline of the planned commissioning phase of the project.

Chapter 2

GHY-3 Telescope optics

This chapter describes the optical configuration of the GHY-3 antenna. First, we will give a short introduction into the basic theory of antennas and discuss some important antenna parameters, like the aperture efficiency, the beam efficiency, and common antenna designs. We then analyse the optical configuration of the GHY-3 antenna, which includes the measurement of the primary and secondary reflector and a simulation of the far-field beam pattern.

2.1 Introduction

Antennas are reciprocal devices, which means that the parameters describing the antenna are identical for it being used for transmission or for reception. A receiving antenna is generally considered a device that transforms free space waves into guided waves [34]. It is an essential element of a radio telescope and defines the overall performance. In this introduction we will only focus on reflector antennas and the theory relevant for the further understanding of the component design for the GHY-3 receiver system.

2.1.1 Reflector Antenna Designs

Reflector antennas have been used for a wide range of applications, from radar, deep-space communication to radio astronomy [35]. There are a number of different designs established, out of which we will describe the four most common ones.

Figure 2.1 shows the optical configuration of four different reflector antenna types. The antenna configuration (a) is called a Prime Focus antenna, which uses a parabolic shaped primary reflector to focus the wave front at a focus point on front of the reflector, an example for such an antenna is the Lovell Telescope. This means that the receiver system is located in front of the reflector, which can make it difficult to access it. On top of that, most radio astronomy receivers require cryogenically cooled hardware, which makes the receiver system heavy and bulky, to the extent that it might not be feasible to mechanical support it without causing substantial amount of blockage. The advantage of a prime focus configuration is that it provides a short focal length, which requires feed horns with a wide illumination angle. This is particularly advantageous at low frequencies, where a horn producing a narrow illumination angle would require a large aperture. The second configuration (b) is

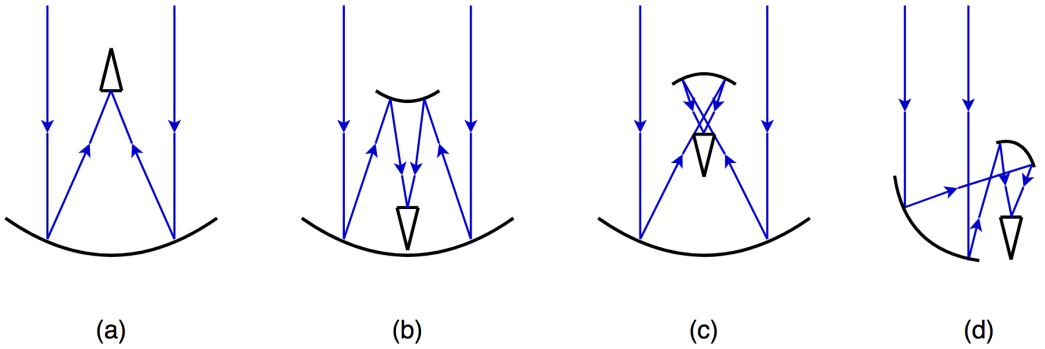

Figure 2.1: The optical configuration of (a) Prime Focus Antenna, (b) Cassegrain Antenna, (c) Gregorian Antenna, (d) Offset Gregorian Antenna.

called a Cassegrain antenna, which uses a parabolic primary reflector and a hyperbolic secondary reflector to focus the wave front close to the vertex of the primary reflector. Hence, the receiver system is located close to the vertex of the primary reflector with the feed horn facing torwards the secondary reflector. This configuration has a number of advantages compared to the prime focus configuration. First, any spillover from the

feed illuminating the secondary reflector points to the sky, which leads to a reduction in ground pickup. Secondly, it enables to increase the aperture efficiency by shaping the profile of the secondary and primary reflector, described in more detail in the next section. Third, the location of the receiver system at the vertex of the primary makes it easier to mount and maintain the receiver system. However, compared to the prime focus antenna, a Cassegrain system requires a high-gain feed horn, as the effective focal length is much longer. This can be a problem at low frequencies where a very large aperture horn may be required. The third configuration (c) is called a Gregorian antenna. It uses an concave elliptical profiled secondary reflector, which must be located behind the focus point of the primary reflector. This configuration has the same advantages as the Cassegrain system, but allows for feed horns with a larger illumination angle. The fourth configuration (d) is called an offset Gregorian antenna. For this design, the secondary reflector is placed off-axis of the primary reflector. The main advantage of this design is that the aperture is non blocked. This design is used by a number of instruments such as MeerKat, SKA, and the Green Bank Telescope.

2.1.2 Basics of Aperture Illumination and Antenna Pattern

A reflector antenna such as GHY-3 can be considered as a two-dimensional aperture, which transforms the aperture field distribution of the reflector into a far-field beam pattern. To discuss the conversion between the aperture field and the beam pattern we introduce a function $g(\boldsymbol{x})$ that defines the aperture illumination distribution, where $\boldsymbol{x}$ is the 2D vector in the aperture plane of the antenna. The function $F(\boldsymbol{n})$ defines the far-field voltage radiation pattern, where $\boldsymbol{n}$ is in polar coordinates as measured with respect to $\boldsymbol{x}$. The conversion between the illumination distribution and the field pattern is a two-dimensional Fourier transformation, which is given by

$$F(\boldsymbol{n}) = \iint_{apt} g(\boldsymbol{x}) e^{\frac{-i2\pi \boldsymbol{n}\boldsymbol{x}}{\lambda}} d\boldsymbol{x}. \tag{2.1}$$

Important transformations between the aperture field distribution and the far-field beam pattern are: the uniform illuminated aperture which converts to a Bessel J_0 function in the far-field beam pattern, and the Gaussian illuminated aperture which converts to a Gaussian far-field beam pattern. Note that most of the illumination field distributions can be considered as a combination of both. This is due to the truncation of the Gaussian aperture field at the edge of the reflector. The far-field beam pattern is best described by the full half power beam width HPBW and the full beam width between the first nulls BWFN. Reference [36] and [34] provide an approximation for the HPBW and BWFN for an uniform illuminated aperture, where the reflector has a diameter of D and receives or transmits a signal with a wavelength of λ.

$$\mathrm{HPBW} = 1.02\frac{\lambda}{\mathrm{D}}\mathrm{rad} \simeq 58.4^\circ\frac{\lambda}{\mathrm{D}}, \tag{2.2}$$

$$\mathrm{BWFN} = 2.439\frac{\lambda}{\mathrm{D}}\mathrm{rad} \simeq 139.8^\circ\frac{\lambda}{\mathrm{D}}. \tag{2.3}$$

These approximations however change with respect to the aperture illumination distribution. However, for most applications this approximation is useful to get an idea of the far-field beam pattern of the antenna.

2.1.3 Aperture Efficiency

The aperture efficiency η describes the relation between the effective collecting area of a reflector antenna and its real physical area. Values for the efficiency lie between $0 \leq \eta \leq 1$, where a value of one means that the effective collecting area is equal the physical area of the antenna. The relation between the aperture efficiency, physical antenna area, and effective antenna area is given by

$$\eta = \frac{A_{\mathrm{eff}}}{A}. \tag{2.4}$$

The aperture efficiency itself is composed of a number of individual factors [37]:

$$\eta = \eta_{\mathrm{illumination}} \cdot \eta_{\mathrm{spillover}} \cdot \eta_{\mathrm{surface}} \cdot \eta_{\mathrm{blockage}}, \tag{2.5}$$

respectively the illumination efficiency, the spillover efficiency, the surface efficiency, and the blockage efficiency.

The illumination efficiency defines the loss of effective collecting area due to under-illumination of the antenna surface when not being illuminated by a uniform aperture field. It is given by

$$\eta_{\text{illumination}} = \frac{\left(\iint_{apt} g(\boldsymbol{x}) d\boldsymbol{x}\right)^2}{A \iint_{apt} g(\boldsymbol{x})^2 d\boldsymbol{x}}. \tag{2.6}$$

A more uniform illumination will result in a higher illumination efficiency, however the disadvantage of a uniform aperture illumination is the sharp drop at the edge of the reflector which causes high side lobes in the far-field beam.

The spillover efficiency defines how much of the overall power emitted or received by the feed horn comes from the antenna aperture and how much power comes from beyond the aperture. The spillover efficiency is given by

$$\eta_{\text{spillover}} = \frac{\iint_{apt} g(\boldsymbol{x})^2 d\boldsymbol{x}}{\iint_{\infty} g(\boldsymbol{x})^2 d\boldsymbol{x}}. \tag{2.7}$$

A high spillover efficiency usually leads to a low illumination efficiency and vice versa. This is true for most antennas unless the profile of the reflectors are modified, usually called "shaped". A shaped system uses a special modified secondary reflector to produces a more uniform illumination pattern on the primary aperture, while keeping the spillover as small as possible. Therefore, this technique allows the designer to increase the illumination efficiency while preserving the spillover efficiency. Although this method increases the aperture efficiency it also increases the level of the first side-lobe, which depending on the application might or might not be acceptable. GHY-3 is an example of such a shaped antenna, which we will describe in more detail in Section 2.2.

The surface efficiency depends on the wavelength of the signal and the irregularities of the reflector surface. It is given by

$$\eta_{\text{surface}} = e^{-(4\pi\sigma/\lambda)^2}, \tag{2.8}$$

where λ represents the wavelength of the signal being transmitted or received and σ the RMS error of the of the reflector surface. Note that for an accurate calculation of the surface efficiency the RMS error must be weighted by the aperture illumination.

The blockage efficiency defines the loss of collecting area caused by blockage through a secondary reflector, struts or other components. It is given by

$$\eta_{\text{blockage}} = \left(1 - \frac{\iint_{blockage} g(\boldsymbol{x}) d\boldsymbol{x}}{\iint_{apt} g(\boldsymbol{x}) d\boldsymbol{x}}\right)^2. \tag{2.9}$$

The calculation of the blockage efficiency must also be weighted by the aperture illumination to get the correct result. Another approach to calculate the aperture efficiency that does not involve computing each efficiency factor individually is to calculate the maximum forward gain of the antenna. With the maximum forward gain we can calculate the effective antenna area and therefore the aperture efficiency. The effective antenna area is given by

$$A_{\text{eff}} = 10^{\frac{G}{10}} \frac{\lambda^2}{4\pi}, \tag{2.10}$$

where G is the maximum forward gain of the main beam in dBi and λ the wavelength of the signal transmitted or received.

2.1.4 Beam Efficiency

The beam efficiency η_{beam} defines how much of the total received or transmitted power is confined within the main beam. It is typically bound by the first nulls in the beam pattern, although for beam shapes that do not have those first nulls the definition of the main beam becomes arbitrary and must be defined. The beam efficiency is given by

$$\eta_{\text{beam}} = \frac{P_{\text{beam}}}{P_{\text{total}}} = \frac{\int_{beam} F^2(\boldsymbol{n}) dn}{\int_{4\pi} F^2(\boldsymbol{n}) dn}. \tag{2.11}$$

For radio astronomy applications it is important to be aware that the remaining power in the sidelobes can increase the system temperature of the telescope. This is

especially critical for sidelobes which are far out, as these tend to point at the hot ground rather than at the cold sky.

2.2 GHY-3 Optical Configuration

The GHY-3 antenna is a shaped Cassegrain system which has a primary reflector of 29.6 m in diameter and a secondary reflector of 3 m in diameter. The antenna was originally designed for communication applications, hence the primary and the secondary reflector were modified in their contour to produce a more uniform field distribution across the primary aperture, which improves the aperture efficiency and antenna gain at the expense of higher sidelobes. In the following sections we present the GHY-3 antenna model and its verification. The model allows us to simulate the far-field beam pattern of the antenna, based on the measured contour of the primary and secondary reflectors, enabling us to reveal any potential misalignments or problems with the current configuration of the antenna. In addition to that, the simulation also allows us to determine the position of the focus point in front of the primary vertex which is required to design the GHY-3 corrugated feed horn, presented in Chapter 4. It is worth pointing out that Goonhilly does not have any documents which describe the original design and reflector profiles of the antenna. That is why we rely entirely on the measurements of the reflectors to construct the antenna model.

2.2.1 Reflector Measurement

The primary and secondary reflectors were measured in January 2012 by Grahame Faulkner from the Engineering Department of the University of Oxford. Each reflector was measured using a different technique suitable for its physical size and accessibility at that time.

The secondary reflector was measured using a method called photogrammetry, which uses photographs from different positions to reconstruct the 3D surface of an object [38]. In our case, this is done by sticking a number of targets on the surface of the reflector, so that the software can identify the positions of it in all images. With

this, the software can calculate the position and distance at which the photograph was taken as well as calculate an accurate 3D model of the object in the pictures. The accuracy of this method is determined by the resolution of the camera and the number of photographs from different perspectives.

The primary reflector was not measured using photogrammetry, which was mainly due to two reasons. First the area of the reflector would have required a vast number of targets to be attached to and second the antenna could not be steered at that time, which made it impossible to attach targets at all. Therefore, it was decided to use a theodolite to measure the profile of the primary reflector. A theodolite is generally used to measure distances and angles in vertical and horizontal planes.

For our analysis of the optical configuration of the antenna, we received the unprocessed measurement data of the secondary and the primary reflector. In the following two Sections, we briefly describe the work carried out to reconstruct the reflector surface based on these measurements.

2.2.1.1 Primary Profile

The primary reflector measurement was performed with a theodolite, which measured and recorded the angles and distances between its position and points along a vertical cut through the centre of the reflector. At the time the primary reflector was measured the antenna was not only unable to move, it also was stalled at a tilted position which lead to a distortion in the measured profile.

The measurement setup is illustrated in Figure 2.2, the theodolite is marked with an T on the left-hand side and the tilted primary reflector is represented by the red curve on the right-hand side. The original recorded profile together with the profile after we applied the correction is shown in Figure 2.3. In both plots the measured positions along the reflector surface are represented by the blue dots and the black line represents a 4th order polynomial fit of the data points. The fit of the profile was necessary to interpolate between the discrete measurement points as well as to construct the reflector profile at the vertex, where no measurement points were available due to the blockage of the secondary reflector.

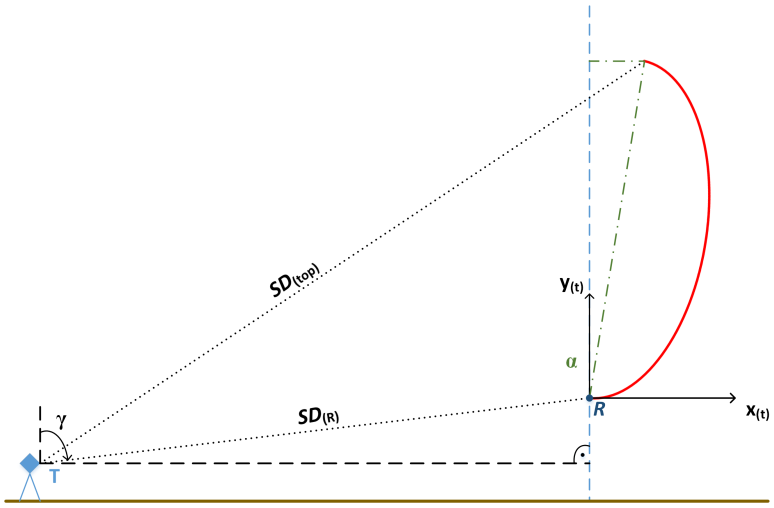

Figure 2.2: Measurement arrangement for the primary mirror. The theodolite is marked with a T and the reflector is represented by the red semi-circle. R and α are indicating the rotation point used to correct the profile.

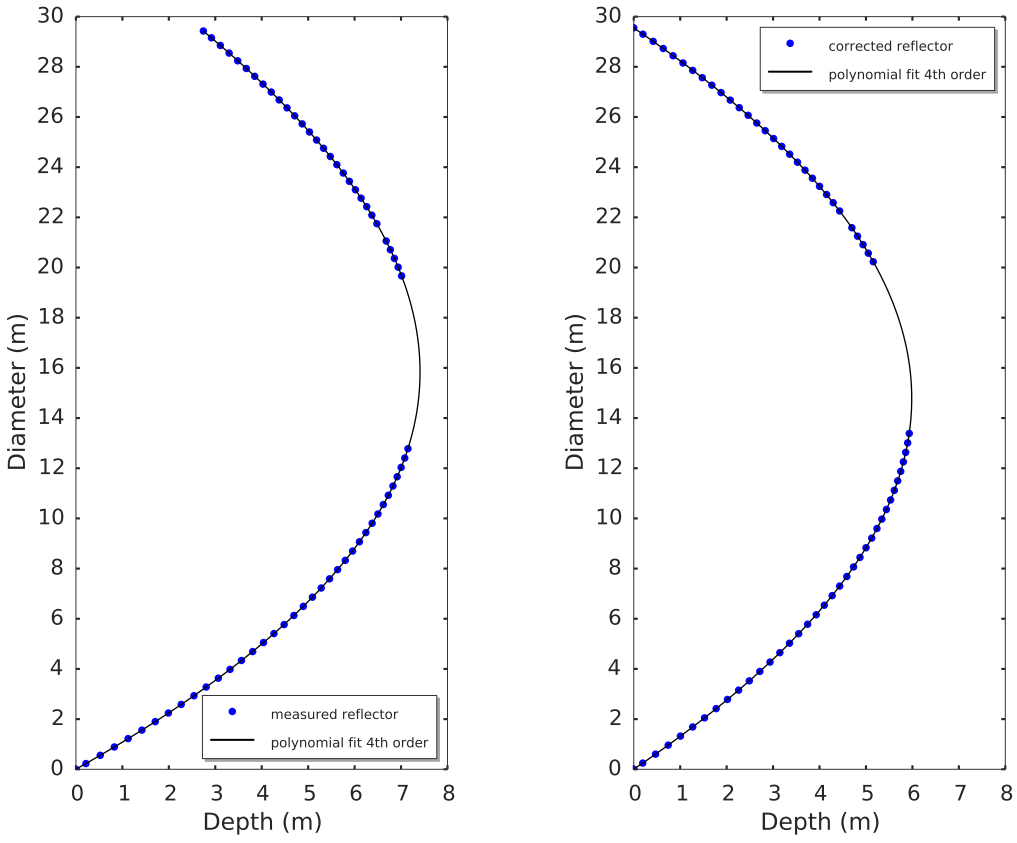

(a) Measured profile.

(b) Reconstruct profile.

Figure 2.3: GHY-3 primary reflector profile. (a) Profile as measured by the theodolite. (b) Profile after the geometrical reconstruction took place.

The 4th order polynomial fit of the reconstructed profile for the GHY-3 primary reflector is given by

$$2.2122e^{-6}x^4 - 1.3100e^{-4}x^3 - 2.4995e^{-2}x^2 + 0.7959x - 1.3047e^{-3}. \quad (2.12)$$

The correct order of the polynomial fit was verified by looking at the distribution of the residuals between the fit and the data points. The residuals for the 4th order polynomial shown in Equation 2.12 are random distributed, which shows that this fit is sufficient to describe the profile of the primary reflector.

2.2.1.2 Seccondary Profile

The GHY-3 antenna has two identical secondary reflectors, one which is currently mounted as part of the antenna and the other which is stored as a spare reflector. Since both reflectors are identical, the photogrammetry was done with the spare reflector. An image of the reflector with the attached targets used in the photogrammetry analysis is shown in Figure 2.4a. The corresponding reflector profile constructed via the photogrammetry is shown in Figure 2.4b. The blue dots represent the extracted reflector profile and the black line shows the 4th order polynomial fit of the data points. The coefficients describing the secondary profile are given by

$$3.22425e^{-2}x^4 - 2.32031e^{-1}x^3 + 5.82073e^{-1}x^2 - 7.55726e^{-3}x - 2.23597e^{-3}. \quad (2.13)$$

The correct order of the polynomial fit was also verified by looking at the distribution of the residuals between the fit and the data points. The residuals for the 4th order polynomial shown in Equation 2.13 are random distributed, which shows that this fit is sufficient to describe the profile of the secondary reflector.

2.2.2 Simulation of the Optical Configuration

The GHY-3 antenna was simulated using GRASP, General Reflector Antenna Software Package [39], which is used to model the optical configuration of reflector anten-

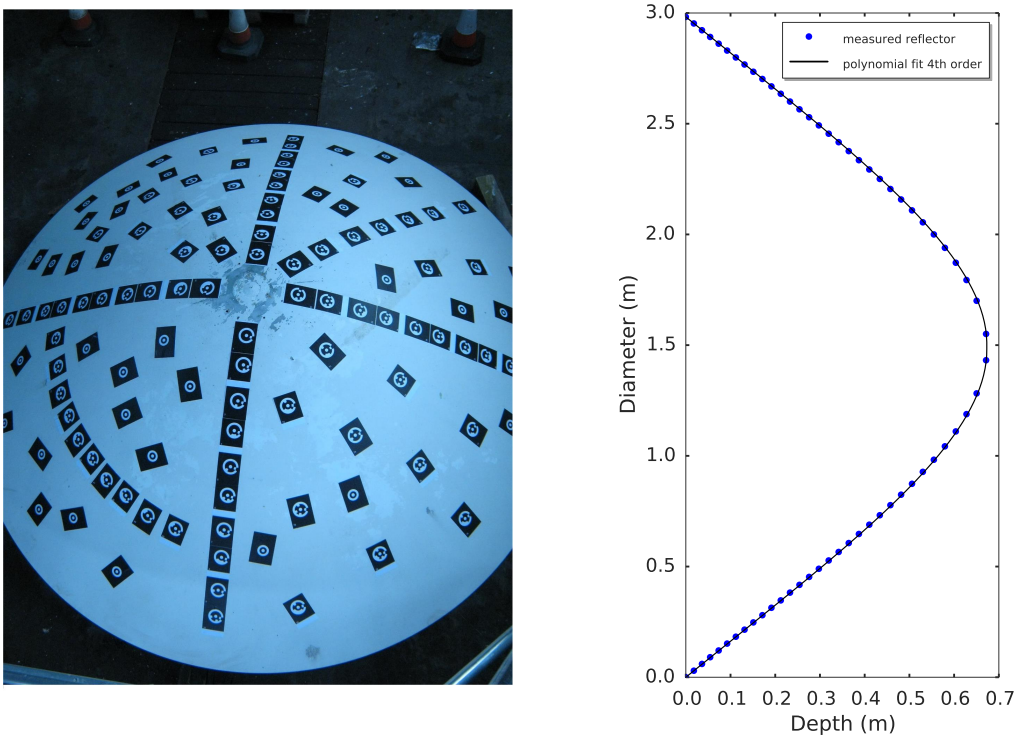

(a) Spare secondary reflector.

(b) Secondary profile.

Figure 2.4: GHY-3 secondary reflector. (a) Image of the spare secondary reflector including the targets used to perform the photogrammetry. (b) Measured and fitted secondary reflector profile.

nas. In our case, we use GRASP to create a model based on the measured reflector profiles and dimensions. We then use this model to simulate the overall performance of the antenna when it is illuminated by the GHY-3 corrugated feed horn.

However, before we can use the GRASP model to simulate the far-field beam pattern of the antenna, we needed to determine the exact position of the secondary reflector and the phase centre of the antenna. As mentioned before we do not have any of the original documents describing the optical configuration. Therefore, our approach was to use the measured profiles of the primary and secondary reflector to create a model that allows us to move the position of the secondary reflector up and down until the antenna focuses the wavefront. The optimization showed that the antenna performs best for a configuration where the distance between the secondary and primary vertex is 8.513 m, as shown in Figure 2.5. With this configuration the antenna has its phase centre at 1.82 m above the vertex of the primary reflector.

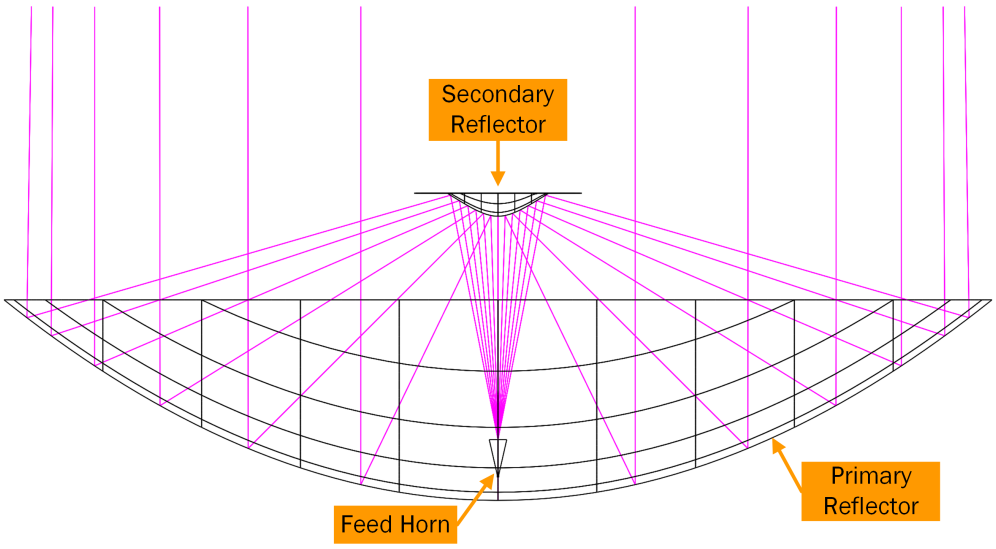

Figure 2.5: GRASP model of the GHY-3 antenna optical configuration.

2.2.2.1 Verification of the Antenna Model

In order to verify our optimized antenna model we went to Goonhilly and measured a number of dimensions including the distance between the secondary and primary vertex. The distance between both reflectors was measured directly by going into the dish and using a laser distance measurer with an accuracy of ±2 mm. Figure 2.6 shows us measuring the distance between both reflectors. We measured the distances between the reflectors once from the secondary to the primary and once from the primary to the secondary. Both measurements provided similar results. The first measurement resulted in a distance of 8.511 m and the second measurement in a distance of 8.517 m. Since the measured distance agreed very well with the predicted distance of the GRASP model we consider this model as validated and will use it for the simulation of the far-field beam pattern and aperture efficiency.

2.2.3 Simulation of the Antenna Performance

In this section we present the simulated far-field beam pattern of the GHY-3 antenna together with a number of parameter which describe its performance. The simulation imports the beam pattern of the simulated GHY-3 corrugated feed horn to illumi-

Figure 2.6: Verification of the antenna model by measuring the distance between the secondary and primary vertex.

nate the secondary reflector. The design of the GHY-3 corrugated feed horn will be described in Chapter 4. This allows us to simulate a more accurate beam pattern compared to a simulation that would illuminate the optics by an ideal feed horn beam pattern. The simulation produces the far-field beam pattern at four frequencies across the receiver pass band, 4.0 GHz, 5.5 GHz, 7.0 GHz, and 8.5 GHz.

In order to discuss a number of important aspects in the antenna far-field we show two sets of plots. The first one shows the beam pattern over a solid angle of $-1 \leq \theta \leq 1$ degree, thereby allowing us to discuss the properties of the main beam, first sidelobe level, and cross polarisation level. The second one shows the beam pattern over a solid angle of $-180 \leq \theta \leq 180$ degree, which allows us to discuss the effect of spillover at the secondary and primary reflector. Figure 2.7 shows the normalised main beam of the antenna radiation pattern at four frequencies. The traces plotted for each simulated frequency are; E-field (red), H-field (blue), D-field (green) which represents the 45 deg copolar field, and the cross-polarisation at $\phi =$ 45 deg (black). As an addition to this figure, Table 2.1 provides the simulated values

for the, maximum forward gain, the first sidelobe level, the peak cross-polarisation, the aperture efficiency, the beam efficiency, the full half power beam width, and the beam width between the first nulls.

The beam pattern plots show that the main beam is circular symmetric at all frequencies, which is also supported by the fact that the cross polarisation level remains below $-37\,\mathrm{dB}$. The first side lobe level is with a value of approximately $-15\,\mathrm{dB}$, typical for a shaped antenna system [40]. In addition to that, the aperture efficiency of approximately 80 % also shows that the GHY-3 feed horn performs very well with the existing optical configuration of the antenna.

Figure 2.8 shows the entire normalised antenna radiation pattern at four frequencies. The traces plotted for each simulated frequency are; E-field (red), H-field (blue), D-field (green) which represents the 45 deg copolar field, and the cross-polarisation at $\phi = 45\,\mathrm{deg}$ (black). It is important when looking at the radiation pattern to keep in mind that we did not simulate any support structure of the secondary reflector, hence the radiation pattern looks symmetric. The two features to look at in these plots are the increase in sidelobe level caused by the spillover of the feed horn past the secondary reflector, and by illumination from the secondary reflector spilling past the primary reflector.

The first feature can be seen as an increase at $\theta \approx 15\,\mathrm{deg}$ which corresponds to the edge of the rim around the secondary reflector. As those sidelobes are close to the

Table 2.1: Simulated antenna performance when illuminated with the GHY-3 corrugated feed horn.

Parameter		4.0 GHz	5.5 GHz	7.0 GHz	8.5 GHz
max forward gain	dBi	60.702	63.628	65.656	67.057
first sidelobe level	dB	-16.01	-16.02	-14.91	-14.47
peak cross-polarisation	dB	-43.02	-51.12	-37.65	-43.43
aperture efficiency	(%)	79.66	82.51	79.49	76.11
beam efficiency	(%)	61.82	60.13	58.02	45.51
HPBW	(deg)	0.1506	0.1119	0.0881	0.0727
BWFN	(deg)	0.3534	0.2600	0.2047	0.1673

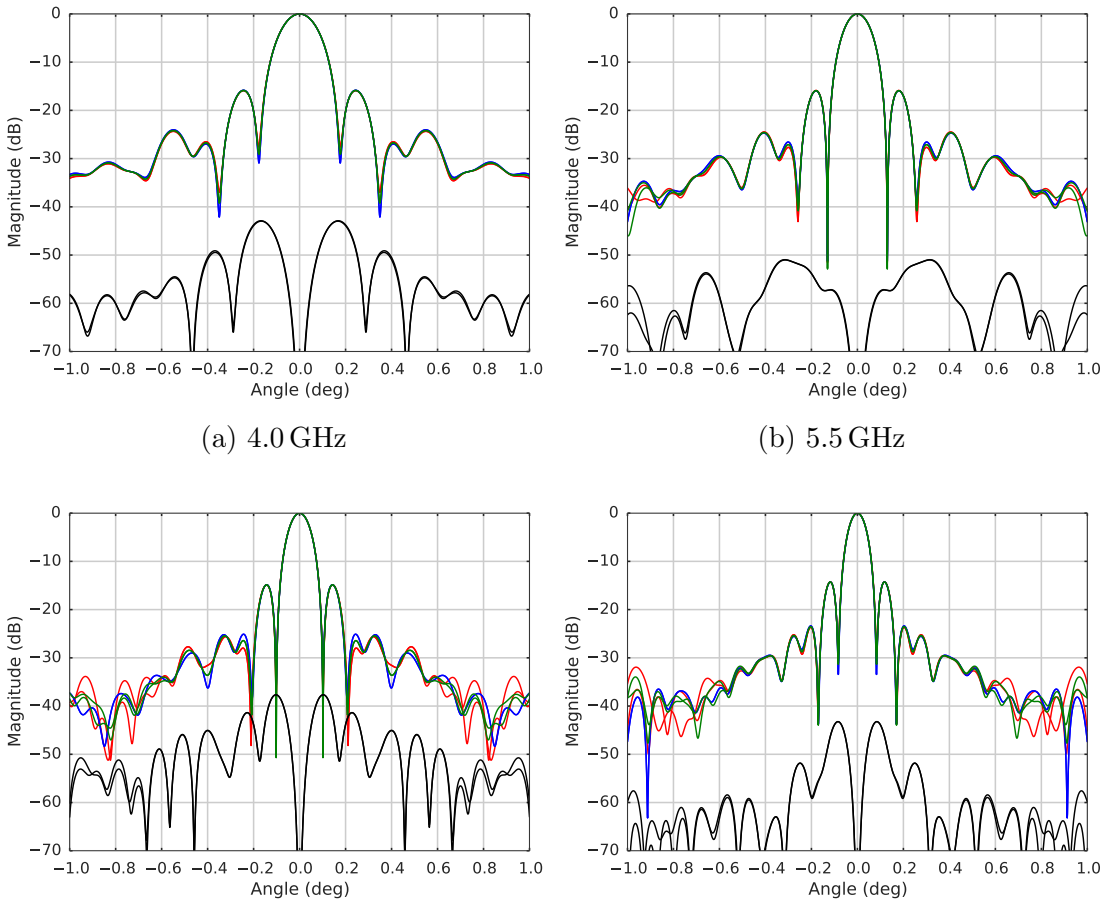

(a) 4.0 GHz (b) 5.5 GHz

(c) 7.0 GHz (d) 8.5 GHz

Figure 2.7: The far-field radiation patterns in rectangular coordinates of the GHY-3 antenna in the range $-1 \leq \theta \leq 1$ deg. E-field (red), H-field (blue),D-field (green), and cross-polarisation at $\phi = 45$ deg (black).

main beam for most observations it will be likely that they end up pointing at the cold sky. The second feature can be seen as an increase of the sidelobe level far out, which in fact points in the rearward direction of the antenna at $\theta \approx 100$ deg. The power within these sidelobes will most likely end up pointing at the ground. Nevertheless, the simulation predicts that these sidelobes are below -70 dB which implies a only small temperature contribution. To get an estimate of the temperature contribution caused by the sidelobes we integrated over the beam pattern and assumed that all sidelobes for $\theta \geq 90$ deg pick up ground radiation. The simulation showed that the temperature contribution is: 4.89 K at 4.0 GHz, 2.69 K at 5.5 GHz, 3.65 K at 7.0 GHz, and 2.44 K at 8.5 GHz.

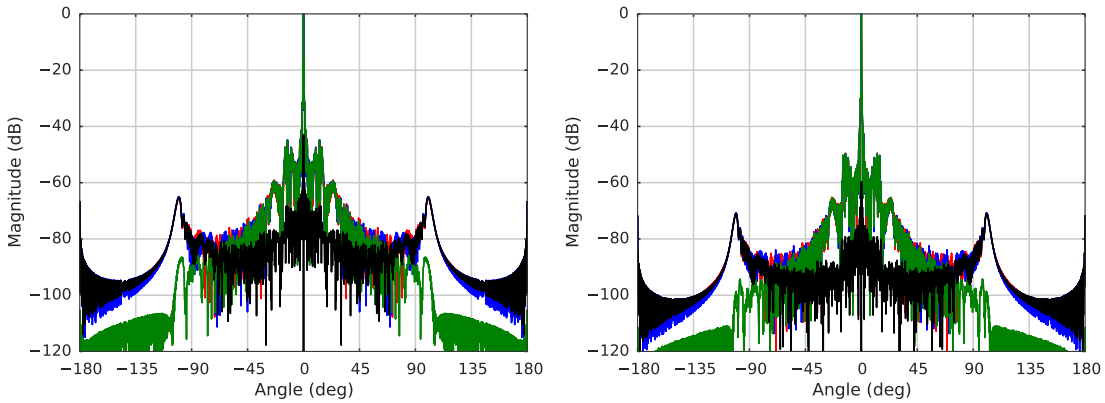

(a) 4.0 GHz

(b) 5.5 GHz

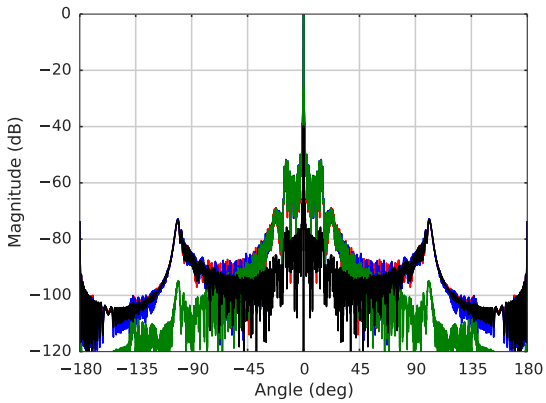

(c) 7.0 GHz

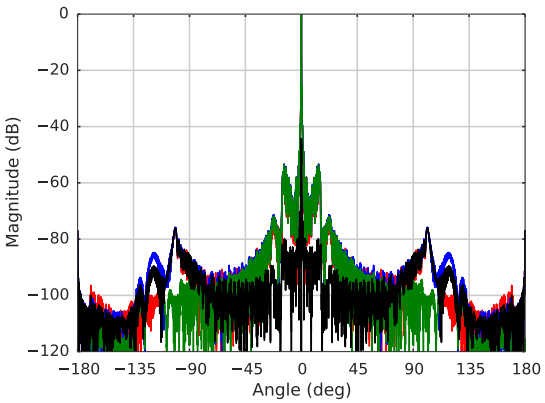

(d) 8.5 GHz

Figure 2.8: The far-field radiation patterns in rectangular coordinates of the GHY-3 antenna in the range $-180 \leq \theta \leq 180$ deg. E-field (red), H-field (blue),D-field (green), and cross-polarisation at 45° (black).

2.3 Summary

In this chapter we presented the simulation of the existing GHY-3 antenna optics. The originally measured reflectors have been analyzed and a GRASP model was created. The model has been validated by us measuring the position of the secondary reflector with respect to the primary vertex. The simulated antenna far-field radiation pattern using the GHY-3 corrugated feed horn, from Chapter 4, to illuminate the secondary reflector predicted good performance with respect to the beam circularity, first sidelobe level, peak cross-polarisation level, and aperture efficiency.

Chapter 3

Compact Quad-Ridge Orthogonal Mode Transducer

The feed system forms the transition from free-space waves to waves confined in coaxial cables. It consists of two parts, the feed horn and the orthomode transducer, both of which were designed to match the existing GHY-3 optics. An orthomode transducer (OMT) is commonly used to extract the two orthogonally polarized modes from a waveguide and transfer these into two coaxial cables. In the case of a circular waveguide, it extracts the signal from the fundamental TE_{11} modes. This chapter describes the design of the compact quad-ridge orthomode transducer, which we published in [41].

3.1 Requirements

The GHY-3 OMT design is driven by a number of requirements. The first requirement specifies the operational bandwidth, which has to cover the $4 - 8\,\mathrm{GHz}$ C-band as well as the deep-space communication downlink at $8.4\,\mathrm{GHz}$. This results in a total operational bandwidth of $4 - 8.5\,\mathrm{GHz}$, which corresponds to a fractional bandwidth requirement of approximately 2.1:1. The second requirement constrains the physical size of the OMT. As the receiver operates at C-band traditional, wideband OMTs form large masses with respect to the overall mechanical receiver size, which can

affect the design of the cooling system and increase the heat load on the system. The existing cryostat for the GHY-3 receiver system, restricted the available length for the OMT design to approximately 100 mm. Therefore, we specify that the GHY-3 OMT must have a five times shorter transition length compared to traditional quad-ridged OMT designs employing a smooth ridge profile, without compromising the broad performance. The third requirement specifies the performance of the OMT. For the receiver to meet its sensitivity and system temperature requirements the OMT must have an insertion loss of less than 0.4 dB and a return loss better than −15 dB over the operational frequency band. Note that these values are typical for OMTs.

3.2 Traditional Orthomode Transducers

This section gives a brief overview of different OMT designs from literature. There are four established designs that are commonly used, a planar-probe OMT [42], a turnstile junctions OMT [43, 44], a Bøifot junction OMT [45, 46], a double-ridged OMT [47], and a quad-ridged OMT [48] design.

A planar-probe OMT uses four probes, aligned at 90° spacing, to extract both polarisations. The signal of each pair of opposite probes is combined using a 180° hybrid, which is a device that allows one to sum both probe signals with the correct phase difference. A photo of a planar-probe OMT is shown in Figure 3.1a. The impedance matching between the waveguide impedance and the probe impedance is done using a quarter-wave backshort. This matching technique limits the operational bandwidth of the planar-probe OMT to approximately 1.5:1.

Turnstile junction and Bøifot junction OMTs extract the two polarisations from the common port using a waveguide junction. The five-port junction separates each orthogonal polarized signal into two designated rectangular waveguides, which are then combined. The signal is then extracted using a standard rectangular waveguide to coaxial adapter. An image illustrating both OMT designs is shown in Figure 3.1b. The Bøifot OMT design can be seen as a modification of the turnstile OMT, where two of the ports are folded parallel to the common port. These OMT designs enable

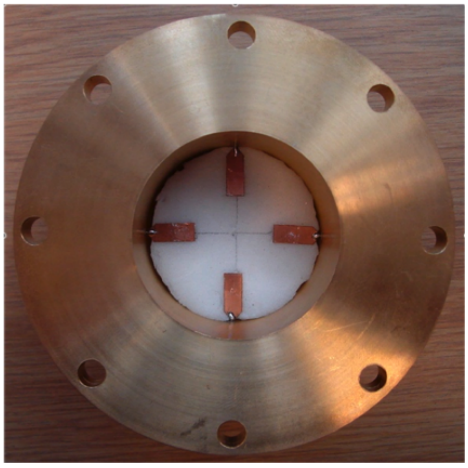

(a)

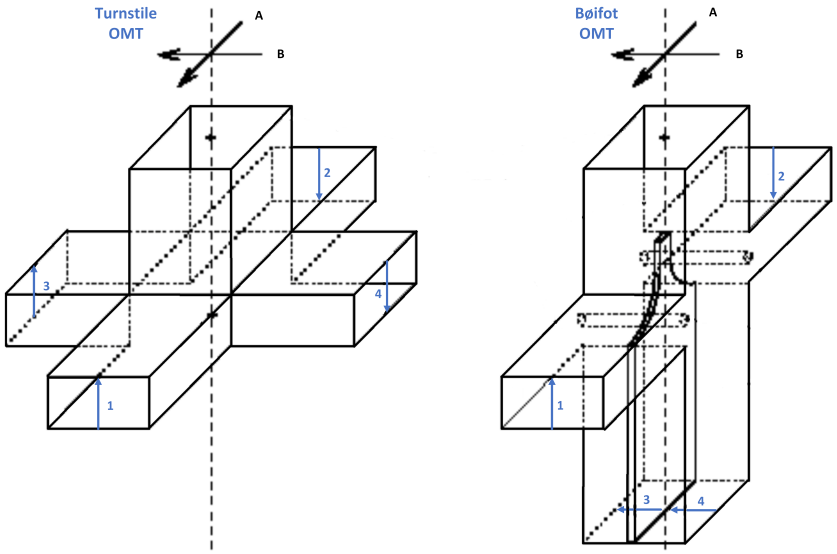

(b)

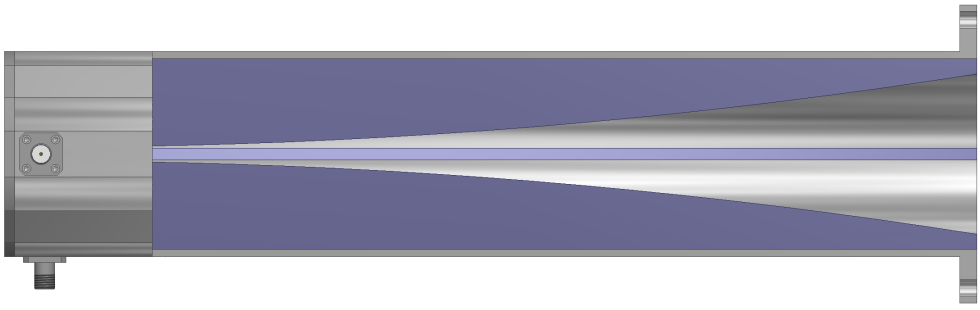

(c)

Figure 3.1: (a) Top view of the compact planar OMT from [42]. The four probes are aligned at 90° spacing, to extract both linear polarisations. (b) Schematic of a Turnstile and Bøifot OMT [49]. (c) Cross-sectional view of a traditional quad-ridged OMT, showing a smooth tapering profile.

an operational bandwidth of approximately 1.8:1.

Double-ridged and quad-ridged OMTs use a tapering ridge design to concentrate the signal in a small gap between the ridges at the centre of the waveguide. The signal is then extracted using a coaxial probe which crosses the gap. An illustration of a quad-ridged OMT is shown in Figure 3.1c. The impedance matching between the waveguide impedance and the coaxial probe impedance is done by gradually decreasing the gap between the opposite ridges. Reference [48] demonstrates that the useable bandwidth of a quad-ridged OMT with smoothed tapered ridges corresponds directly to the physical length and shape of the ridges, e.g. a transition length of $2\lambda_L$ allows for a bandwidth of approx. 1.7:1 whereas $4\lambda_L$ allows for a bandwidth up to 2.2:1, where λ_L corresponds to the wavelength of the lowest operational frequency. For our application this means that a traditional OMT using a transition length of $4\lambda_L$ would have a physical length of approximately 300 mm.

The GHY-3 OMT design is based on the traditional quad-ridged OMT design from [48] and an optimization technique for finline taper presented in [50]. This optimization technique starts with a small number of parameter to find the rough ridge shape which provides the best transmission performance. It then increases the number of parameter to refine the shape which further improves the transmission performance. The detailed optimization process used to design the GHY-3 OMT is described in the next section.

3.3 Design and Simulation

Since the GHY-3 OMT will be used with a C-band corrugated horn with a circular aperture and connected via two coaxial cables to the receiver, it needs to be optimized to serve two separate but interconnected purposes. Firstly, we need to ensure that the energy from the TE_{11} modes propagating in the unloaded waveguide is transferred efficiently to the section where the coaxial probes cross the gap between the quad-ridged fins. Secondly, we need to transfer the energy concentrated in the gap between the ridges to an SMA connector efficiently via a quarter-wavelength backshort.

We used a combination of MATLAB R2014b [51] and Ansys's High Frequency Structural Simulator HFSS v.15 [52] for the design and optimization process. MATLAB is used to define the HFSS 3D model, allowing it to be changed in a time saving manner, while HFSS is used to analyse and optimise the model. In order to use MATLAB to create HFSS models and set up optimization processes we used the "HFSS-MATLAB-SCRIPTING-API" from [53]. This library provides a set of MATLAB functions that allowed us to interact with HFSS. To implement our optimization process we extended the existing list of functions with a number of specialised functions that allowed us to describe the complex structure of the compact quad-ridged OMT. The flow diagram of the optimization process used to design the ridge profile of the quad-ridged OMT is shown in Fig. 3.2. Blue and red represents the steps which were executed in MATLAB and HFSS, respectively. The final step shown in green represents a user decision where we check the result of each optimization run and decide if another run is necessary or if the optimization process is complete.

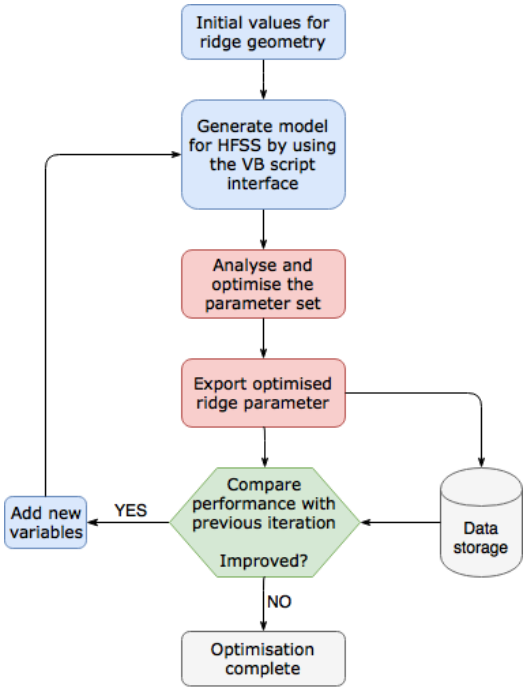

Figure 3.2: The optimization process used to design the ridge profile of the OMT. Blue and red represent the steps which are executed in MATLAB and HFSS, respectively. Once the optimization has been completed for a particular set of variables, we look at the result and decide whether to add more variables (green).

Table 3.1: List of individual goals used to optimise the transmission between the quad-ridged waveguide and the SMA connector.

Calculation	S-Parameter	Frequency range	Condition	Goal	Weight
return loss	S_{11}	$4.0 - 9.0\,\mathrm{GHz}$	<=	$-20\,\mathrm{dB}$	1
isolation	S_{21}	$4.0 - 9.0\,\mathrm{GHz}$	<=	$-40\,\mathrm{dB}$	1
insertion loss	S_{31}	$4.0 - 9.0\,\mathrm{GHz}$	>=	$0\,\mathrm{dB}$	1
cross-polarisation	S_{41}	$4.0 - 9.0\,\mathrm{GHz}$	<=	$-40\,\mathrm{dB}$	1

3.3.1 Coaxial to Quad-Ridge Transmission

The first step to develop the OMT was to design a broadband transmission between the quad-ridged waveguide and the two coaxial probes. This was done by setting up a model that consisted of a quad-ridged waveguide segment with two coaxial probes at each end. An image of this model is shown in Figure 3.3a and the cross sectional view from the backshort side is shown in Figure 3.3b. This model was optimized using the Non-linear Programming optimiser in HFSS v.15. The optimiser allows us to specify a list of goals with individual weightings. For this optimization we specified the simulated return loss, insertion loss, isolation and cross-polarization between the four coaxial ports. The cost function implemented in HFSS for this optimiser is given by

$$\mathrm{Cost} = \sum_{1}^{\mathrm{N}} w_i \epsilon_i^2 \,, \tag{3.1}$$

where N represents the number of individual goals, w_i the individual weighting factor, and ϵ_i the residual error for each goal. We applied a uniform weight for all goals and a maximum of 500 iterations. Usually the cost function converged to a minimum after a few hundred iterations. A list of the specified goals including the frequency range, condition and weighting factors for the coaxial to quad-ridge transmission is shown in Table 3.1.

The optimization process led to a set of optimized parameters, which define a geometrical solution that allows for a broad band transmission over the required frequency range of $4 - 8.5\,\mathrm{GHz}$. The final parameters used for the quad-ridged to SMA connecter transmission are shown in Table 3.2.

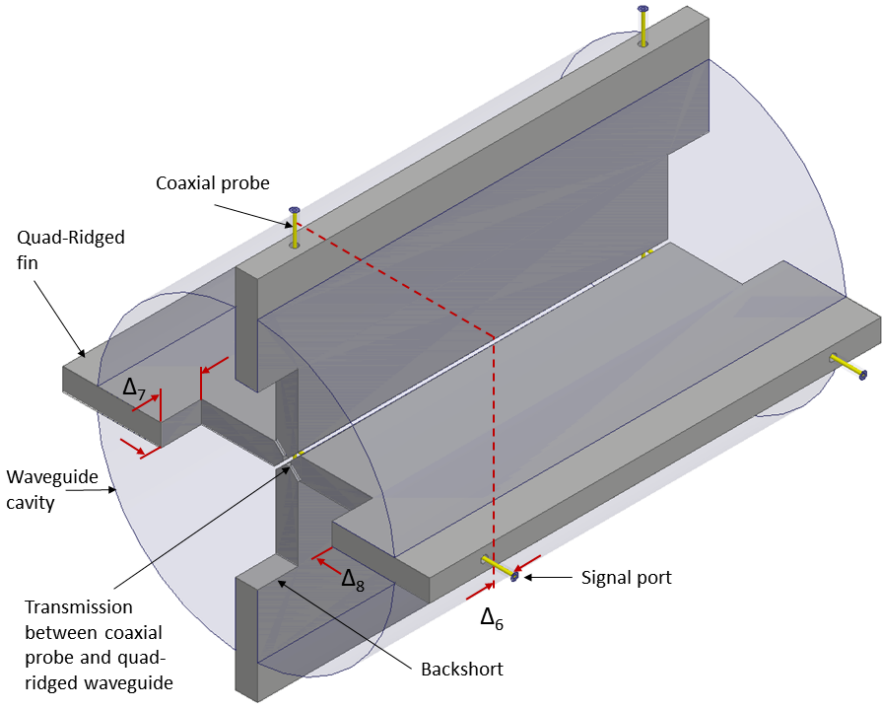

(a)

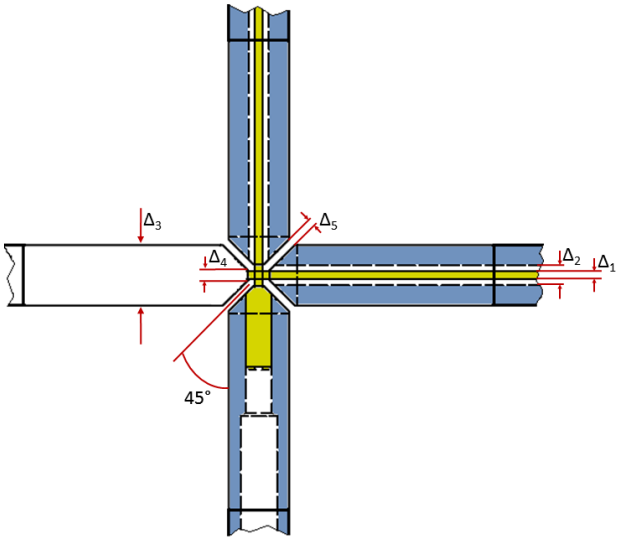

(b)

Figure 3.3: (a) Shows the transmission model. The signal ports are attached to the coaxial probes to simulate the signal to the SMA connector. The dimensions Δ_6, Δ_7, and Δ_8 are the free design parameters for the offset between the probes, the length of the backshort, and the width of the backshort, respectively. (b) Cross sectional view from bottom. Δ_1 and Δ_2 are the fixed dimensions for the coaxial transmission line. Δ_3, Δ_4, and Δ_5 are the free design parameters for the ridge thickness, the centre gap, and the gap at 45° between the perpendicular ridges, respectively.

Table 3.2: Optimized geometrical parameters for the transmission between the quad-ridged waveguide and the SMA connector.

Designation	Parameter	Value	Fixed/variable
waveguide radius	Δ_0	24.4 mm	fixed
coaxial pin diameter	Δ_1	0.254 mm	fixed
coaxial probe outer diameter	Δ_2	0.59 mm	fixed
ridge thickness	Δ_3	3.6 mm	variable
centre gap	Δ_4	1.3 mm	variable
45° gap	Δ_5	0.48 mm	variable
offset between both probes	Δ_6	1.08 mm	variable
length of the backshort	Δ_7	6.70 mm	variable
width of the backshort	Δ_8	28.0 mm	variable

3.3.2 Ridge Profiling

The second step to develop the OMT was to reduce the transmission length between the field in the unloaded waveguide and the field concentrated in the centre gap of the final quad-ridged structure, as defined by the transmission model. This was done by adopting a method presented in [50], which uses a focusing approach, where the optimization process includes an increase in the number of variables as the optimization progresses. We started the optimization procedure by fixing the transmission length of the ridge section to be $0.8\lambda_L$, which corresponds to a physical length of approximately 75 mm. We then defined a set of parameters that describes the ridge geometry as a cubic spline interpolation between a number of points along the length of the ridge. The first and the last point in each set of parameters are fixed to match the waveguide radius and the final centre gap dimensions, respectively. Each of the remaining points can be chosen randomly within sensible constraints.

To optimise a given set of parameters, we used the optimization procedure which we presented earlier in Figure 3.2. The applied optimiser in HFSS v.15 is the same as used for the optimization of the coaxial to quad-ridge transmission. A list of the specified goals including the frequency range, condition and weigthing factors for the ridge profiling optimization is shown in Table 3.3.

The optimization process starts initially with a small set of parameters, usually

Table 3.3: List of individual goals used to optimise the transmission between the quad-ridged waveguide and the SMA connector.

Calculation	S-Parameter	Frequency range	Condition	Goal	Weight
return loss	S_{11}	$4.0 - 8.5\,\text{GHz}$	$<=$	$-20\,\text{dB}$	1
isolation	S_{21}	$4.0 - 8.5\,\text{GHz}$	$<=$	$-40\,\text{dB}$	1
insertion loss	S_{31}	$4.0 - 8.5\,\text{GHz}$	$>=$	$0\,\text{dB}$	1
cross-polarisation	S_{41}	$4.0 - 8.5\,\text{GHz}$	$<=$	$-40\,\text{dB}$	1
TE_{21}	–	$7.3 - 8.5\,\text{GHz}$	$<=$	$-40\,\text{dB}$	1
TE_{31}	–	$8.0 - 8.5\,\text{GHz}$	$<=$	$-40\,\text{dB}$	1
TM_{11}	–	$5.5 - 8.5\,\text{GHz}$	$<=$	$-40\,\text{dB}$	1

$2 - 4$, to find the general form of the ridge. We then retain this shape and add new variables, to form a larger set of parameters. All variables in the new parameter set are then optimized again to refine the ridge shape. This procedure is repeated until adding further variables does not lead to an improvement in performance, as measured by the cost function.

3.3.3 Preliminary Optimization Results

After we finished the first OMT model, we identified that the optimization in favour of return loss, insertion loss, cross-polarisation and isolation was not sufficient to achieve the required performance over the operational frequency band. Investigation showed that we also needed to consider the production of higher-order modes. Our simulation showed the appearance of three spurious modes, which limited the performance of the OMT. The modes were identified as TE_{21}, TE_{31}, and TM_{11}. The field distribution for these modes, including the wanted TE_{11} mode, is shown in Figure 3.4. We included these modes into the optimization process, by defining the transmission from the coaxial port to the respective mode as an individual goal, which then can be suppressed by the optimization process. After modifying the list of individual goals, we started a new optimization run.

The simulation initially started with 4 independent variables and was refined twice. The third refinement did not lead to an improvement. Therefore, the optimization process finished with 16 optimized parameters, shown in Table 3.4, which describe

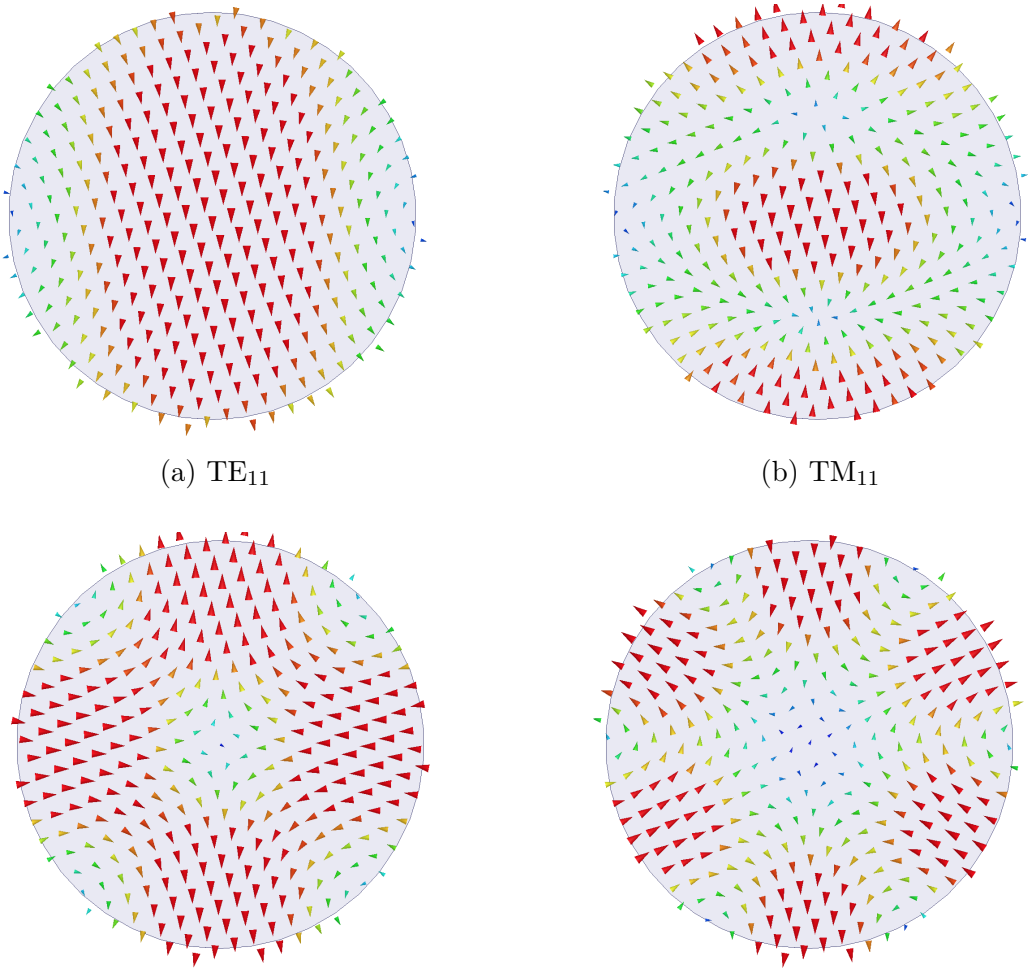

(a) TE_{11} (b) TM_{11}

(c) TE_{21} (d) TE_{31}

Figure 3.4: Field distribution for TE and TM modes in a circular waveguide.

Table 3.4: Geometrical parameters describing the optimized spline interpolation along the ridge.

parameter	value	parameter	value
Δ_{wg}	24.4 mm	Δ_9	9.4737 mm
Δ_1	19.3133 mm	Δ_{10}	7.0581 mm
Δ_2	18.5003 mm	Δ_{11}	4.8541 mm
Δ_3	17.4781 mm	Δ_{12}	4.6190 mm
Δ_4	20.8090 mm	Δ_{13}	3.4956 mm
Δ_5	15.1357 mm	Δ_{14}	2.4681 mm
Δ_6	13.9231 mm	Δ_{15}	1.4347 mm
Δ_7	14.1476 mm	Δ_{16}	2.2798 mm
Δ_8	12.7779 mm	Δ_{gap}	1.3 mm

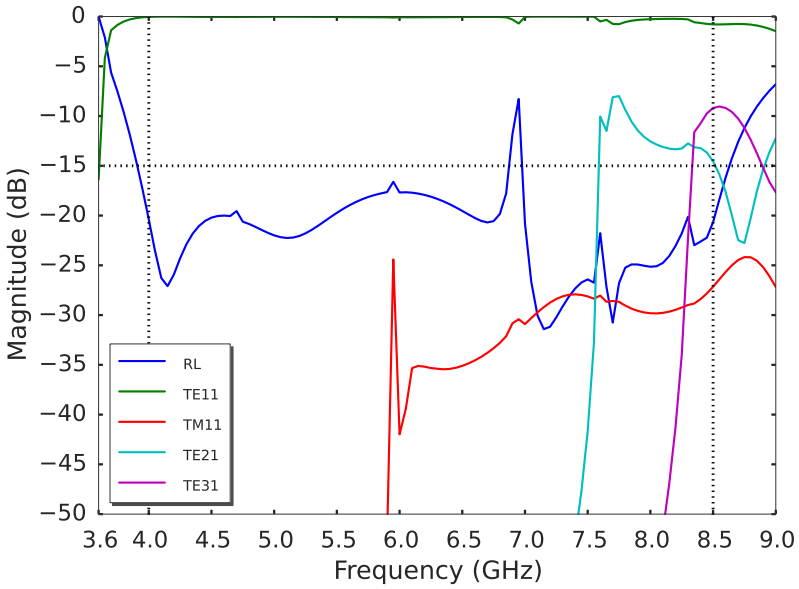

Figure 3.5: Shows the simulated mode production of the OMT relative to the TE_{11} mode.

the spline interpolation along the length of the ridge. The simulated performance including the production of higher order modes for the OMT is shown in Figure 3.5. The plot shows a wideband transmission of the wanted TE_{11} mode. The TM_{11} mode is produced at a relatively low and constant level, whereas the production of the TE_{31} and TE_{21} mode is relatively high, especially directly above their cutoff frequencies. Simulations have indicated several approaches to even further suppress these modes. The TE_{21} mode could be suppressed by offsetting the two pairs of perpendicular ridges, which would break the symmetry required to produce this mode. The TE_{31} mode could be suppressed even more effectively, by widening of the ridges towards the circular waveguide port. However, each of these options can also result in an increase of mode production for the other two remaining modes. The return loss is well below $-15\,\mathrm{dB}$ except for one spike at $6.9\,\mathrm{GHz}$. Simulations showed that this spike corresponds to a trapped mode or cavity mode resonance within the OMT structure. Such resonances appear when there are modes present that can only propagate within certain parts of the OMT structure and have no means to dissipate their energy [54].

3.3.4 Trapped Mode Investigation

At first we investigated the correlation between the optimized ridge form and the trapped mode resonance. This was done by comparing our profile to a standard form with the same physical length. It turned out that the resonance is present in both cases, which indicates that the profile of the ridge does not cause the resonance. A literature review showed that such trapped mode resonances can also be found in traditional quad-ridged OMT designs e.g. in [55, 56].

There are two conceivable solutions to suppress such a resonance, either by allowing it to propagate into the direction of the waveguide port or by absorbing the energy internally. Before we considered any major changes to our optimized design, we decided to simulate first what improvement an internal absorber would provide. The absorber is modelled as a circle with a centre hole, allowing the field to be reflected in the centre and absorbed at greater radii. Figure 3.6 shows the location of the absorber at the back of our simulation model. To better visualise the absorber we coloured the absorbing area in orange.

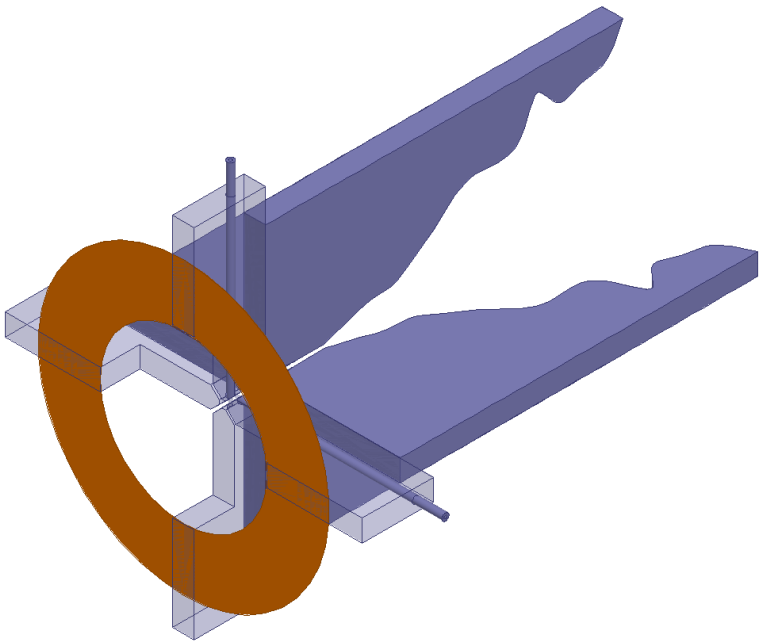

Figure 3.6: Shows the location of the absorber in our simulation model. The absorber is coloured in orange.

To analyze the effect of the absorber we compared the internal field distribution of the OMT model for both cases. The simulation of the field distribution is shown in Figure 3.7. The right-hand side and left-hand side show the field with and without an internal absorber present, respectively. Note, that in these plots the absorber is not coloured. On the left-hand side, the resonance builds up at 6.8 GHz (3.7c), peaks at 6.9 GHz (3.7e), and decreases again at 7.0 GHz (3.7g). Parallel to that, on the right-hand side the field remains within the ridge structure and no resonance can be seen. At 6.9 GHz (3.7f) and 7.0 GHz (3.7h) one can clearly see how energy is dissipated in the absorber. It is worth noting that this energy increases the insertion loss of the OMT. However, this is only the case at the resonance frequency. For lower or higher frequencies, the absorber does not influence the insertion loss. As seen by comparing the field at 6.0 GHz (3.7a,3.7b) where the presence of the absorber does not change the field distribution within the OMT.

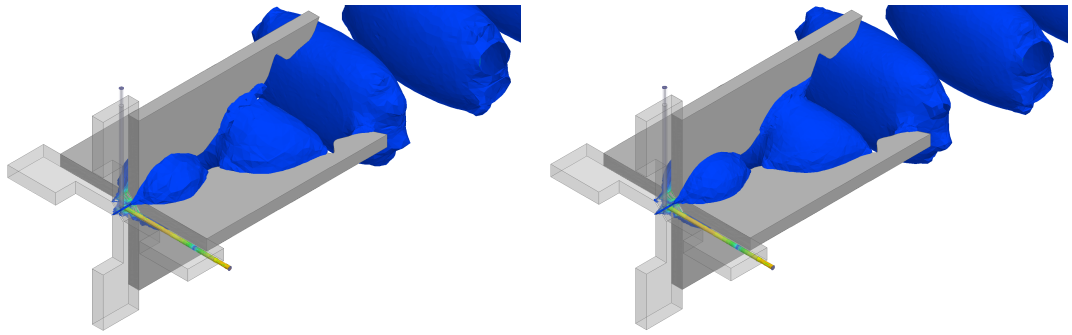

(a) 6.0 GHz without absorber

(b) 6.0 GHz with absorber

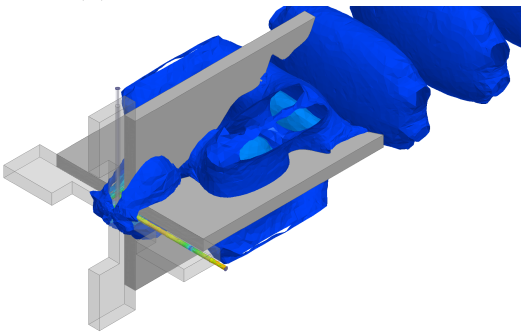

(c) 6.8 GHz without absorber

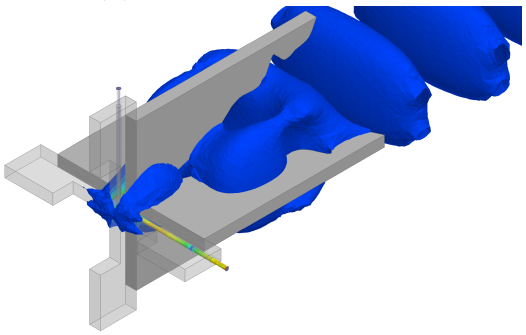

(d) 6.8 GHz with absorber

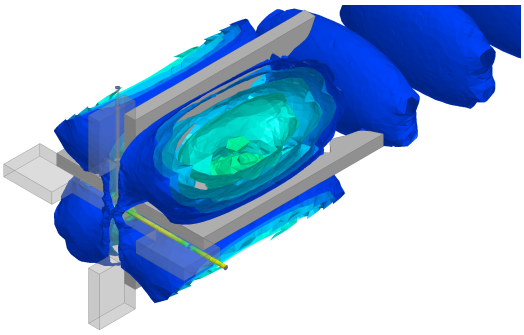

(e) 6.9 GHz without absorber

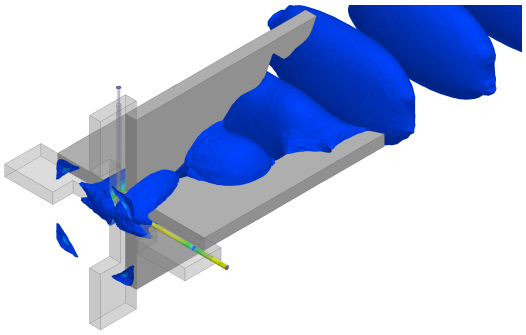

(f) 6.9 GHz with absorber

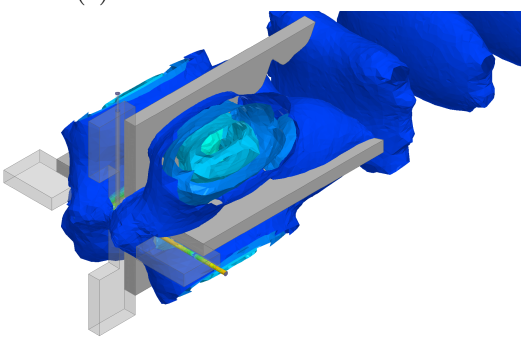

(g) 7.0 GHz without absorber

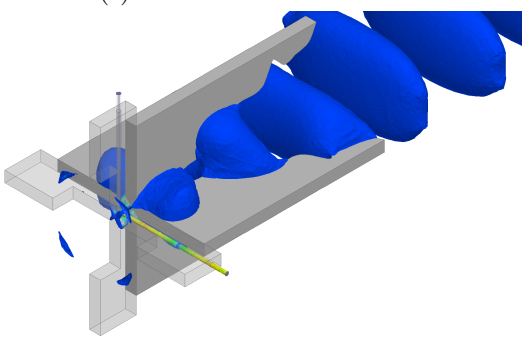

(h) 7.0 GHz with absorber

Figure 3.7: Shows the field distribution in the OMT model. The right-hand side and left-hand side show the field with and without an internal absorber present, respectively.

3.3.5 GHY-3 Design

The simulated performance of the OMT including the absorber is shown in Figure 3.8. The sharp spike in return loss at 6.9 GHz is diminished by the absorber and the return loss remains well below −15 dB over the designed frequency band. Furthermore, one can see by comparing the response to Figure 3.5 that the absorber also improved the suppression of the TE_{21} mode around 7.7 GHz. This shows that the design fulfils the GHY-3 requirements with respect to its physical size, bandwidth, insertion loss, and return loss.

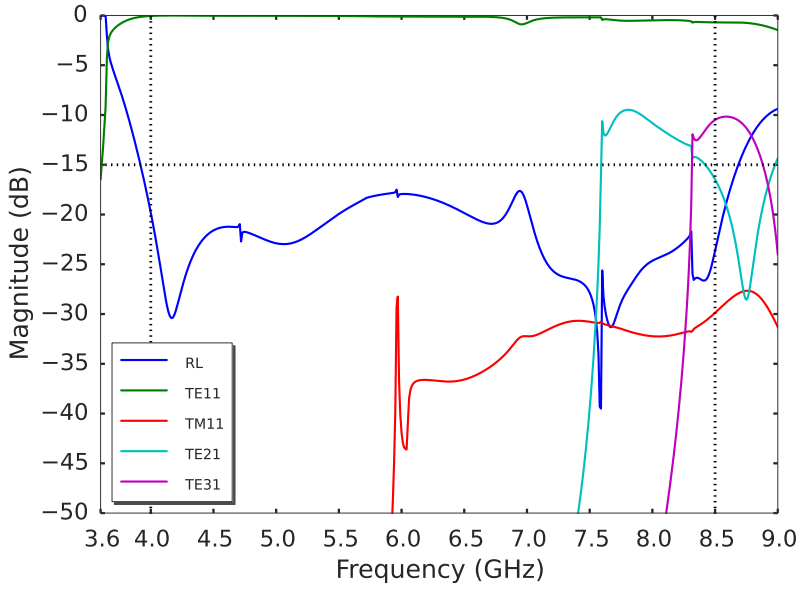

Figure 3.8: The simulated mode production of the OMT relative to the TE_{11} mode, with an absorber present.

3.4 Prototype and Experimental Results

We manufactured two identical prototypes, from aluminium, based on the CAD model shown in Figure 3.9. Both were fabricated in five steps, using wire eroding technology, with a tolerance better than 50 μm. At the first step, the waveguide including the grooves aligning the ridges were wire eroded. In the second step, the ridges without their final profile were fitted and aligned into the grooves and the holes for the coaxial probes were drilled. In the third step, the centre gap, the final ridge thickness, and

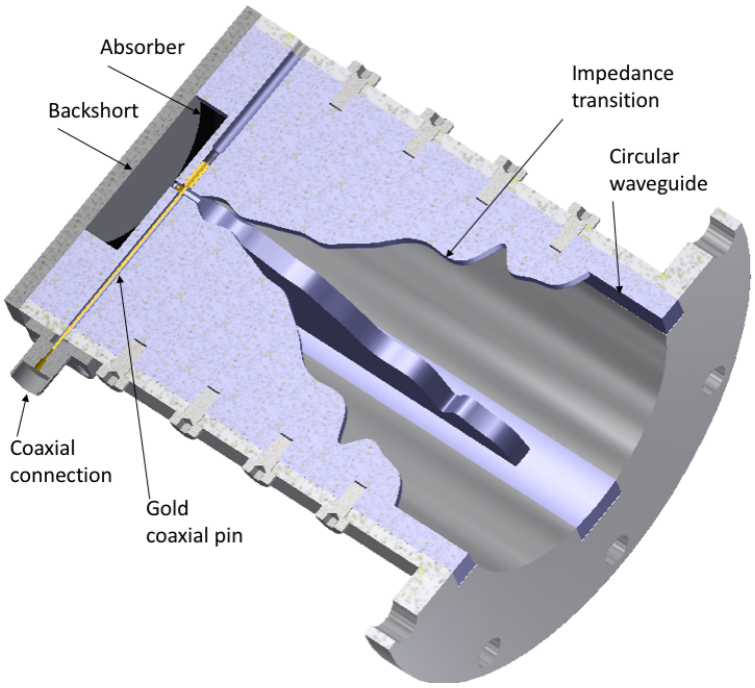

Figure 3.9: Cross-sectional view of the OMT through the centre line. The four ridges are slid into the groove of the circular waveguide and held in place by radial screws. The golden coaxial pin is inserted through the hole opposite the SMA connector and set into position by the thread at the centre of the ridge.

chamfer were wire eroded. In the fourth step, the ridges were removed and the varying height profile was wire cut along the ridge length. Finally, the ridges were aligned again and the coaxial pins were fitted in. The actual matching of the coaxial probes was done later, by terminating the waveguide port and measuring the return loss of both polarisations while aligning the pins with a screwdriver.

All measurements were performed using an Anritsu 37369C Vector Network Analyser (VNA) which was calibrated to its coaxial ports. The return loss and isolation were measured by connecting the two VNA ports to each polarisation port of the OMT, with the waveguide port terminated by a circular waveguide load with an integrated absorber spear in its centre. We treated this termination as an ideal absorber, therefore no calibration was applied to remove any reflections from this termination method.

The simulated and measured response for the return loss and isolation between the two coaxial ports is shown in Figure 3.10. The operational frequency band is indicated

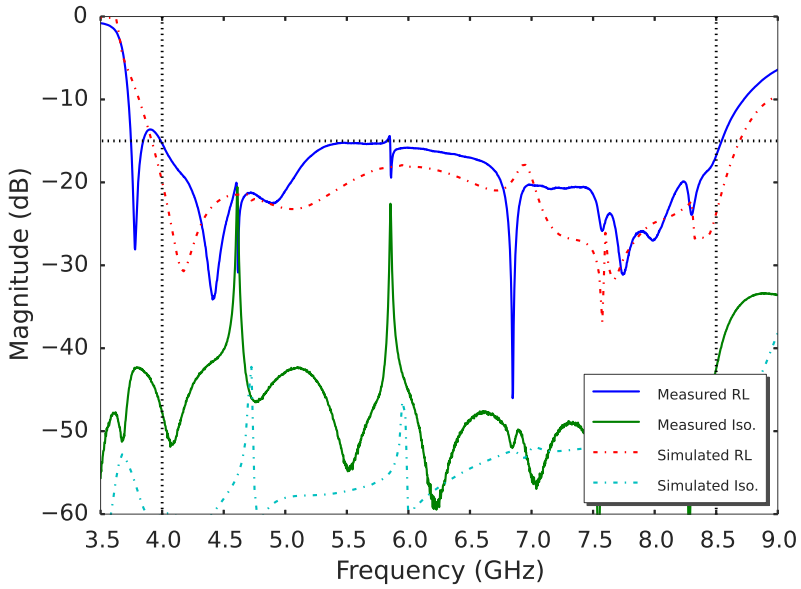

Figure 3.10: Simulated and measured characteristics of the OMT, terminated with a waveguide load. Traces plotted are return loss and isolation between the two coaxial ports. The solid lines show the measured responses for return loss (blue) and isolation (green). The dashed-dotted lines show the simulated performances for return loss (red) and isolation (turquoise). The design band of the OMT is indicated by vertical lines and the requirement in return loss by the horizontal line.

by two vertical lines and the requirement in return loss by a horizontal line. The measured return loss is below $-15\,\mathrm{dB}$ over the entire frequency range from $4-8.5\,\mathrm{GHz}$ and agrees very well with the simulated prediction. The isolation remains well below $-40\,\mathrm{dB}$ except for two spikes at $4.7\,\mathrm{GHz}$ and $5.9\,\mathrm{GHz}$. We assume that these spikes also correspond to trapped-mode resonances within the OMT structure which are not fully absorbed by the integrated absorber. Nevertheless, their appearance does not compromise the performance of the OMT and therefore we did not investigate these any further.

The insertion loss and the cross-polarization coefficient were measured by connecting both OMTs at their circular waveguide ports, as shown in Figure 3.11. This setup was required as no commercial SMA to waveguide adapter covers the entire operational bandwidth of our OMT. As we can not measure the insertion loss of a single OMT directly, we modelled the measurement setup using both OMTs and compared the predicted results with our measurement. This configuration allowed us to con-

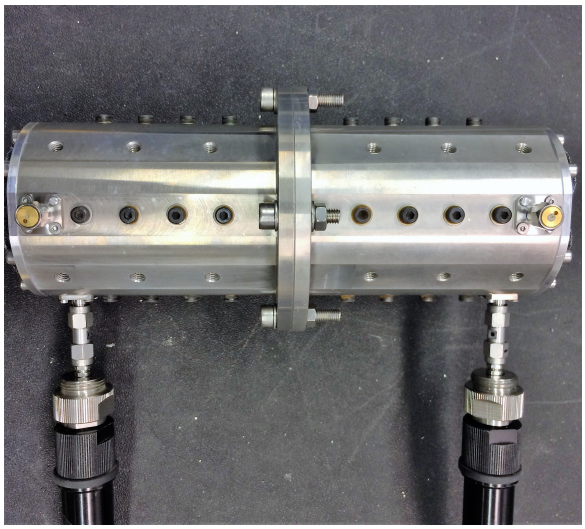

Figure 3.11: Measurement setup showing the two OMT's connected at their circular waveguide ports. The VNA is connected to one polarisation at each OMT, to measure the combined insertion loss.

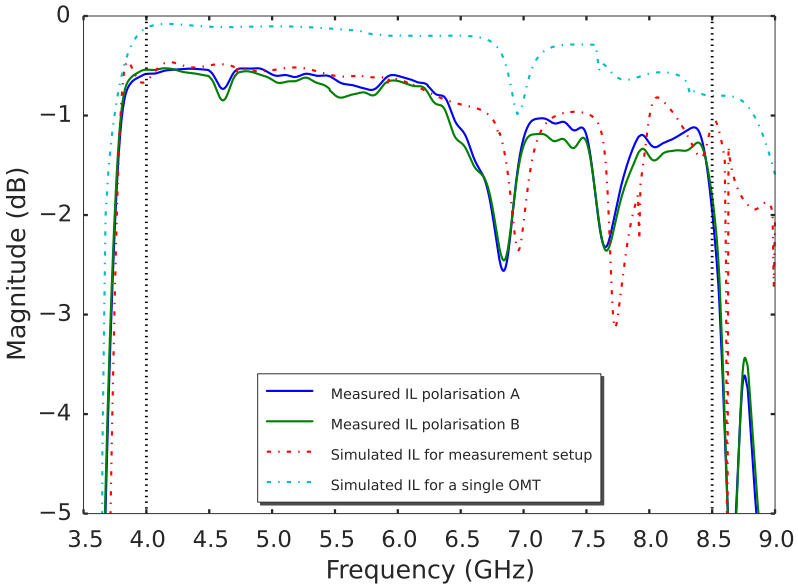

Figure 3.12: Simulated and measured insertion loss of the measured OMT setup. Traces plotted are the measured insertion loss for both polarization A and B, the simulated insertion loss of the measurement setup and the simulated performance of a single OMT. The design bandwidth of the OMT is indicated by vertical lines.

sider the measurement setup as a 4-port device, where the combined insertion loss is represented by the scattering parameters S_{31}, S_{42} and the combined cross-polarisation by S_{41}, S_{32}. The S parameter matrix describes the electrical behaviour of a N-port

device by measuring the relationship between the reflected and incident power waves at each network port. For each S parameter measurement, the unused ports were terminated using two 50 Ω SMA terminations.

Figure 3.12 shows the measured insertion loss for both polarisations in comparison to the predicted response of the model. The two solid lines represent the measured insertion loss for both linear polarisations. The measured performance agrees very well with the modelled prediction of this setup. Therefore, we are confident that the physical performance for the insertion loss of a single OMT also agrees with the simulated prediction. The drop in insertion loss at 6.9 GHz can be seen in all three traces, the measured data, the simulated measurement setup, and the single OMT simulation. This feature corresponds to the loss of energy which is dissipated in the backshort absorber and has been discussed earlier. However, the second dip at 7.7 GHz is only present in the measurement setup and not in the simulation of the single OMT, which is why we conclude that this dip is due to a resonance which is created by having a closed cavity measurement setup.

The cross-polarisation in our measurement setup is defined as the coupling between the TE_{11} mode of polarisation A into polarisation B. The signal is emitted in the first OMT at polarisation A and received in the second OMT at Polarisation B, which corresponds to the S parameter S_{41}, S_{32} in our measurement setup. The comparison of the measured cross-polarisation together with the simulated predictions of the measurement setup and the single OMT is shown in Figure 3.13. The measured data shows a high number of resonances, which are due to reflections within the cavity of the measurement setup. The data agrees very well with the predicted performance of the simulated measurement setup, which further validates our model. Therefore, we are confident that the cross-polarisation for a single OMT matches the simulation with a cross-polarisation level below −50 dB. However, the simulation of the single OMT (red line) also shows two spikes at 4.7 GHz and 5.9 GHz. We have seen similar spikes at the same frequency in the isolation measurement before and conclude that the spikes in cross-polarisation correspond to the same trapped mode resonance as the spikes in insertion loss, although, we are confident that these spikes do not compromise

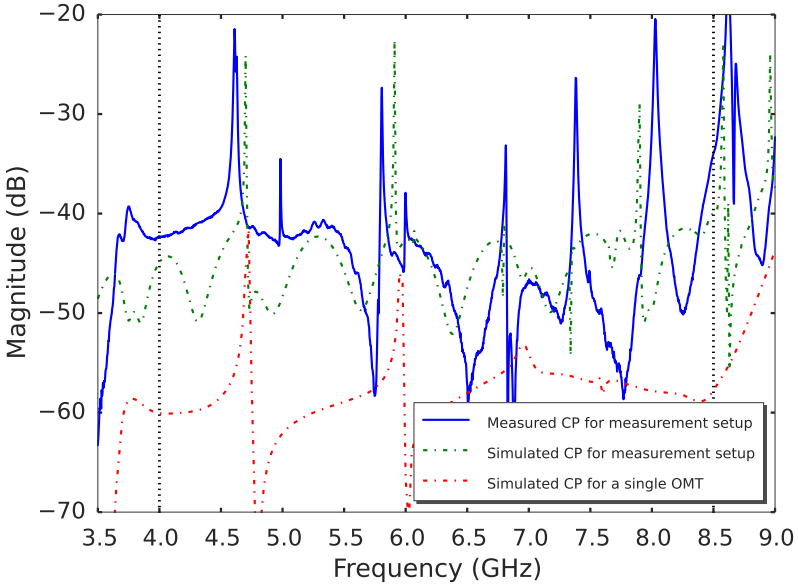

Figure 3.13: Simulated and measured cross-polarisation of the measured OMT setup. Traces plotted are measured and the simulated cross-polarisation of the measured setup, and the simulated performance of a single OMT. The design band of the OMT is indicated by vertical lines.

the performance of the OMT as their peaks remain below $-40\,\mathrm{dB}$.

3.5 Summary

In this chapter we presented the design, optimisation, and measurement of the GHY-3 compact quad-ridged orthomode transducer. The GHY-3 OMT uses a novel approach which reduced the transition length by a factor of five compared to traditional wideband OMTs while retaining a fractional bandwidth of 2.1:1. The reduction in transition length was achieved by optimizing the ridge profile using an optimization technique which increases the number of parameter throughout the optimization process.

Two prototypes were manufactured and tested in the frequency range $4-8.5\,\mathrm{GHz}$, and we found excellent agreement between the measured and simulated performance. The measured cross-polarisation is low at $-40\,\mathrm{dB}$ and indicates that the simulated cross-polarisation of a single OMT of less than $-50\,\mathrm{dB}$ is possible. The measured return loss remains below $-15\,\mathrm{dB}$ over the whole frequency band.

Chapter 4

Corrugated Ring-loaded Feed Horn

A feed horn is commonly used to illuminate reflectors and lenses. It can be found in any communication, satellite tracking, and radio astronomy dish throughout the world. A important feed horn design is the so-called corrugated feed horn, which uses a corrugated surface to support the propagation of hybrid modes. These modes are a combination of TE and TM modes. The advantage of a corrugated feed horn compared to a smooth-wall feed horn is that it has a higher efficiency, lower sidelobe levels, a better rotational symmetry, and a lower cross-polarisation level [57]. These benefits make a corrugated feed horn very popular for radio astronomy applications and for dual-polarisation systems [35].

In the first part of this chapter we describe the requirements on the GHY-3 feed horn, which are derived by the existing antenna configuration and the receiver requirements. This is followed by the description of the design process used to develop the GHY-3 feed horn. In the second half we discuss the simulated performance of a number of different feed horn designs and compare their performance. Finally we present a combined simulation of the GHY-3 OMT together with the GHY-3 corrugated feed horn.

4.1 Requirements

The GHY-3 corrugated feed horn is designed to match the existing optical configuration of the antenna, as well as to enable the receiver system to meet its sensitivity requirements. There are four key requirements, which are outlined below. Firstly, the feed horn needs to support the receiver bandwidth $4 - 8.5\,\text{GHz}$ with a return loss better than $-30\,\text{dB}$. Secondly, the aperture efficiency of the antenna system should be maximised by the illumination pattern of the horn. Therefore, the optimum edge taper illumination level must be defined. Thirdly, the cross-polarisation level must be 30 dB below the corresponding co-polarisation level. The final requirement addresses the physical length of the feed horn, in order to keep manufacturing costs low we decided that the physical length of the horn should be restricted to approximately 1 m.

4.2 Design and Simulation

The GHY-3 feed horn design is based on the guideline for corrugated feed horn designs, "Design of Corrugated Horns: A Primer" from [58]. Table 4.1 shows a list of parameters that are required to design and describe a corrugated feed horn. Some of the parameters are defined in the initial requirements, such as the return loss and cross-polarisation level. Others are design parameters that need to be determined in order to fulfil the initial requirements.

The design procedure begins in Section 4.2.1 by defining the general feed horn geometrics which determine the coupling to the existing antenna optics. Section 4.2.2 then describes the design of the corrugations, which is followed by a discussion of three types of mode converter in Section 4.2.3. This section then finishes by choosing the most suitable mode converter for the GHY-3 feed horn. The final design Section 4.2.4 discusses a number of empirical feed horn profiles that we considered for the GHY-3 feed horn.

Table 4.1: Parameters describing the corrugated feed horn.

Description	Symbol
Lowest operational frequency	f_{min}
Highest operational frequency	f_{max}
Design frequency	f_{d}
Output frequency	f_{o}
Input radius	r_{i}
Output radius	r_{o}
Length	L
Number of corrugations in the horn	N
Pitch	p
Pitch-to-width ratio	δ
Depth of the corrugations	d
Number of corrugations in the mode converter	N_{mc}
Mode converter type	–
Corrugated surface profile	–
Half-subtended angle for the edge-taper	α
Edge taper value	ET
Cross-polarisation level	CP
Return loss	RL

4.2.1 Coupling to the Optics and Horn Geometrics

The coupling of the feed horn to the reflector determines the overall efficiency of the system. In order to optimise the system for a high aperture efficiency we need to design the feed horn to have a specific illumination level at the edge of the secondary mirror. The edge-taper value defines the difference in illumination power from the centre of the secondary mirror to its edge. For example an edge-taper value of 15 dB means that the relative power level illuminating the mirror decreases by 15 dB from its peak value at the centre to the edge of the mirror. The edge-taper value is a compromise between the illumination efficiency and the spillover efficiency of the system. Figure 4.1 taken from [59] shows the antenna aperture efficiency as a function of the edge-taper value, where f_b shows the different aperture efficiencies for different percentage of blockage by the secondary mirror. The blockage caused by the GHY-3 secondary mirror is approximately 10 %, which corresponds to $f_b = 0.10$. The edge-taper value for the optimum aperture efficiency in this case is between $10 - 12$ dB. To use this

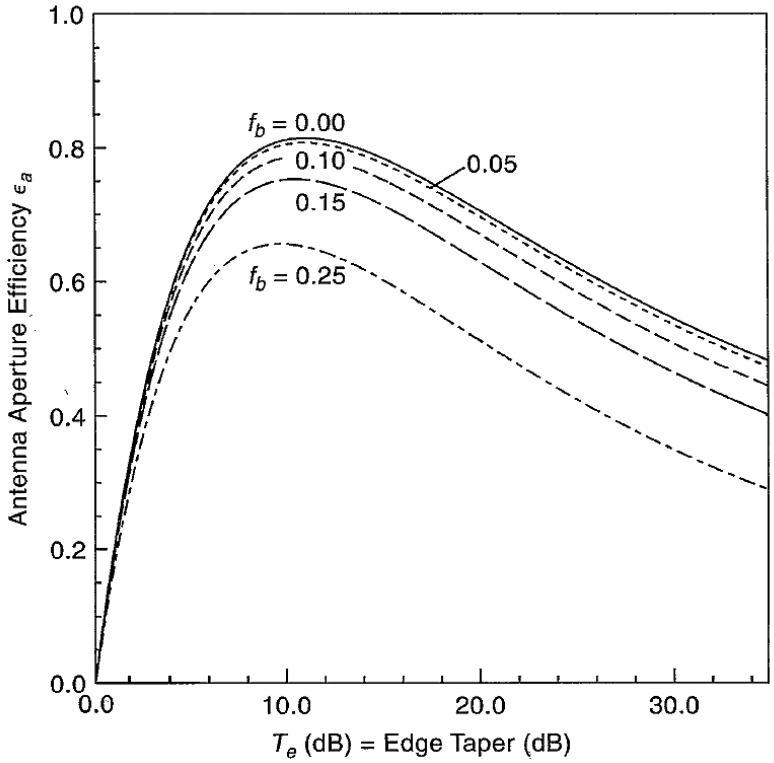

Figure 4.1: Antenna aperture efficiency ϵ_a as a function of the edge-taper value T_e and the fraction of the radius blocked by the secondary mirror f_b, [59].

value with the GHY-3 antenna, we need to associate the edge-taper value with the angle defining the edge of the secondary mirror as seen from the focus point of the feed horn. This angle can be derived from the GRASP model, which we used in Chapter 2 to simulate the optical configuration of the antenna. The GHY-3 half-cone angle for an edge-taper value of 12 dB is 12.8 deg.

In the next step, we define the input radius and estimate the output radius which allows us to define the edge-taper value at the corresponding half-cone angle. The input radius is defined by the waveguide radius of the OMT, $r_{\mathrm{i}} = 24.4\,\mathrm{mm}$. The exact value of the output radius depends on a number of parameters, which are the opening angle of the feed horn, the value and angle of the edge-taper, the length of the horn, and the horn profile. Figure 4.2 provides an estimate of the output radius for a 12 dB edge-taper along a range of half-subtended angle between 40 deg and 12 deg. The values for producing this plot are taken from [58]. The estimated value for the

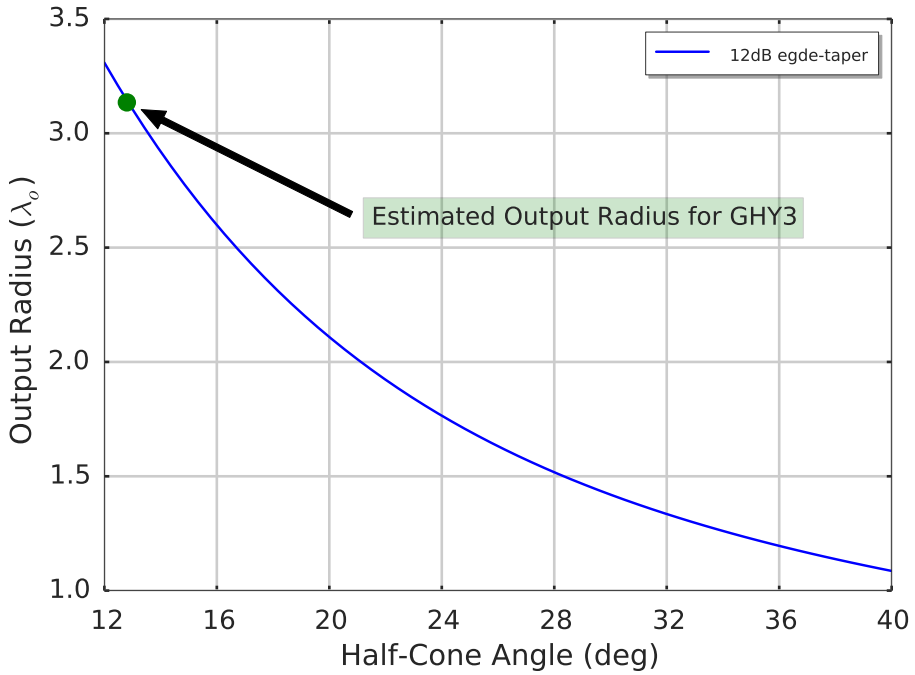

Figure 4.2: The estimated output radius of the feed horn aperture for a 12 dB edge-taper value. The output radius is normalised to the wavelength of the lowest operational frequency λ_o. In our case this is 4.0 GHz which corresponds to approximately 74 mm. The green point indicates the estimated value for the GHY-3 feed horn. Note, this value changed throughout the design process to approximately $\lambda_o = 3.6$.

GHY-3 feed horn is indicated by the green dot. Note, that this value represents just an estimate.

With these values we now can approximate the geometrical dimensions of the feed horn. To do this we still need to calculate the design (f_d) and output (f_o) frequency, these two parameters are used to define frequency-dependent dimensions in the horn design. Since our feed horn classifies as a wideband feed horn, according to the definition in [58], the design and output frequency can be calculated by

$$f_d \approx 1.2 f_{min}, \tag{4.1}$$

and

$$1.05 f_d \geq f_o \leq 1.15 f_d. \tag{4.2}$$

The final step in defining the feed horn geometry is to set the overall length. The

guideline from [58] generally recommends to choose the length within a range of $5\lambda_d$ and $30\lambda_d$. However, it is important to keep in mind that the length of the feed horn influences the sidelobe levels and the stability of the phase centre over the operational bandwidth. In our case we optimise the design to be compact as we want to reduce manufacturing costs and weight. Therefore we choose a length of approximately 1 m. The exact length can be slightly longer or shorter as it is a function of the number of corrugations and their pitch.

4.2.2 Design of Corrugations

The corrugations are an important aspect of the horn design and are generally defined by three parameters: the depth, the number of corrugations, and the pitch-to-width ratio. The latter defines the ratio between the width of the metal and the width of the slot for a single corrugation.

The publication which we based our design on states that the dept of the corrugations along the length of the feed horn has a direct effect on the overall performance, which is why they provide a number of equations to calculate the exact slot dept for the corrugations along the length of the feed horn. The depth of the slots vary from approximately $0.25\,\lambda_d$ at the mode converter to approximately $0.25\,\lambda_o$ at the throat of the horn and can be calculated by

$$d_i = \kappa \frac{\lambda_d}{4}, \tag{4.3}$$

where

d_i : slot depth,

κ : correction factor,

λ_d : wavelength of the design frequency.

The correction factor κ is given by

$$\kappa = \exp\left[\frac{1}{2.114\left(\frac{2\pi}{\lambda_d} a_i\right)^{1.134}}\right], \tag{4.4}$$

where a_i represents the corresponding horn radius.

The total number of corrugations can be calculated by the pitch and the total length of the feed horn, where the pitch defines the physical length of one corrugation. Hence, we can calculate the total number of corrugations by

$$N = \frac{L}{p}. \tag{4.5}$$

A typical pitch parameter range taken from [58] is $\frac{\lambda_\mathrm{d}}{10} \leq p \leq \frac{\lambda_\mathrm{d}}{5}$. For narrowband applications it is stated that a pitch close to $\frac{\lambda_\mathrm{d}}{5}$ is sufficient and for wideband applications with a fractional bandwidth greater than $1.8 : 1$ a pitch closer to $\frac{\lambda_\mathrm{d}}{10}$ is recommended.

The pitch-to-width ratio δ influences the cross-polarisation performance of the feed horn. Typical values for δ usually lie between $0.7 \leq \delta \leq 0.9$. The optimum value for a specific feed horn design is usually determined by simulations, it is also important to keep in mind that this parameter might be constrained by mechanical manufacturing tolerances.

4.2.3 Mode Converter Choice

The mode converter provides an impedance match from the TE_{11} mode propagating in the smooth-walled waveguide segment to the HE_{11} mode propagating in the corrugated horn segment. There are a number of techniques to perform the impedance matching between both segments. The most commonly used technique is the variable-depth mode converter. In this approach the first corrugation employs a depth of about half the design frequency wavelength λ_d, which has electrically the same behaviour as a smooth walled waveguide. Over the specified number of mode converter corrugations the slot dept decreases to the depth d_i defined by Equation 4.3, which provides a smooth impedance match between the waveguide and the corrugated horn. The variable-depth mode converter can be used up to a fractional bandwidth of $1.8 : 1$.

For applications exceeding the bandwidth capabilities of the variable-slot mode converter, such as the GHY-3 feed horn, we need to consider a ring-loaded mode

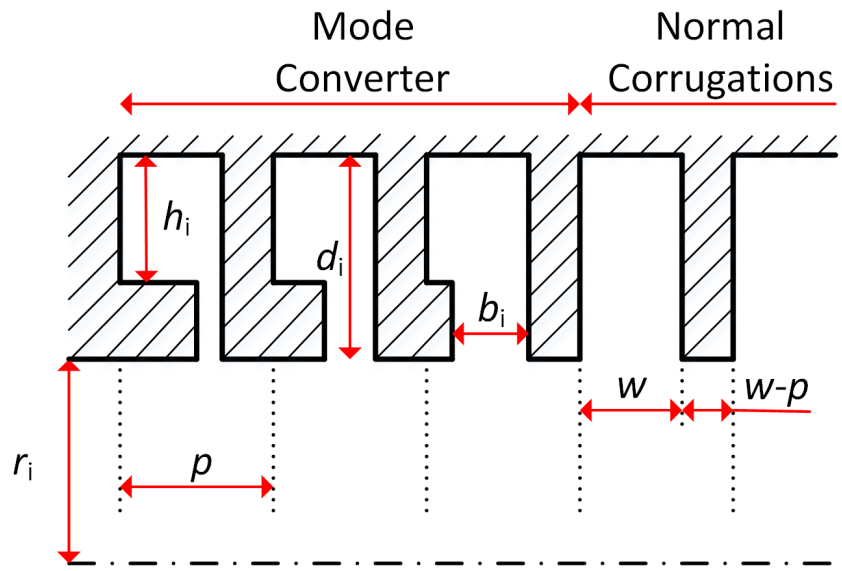

Figure 4.3: The detailed structure of a three-slot ring-loaded mode converter. The dashed-dotted line defines rotationally centre line of the horn. The OMT is connected on the left-hand side to the mode converter.

converter. This type of mode converter allows one to match the impedance over a fractional bandwidth up to $2.4:1$ [58].

The ring-loaded technique allows for a broadband transmission, because the reactance of the slots varies slowly with frequency. Therefore, the impedance matching characteristics are much less frequency dependent compared to the variable-slot mode converter. A detailed analysis of ring-loaded mode converters can be found in [60].

A schematic of the geometrical design of a ring-loaded mode converter is shown in Figure 4.3. The schematic illustrates three mode converter corrugations and two feed horn corrugations. The waveguide leading to the OMT would be connected on the left side of the mode converter.

The geometrical dimensions of the mode converter corrugations are given by

$$h_\mathrm{i} = \frac{2}{3} d_\mathrm{i}, \tag{4.6}$$

and

$$b_\mathrm{i} = p \left[0.1 + (\mathrm{i} - 1) \frac{\delta - 0.1}{N_\mathrm{mc}} \right]. \tag{4.7}$$

where

p : pitch,

i : corrugation number,

δ : pitch-to-width,

N_{mc} : total number of mode converter corrugations,

h_{i} : internal hight,

b_{i} : input width.

The depth of each mode converter corrugation d_{i} is also defined by Equation 4.3.

4.2.4 Empirical Horn Profiles

The last design stage is to choose the surface profile of the horn. In general terms a horn is considered a profiled-horn when it employs a non-linear flare angle e.g. a flare angle which follows a hyperbolic shape. The correct choice in profile can reduce the physical length of the horn and improve its performance [61]. The most commonly used empirical profiles are sine-squared, sinusoid, and hyperbolic [58]. A list of these profiles including their mathematical equations to implement them based on the geometrical dimensions of the feed horn is shown in Table 4.2. Note that some of the profiles require additional design parameters.

The equation implementing the sinusoid profile requires two additional design parameters, A and q. For a value of $A = 0$ the horn profile is entirely linear and for a value of $A = 1$ the horn profile is entirely sinusoidal. Thus, A controls the ratio between the profiles implemented in the feed horn. The power law of the sinusoid function can be controlled by the parameter q. Reference [61], recommends that the value for A should be somewhere between 0.7 and 0.9 with a value for the power law of $q = 2$. This recommendation provides a good starting point when investigating the performance of the sinusoid horn profile. However, the optimum value for A and q depends always on the specific requirements of the to be designed feed horn and must be determined by simulations.

The asymmetric sine-squared profile has one additional parameter γ. This parameter defines the location of the maximum flare angle along the length of the feed

Table 4.2: Profiles considered for the GHY-3 feed horn, all equations describing the profiles are taken from [58]. The additional parameters required to describe some of the profiles are: q the exponent of the sinusoid, and A which defines how much of the linear profile is added. In these equations z represents the position along the length of the horn.

Profile	Equation
Linear	$r(z) = r_\mathrm{i} + (r_\mathrm{o} - r_\mathrm{i})\,\frac{z}{L}$
Sinusoid	$r(z) = r_\mathrm{i} + (r_\mathrm{o} - r_\mathrm{i})\left[(1-A)\,\frac{z}{L} + A\sin^q\left(\frac{\pi z}{2L}\right)\right]$ where $A \in [0;1]$, and $0.5 \leq q \leq 5$
Asymmetric sine-squared	$r(z) = \begin{cases} r_\mathrm{i} + \frac{2(r_\mathrm{o}-r_\mathrm{i})}{1+\gamma}\sin^2\left(\frac{\pi z}{4L_1}\right) & 0 \leq z \leq L_1 \\ r_\mathrm{i} + \frac{2(r_\mathrm{o}-r_\mathrm{i})}{1+\gamma}\left\{\gamma\sin^2\left[\frac{\pi(z+L_2-L_1)}{4L_2}\right] + \frac{1-\gamma}{2}\right\} & L_1 \leq z \leq L \end{cases}$ where $L = L_1 + L_2$, and $\gamma = \frac{L_2}{L_1}$.
Hyperbolic	$r(z) = \sqrt{r_\mathrm{i}^2 + \frac{z^2(r_\mathrm{o}^2 - r_\mathrm{i}^2)}{L^2}}$

horn [57]. For a value of $\gamma = 1$ the maximum flare angle is located half way along the length of the feed horn ($L/2$). A good starting value for γ when investigating the effect of the asymmetric sine-squared profile on the feed horn performance is provided in [61] who stated that $\gamma = 2$.

The equation to calculate the hyperbolic profile uses only three geometrical parameter of the feed horn design. These are the input radius, the output radius and the overall length of the feed horn.

4.2.5 Simulation of Horn Profiles

In this section we show the results for the simulated feed horns using different surface profiles. All horns were simulated with Champ 3.0.1 [62] and the simulation results of the various profiles were compared with respect to the beam symmetry, constant edge-taper, sidelobe level, and cross-polarisation. For each simulation we plot the beam pattern at six different frequencies 4.0 GHz, 5.0 GHz, 6.0 GHz, 7.0 GHz, 8.0 GHz, and 8.5 GHz. The traces plotted for each frequency plot are; E-field (red), H-field (blue),

D-field (green), and the cross-polarisation at 45° (black). The edge of the secondary mirror is indicated by two vertical dotted lines.

The first feed horn applies a linear profile, its performance is shown in Figure 4.4. The beam pattern remains stable with respect to its shape and symmetry up to 6.0 GHz. Above this frequency the cross-polarisation increases by approximately $8 - 10$ dB. This is due to an decrease of the symmetry of the beam, as one can see by comparing the beam shape of the E-field (red), the H-field (blue), and the D-field (green) in Figures 4.4d to 4.4f. The edge-taper value for this profile is fairly constant for frequencies lower than 6.0 GHz. For frequencies above 6.0 GHz the edge-taper value drops significantly. This can be seen best in Figure 4.4f, by looking at the power levels for the different field orientations of the beam at the point where these intersect with the two vertical dotted lines that represent the edge of the secondary reflector.

The beam pattern for the asymmetric sine-squared and the sinusoid profile are shown in Figure 4.5 and 4.6, respectively. Both profiles show similar characteristics of their beam patterns with respect to the performance over the operational frequency band. The beam shape of both feed horns changes from 4.0 GHz to 8.5 GHz significantly. At a frequency of 4.0 GHz the field illuminating the secondary reflector has a Gaussian-like field distribution with a first sidelobe level that is extremely high compared to the linear profiled feed horn. At a frequency of 6.0 GHz, shown in Figure 4.5c and 4.6c both feed horns perform extremely well with respect to their cross-polarisation level. Although, we can also see that the main lobe flattens on both sides of the peak value and forms a shape which looks like small shoulders. The dominance of these shoulders also increase with frequency which can be seen by comparing the beam shape shown in Figure 4.5d, 4.6d and 4.5f, 4.6f for the asymmetric sine-squared and the sinusoid profile, respectively. Finally, the simulation also shows that the beam shape of both designs is highly symmetric over the entire operational frequency band.

The last simulated feed horn employs the hyperbolic surface profile, its beam pattern is shown in Figure 4.7. By comparing the beam shape over the simulated six

different frequencies we can see that the shape of the beam pattern behaves stably with respect to its beam waist and symmetry over the operational frequency band. As a result of the stable beam waist we can also see that the edge-taper illumination, where the beam intersects the two vertical dotted lines is at a constant value. Although the beam waist remains stable over the operational frequency range we can see that the peak value of the beam flattens at higher frequencies. This is most noticeable at 8.5 GHz, shown in Figure 4.7f. Finally the simulation shows that the cross-polarisation performance of the hyperbolic profiled feed horn remains well below −30 dB over the entire operational frequency band.

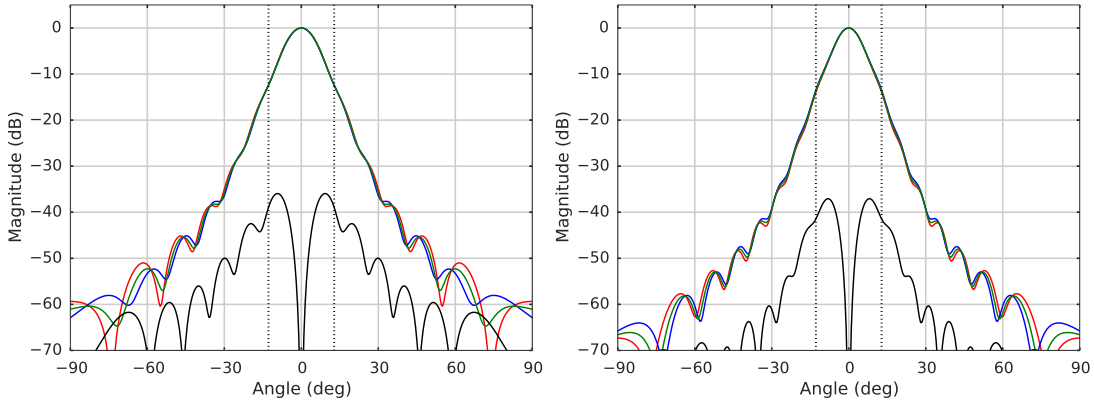

(a) 4.0 GHz

(b) 5.0 GHz

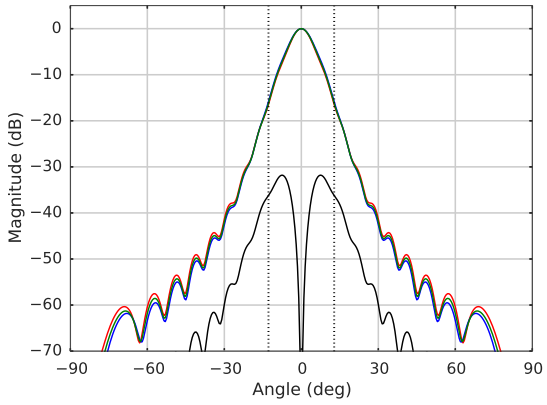

(c) 6.0 GHz

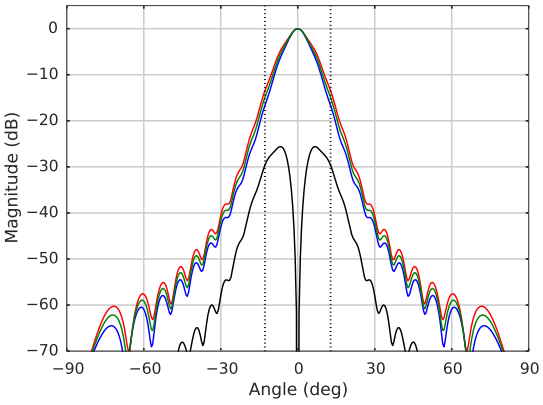

(d) 7.0 GHz

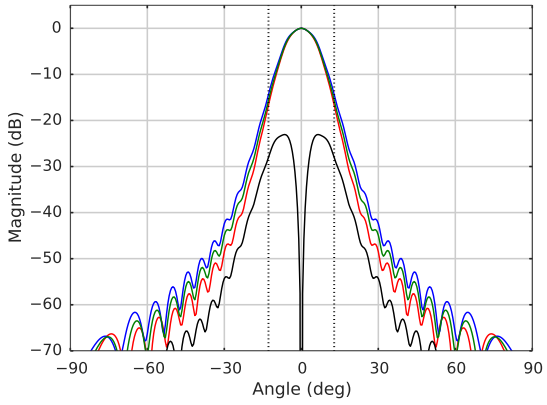

(e) 8.0 GHz

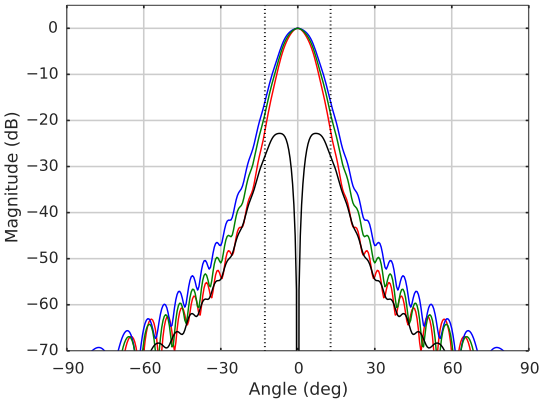

(f) 8.5 GHz

Figure 4.4: The radiation patterns for the linear profiled horn. E-field (red), H-field (blue),D-field (green), and cross-polarisation at 45° (black). The vertical dotted lines indicate the edge of the secondary mirror.

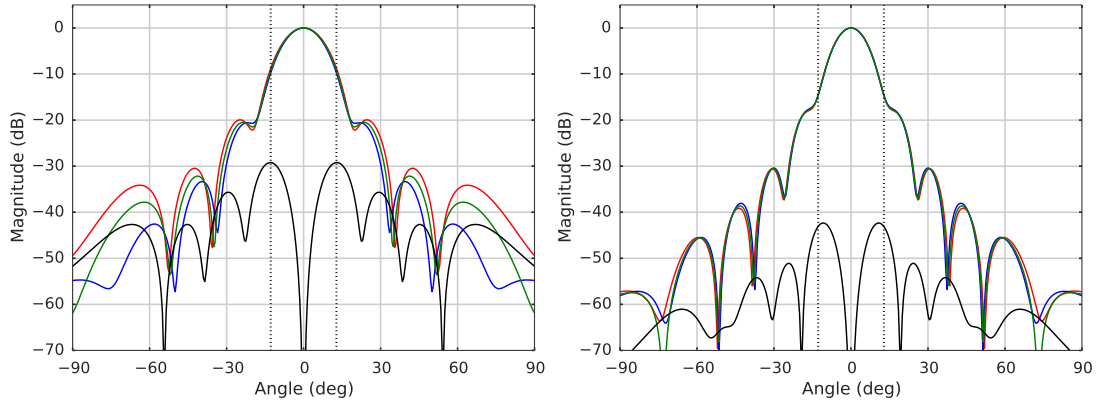

(a) 4.0 GHz

(b) 5.0 GHz

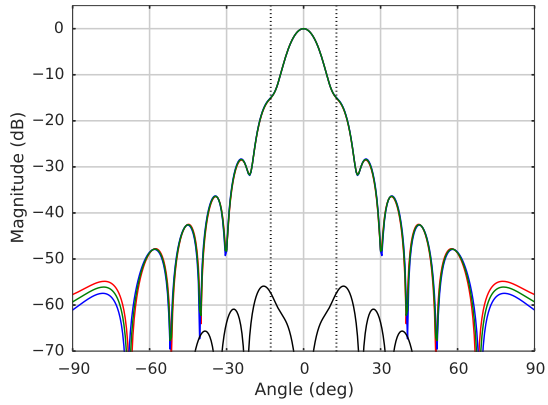

(c) 6.0 GHz

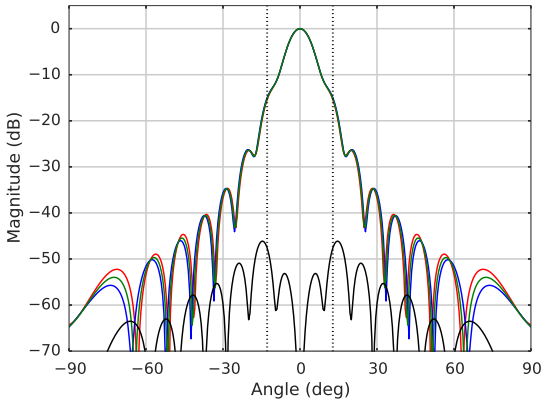

(d) 7.0 GHz

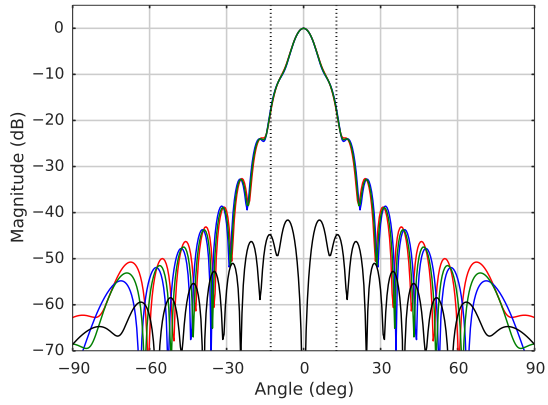

(e) 8.0 GHz

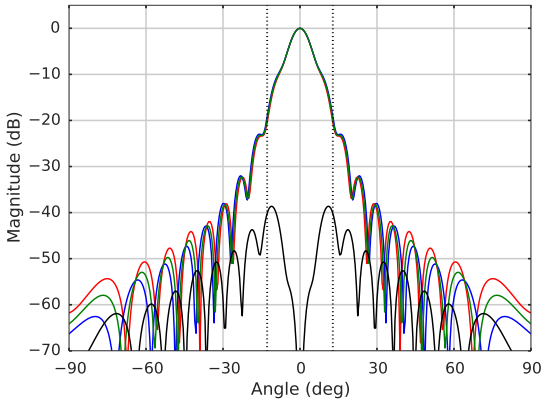

(f) 8.5 GHz

Figure 4.5: The radiation patterns for the sinesquared profiled horn. E-field (red), H-field (blue), D-field (green), and cross-polarisation at 45° (black). The vertical dotted lines indicate the edge of the secondary mirror.

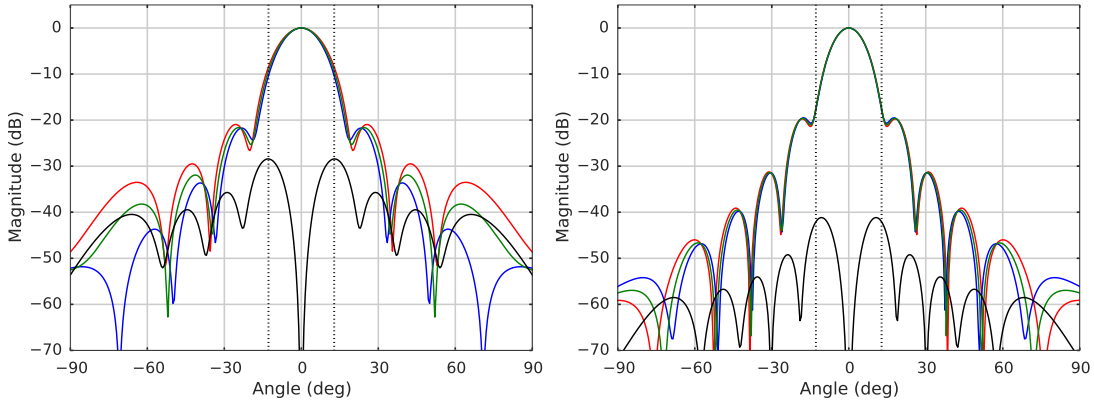

(a) 4.0 GHz

(b) 5.0 GHz

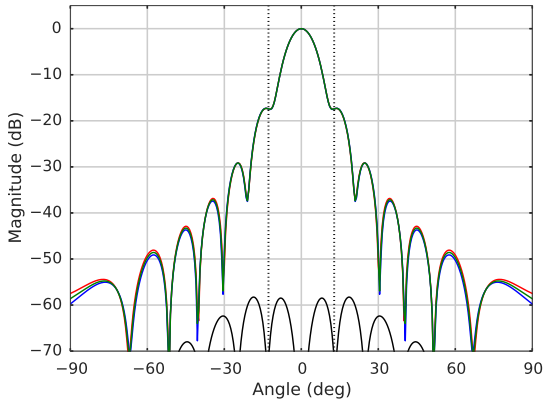

(c) 6.0 GHz

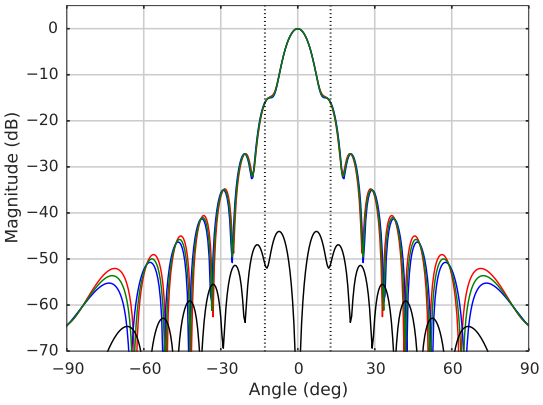

(d) 7.0 GHz

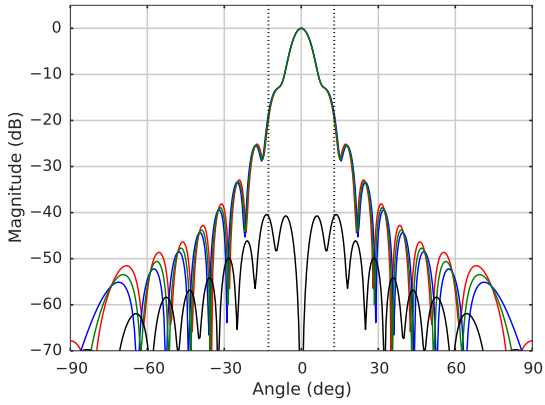

(e) 8.0 GHz

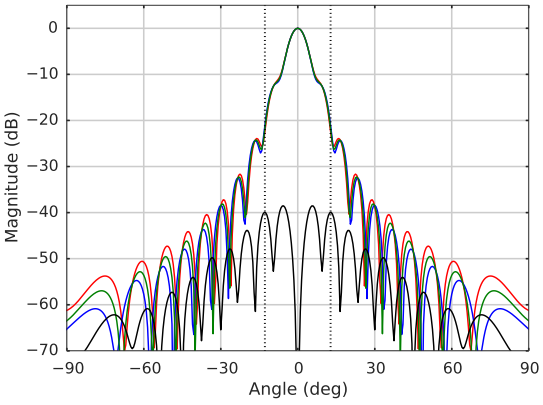

(f) 8.5 GHz

Figure 4.6: The radiation patterns for the sinusoid profiled horn. E-field (red), H-field (blue), D-field (green), and cross-polarisation at 45° (black). The vertical dotted lines indicate the edge of the secondary mirror.

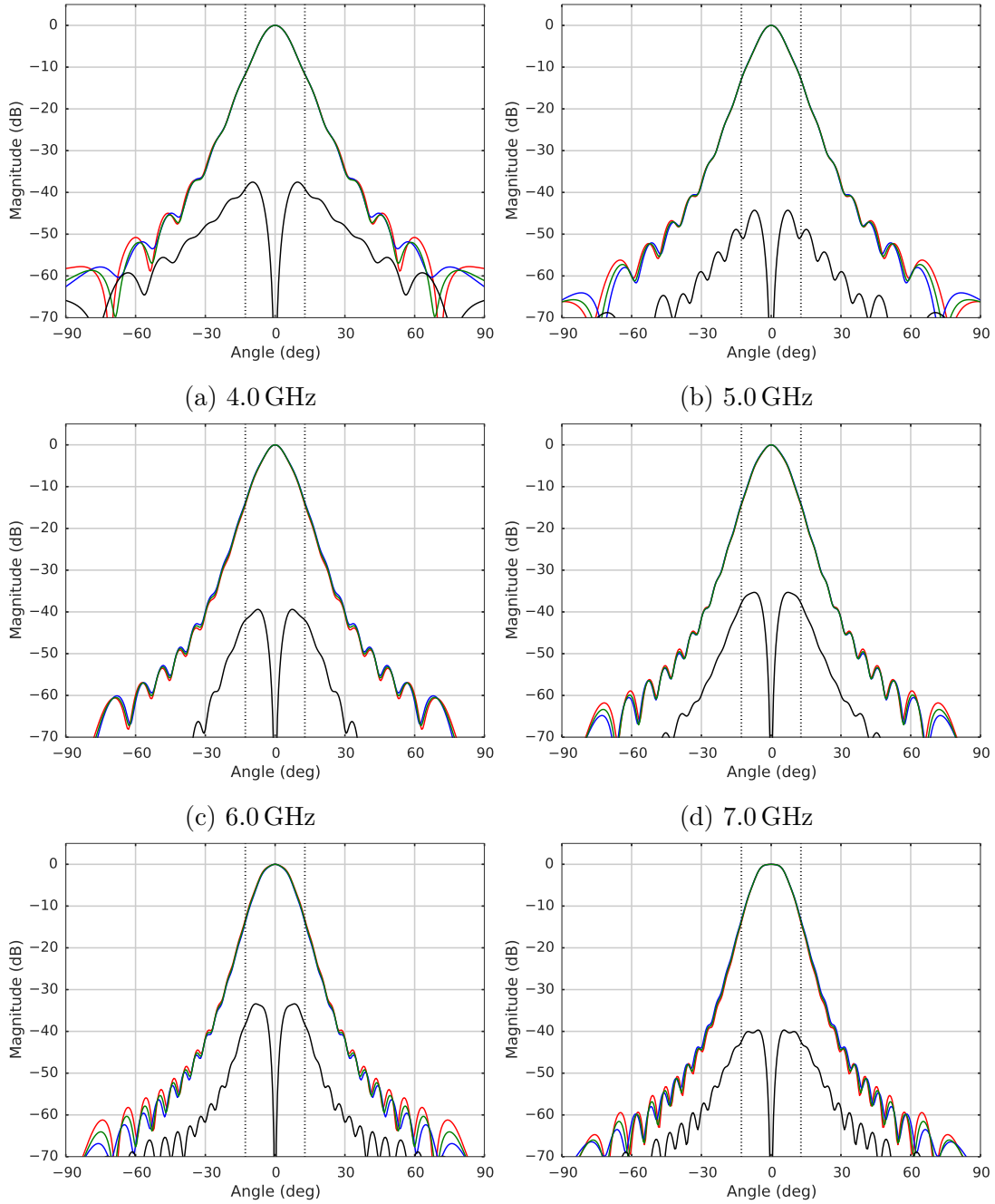

(a) 4.0 GHz (b) 5.0 GHz

(c) 6.0 GHz (d) 7.0 GHz

(e) 8.0 GHz (f) 8.5 GHz

Figure 4.7: The radiation patterns for the hyperbolic profiled horn. E-field (red), H-field (blue), D-field (green), and cross-polarisation at 45° (black). The vertical dotted lines indicate the edge of the secondary mirror.

4.3 GHY-3 Corrugated Ring-loaded Feed Horn

We compared the performance of all four profiles and found that for narrowband applications the asymmetric sine-squared and sinusoid profile give the best result, as those two allow for very low cross-polarisation level and Gaussian like main lobe. However, the beam pattern of both horns change significantly over a bandwidth greater than $1.8:1$. Hence, these two profiles are not suitable for our application. The linear and hyperbolic profile performed well for wideband applications. However, the linear profiled horn looses its symetry at the top end of the frequency band, whereas the hyperbolic profile performs best over the entire operational bandwidth in terms of symmetry, cross-polarisation, sidelobe level, and constant edge-taper value.

Based on the results of these simulations we choose to use the hyperbolic shaped feed horn design to illuminate the GHY-3 antenna optics. The design parameters describing the corrugated ring-loaded feed horn are shown in Table 4.3.

Table 4.3: Parameters describing the GHY-3 hyperbolic corrugated feed horn.

description	symbol	design value
Lowest operational frequency	f_{min}	4.0 GHz
Highest operational frequency	f_{max}	8.5 GHz
Design frequency	f_{d}	4.68 GHz
Output frequency	f_{o}	5.616 GHz
Input radius	r_{i}	24.4 mm
Output radius	r_{o}	272.69 mm
Length	L	1040.946 mm
Number of corrugations in the horn	N	130
Pitch	p	8.007 mm
Pitch-to-width ratio	δ	0.7
Depth of the corrugations	d	$19.05 - 11.4$ mm
Number of corrugations in the mode converter	N_{mc}	16
Mode converter type	–	ring-loaded
Corrugated surface profile	–	hyperbolic
Half-subtended angle for the edge-taper	α	12.8°
Edge taper value	ET	$10 - 12$ dB
Cross-polarisation level	CP	≤ -30 dB
Return loss	RL	≤ -25 dB

4.4 Combined Simulation with OMT

After we finalized the GHY-3 feed horn design we wanted to investigate how well the feed horn and the GHY-3 OMT from Chapter 3 perform together. To do this we set up a HFSS model where the circular waveguide port of the OMT is connected to the feed horn in the same way as it will be in the assembled GHY-3 receiver system. An image of this model is shown in Figure 4.8. The OMT is located on the left-hand side and connected to the feed horn on the right-hand side via a short waveguide segment. The internal electric field distribution is made visible at distinct positions along the waveguide and feed horn. This is done to illustrate the mode conversion from the TE_{11} mode propagating in the waveguide to the HE_{11} mode propagating in the feed horn after the mode converter.

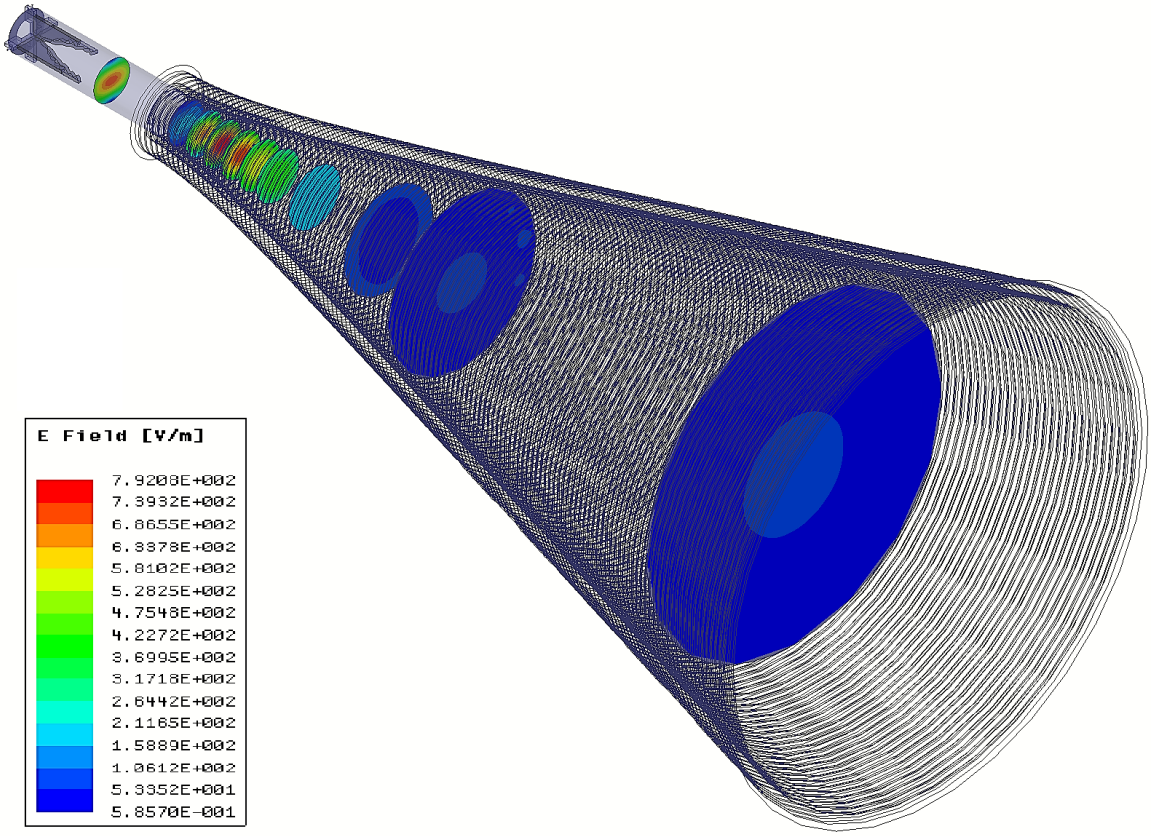

Figure 4.8: HFSS model of the GHY-3 feed system, the OMT is shown at the top left and is connected to the feed horn via a short waveguidesegment. The mode conversion form TE_{11} mode to the HE_{11} and vice versa is illustrated at distinct points along the model.

The simulation provides an estimate of the transmission performance from the coaxial port to the far field beam pattern of the feed horn and vice versa. The beam pattern is plotted at the same frequency points as the previous feed horn simulations which were shown in Section 4.2.5. The traces plotted for each frequency plot are; E-field (red), H-field (blue), D-field (green), and the cross-polarisation at 45° (black) and the edge of the secondary mirror is indicated by two vertical dotted lines. The simulation results are shown in Figure 4.9. We can see that the HFSS simulated main beam agrees very well with the CHAMP simulation for the first four frequency points from 4.0 GHz to 7.0 GHz, which are shown in Figure 4.9a to 4.9d. At the top end of the operational frequency band at 8.5 GHz, shown in Figure 4.9f the main lobe forms two peaks at the E-field (red) and D-field (green). We believe that this feature can be explained by the higher order mode production of the OMT. Referring back to the simulated mode production of the OMT, which we showed in Section 3.3.5 in Figure 3.8, we showed that at 8.5 GHz the excitation of the TE_{31} mode peaks with a value of approximately -10 dB. Therefore, we believe that the propagation of this mode is responsible for the change in the shape of the beam pattern at this frequency.

When looking at the cross-polarisation level predicted by the HFSS simulation we can see that the simulated cross-polarisation is asymmetric. This indicates that the accuracy of the HFSS simulation came to a limit. Since we have a symmetrical feed horn, the beam pattern produced by it must be symmetrical too. For this reason, we cannot rely on the values of the cross-polarisation in this simulation.

4.5 Summary

In this chapter we presented the design and simulation of the GHY-3 corrugated ring-loaded feed horn. We provided a description on the design process followed by an investigation of the effect on the performance for a number of different feed horn profiles. This was done by comparing the far-field beam pattern at six different frequencies over the operational frequency band. This investigation showed that the hyperbolic profiled feed horn performs best over the entire operational bandwidth in

terms of symmetry, cross-polarisation, sidelobe level, and constant edge-taper value.

At last we simulated the combined performance of the GHY-3 OMT and feed horn using HFSS. The HFSS simulation results agreed with the previous simulation done with CHAMP and therefore we are confident that the GHY-3 feed system will perform as expected.

At the time of writing this thesis the GHY-3 feed horn was still in production and therefore we were not able to validate our simulations through a set of measurements.

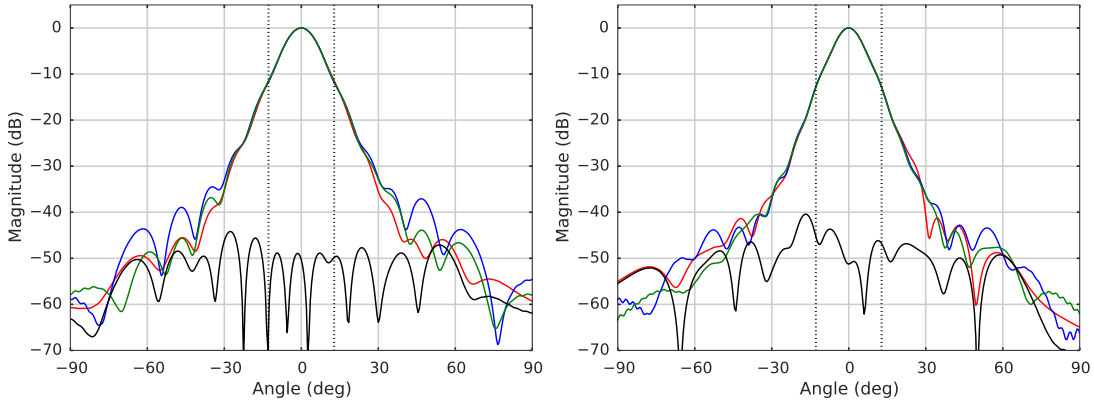

(a) 4.0 GHz

(b) 5.0 GHz

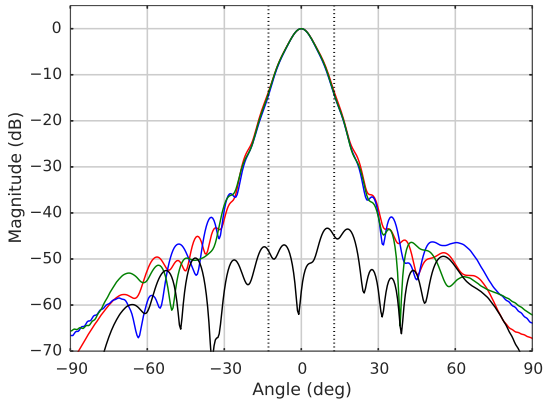

(c) 6.0 GHz

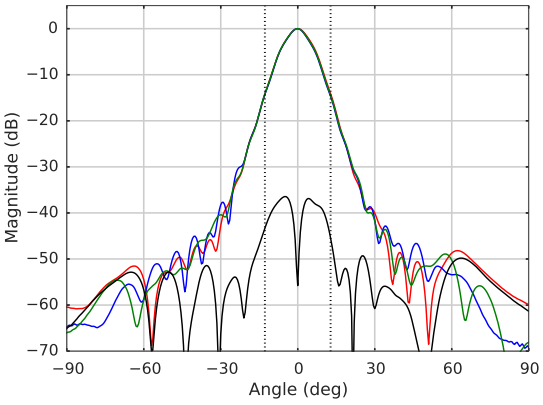

(d) 7.0 GHz

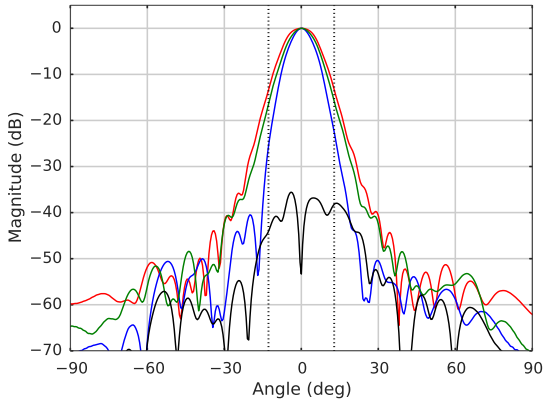

(e) 8.0 GHz

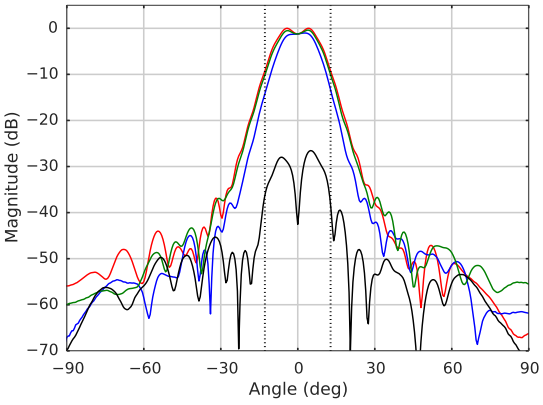

(f) 8.5 GHz

Figure 4.9: The radiation patterns for the combined model of OMT and the GHY-3 feed horn. E-field (red), H-field (blue), D-field (green), and cross-polarisation at 45° (black). The vertical dotted lines indicate the edge of the secondary mirror.

Chapter 5

Gain Stabilisation for Coherent Radio Receivers

The first part of this chapter provides an introduction to coherent radio receivers. We show the fundamental architecture of such a receiver and talk about noise as a signal. We then discuss the sensitivity limits caused by receiver noise and gain instabilities, as well as different approaches to stabilise and improve the sensitivity. This introduction provides the fundamental knowledge required to make use of the detailed gain stabilisation analysis presented in the second half of this chapter, where we discuss the two stabilisation methods that we considered for the GHY-3 receiver. The first approach uses a broadband noise signal and second approach a continuous-wave calibration signal.

5.1 Radio Receiver Introduction

A radio astronomy receiver is a device to measure signals emitted by astronomical sources. Depending on the type of receiver the signal detection may be coherent or incoherent. The latter does not preserve the phase information of the signal and is called a bolometer [34]. In this work we focus on the design of coherent receivers which preserve the phase of the oncoming electric field.

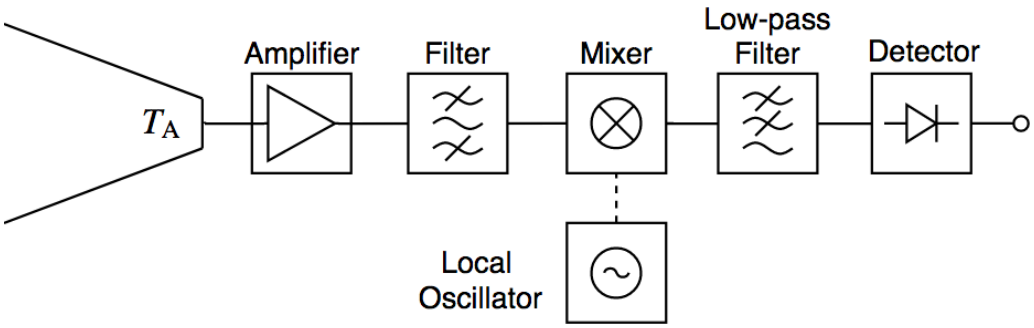

Figure 5.1: The fundamental parts of a heterodyne receiver. The signal is received by the antenna on the left-hand side and passes through the signal chain until it is detected on the right-hand side.

5.1.1 Fundamental Components of a Radio Receiver

A coherent radio receiver consists of components which amplify and filter signals while preserving their phase information. When the receiver also shifts the initial frequency band down in frequency, it is called a heterodyne receiver. The frequency shift implemented in those receivers is done by mixing the received signals with a local oscillator (LO) signal which is fixed at a specific frequency. This results in two so-called intermediate frequency (IF) bands, which are the sum and the difference of the local oscillator and input signal frequency. The fundamental signal chain of a heterodyne receiver is shown in Figure 5.1, where the signal is received by the antenna on the left-hand side and then amplified, filtered, frequency converted, low-pass filtered, and finally detected on the right-hand side.

5.1.2 Noise as a Signal

Before we can discuss the sensitivity of a receiver we first have to talk about the nature of the signals that it needs to detect. In the radio part of the spectrum most astronomical sources produce signals that are composed of Gaussian or Rayleigh noise, i.e. noise-like signals [63]. However, radio receivers will also be likely to detect artificial signals such as communication signals or electronic noise from nearby equipment. Those signals are usually called radio frequency interference (RFI) and are unwanted. The main difference, which distinguishes astronomy from communication signals is

that astronomy signals are noise-like i.e. have no long-term coherence that can be locked on to.

5.1.2.1 Types of Receiver Noise

Any receiver system introduces noise on a detected signal. There are two types of noise in a radio receiver system, uncorrelated and correlated noise. The uncorrelated noise has a white noise characteristic i.e. has a flat frequency spectrum, whereas the correlated noise follows a pink noise characteristic i.e. has a greater power at lower frequencies.

White noise is caused by the thermal motion of free electrons in electrical conductors colliding with atoms and continuously exchanging energy [64]. Band-limited receiver white noise can be represented by a Gaussian distribution with a mean value $\mu = 0\,\mathrm{V}$ and a standard deviation σ that is equal to the root-mean-squared voltage. The probability of measuring a certain voltage amplitude v is given by

$$f(v|\mu,\sigma) = \frac{1}{\sigma\sqrt{2\pi}} e^{\frac{-(v-\mu)^2}{2\sigma^2}}\,, \tag{5.1}$$

where

μ : mean value, in case of noise voltage $\mu = 0\,\mathrm{V}$,
σ : standard deviation, in case of noise voltage $\sigma = v_{\mathrm{rms}}$.

The rms noise voltage of a resistor with a given bandwidth, resistance, and thermal temperature is given by

$$v_{\mathrm{rms}} = \sqrt{4k_{\mathrm{B}}TBR}\,, \tag{5.2}$$

where

k_{B} : Boltzmann constant,
T : Absolute temperature in Kelvin,
B : Bandwidth in Hz, and
R : Resistance in Ohm.

Pink noise, also known as $1/f$ noise or flicker noise, is used to represent noise properties in a wide range of physical situations, such as in condensed matter physics, electronic devices, and biological processes [65]. Pink noise lies between the white noise characteristic with no correlation in time and the red noise (brown noise) characteristic representing a random walk with no correlation between increments. In a radio astronomy receiver pink noise best represents the correlated gain fluctuations of the system. The origins of $1/f$ noise in a electronic device have been discussed in the literature for several decades. Some suggest that the dominant source in a HEMT amplifier is due to traps in the gate oxide, others say that bulk mobility fluctuations are the dominant source [66]. Macroscope effects such as temperature fluctuations can also contribute to the $1/f$ noise.

5.2 Receiver Sensitivity Limits

Radio astronomy receivers need to be sensitive in order to detect the faint astronomical signals which are orders of magnitude weaker than the system noise. The sensitivity of a radio telescope is a function of collecting area, efficiency, and system temperature. The collecting area of the GHY-3 antenna is fixed, but we can influence the system temperature T_{sys} and the gain stability ΔG of the receiver system.

5.2.1 Receiver Noise Limit

A receiver generates an output signal even if there is no input signal present. This signal is the thermal noise of the receiver, which is amplified by the signal chain and cannot be distinguished from any input signals. Experiments have shown that the spectral power density of the receiver noise is well represented by a white noise spectrum [34]. The system temperature for a real receiver system consists of a number of individual noise sources such as, amplifier noise, cable attenuation, OMT insertion loss, antenna spillover, etc. The contribution of these individual components is considered additive. However, to determine the effective contribution of each component we also need to take into account the gain of the system at which the contribution

take place. Thus, the system temperature is calculated using the *Friis* formula for cascaded amplification stages which is given by

$$T_{\mathrm{sys}} = T_1 + \frac{T_2}{G_1} + \frac{T_3}{G_1 G_2} + ... + \frac{T_{\mathrm{i}}}{G_1 G_2 ... G_{\mathrm{i}-1}}, \tag{5.3}$$

where T_{i} and G_{i} represent the noise temperature and gain of the individual component in the receiver chain [34]. Lossy components with $G_{\mathrm{i}} < 1$ contribute a noise temperature T_{i} which is given by

$$T_{\mathrm{i}} = (1 - G_{\mathrm{i}})\, T_{\mathrm{p}} \tag{5.4}$$

where T_{p} is the physical temperature of the device e.g. cable, connector, splitter, etc. Note, that this equation does not take into account contributions which are caused by reflections between components. To take into account those contributions, reference [67] provides a detailed analysis of this topic. However, for well-matched components with individual return losses $S_{11} \lesssim -20\,\mathrm{dB}$ these effects are negligible.

Furthermore, the sensitivity of the receiver also depends on the receiver bandwidth $\Delta\nu$ and the integration time τ. From the Nyquist sampling theorem we know that the total number of independent samples in an integration time τ with a defined bandwidth $\Delta\nu$ is given by

$$N = 2\tau\Delta\nu. \tag{5.5}$$

As the receiver samples noise-like signals which are drawn from a normal distribution with a variance of $2T_{\mathrm{sys}}^2$, we can average the samples to reduce the noise [68, 69]. Gaussian statistics tells us that the uncertainty on a sample comprising N subsamples is reduced by a factor of $1/\sqrt{N}$, which allows us to calculate the receiver sensitivity noise limit by

$$\Delta T_{\mathrm{noise}} = \frac{\sqrt{2}T_{\mathrm{sys}}}{\sqrt{2\tau\Delta\nu}} = \frac{T_{\mathrm{sys}}}{\sqrt{\tau\Delta\nu}}. \tag{5.6}$$

This shows that the receiver noise limit depends directly on the system temperature and the square-root of the integration time and bandwidth. Hence a low T_{sys} is an important design aspect.

5.2.2 Receiver Stability Limit

The sensitivity of the receiver can also be limited by the stability of the gain in the amplifier chain. A typical radio receiver needs an amplification of approximately 80 dB in order to be able to detect faint astronomical sources. The required gain of a receiver system can be estimated by its bandwidth $\Delta\nu$, the power level required by the detector P_{detector} and the temperature of the to be detected input signal T. The noise power produced by a resistor at temperature T for a receiver with the bandwidth $\Delta\nu$ is given by

$$P = k_{\text{B}} T \Delta\nu, \tag{5.7}$$

where k_{B} is the Boltzmann constant. Assuming that our detector requires a signal power of approximately -20 dBm. The thermal noise power produced by a signal at the input which has a temperature of 10 K with a bandwidth of 500 MHz is approximately -100 dBm. The required receiver gain is the difference between both values, for this example 80 dB.

As a result of the high system gain, any fluctuations in amplification have a direct effect on the detected signal. The receiver sensitivity limit can be calculated from the gain fluctuations by

$$\Delta T_{\text{gain}} = \frac{\Delta G}{G} T_{\text{sys}}. \tag{5.8}$$

5.2.3 Practical Receiver Sensitivity Limit

In order to determine the practical sensitivity limit of the receiver we need to combine both uncertainties. Since the uncertainty for the noise limit and gain stability are independent random processes we can add them in quadrature

$$\Delta T^2 = \Delta T^2_{\text{noise}} + \Delta T^2_{\text{gain}}. \tag{5.9}$$

Equations 5.6, 5.8, 5.9 lead to the practical receiver sensitivity equation which can be found in literature e.g. [34, 69] and is given by

$$\Delta T = T_{\text{sys}} \sqrt{\frac{1}{\tau \Delta \nu} + \left(\frac{\Delta G}{G}\right)^2}. \tag{5.10}$$

This summarizes that the design of a sensitive radio receiver requires T_{sys} and ΔG to be as low as possible.

5.3 Values for the GHY-3 Receiver

This section provides a brief analysis of the expected system temperature and required gain stability of the GHY-3 receiver.

5.3.1 Expected Receiver Temperature

The system temperature of the GHY-3 receiver is estimated using Equation 5.3 for cascaded amplification stages which we showed in Section 5.2.1. Using this equation we calculated the temperature contribution caused by the individual components of

Table 5.1: A simplified estimation of the receiver system temperature. The calculation is based on Equation 5.3. Note that T_{sys} does not increase significantly after the first amplifier.

Component	Gain	Physical temp.	Gain temp.	Power	T_{sys}
CMB		2.70 K		-97.76 dBm	2.700 K
Atmosphere	-0.060 dB	220.0 K		-94.52 dBm	5.761 K
Primary Ref.	-0.020 dB	290.0 K		-93.63 dBm	7.118 K
Secondary Ref.	-0.020 dB	290.0 K		-92.88 dBm	8.481 K
Feed Horn	-0.040 dB	290.0 K		-91.71 dBm	11.227 K
OMT	-0.300 dB	15.0 K		-91.60 dBm	12.335 K
Cable1	-0.100 dB	12.0 K		-91.59 dBm	12.644 K
90deg Hybrid	-1.000 dB	10.0 K		-91.68 dBm	15.576 K
Cable2	-0.100 dB	10.0 K		-91.69 dBm	15.908 K
Signal Coupler	-0.100 dB	10.0 K		-91.70 dBm	16.248 K
Cable3	-0.100 dB	10.0 K		-91.71 dBm	16.596 K
Connector	-0.050 dB	10.0 K		-91.71 dBm	16.773 K
LNA	45.000 dB	10.0 K	3.0 K	-45.65 dBm	21.409 K

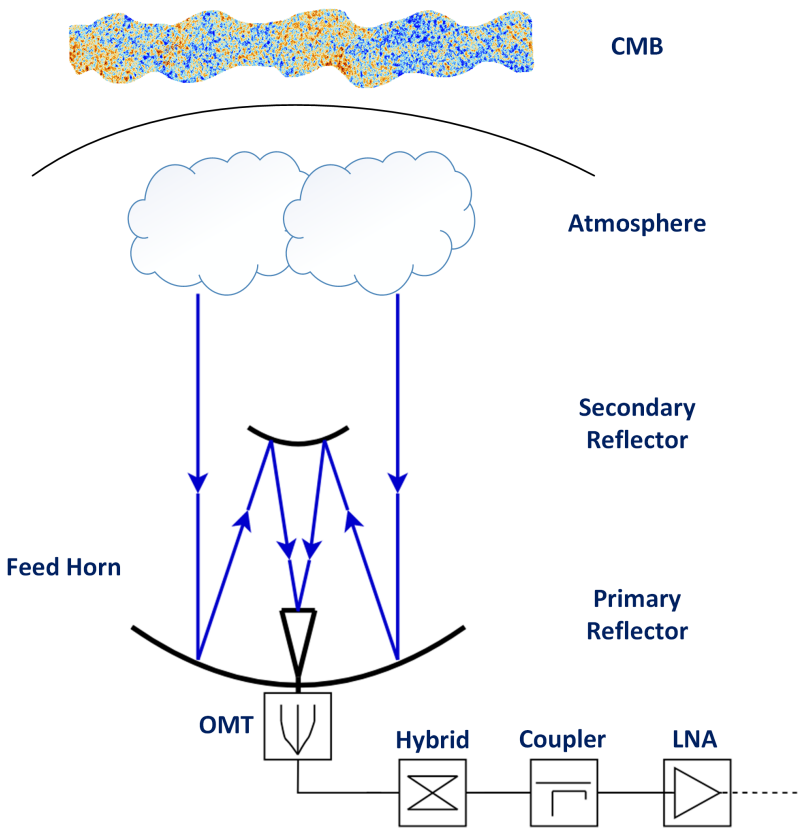

Figure 5.2: Schematic illustrating the individual components which contribute to the system temperature of the receiver system. The individual component values are shown in Table 5.1.

the GHY-3 receiver system. Table 5.1 shows the physical temperature and the gain of the individual contributions as well as the running system temperature along the signal chain. The table includes all components down to the first amplifier, after which the system temperature does not increase significantly anymore. A diagram to illustrate the order of the individual components used to estimate the system temperature is shown in Figure 5.2. The calculation shows that the estimated system temperature for the GHY-3 receiver system is approximately $T_{\mathrm{sys}} = 22\,\mathrm{K}$. Furthermore, one can also see that any attenuation before the low noise amplifier has a significant effect on the system temperature. Note, that for this calculation the gain and temperature values for all components have either been measured or typical values were chosen based on previous projects and experience.

5.3.2 Expected Receiver Stability

To estimate the required gain stability, we assume that the maximum integration time is $\tau = 180\,\text{sec}$. This value is based on the time estimated for a full turn in azimuth of the GHY-3 telescope. In order to ensure that the receiver sensitivity is not limited by gain instabilities when used in single dish observation mode, we assert that the sensitivity limit caused by the gain fluctuations for this integration time must be less than or equal to the sensitivity noise limit.

$$\Delta T_{\text{gain}} = \Delta T_{\text{noise}}. \tag{5.11}$$

To estimate the receiver noise limit we assume a bandwidth of $\Delta\nu = 4.0\,\text{GHz}$, which is the default bandwidth processed by the digital signal processing when used in single-dish observation mode. The value for the system temperature is $T_{\text{sys}} = 22\,\text{K}$, which we estimated in Section 5.3.1. With these values we can calculate the expected noise sensitivity limit of the receiver using Equation 5.6, which results in $\Delta T_{\text{noise}} = 25.93\,\mu\text{K}$.

The integration time at which the sensitivity noise limit and sensitivity gain limit are equal is called the $1/f$ knee frequency. For an integration time τ greater or smaller than the $1/f$ knee the receiver sensitivity is limited by either ΔT_{gain} or ΔT_{noise}, respectively. This can be seen by looking at the power spectrum output of the receiver system. Figure 5.3 shows an illustration for a receiver power spectrum that includes both white noise and pink noise characteristics. The thermal noise of the receiver is represented by the flat white noise spectrum and the gain instability by the pink noise spectrum which increases power with decreasing frequency. The point at which both spectra intersect is the $1/f$ knee frequency.

In order to not limit the sensitivity of the receiver system through gain instabilities during a integration period of $\tau = 180\,\text{sec}$ the gain fluctuational must be less than $\Delta G/G = 1.178 \times 10^{-6}$. Another way of looking at this is that the knee frequency of the receiver power spectrum must be lower than the longest integration time, $f_{\text{knee}} \leq 1/\tau$.

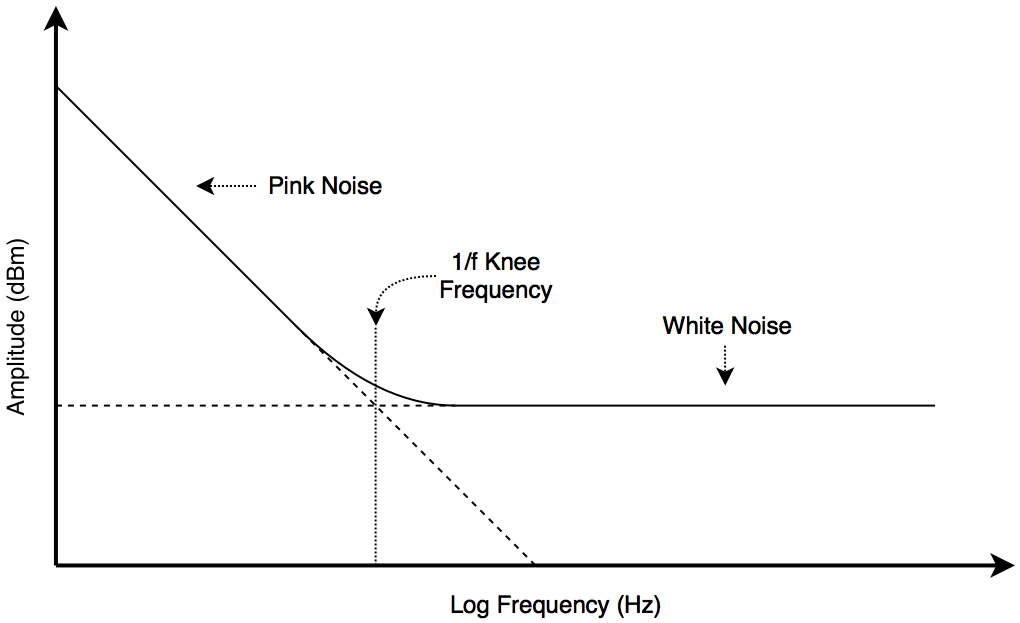

Figure 5.3: Power spectrum of a typical receiver output. The thermal noise is represented by the white noise and the gain fluctuations which follow a 1/f characteristic are represented by the pink noise. The knee frequency is the point where the white noise and pink noise have the same power.

5.4 Methods of Gain Tracking

In this section, we discuss four methods that can be used to either track the gain fluctuations and correct the detected signal or to reduce the effect of the gain fluctuations directly. Each method is discussed using a simplified system diagram and is summarised with the practical receiver sensitivity equation.

5.4.1 Dicke Switching

A Dicke-switched receiver is based on a differential compensation approach that subtracts a known reference signal from the antenna signal. This is done by installing a switch before the first amplifier, as shown in Figure 5.4. The input signal of the amplifier switches between the antenna signal and the reference signal. At the end of the signal chain both states are then multiplied with either $+1$ or -1 and integrated so that the reference signal is subtracted from the antenna signal [34]. The uncertainty

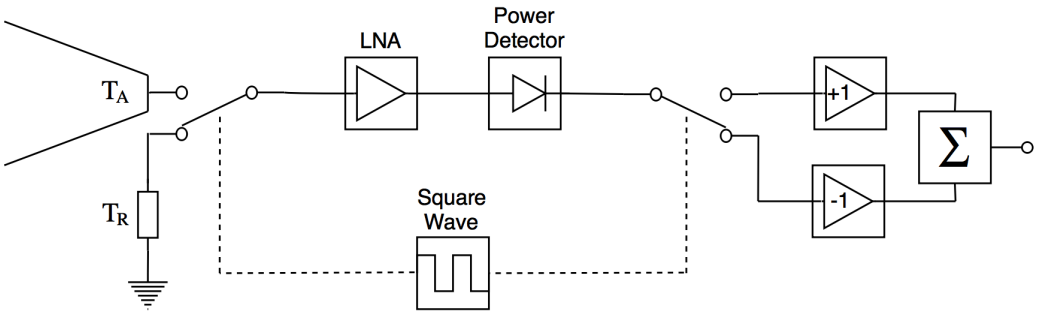

Figure 5.4: Schematic of a Dicke receiver which switches between the antenna signal T_A and a reference load T_R. The two switches are controlled by a square wave signal with a duty cycle of 50 percent. The reference signal is then subtracted from the antenna signal in the integration block.

caused by the gain fluctuations is then given by

$$\Delta T = \frac{\Delta G}{G} \left(T_\mathrm{A} - T_\mathrm{R} \right). \tag{5.12}$$

The influence of the gain fluctuations has a much lower effect on the sensitivity limit when $T_\mathrm{A} \approx T_\mathrm{R}$. When $T_\mathrm{A} = T_\mathrm{R}$, then ΔT is independent of any gain fluctuation. Although this method can in principle remove any gain fluctuation, it requires half of the observation time to be spent measuring the reference signal T_R, which decreases the receiver sensitivity by a factor of $\sqrt{2}$. In addition to that the measurement of the difference between two uncorrelated random noise signals introduces another loss in sensitivity by another factor of $\sqrt{2}$. This leads to a combined decrease in sensitivity for the Dicke radiometer by a factor of 2 compared to the practical receiver sensitivity limit of a total power receiver represented by Equation 5.6. Hence, achieving a noise limiting sensitivity of

$$\Delta T_\mathrm{noise} = \frac{2T_\mathrm{sys}}{\sqrt{\tau \Delta \nu}}. \tag{5.13}$$

The practical receiver sensitivity limit for a Dicke receiver is therefore

$$\Delta T = 2T_\mathrm{sys} \sqrt{\frac{1}{\tau \Delta \nu} + \left(\frac{\Delta G_\mathrm{res}}{G} \right)^2}, \tag{5.14}$$

where ΔG_res represents any residual gain fluctuations.

5.4.2 Pseudo-Correlation

The pseudo-correlation receiver uses a hybrid to combine a stabilised reference signal with the antenna signal, thereby allowing it to track the gain fluctuations by measuring the change in amplitude of the reference signal after it has been separated from the antenna signal again. A hybrid is a four-port device with two input and two output ports. Depending on its design it allows us to combine two signals with a defined phase shift. The pseudo-correlation architecture uses a 180 degree hybrid to combine the antenna and reference signal. The behaviour of this hybrid is described by the matrix

$$\begin{bmatrix} A \\ B \end{bmatrix} = \frac{1}{\sqrt{2}} \begin{bmatrix} 1 & 1 \\ 1 & -1 \end{bmatrix} \cdot \begin{bmatrix} v_A \\ v_R \end{bmatrix}, \tag{5.15}$$

where v_A and v_R represent the voltage produced by the antenna and the reference load, respectively. If we connect the antenna and reference signal to the input as shown in Figure 5.5, the two output signals are $A = \frac{1}{\sqrt{2}}[v_\mathrm{A} + v_\mathrm{R}]$ and $B = \frac{1}{\sqrt{2}}[v_\mathrm{A} - v_\mathrm{R}]$. These are then amplified by two independent RF-chains and afterwards separated again using a second hybrid. Since the two signals went through the same amplifiers, they also experienced the same gain fluctuations. Hence, we can use the change in

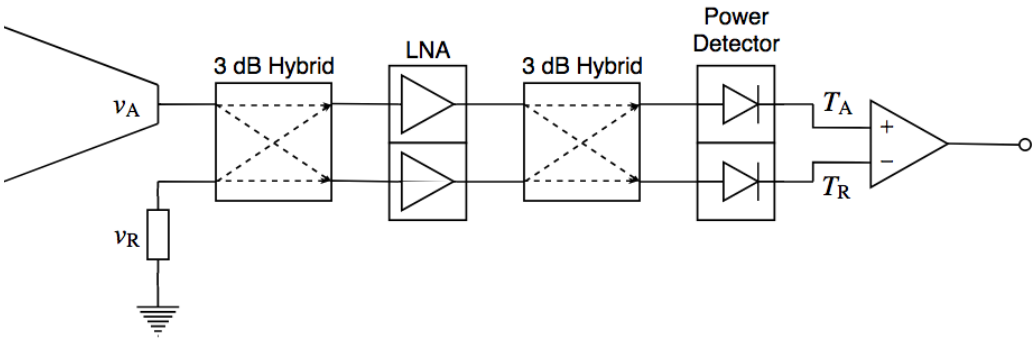

Figure 5.5: Schematic of a pseudo-correlation receiver using a 3 dB hybrid to combine the antenna and reference signal before the amplification. The combined signals go through both amplifiers and are then separated again using a second hybrid. The output signals are the antenna signal and the reference signal, both signals experienced the same gain fluctuations and the reference signal can be used to correct the antenna signal.

the reference signal T_{R} (v_{R}^2) to correct for any gain fluctuation, provided that the reference temperature is stable.

This type of gain tracking method has an advantage over the Dicke method that, the receiver measures the antenna signal continuously and that the stabilisation does not depend on the fact that the input signal must be levelled with a reference signal. However, this stabilisation architecture requires twice the number of components, as it needs to process both output signals of the hybrid. Although this method allows for continuous observation, its sensitivity also decreases due to the additional noise of the reference signal by a factor of $\sqrt{2}$ compared to the total power receiver from Equation 5.6. In addition to this there is also an increase of T_{sys} caused by the loss of the hybrid before the first amplifier. Therefore, the pseudo-correlation receiver achieves a sensitivity of

$$\Delta T = \sqrt{2} T_{\mathrm{sys}} \sqrt{\frac{1}{\tau \Delta \nu} + \left(\frac{\Delta G_{\mathrm{res}}}{G} \right)^2}. \tag{5.16}$$

5.4.3 White-Noise Stabilised

The white-noise stabilised receiver uses a bright reference signal, usually produced by a stabilised noise diode to track the gain fluctuations. The reference signal is added to the antenna signal by a coupler before the first amplifier, as shown in Figure 5.6. The added reference signal allows the receiver system to determine the current gain of the receiver. This is done by comparing the measured power for both signal states, with and without the reference signal present.

If we would assume the worst case for this stabilisation method, we would require the reference signal to be present with a duty-cycle of 50 percent, which would give us similar performance than a Dicke switched radiometer. Although, if the dynamic range of the receiver system allows for the reference signal to be $T_{\mathrm{R}} \gg T_{\mathrm{A}}$, it is possible to reduce the duty-cycle and still be able to determine the gain precisely. Hence, a receiver using this method has a sensitivity decrease which lies somewhere between $1 < K \leq \sqrt{2}$ depending on the applied duty-cycle of the reference signal, where

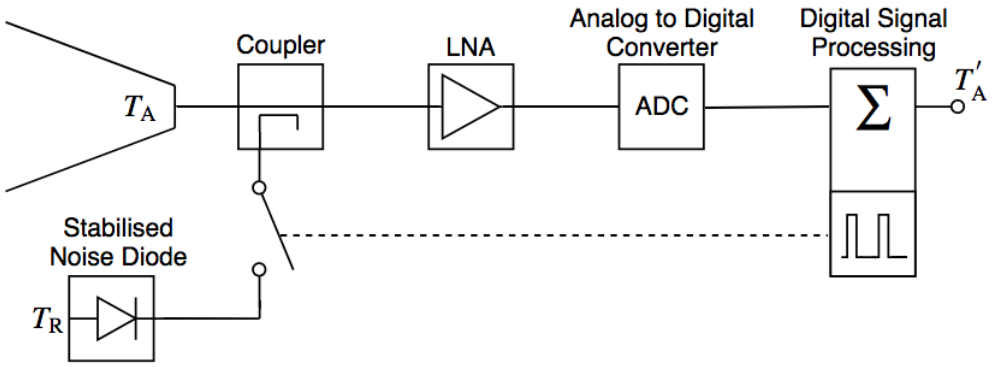

Figure 5.6: Schematic of a noise-adding receiver using a stabilised noise diode signal to track the gain fluctuations. The noise signal is added via a coupler and modulated with a switch. The duty-cycle and the modulation frequency is controlled by the digital backend of the receiver, which applies either an online calibration or writes the measured gain together with the antenna data to disk. Hence, the gain correction can be applied offline.

K represents the sensitivity decrease in the modified practical receiver sensitivity equation

$$\Delta T = K T_{\mathrm{sys}} \sqrt{\frac{1}{\tau \Delta \nu} + \left(\frac{\Delta G_{\mathrm{res}}}{G}\right)^2}. \tag{5.17}$$

The white-noise stabilised receiver will be discussed in more detail in Section 5.5.1.

5.4.4 Continuous-Wave Stabilised

The continuous-wave stabilised receiver uses a local oscillator as a reference signal to track the gain fluctuations. This signal is added to the antenna signal using a coupler as shown in Figure 5.7. It uses the assumption that the gain fluctuations are not frequency dependent or at least constant over a certain bandwidth. The gain of the receiver is then determined by measuring the power level of this narrowband signal, assuming that the noise contribution from the antenna signal is negligible. This can be done by either designing a narrowband filter, where the centre frequency of the filter is equal to the reference signal frequency, or by computing the power density spectrum with a digital backend and using one channel as the reference channel. The advantage of this system is that it allows for a continuous observation and that the reference signal is band-limited to either a narrowband filter or one channel of

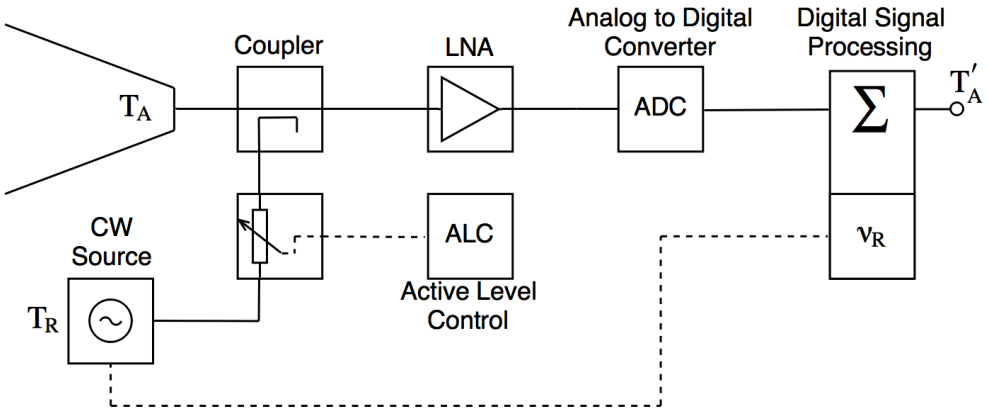

Figure 5.7: Schematic of a continuous-wave stabilised receiver using an amplitude stabilised local oscillator to track gain fluctuations. The reference signal is added via a coupler and stabilised with an analogue active level control loop. The local oscillator frequency can be controlled by the digital backend of the receiver, allowing to map the entire receiver band with the reference signal. The measured gain fluctuation is either corrected in real time or written to disk allowing for an offline correction.

a spectrometer. Hence, this method allows to track the gain fluctuation whilst not compromising the antenna signal, its sensitivity is given by

$$\Delta T = T_{\mathrm{sys}} \sqrt{\frac{1}{\tau \Delta \nu} + \left(\frac{\Delta G_{\mathrm{res}}}{G} \right)^2}. \tag{5.18}$$

The continuous-wave stabilised receiver will be discussed in more detail in Section 5.5.2.

5.5 Analysis of Methods for Gain Tracking

In this section, we will discuss the white-noise and continuous-wave gain tracking methods in more detail, as we want to implement one method into the GHY-3 receiver system. We will introduce the fundamental theory and then discuss the uncertainty on the gain measurement for each method.

5.5.1 White-Noise Stabilised

In this section, we discuss the theory of the white noise stabilisation method. This is followed by a brief analysis of the uncertainty calculation of the measured gain value.

5.5.1.1 Theory

The basic idea of the white noise stabilised receiver is that by modulating a broadband reference signal on the input signal of the amplifier, we are able to determine the real time gain of the system, which allows us to track any gain fluctuations over time. A simplified system diagram for this method has been shown in Figure 5.6, where the reference signal is modulated on the input signal using a switch and a coupler. The modulation frequency and duty-cycle is controlled by the digital backend of the receiver and is indicated by the dashed line. The output signal for this configuration in the time domain has the form of a noisy square-wave, where the low state represents the signal from the antenna T_A (v_A^2) and the high state represents the antenna plus the reference signal $T_\mathrm{A} + T_\mathrm{R}$ $(v_\mathrm{A}^2 + v_\mathrm{R}^2)$, see Figure 5.8. The rms voltage for those two states can be calculated with Equation 5.2, using T_A and $T_\mathrm{A} + T_\mathrm{R}$ as the temperature value. In further calculations we will refer to the rms voltage $v_\mathrm{rms,OFF}$ and $v_\mathrm{rms,ON}$ for the two states where the reference signal OFF and ON.

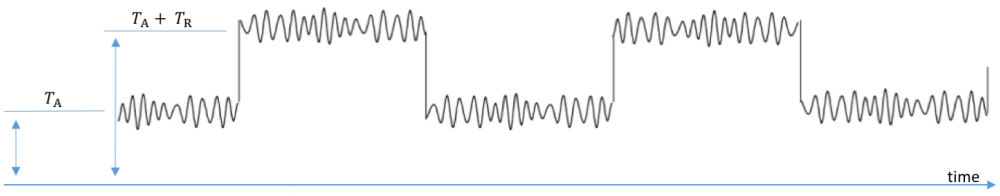

Figure 5.8: Periodicity of the output signal of the receiver in the time domain.

The output voltage signal of the receiver is defined as the input voltage signal multiplied by the gain. Therefore we can say that the difference in amplitude between $v_\mathrm{rms,ON}$ and $v_\mathrm{rms,OFF}$ is proportional to the added reference input voltage signal

multiplied by the gain. Hence, the gain can be determined by

$$G_{\mathrm{RE}} = \frac{\sqrt{v_{\mathrm{rms,ON}}^2 - v_{\mathrm{rms,OFF}}^2}}{v_{\mathrm{rms,R}}} = \frac{v_{\mathrm{rms},\Delta}}{v_{\mathrm{rms,R}}}\,, \tag{5.19}$$

where

G_{RE} : recovered gain,
$v_{\mathrm{rms,ON}}$: amplitude of the detected signal when the reference signal is ON,
$v_{\mathrm{rms,OFF}}$: amplitude of the detected signal when the reference signal is OFF, and
$v_{\mathrm{rms,R}}$: amplitude of the reference signal at the input.

This allows us to measure the gain for each period of the modulated reference signal. As our signal is Gaussian noise, the most straightforward way to determine the gain is to calculate the standard deviation of the detected voltage signals for both states $v_{\mathrm{rms,ON}}$ and $v_{\mathrm{rms,OFF}}$. The equation to calculate the standard deviation from a set of sampled voltages can be found in [70] and is given by

$$\sigma = v_{\mathrm{rms}} = \sqrt{\frac{1}{N-1}\sum_{k=1}^{N}\left(v_k - \mu_0\right)^2}\,, \tag{5.20}$$

with

$$\mu_0 = \frac{1}{N}\sum_{k=1}^{N} v_k \tag{5.21}$$

where

σ : standard deviation,
v_k : voltage value of sample k,
μ_0 : the mean value of the sample set, and
N : the number of individual samples.

Now we are able to determine the gain of the system for each period of the modulated reference signal, but in order to make use of this method we need to know the uncertainty on the measured gain. The next section describes the uncertainty propagation from the sampled voltage signal to the calculated gain value.

5.5.1.2 Uncertainty of the Gain Tracking

The calculation of the uncertainty on the gain measurement does not include any errors introduced by the quantisation process of the analogue-to-digital conversion. These effects have been discussed in detail in [71] before and as we use an 8-bit analogue-to-digital converter we can treat this conversion with a quantisation efficiency of approximately one, as we can seen in Table 5.2. Even if we consider a worst case where we only use 4 bits of the ADC, we still have a quantisation efficiency of 0.988.

Table 5.2: Quantisation efficiency examples for different number of ADC bits, sampled at the Nyquist rate. All values are taken from [71].

Number of bits	Number of levels	Quantisation efficiency
2	4	0.88115
4	16	0.98846
8	256	0.99991

The uncertainty on the measured standard deviation for a Gaussian noise signal for a given set of voltage samples is discussed in detail in [70], and the equation to compute the uncertainty is given by

$$v_{\mathrm{rms}} = \sigma \pm \frac{\sigma}{\sqrt{2\,(N-1)}}, \tag{5.22}$$

$$\delta v_{\mathrm{rms}} = \frac{\sigma}{\sqrt{2\,(N-1)}} \tag{5.23}$$

where σ is calculated using Equation 5.20. As long as the mean value of the both signals is $\mu = 0$, we can compute the difference Δv_{rms} between both signal states by subtracting the standard deviation in quadrature

$$v_{\mathrm{rms},\Delta} = \sqrt{v^2_{\mathrm{rms,ON}} - v^2_{\mathrm{rms,OFF}}}, \tag{5.24}$$

therefore, the uncertainty on this operation is calculated using the general formula

for computing the propagated error for a function of several uncorrelated variables

$$\delta q = \sqrt{\left(\frac{\partial q}{\partial x}\delta x\right)^2 + ... + \left(\frac{\partial q}{\partial z}\delta z\right)^2}, \tag{5.25}$$

which leads to the uncertainty on the differential signal $v_{\mathrm{rms},\Delta}$

$$\delta v_{\mathrm{rms},\Delta} = \sqrt{\left(\frac{v_{\mathrm{rms,ON}} \cdot \delta v_{\mathrm{rms,ON}}}{\sqrt{v_{\mathrm{rms,ON}}^2 - v_{\mathrm{rms,OFF}}^2}}\right)^2 + \left(\frac{-v_{\mathrm{rms,OFF}} \cdot \delta v_{\mathrm{rms,OFF}}}{\sqrt{v_{\mathrm{rms,ON}}^2 - v_{\mathrm{rms,OFF}}^2}}\right)^2} \tag{5.26}$$

and

$$v_{\mathrm{rms},\Delta} = v_{\mathrm{rms},\Delta} \pm \delta v_{\mathrm{rms},\Delta}. \tag{5.27}$$

The recovered gain is calculated by dividing the differential signal $v_{\mathrm{rms},\Delta}$ with the reference input signal $v_{\mathrm{rms,R}}$, therefore both uncertainties are added in quadrature.

$$\delta G_{\mathrm{RE}} = G_{\mathrm{RE}}\sqrt{\left(\frac{\delta v_{\mathrm{rms},\Delta}}{v_{\mathrm{rms},\Delta}}\right)^2 + \left(\frac{\delta v_{\mathrm{rms,R}}}{v_{\mathrm{rms,R}}}\right)^2} \tag{5.28}$$

5.5.2 Continuous-Wave Stabilised

In this section, we present the theory of the continuous-wave stabilisation method. This is followed by a brief discussion of the uncertainty of the gain measurement using this method.

5.5.2.1 Theory

The continuous-wave stabilised receiver uses a similar approach as the white noise stabilised receiver in that it also adds a reference signal to the input of the first amplifier. However, it assumes that the gain variations are not frequency dependent and therefore measuring the gain at a particular frequency allows us to correct the fluctuations for the entire observational frequency band. An example of a measured power-density spectrum with a reference signal present is shown in Figure 5.9. To apply this method, we need a digital receiver backend which can compute the power-

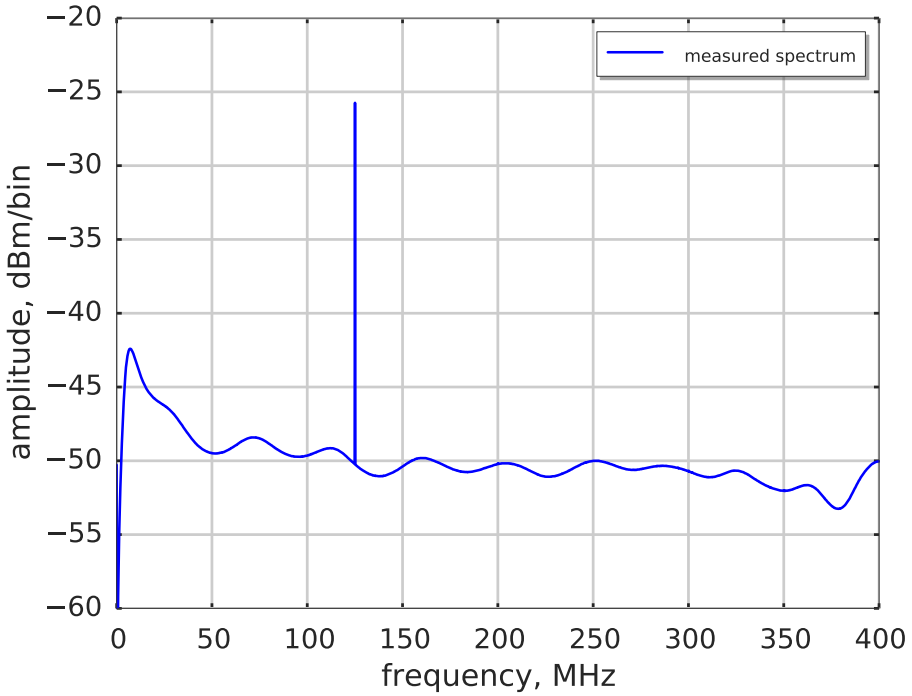

Figure 5.9: The power spectrum of a 400 MHz receiver band. The continuous-ware reference signal is added at a frequency of 125 MHz.

density spectrum of the receiver band. The reference signal is set to be at the centre frequency of the spectral bin which is used to track the gain fluctuations. From Section 5.5.1.1 we know that the output voltage signal sampled by the ADC is defined as the input voltage signal multiplied by the gain. Therefore, we can say that when detecting the power of the reference signal, the gain of the system is given by

$$G_{\mathrm{RE}} = \sqrt{\frac{P_{\mathrm{cw}}}{P_{\mathrm{cw,R}}}}\,, \tag{5.29}$$

where

G_{RE} : recovered gain,
P_{cw} : detected power of the reference signal,
$P_{\mathrm{cw,R}}$: power of the reference signal at the input.

Note, that we require the voltage gain of the system and therefore we need to take the square root when measuring power signals.

Next, we will go through the process of calculating the power density spectrum, which then contains our reference signal bin. This is done by calculating the autocorrelation function and then transforming its output into the spectral domain. The autocorrelation function multiplies the signal with itself but delayed by a time interval. It is given by

$$\Psi_{xx}(\tau) = \lim_{T\to\infty} \frac{1}{T} \int_{-T/2}^{+T/2} x(t)x(t-\tau)dt\,. \tag{5.30}$$

Since the output of the autocorrelation function is the signal power, the corresponding power density spectrum can be calculated by

$$S(\omega) = \int_{-\infty}^{\infty} \Psi_{xx}(\tau)e^{-i\omega\tau}d\tau\,. \tag{5.31}$$

As we sample the output signal of our receiver with an ADC, we need to use the

autocorrelation estimator which is given by

$$C_{xx}(m) = \frac{1}{N} \sum_{m=0}^{N-|m|-1} x(n)x(n+m)\,, \tag{5.32}$$

and the corresponding Discrete Fourier Transform gives us the Periodogram $I(n)$

$$I(n) = \frac{1}{N} \sum_{k=0}^{N-1} C_{xx}(k) e^{-i2\pi \frac{nk}{N}}\,. \tag{5.33}$$

We then can calculate the power of the detected reference signal P_{cw} by integrating over the frequency bins at which the reference signal is present.

$$P_{\text{cw}} = \frac{1}{\pi} \int S(\omega) d\omega \tag{5.34}$$

For a discrete spectrum this is done by taking the normalised sum over the discrete frequency bins, given by

$$P_{\text{cw}} = \frac{1}{N} \sum I(n). \tag{5.35}$$

5.5.2.2 Uncertainty of the Gain

For the uncertainty calculation on the recovered gain using a continuous-wave signal we also do not consider any quantisation errors. Section 5.5.1.2 explained that the quantisation efficiency for our system is considered to be one. However, if we would use a different ADC with fewer bits we would need to include the quantisation uncertainty in our calculation.

The uncertainty on the measured signal power in the reference bin of the power density spectrum is given by the signal-to-noise ratio (SNR) for that bin, where we assume that the measured amplitude consists of two individual signals. First the reference signal P_{cw} and second the noise signal P_{noise} causing the uncertainty. The SNR is calculated by

$$\text{SNR} = \frac{\text{P}_{\text{cw}}}{\text{P}_{\text{noise}}}, \tag{5.36}$$

where P_{noise} is the power produced by the receiver system temperature P_{sys} plus the

power of the received antenna signal P_{A}. There are two factors which determine the uncertainty of the amplitude in the calibration bin. The first factor concerns the spectral resolution of the power spectrum. As the received noise power is proportional to the bandwidth $P = k_{\mathrm{B}} T \Delta\nu$, increasing the spectral resolution leads to an bandwidth decrease for each frequency bin of the discrete power spectrum. Hence, we can say that the uncertainty is proportional to $1/N$. For example a spectral resolution of 1000 frequency channels increases the signal-to-noise ratio by 30 dB. The second factor concerns the power level ratio between the reference tone and the power level of the receiver input signal. By increasing the power level of the reference signal, we directly increase the signal-to-noise ratio of the measurement. However, the reference signal power must not exceed the dynamic range of the signal chain and the ADC.

Averaging the reference channel of independent spectra does not necessarily improve the uncertainty of the reference power measurement, however it will reduce the uncertainty of the underlying noise within the calibration bin. For signal-to-noise ratios where the amplitude is affected by noise in the reference signal frequency bin, averaging will improve the measurement result. This means that the total average time then provides the refresh rate for independent gain measurements. These must be at least twice the knee frequency of the system in order to Nyquist sample the gain fluctuations.

Chapter 6

Experimental Verification of Gain Stabilisation Methods

In this chapter, we verify the white-noise and continuous-wave stabilised methods presented in the previous section. In the first part of this chapter we give an overview of the laboratory setup used to verify both methods. We characterise the setup with respect to its intrinsic gain stability, as well as discuss the calibration of the readout system. The second part of the chapter presents for each method the individual parameter settings and the experimental results.

6.1 Laboratory Setup

This section describes the laboratory setup used for the verification of the gain stabilisation methods. We first describe the hardware setup and then the FGPA firmware design of the readout system.

6.1.1 Hardware Setup

A system diagram of the experimental setup is shown in Figure 6.1. The blue surrounded area shows the components that are located within the cryostat and are cooled to approximately 10 K. The green surrounded area shows the components

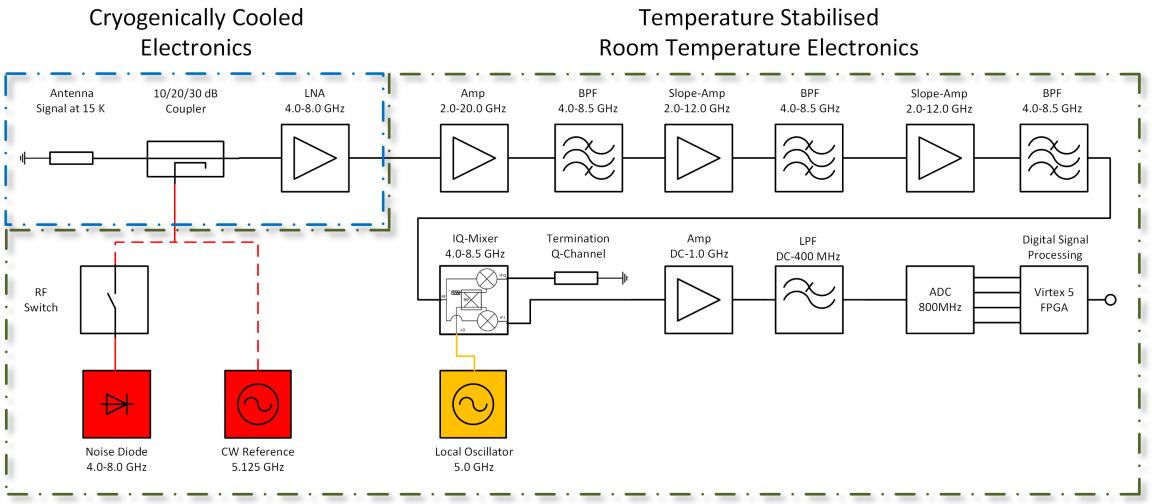

Figure 6.1: Schematic of the laboratory setup used to verify the both gain tracking methods. The component located in the cryostat are the low noise amplifier, the coupler, and a 50 Ohm resistor which simulates the antenna input signal. The resistor is temperature stabilised to 15K, hence no input signal fluctuations are present.

which are located at room temperature and are temperature stabilised to 40° C. The signal chain of the laboratory setup is designed to be as close as possible to the final signal chain used in the GHY-3 receiver. This allows us to predict what performance the gain tracking would have in the actual receiver system. The input signal of the laboratory setup is generated by a 50 Ohm resistor which is temperature stabilised to a set value. The stabilisation is done by using a heated bobbin which is weakly thermally coupled to the cold plate and fitted with a precision Cernox temperature sensor. An external PID controller allows us to stabilise the temperature to approximately $\pm 1\,\mathrm{mK}$, therefore we can treat the input signal as constant. The reference signal is added in to the signal chain by a coupler right before the first low-noise amplifier. After that, the signal goes through several stages of amplifiers and filters until it is down-converted by the mixer stage. We use a 5 GHz local oscillator signal and a 400 MHz IF filter, thereby selecting the RF signal from $4.6 - 5.4\,\mathrm{GHz}$. Hence, this configuration allows us to measure the overall gain drift of the system over an effective bandwidth of 800 MHz. As we only use the in-phase output of the GHY-3 IQ-mixer, we can consider this system as a dual-sideband system (DSS), where the upper and lower sideband are mixed to the same intermediate frequency. This config-

uration is fine for the verification of the two gain stabilisation techniques. In the case of the white-noise stabilisation the calibration signal is present in all frequencies and we do not need to distinguish between the lower-sideband and the upper-sideband frequencies. In the case of the continuous-wave stabilisation technique we know the calibration frequency and the DSS configuration only introduces additional noise into the calibration channel. Finally, the intermediate frequency is amplified and filtered again before it is digitised. Compared to the GHY-3 receiver readout system we reduced the sampling frequency from 1 GHz to 800 MHz. This was done to decrease timing constraints on the digital readout system which makes the firmware design easier.

6.1.2 Digital Readout System

For the digital readout system, we use an FPGA based hardware platform developed by the CASPER collaboration [72]. We chose this particular hardware platform for two reasons. The first one was that the high level firmware design tool makes it an ideal platform to develop a number of different readout designs. The second one was that this hardware platform was already available at the time we set up the experiment, whereas the GHY-3 DSP which will be deployed with the receiver system became only available close to the end of the project.

Figure 6.2 shows the ROACH DSP board including two analogue-to-digital converter cards, as used in the laboratory setup. The ADCs allow for a maximum sample frequency of 1 GHz with a 8 bit resolution over the voltage range of ±250 mV. The advantage of using the CASPER based hardware is that the firmware design uses MATLAB's Simulink as a high-level programming language. An example which illustrates these advantages and explains how FPGA firmware is designed using the Simulink based CASPER library is presented in [73]. CASPER provides an extensive library of function blocks and hardware specific blocks which cover a wide range of applications. In the next section, we present the three different firmware versions used to measure the gain tracking methods.

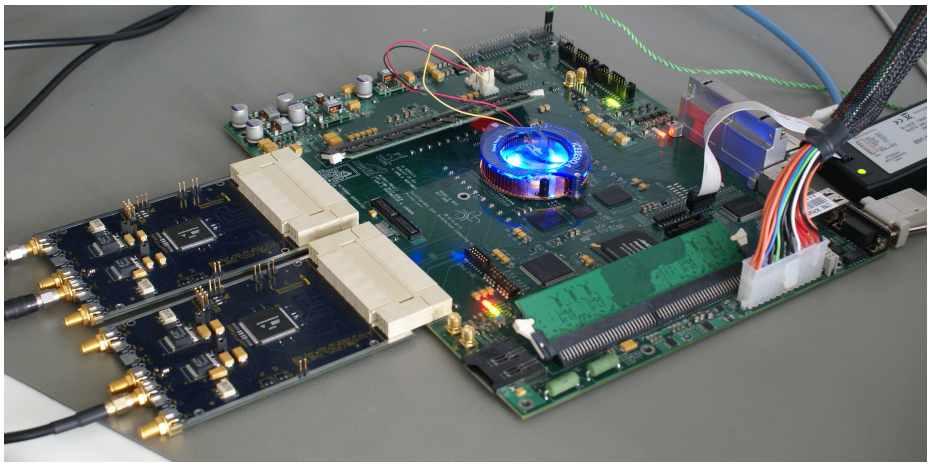

Figure 6.2: ROACH, digital signal processing board with two iADC cards connected [74].

6.1.2.1 Total Power Meter Firmware

The first firmware design implements a total power meter with a bandwidth of 400 MHz. The Simulink design describing the firmware is shown in Figure 6.3. The ADC is implemented by the yellow block on the left-hand side, whose output is four sampled 8 bit values. The reason for this is that the FPGA clock runs at a quarter of the ADC sample frequency. Therefore, for each FPGA clock cycle we have four ADC samples. The sampled voltage signals are then squared and accumulated and

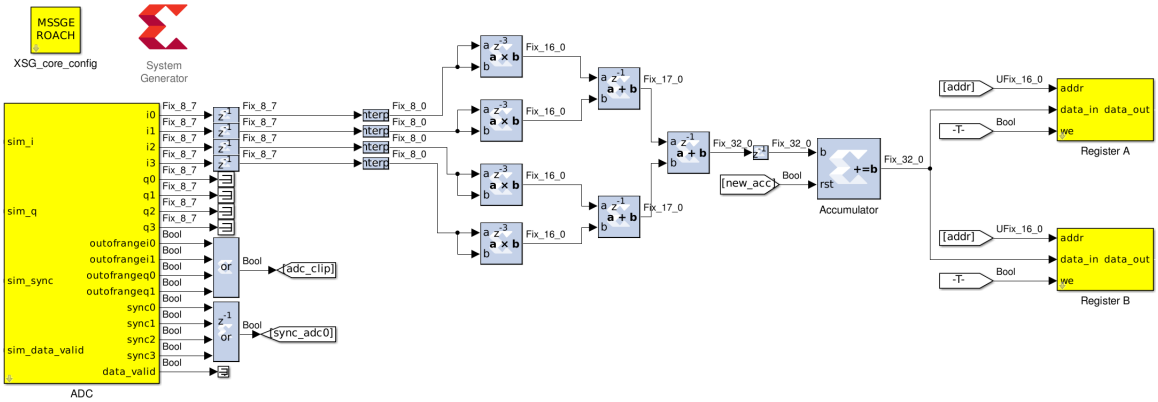

Figure 6.3: Schematic of the FPGA firmware used to measure the total power. The signal is digitised on the left-hand side by the ADC and then squared and accumulated. After that, the accumulated v^2 samples are written into registers on the right-hand side and read out by the control computer.

then stored in the readout registers on the right-hand side. The firmware writes the accumulated samples in a double-buffered register, which means that when register A is full the FPGA stores the samples in register B and the control computer reads the values in register A and vice versa. Using this method, we can read out the samples continuously, provided that the read out process is faster then the write process. If we look at the equation used to compute the rms voltage from a set of sampled voltages

$$v_{\mathrm{rms}} = \sqrt{\frac{1}{N-1}\sum_{k=1}^{N} v_k^2}\,, \tag{6.1}$$

we implemented the operations depicted in red in the FPGA firmware. The remaining operations are then carried out by the control computer after the content of the read out registers have been transferred.

The main reason we implement the accumulation in firmware is to reduce the read out data rate. Assuming we would transfer the sampled voltages directly, we would produce a data rate of 6.4 Gbps which makes the read out system unpractical. Hence, we decided to accumulate 2^{14} samples and therefore reduce the read out data rate to 781.25 kbps. It is important to note that the accumulation basically implements a low-pass filter, where all frequencies above the filter cut off are suppressed. An accumulation length of 2^{14} samples lead to an effective sample frequency of 24.414 kHz with the corresponding bandwidth of 12.207 kHz. This process of data reduction is fine as long as the signal which we are interested in is still Nyquist sampled by the effective sample frequency.

6.1.2.2 Spectrometer Firmware

The second firmware implements a real-time spectrometer. The Simulink design which describes the firmware is shown in Figure 6.4. The two green blocks represent the implemented polyphase filter bank (PFB) and the Fast Fourier Transformation (FFT), respectively. The signals after the FFT represent the complex voltage amplitude of the frequency spectrum. In the next step these values are multiplied with their complex conjugate to produce a real power spectrum and are then accumulated. Finally,

the integrated power spectrum is written into the registers for even and odd frequency channels and read out by the control computer.

The PFB implements a finite impulse response (FIR) filter which improves the amplitude isolation of the frequency channels [75]. This is of great importance when the sampled signal contains strong narrowband signals such as RFI or in our case a CW reference signal. A comparison of the frequency channel isolation for different spectrometer implementation taken from [75] is shown in Figure 6.5. The plot shows three different implementations. First, the dotted line which shows the channel isolation for an autocorrelation spectrometer where the power spectrum is computed by a discrete range of delays. Second, the dashed line which shows the channel isolation for an implemented fast fourier transform without a digital filter applied. Third, the solid line which represents the channel isolation for a FFT combined with a polyphase filterbank using a 8-tap Hann-window function. Based on this figure, we can say that an implementation of a PFB increases the frequency isolation by >60 dB for adjacent channels and >80 dB for more widely spaced channels.

The implemented PFB in our test setup applies a Hamming window and a 4 tap filter implementation to increase the frequency isolation. The length of the filter is

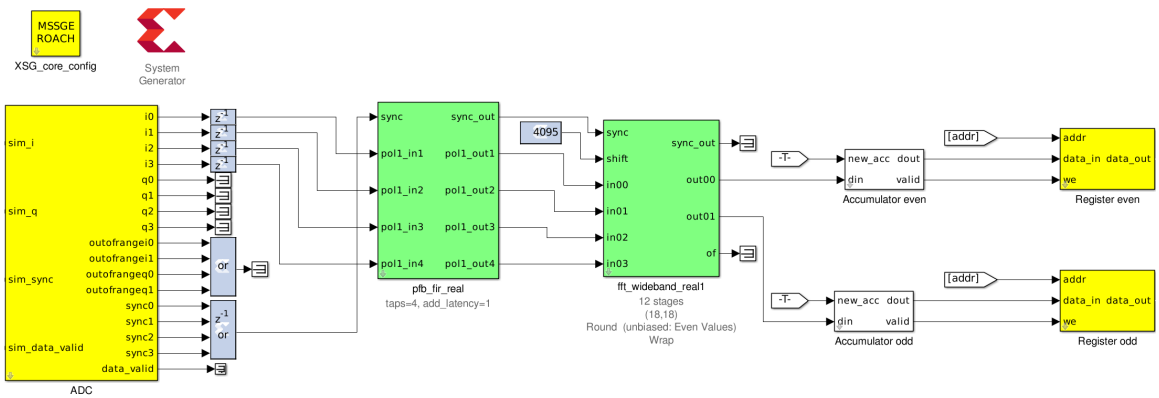

Figure 6.4: Schematic of the FPGA firmware used to measure the power spectrum. The signal is digitised on the left-hand side by the ADC and then filtered and Fourier Transformed by the two green blocks. The output samples represent now the complex amplitude of the spectral bins. These are then multiplied by the complex conjugated and accumulated. In the final step, the integrated spectra are written into the read out registers on the right-hand side.

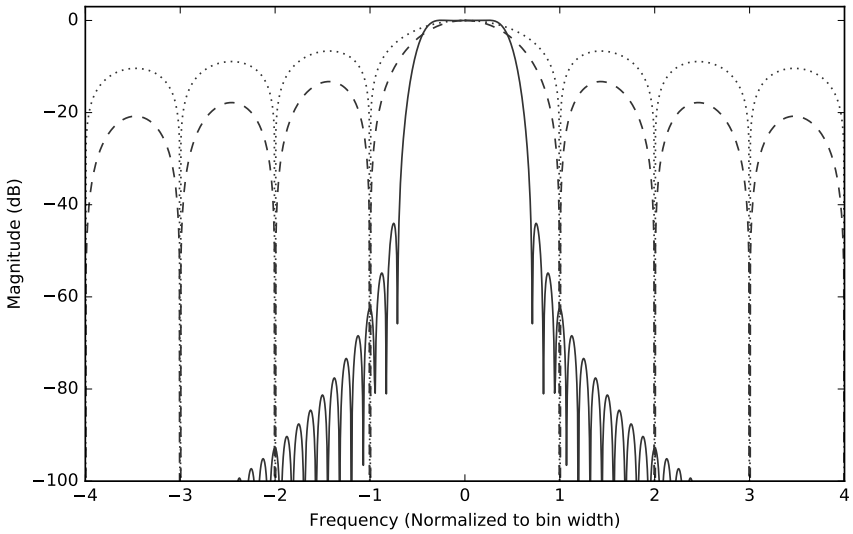

Figure 6.5: The comparison of different channel isolations for different spectrometer implementations. The dotted line shows the channel isolation for an autocorrelation spectrometer where the power spectrum is computed by a discrete range of delays. The dashed line shows the channel isolation for an implemented FFT. The solid line represents the channel isolation for a FFT combined with a polyphase filterbank using a 8-tap Hann-window function. The image has been used with the permission of the author from [75].

matched with the length of the FFT, so that the window function is applied at each complete spectrum. The implemented FFT has a size of 2^{12} samples per spectrum. As we use a real FFT the negative and positive frequency channels contain the same information, so we discard the negative frequencies and end up with 2^{11} complex positive frequency channels. Since we have a bandwidth of 400 MHz and 2^{11} frequency channels, our spectral resolution is 195.3125 kHz. To reduce the read out data rate we further integrate over 2^{12} spectra, resulting in an effective read out frequency of 47.68 Hz.

6.1.2.3 Combined Spectral and Power Meter Firmware

The third firmware implements both previous designs, allowing measurements of the total power of the sampled signal as well as the power of a certain frequency channel. The Simulink design for this firmware is shown in Figure 6.6. This configuration allows

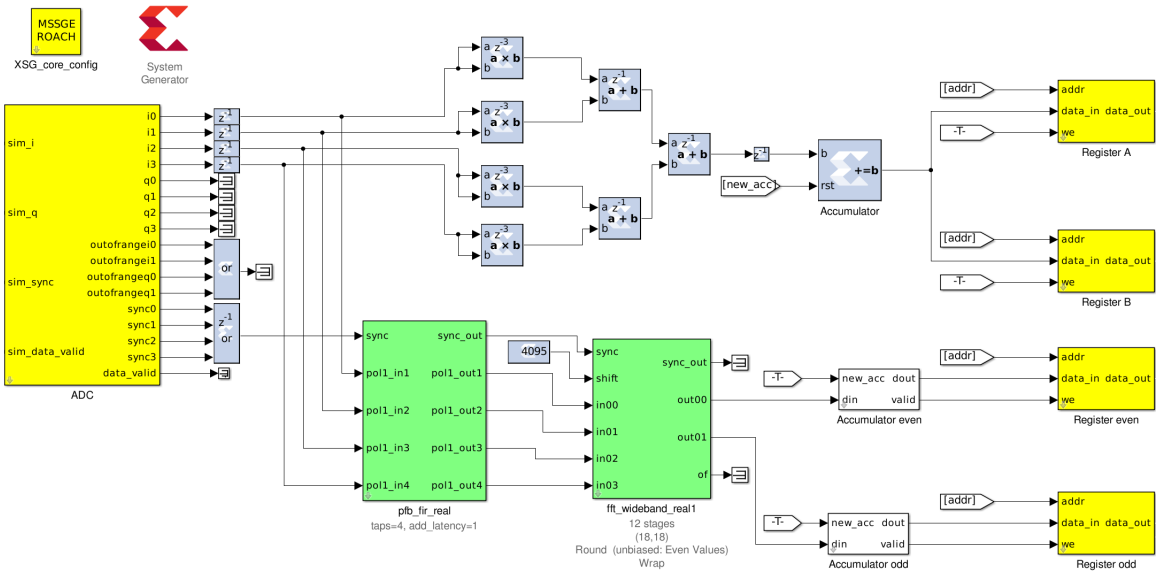

Figure 6.6: Schematic of the FPGA firmware used to validate the continuous wave gain tracking approach. This firmware combines both previous firmware designs, allowing to measure to total power while also measuring the power in a certain frequency channel.

us to validate the continuous-wave gain-tracking method, as we can independently measure the change in amplitude of the entire received signal as well as the change in power of a single frequency bin containing the reference signal, for the same set of samples.

This configuration uses the same read out rate as the total power meter implementation shown in Section 6.1.2.1. However, the read out rate for the spectral information has been reduced to approximately 23.84 Hz. This means that for every 1024 power meter samples we have one corresponding sample from the spectrometer implementation.

6.1.3 Readout Calibration

As the ADC card has a pre-amplifier with an unknown gain, we needed to calibrate the DSP read out system, in order to ensure that the measured voltage and power levels are correct. This was done by applying a known input signal to the ADC and comparing the output of the DSP to the measured values of a calibrated power meter. The schematic for this calibration setup is shown in Figure 6.7. The read out system

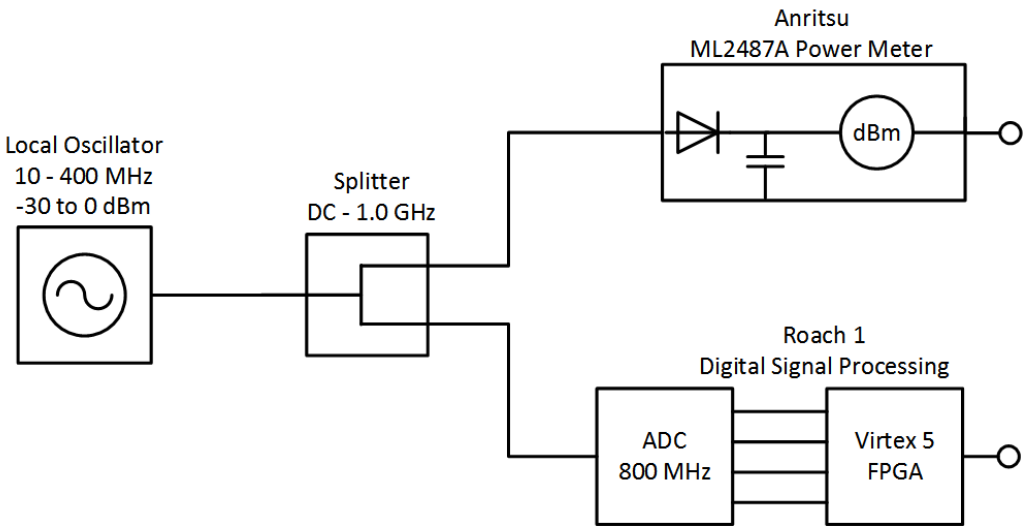

Figure 6.7: Schematic of the calibration setup.

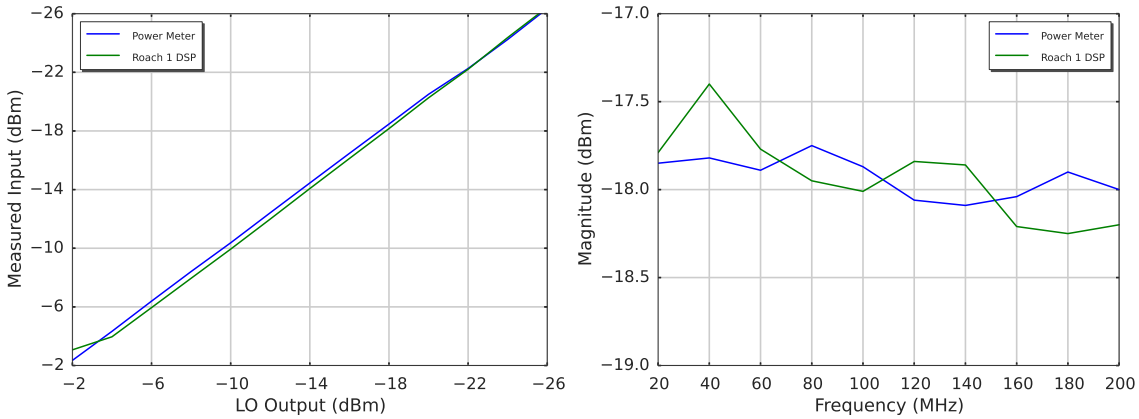

(a) Power Sweep

(b) Frequency Sweep

Figure 6.8: Response after ADC calibration, (a) shows a power sweep at 70 MHz and (b) shows a frequency sweep with a constant output power of the local oscillator.

was calibrated with a frequency sweep at a constant input power and a power sweep at a constant frequency. The measured response for both measurements is shown in Figure 6.8. The power sweep shown in Figure 6.8a was done at a frequency of 70 MHz and covers 2/3 of the dynamic input power range of the ADC. The absolute range of the ADC used in our setup goes from 0 dBm to −41 dBm. To sample signals with at least 3 – 4 bits the lowest recommended input power level is −22 dBm, therefore we stopped the power sweep at −26 dBm. The important result shown in this plot is that the ADC responds linearly for an input power sweep. The offset between the

power measured by the Anritsu power meter and by the DSP setup could be explained by the splitter or by slightly different attenuations in the cables used to connect the setup. Furthermore, one can see that the ADC becomes non-linear for power levels above $-3\,\mathrm{dBm}$.

Figure 6.8b shows the frequency sweep from 20 MHz to 200 MHz. One can see that the power detected by both, the Anritsu power meter and the DSP setup changes while varying the frequency. This plot shows two distinct features. At first, we can see that there is an overall decrease in power with an increase in frequency of both devices. This can be explained by the frequency-dependent loss in cables and the splitter. The other more obvious feature is the change of power level seen between both devices. The change in detected power between both devices looks like an opposing behaviour. This feature can have a number of origins, which we do not know for certain. A possible cause for this feature could be the transmission characteristics of the pass-band of the ADC and the power meter, or a mismatch causing reflections, or a small wavelength dependence affecting the division in power between the two output signals of the splitter.

Nevertheless, we can say that this measurement confirmed the correct operation of the ADC used in our measurement setup. It is also important to keep in mind that we do not perform an absolute measurement of the system output power, as we are only interested in the relative amplitude change over time.

6.2 Characterisation of the Laboratory Setup

In this section we discuss the characteristics of the measurement setup with respect to its stability. For most of the following experiments we look at timescales of approximately 15 min and show the change in gain over time as well as the corresponding power spectrum.

6.2.1 Intrinsic Gain Fluctuations

In order to get an estimate on the instabilities of the laboratory setup, we measured the output signal of the signal chain using the total power meter firmware from Section 6.1.2.1. The input of the laboratory setup for this and all following measurements was stabilised, therefore we assume that all fluctuations in amplitude over time are due to gain drifts in the LNA and subsequent gain stages.

Figure 6.9 shows the test setup power spectrum for a measurement with no reference signal added into the signal path. The lowest frequency present is $1/\tau$, where τ represents the measurement time and the highest frequency present is $\frac{1}{2}f_s$, where f_s represents the effective sampling frequency of the total power meter readout firmware.

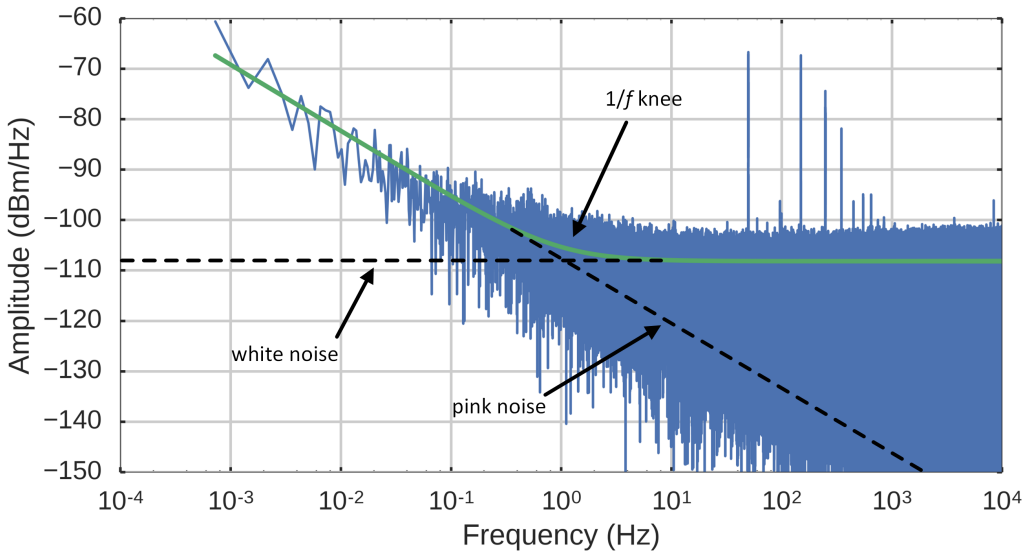

Figure 6.9: Measured power spectrum of the unstabilised laboratory setup. The spikes in the spectrum correspond to the 50 Hz mains frequency and its harmonics.

The spectrum shows two interesting features. The first feature are the spikes at $50, 150, 300\,\text{Hz}$, which correspond to the mains frequency and its harmonics. This tells us that the somewhere along the signal conditioning chain the mains frequency couples into our signal path. The second and more important feature is that the test setup power spectrum shows the expected characteristic, which is a combination of white noise and pink noise. The white noise level produces a flat spectrum above the $1/f$ knee frequency and below that point the pink noise starts to dominate the spectrum with an increase in amplitude for a decrease in frequency.

As the power spectrum is the best way of identifying the stability of the test setup we need a method to accurately characterise it. To do this, we use a noise model and a fitting algorithm which we took from [76]. The noise model allows us to characterise the measured power spectrum using four parameters. The model is given by

$$P_{xx} = \sigma_w^2 + \sigma_c^2 \left(\frac{1}{f_0}\right)^{-\alpha}, \tag{6.2}$$

where

σ_w^2 : white noise level,
σ_c^2 : correlated noise level at f_0,
f_0 : reference frequency, here $0.01\,\text{Hz}$,
α : power law index.

σ_c^2 together with α represents the non-white noise characteristic in the power spectrum for $\alpha = 1$ the correlated noise follows a pink noise characteristic and for $\alpha = 2$ a red noise characteristic.

The fitted noise model is indicated by the green line in Figure 6.9 and the corresponding parameters describing the fit are presented in Table 6.1. The noise model fit results in a $1/f$ knee frequency for the test setup of $0.93\,\text{Hz}$. A few hertz knee frequency is a typical value for HEMT low-noise amplifier receiver systems and agrees with measurements taken of the unstabilised C-BASS South receiver system presented in [77]. It is also important to keep in mind that the $1/f$ knee frequency depends on the white noise level of the power spectrum. For an increase in white noise level, the

knee frequency decreases and vice versa. Therefore, a good practice to compare the stability of a receiver system is to define the pink noise level at a certain frequency. This allows us to compare the difference between the white noise and pink noise level for a certain integration time, which can be seen by the last two values in Table 6.1, where we compare the white noise with the pink noise level at a frequency of 10^{-2} Hz. The corresponding amplitude change over time for this spectrum is shown in Figure 6.10. The signal is smoothed with a moving average filter to reduce the noise, thereby

Table 6.1: Fitted parameter of the noise model for the test setup.

Parameter		Value
α		1.312
σ_w	$(\sqrt{\text{mW}})$	$3.896\,\text{x}10^{-6}$
σ_c	$(\sqrt{\text{mW}})$	$3.729\,\text{x}10^{-6}$
knee freq	(Hz)	0.93
σ_w^2	(dBm)	-108.19
σ_c^2 at 10^{-2} Hz	(dBm)	-82.33

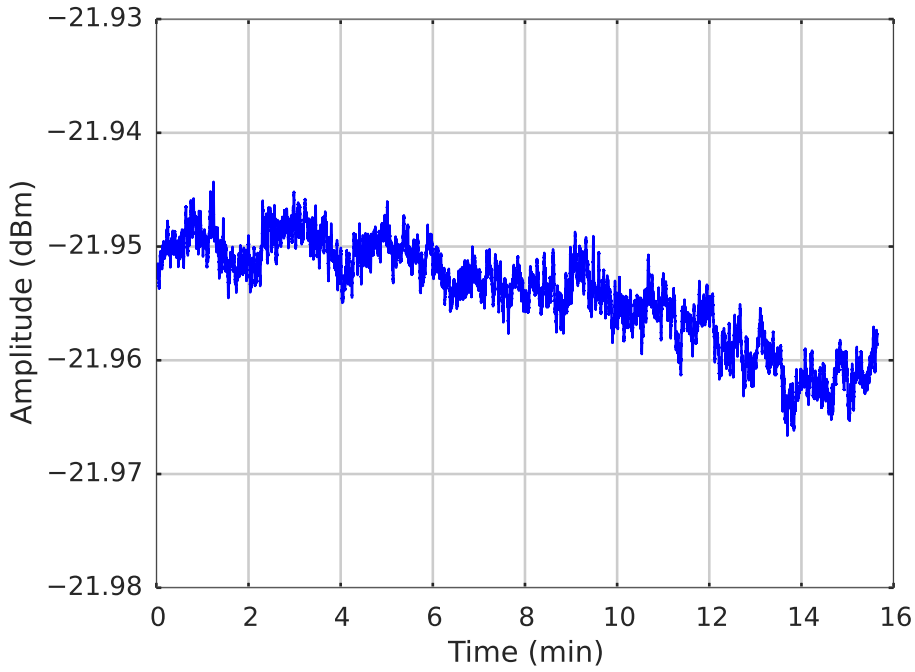

Figure 6.10: Measured output power over 15 min of the test setup, using the total power meter firmware. Note that the signal is low-pass filtered to reduce the noise.

low-pass filtering the signal. The cutoff for the filter used is approximately 2 Hz, hence the fluctuations we see are dominated by pink noise. It can be seen, that the change in gain over 15 min is approximately 0.02 dB. This measurement gives us an estimate on the intrinsic stability of the measurement setup.

6.2.2 Possible Sources of Gain Drift

In this section we discuss briefly possible sources that can cause gain fluctuations in our measurement setup and general receiver systems. Firstly, we were interested to see if physical temperature fluctuations of the low noise amplifier have an effect on the gain stability of the system. Secondly, we are going to discuss other influences which could have an effect on the gain stability.

6.2.2.1 Temperature Sensitivity of the LNA

The cold plate of a cryostat has certain temperature fluctuations over time. Some are caused by the cycle of the cryocooler, others are caused by external temperature cycles. We were interested to see if the present gain fluctuations in our laboratory setup can be significantly reduced by stabilising the physical temperature of the low-noise amplifier.

Therefore, we stabilised the LNA together with the input resistor and repeated the previous measurement. Figure 6.11, shows the physical temperature over time, for the cold plate and the low-noise amplifier. The top plot shows the measured temperature of two independent temperature sensors mounted at the cold plate. The offset seen between the measured temperature of the two sensors is due to a calibration offset. Since we are only interested in the temperature fluctuations over time, the offset between both sensors is not important for our measurement. What is more important is that the measured relative temperature change in both sensors is similar. The bottom plot shows the measured temperature over the same time period for the low-noise amplifier. The temperature range of the bottom plot is set to be the same range as for the cold plate measurement. This allows us to qualitatively compare the

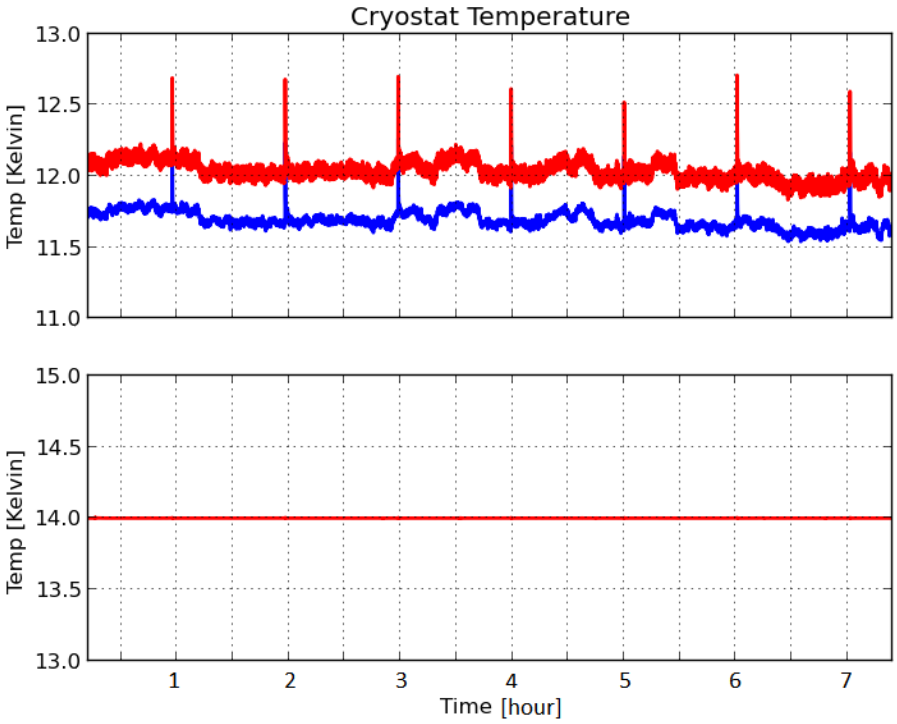

Figure 6.11: Measurement of the cryostat and the amplifier temperature. The top graph shows the temperature of the coldplate and bottom graph shows the stabilised temperature of the low noise amplifier. The Y-axis in both plots shows a temperature range of 2 K.

performance of the temperature stabilisation.

The temperature fluctuations on the cold plate show a number of sharp spikes approximately every hour. These spikes are due to a short decrease in cooling power when the cryocooler cycles a bypass valve. In comparison to that, the temperature of the amplifier shown in the bottom plot remains constant.

The measured power spectrum for this setup is shown in Figure 6.12 and the corresponding amplitude signal over time is shown in Figure 6.13. The results of the fitted noise model are presented in Table 6.2. The noise model gives a value for the $1/f$ knee frequency of 1.47 Hz, which is slightly higher compared with the previous measurement. This increase could be explained by the lower white noise level for the temperature stabilised LNA measurement. Although this measurement does not show a significant change in stability between a temperature stabilised and

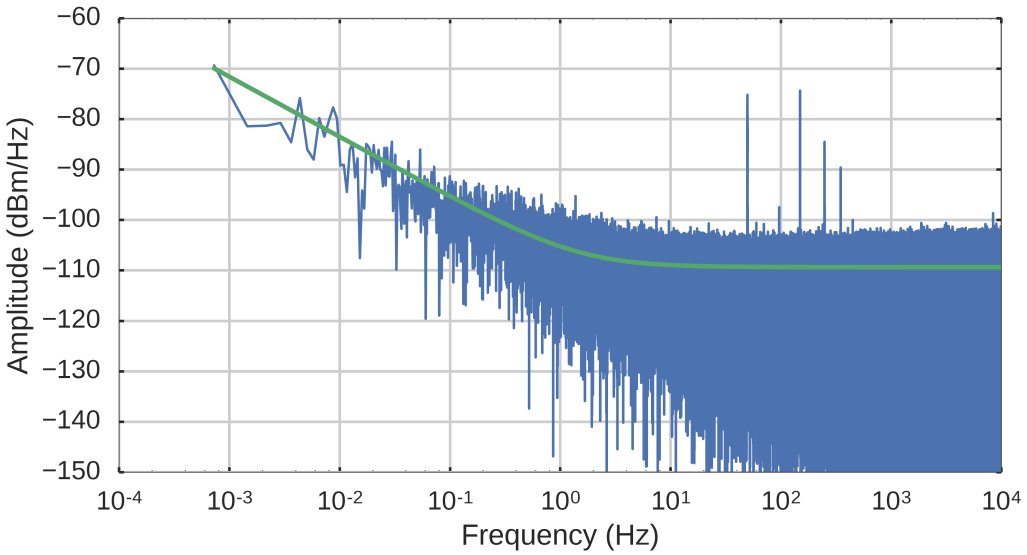

Figure 6.12: Measured power spectrum of the laboratory setup, with the physical temperature of the LNA stabilised to 14 K.

Table 6.2: Fitted parameter of the noise model for the temperature stabilised LNA measurement.

Parameter		Value
α		1.194
σ_w	$(\sqrt{\text{mW}})$	$3.396\,\text{x}10^{-6}$
σ_c	$(\sqrt{\text{mW}})$	$4.277\,\text{x}10^{-6}$
knee freq	(Hz)	1.474
σ_w^2	(dBm)	-109.38
σ_c^2 at 10^{-2} Hz	(dBm)	-83.50

unstabilised LNA, we still can see a decrease in slope of the pink noise, which indicates an improvement of the long term drift. This can be seen by comparing the value for α of both measurements. Although, this experiment indicates some improvement of stability for a system with a temperature stabilised LNA, the effect is minimal and not sufficient to stabilise the gain drift. Hence, we do not consider this approach any further, but it is important keep in mind that a temperature stabilisation is a good idea, just not sufficient.

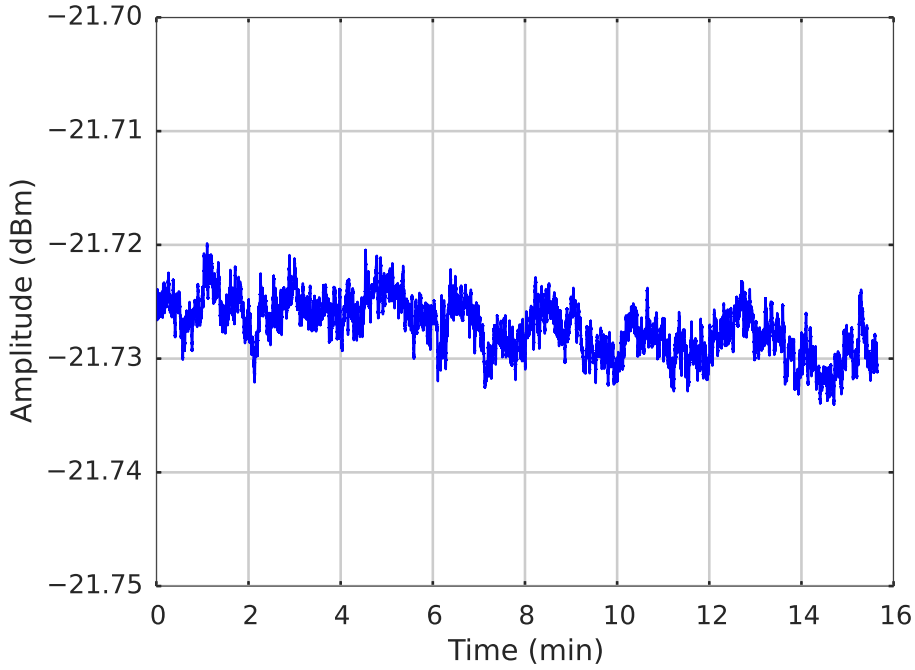

Figure 6.13: Measured output power over 15 min of the test setup with the physical temperature of the LNA stabilised to 14 K. Note, the signal is low-pass filtered to reduce the noise.

6.2.2.2 Other influences

In this paragraph we briefly discuss other influences on the gain stability apart from the amplifier $1/f$ noise, which we already introduced in Section 5.1.2.

As we could see in section 6.2.1, the change in amplitude caused by the gain fluctuations are of the order of 0.02 dBm, which means that small changes in attenuation caused by temperature variation of the warm part of the signal chain could also have a significant effect on the stability. In order to minimise those kinds of influences we temperature stabilised the entire room temperature part of the receiver chain and test setup to 40° C. However, this stabilisation only affects the components and cables that are mounted on the temperature stabilised plates, whereas the RF-cables connecting the cryostat with the temperature stabilised components can still introduce fluctuations.

Another element which is of great importance is the stability of the ADC, which operates by comparing the measured voltage signal with an internal reference signal

[78]. Any instabilities in the reference signal and comparison process lead to variation in the sampled receiver signal. After the signal is digitised, we cannot distinguish between a varying input signal or an unstable ADC reference signal. If it is the case that the ADC is the dominant source of instability in our system, we would require a gain tracking implementation for each ADC and track the fluctuations individually.

In Section 6.2.2.1 we showed that the influence of the physical LNA temperature does not dominate the gain fluctuation of the system, however another important aspect is the bias supply of the amplifier. The supply has direct influence on the gain of the amplifier and therefore any instabilities of the voltage and current supply do effect the stability of the system.

6.3 Continuous-Wave Stabilised Approach

In this section we discuss the experiments conducted to verify the continuous wave gain tracking technique. In the first half, we describe and test the frequency dependence of the gain fluctuations and in the second half we validate the reference signal and apply the stabilisation technique to our test setup.

6.3.1 Frequency Dependence of the Gain Fluctuations

The frequency dependence of the gain fluctuations is the most important factor for the CW stabilisation technique to work. Hence, the first step to verify this method is to measure the change in power over time for a number of independent frequency channels.

For this experiment we used the spectrometer implementation of the ROACH based DSP shown in Section 6.1.2 and measured the change in amplitude over a period of approximately 15 min. The input of the test setup is temperature stabilised and all fluctuations seen in the data are from gain instabilities of the signal conditioning chain. Figure 6.14 shows two measurements, one performed with the ROACH based DSP and an additional one performed with the GHY-3 DSP, which will be deployed with the receiver system to Goonhilly. The GHY-3 DSP hardware will be described in detail in

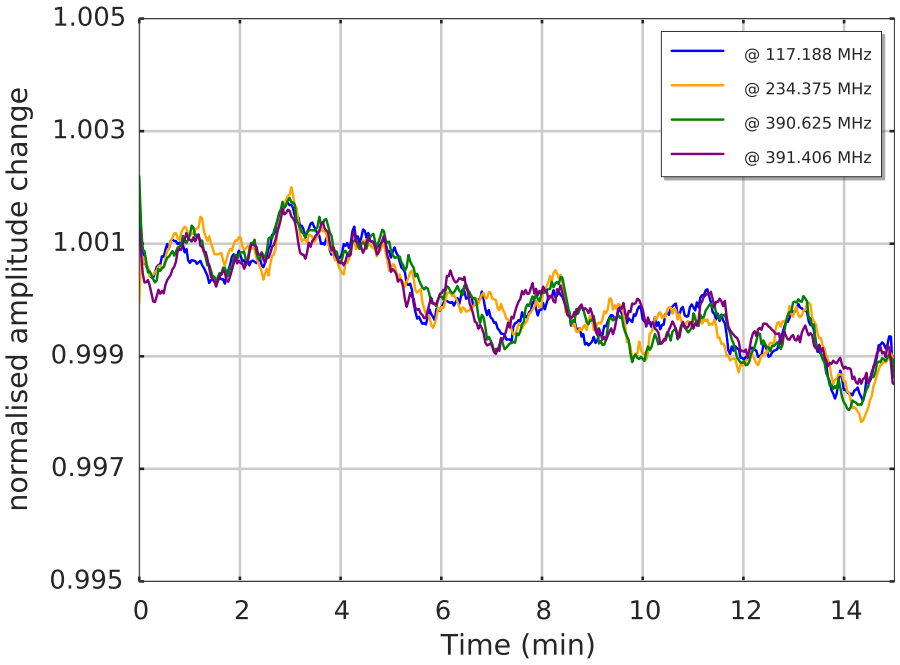

(a) Data captured with the test setup DSP.

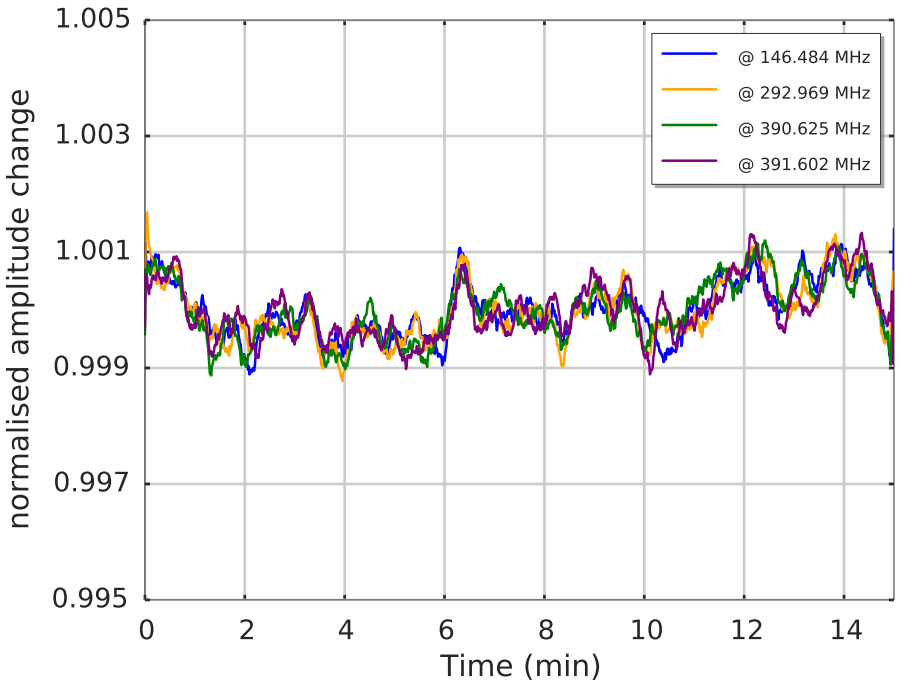

(b) Data captured with the GHY-3 DSP.

Figure 6.14: Measured fractional change in amplitude of independent frequency channels. (a) With the test setup DSP and the spectrometer firmware as presented in Section 6.1.2.2. (b) With the GHY-3 DSP.

Section 7.3. The additional measurement using a different DSP hardware provides an independent measurement to further validate the frequency dependence. Note that this measurement is the only measurement in this thesis which was performed with the GHY-3 DSP. The measurements to verify the gain stabilisation methods were all performed with the ROACH based DSP.

The ROACH based DSP provided a 400 MHz wide spectrum with a resolution of 512 discrete frequencies whereas the GHY-3 DSP provided a 500 MHz wide spectrum with the same number of discrete frequency points. Both plots show the normalised gain change over time at four different frequencies. The first three frequency channels are spaced approximately 100 MHz, which allows to see the correlation of the gain drift over that frequency separation. The third and fourth frequency channel are separated less than 1 MHz, which allows to see the correlation of the gain drift for neighbouring frequency channels. It can be seen that the long-term gain drift applies to all frequency channels equally, but on shorter time scales the change in gain seems to be uncorrelated, which is due to uncorrelated white noise on the measured frequency channels.

To support this argument we calculated the Pearson Correlation Coefficient (PCC) [79] of the time ordered frequency data to see how the gain drift correlates between different frequency channels. The PCC provides an indication of the correlation between two variables and produces an output value that is normalised to be within 1 and 0, where a value of 0 describes an uncorrelated relationship and a value close to 1 describes a perfect correlation. The PCC for the measured frequency channels of the 500 MHz measurement performed with the GHY-3 DSP is shown in Figure 6.15. The yellow diagonal line represents the Pearson coefficient for the autocorrelations of the frequency channels, hence the PCC is 1. More important is that the plot shows no frequency dependence of the gain drift, which can be seen by the uniform coefficient values for the different number of frequency channel combinations and a high value of the correlation coefficient for different channels ($0.8 - 0.9$). The darker lines visible in the plot indicate channels that have a higher noise level compared to others, hence the correlation for these channels is lower.

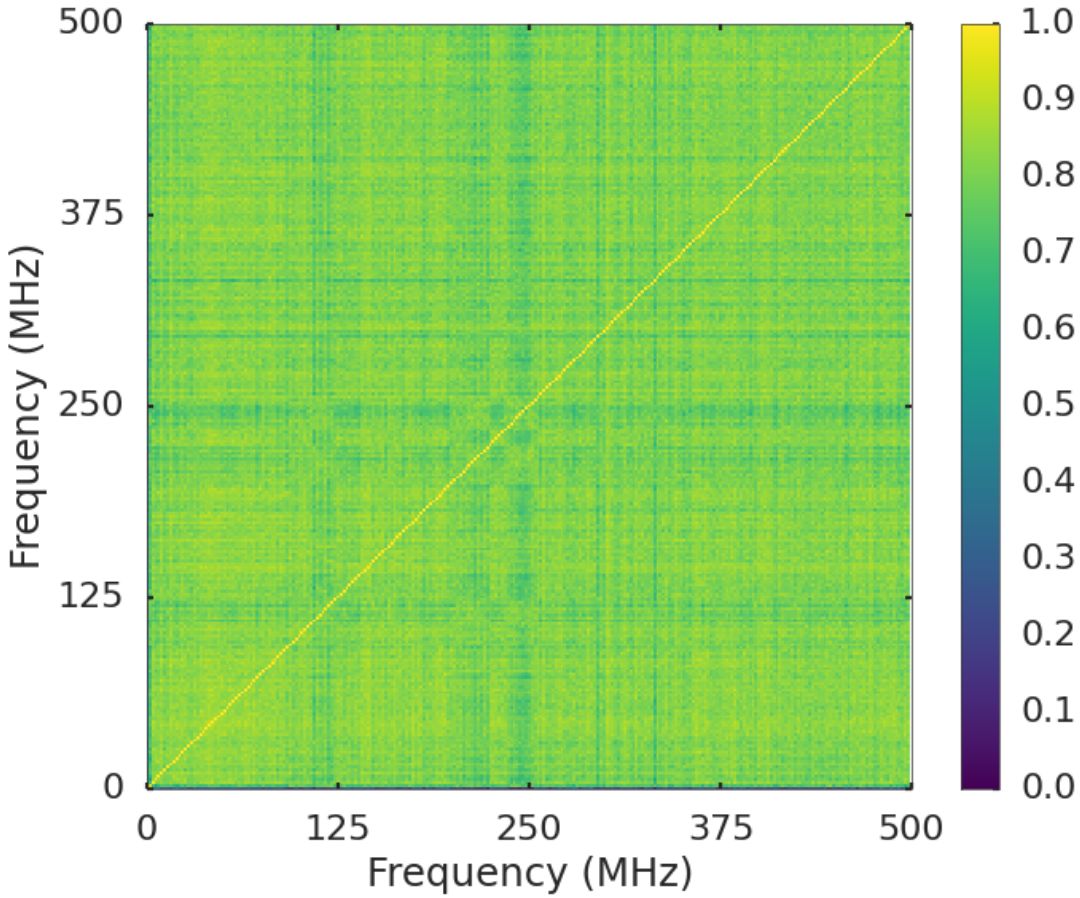

Figure 6.15: Pearson correlation of the frequency depended gain drift.

This analysis showed that the gain drift of the receiver signal conditioning chain is not frequency dependent and therefore a gain tracking approach using a continuous-wave reference signal is feasible.

6.3.2 Reference Signal Sources

The reference signal for the CW gain tracking method is generated by a standard signal generator. We had three signal generators from different manufacturers and price categories available, a Rohde & Schwarz SMA100B, an Anritsu MG3692B, and a Hittite T-2240. In order to see how suitable these signal generators are to be used as a reference source in our application, we measured the stability with respect to the change in amplitude over a period of 15 min. The change in amplitude of the signal was measured by connecting the output of a signal generator to the input of the DSP. The measurement results are shown in Figure 6.16, we can see that all signal generators remain within a drift of 0.2 percent amplitude change over the measured

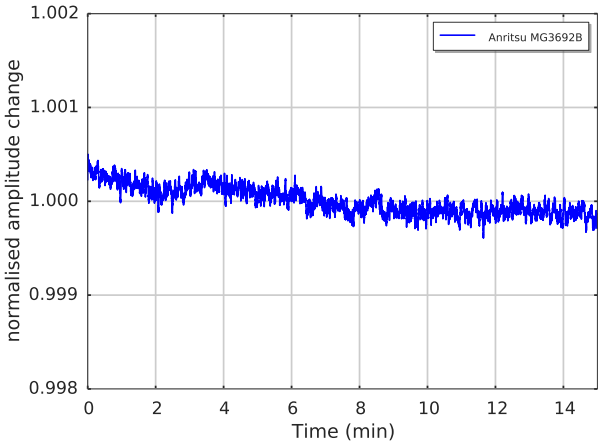

(a) Anritsu MG3692B.

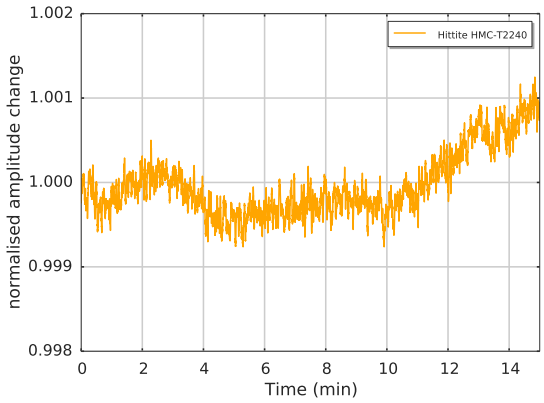

(b) Hittite HMC T-2240.

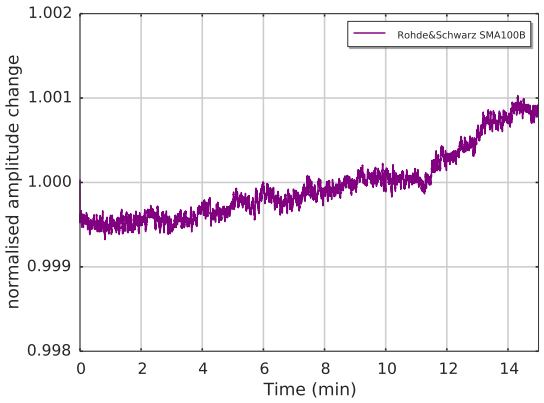

(c) Rohde&Schwarz SMA100B.

Figure 6.16: Measured change in amplitude over a period of 15 min.

15 min. The Anritsu signal generator shown in Figure 6.16a, performed best with respect to its stability, which is why this signal generator will be used as a reference source in the following validation of the CW stabilisation method.

6.3.3 Verification of the CW Stabilisation Method

The CW stabilisation method is tested using the Anritsu signal generator as a reference source and the combined spectral and power meter firmware implementation from Section 6.1.2.3, allowing us to measure the overall gain drift as well as the gain drift in a single frequency channel. The performance of the stabilisation method is determined by a comparison between the uncorrected and the corrected power spectrum of the test setup. This is done by using the noise model presented in Section 6.2.1, which allows us to fit both power spectra and compare the values of the pink noise level and knee frequency.

We have seen in Section 6.3.2 that the amplitude of the signal generator varies with time too. In order to have the most stable reference signal for our measurements we switched of the air-condition in the room and pre-set the frequency and power level of the signal generator 30 min before each measurement.

Using this technique we were able to get several measurements of which we present the best three measurements in this thesis. The improvement of this stabilisation method is compared by stating the pink noise level at a defined frequency of 0.01 Hz before and after the gain correction. The measured power spectra and the fitted noise model is shown in Figure 6.17, the left-hand side shows the unstabilised spectra and the right-hand side the stabilised spectra, both spectra are based on the same measured data set.

The first measurements (A) uses a reference signal at 5.125 GHz which is down-converted to the intermediate frequency of 125 MHz. The power level of the measured reference signal in the corresponding frequency bin was -26.8 dBm and the total detected power over the 400 MHz IF band was -19.27 dBm. The second measurement (B) employs the same reference frequency, but uses a more powerful reference signal of -21.8 dBm in the reference frequency channel and a total detected power of

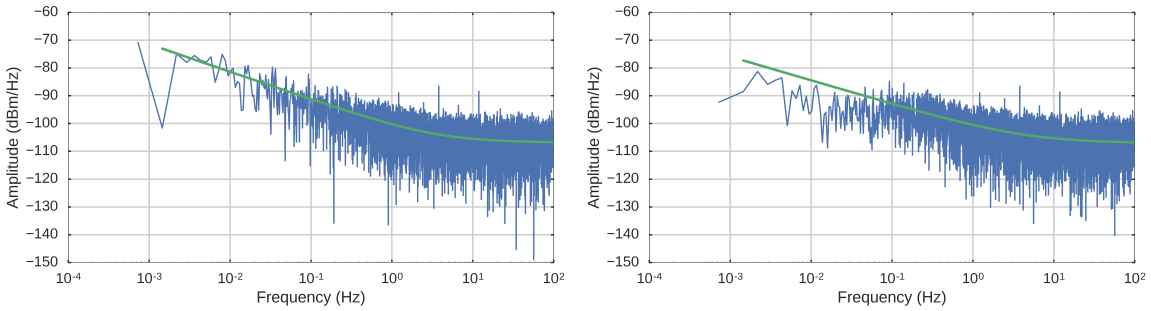

(a) Measurement A unstabilised.

(b) Measurement A stabilised.

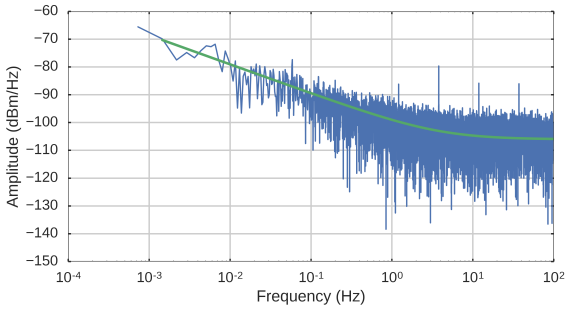

(c) Measurement B unstabilised.

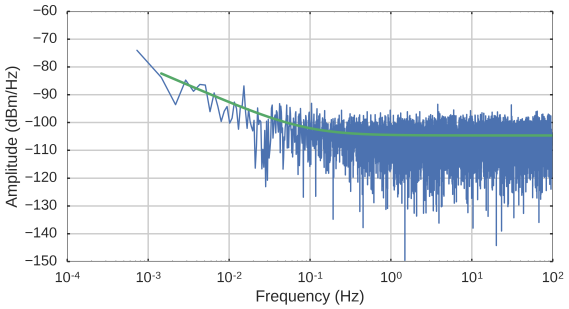

(d) Measurement B stabilised.

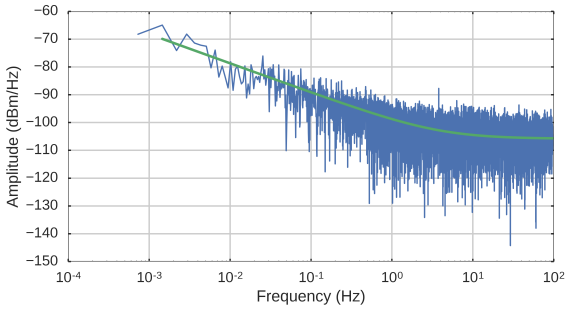

(e) Measurement C unstabilised.

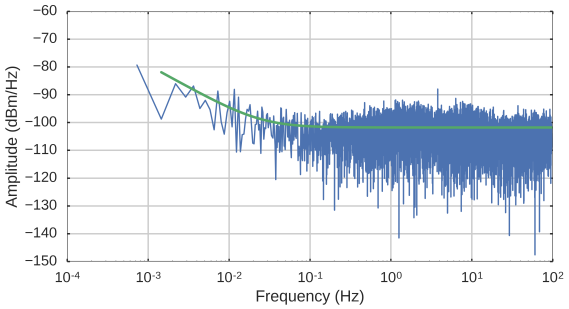

(f) Measurement C stabilised.

Figure 6.17: Measured power spectra for three independent measurements A to C. The plots on the left-hand side show the unstabilised spectra and the plots on the right-hand side show the stabilised spectra. The green line represents the fitted noise model to each power spectrum.

−18.2 dBm. The third measurement (C) employs the same power level for the reference signal, but uses a different reference frequency of 5.250 GHz, which corresponds to the intermediate frequency of 250 MHz. The results of the fitted noise model for all three measurements are shown in Table 6.3.

The unstabilised and stabilised power spectra for measurement A are shown in Figure 6.17a and 6.17b, respectively. When we look at the stabilised spectrum for this

measurement we can see an increase in amplitude between 1 and 0.1 Hz. This increase corresponds to the increase seen in the unstabilised spectrum in Figure 6.17a. For frequencies lower than 0.1 Hz we can see that the stabilised spectrum flattens. This flattening is the effect of the gain drift stabilisation.

Although the stabilisation method reduces the gain fluctuations we can see that the correction only applies for pink noise levels above a certain power level or in other terms only gain changes of a certain fraction can be corrected for. This effect can be explained by the signal-to-noise ratio of the measured reference signal. The power level of the reference signal determines the signal-to-noise ratio and therefore the correlation of the reference signal with the gain drift. To increase the signal-to-noise ratio we increased the reference signal power by approximately 5 dBm and repeated the measurement. This increase in power allowed us to correct for smaller gain drifts.

The unstabilised and stabilised power spectra for measurement B, which uses a stronger reference signal, are shown in Figure 6.17c and 6.17d, respectively. When we look at the stabilised spectrum we can see that the gain fluctuations are entirely corrected down to a frequency of approximately 0.05 Hz, after which we can see an increase in pink noise level that is caused by the instabilities of the reference signal generator. The fitted parameter of the noise model for this measurement shown in Table 6.3 state a reduction of the pink noise level at 0.01 Hz of approximately 14 dB which demonstrates a significant improvement.

Finally we wanted to demonstrate that the continuous-wave stabilisation also works when the reference signal has a different frequency. Hence we decided to double the reference frequency and repeat the measurement with the same reference signal power level.

The spectra for this measurement are shown in Figure 6.17e and 6.17f. The stabilised spectrum also shows that the gain fluctuations are corrected down to a frequency of approximately 0.05 Hz, after which we can see that the pink noise starts to dominate the spectrum. The fitted noise model states a reduction of the pink noise level at 0.01 Hz of approximately 16.5 dB, which is also a significant improvement and

Table 6.3: Comparison of the unstabilised and stabilised power spectra.

Parameter		Unstabilised	Stabilised
Measurement A, CW Power -26.8 dBm, CW Frequency 5.125 GHz			
α		0.995	0.854
σ_w	$(\sqrt{\text{mW}})$	$4.54\,\text{x}10^{-6}$	$4.43\,\text{x}10^{-6}$
σ_c	$(\sqrt{\text{mW}})$	$8.61\,\text{x}10^{-6}$	$8.34\,\text{x}10^{-6}$
knee freq	(Hz)	3.63	4.59
σ_w^2	(dBm)	-106.9	-107.1
σ_c^2 at 10^{-2} Hz	(dBm)	-81.4	-84.5
Measurement B, CW Power -21.8 dBm, CW Frequency 5.125 GHz			
α		1.060	1.256
σ_w	$(\sqrt{\text{mW}})$	$4.94\,\text{x}10^{-6}$	$5.83\,\text{x}10^{-6}$
σ_c	$(\sqrt{\text{mW}})$	$1.00\,\text{x}10^{-5}$	$1.25\,\text{x}10^{-6}$
knee freq	(Hz)	3.82	0.09
σ_w^2	(dBm)	-106.1	-104.7
σ_c^2 at 10^{-2} Hz	(dBm)	-78.8	-92.9
Measurement C, CW Power -21.8 dBm, CW Frequency 5.250 GHz			
α		1.046	1.610
σ_w	$(\sqrt{\text{mW}})$	$4.89\,\text{x}10^{-6}$	$8.12\,\text{x}10^{-6}$
σ_c	$(\sqrt{\text{mW}})$	$1.05\,\text{x}10^{-5}$	$4.14\,\text{x}10^{-7}$
knee freq	(Hz)	4.28	0.02
σ_w^2	(dBm)	-106.2	-101.8
σ_c^2 at 10^{-2} Hz	(dBm)	-78.7	-95.5

verifies that the reference signal can be added to the receiver band at any frequency.

However the stabilised spectrum also shows another feature, which is an increase in noise level between 1 and 10 Hz. This noise increase can also be seen by the increased value of the fitted white noise level when comparing the two values for the unstabilised and stabilised spectrum shown in Table 6.3. We suspect that the increase in noise is caused by additional noise on the reference signal generated by the signal generator, which operated at increasing room temperatures for each measurement. We support our assumption by the fact that for all following measurements with this signal generator setup the noise behaviour got worse.

In summary we can say that this experiment demonstrated that the continuous-wave stabilisation approach can be applied to correct for gain instabilities in a receiver system and significantly improves its stability. We also have seen that the measurements to validate this stabilisation approach are very difficult to perform, which is mainly due to generating a stable reference signal. For further experiments or for an implementation into a receiver system we recommend the implementation of an active level control that further stabilises the amplitude of the reference signal before it is added into the signal chain. The design and prototype of an active level control which we developed for the GHY-3 receiver system is presented in Chapter 7, Section 7.2.1.5.

6.4 White-Noise Stabilised Approach

In this section we discuss the experiments conducted to verify the white-noise gain tracking technique. At first we describe the reference signal and the way it is being modulated in to the test setup signal conditioning chain. The second part of this section presents the experimental results determining the performance of the white-noise stabilisation technique.

6.4.1 Reference Signal

The reference signal is generated by an AtlantecRF AS6333 noise diode module, shown in Figure 6.18a. Those types of noise sources are commonly used up to 18 GHz and provide a stable signal over a wide frequency range [64]. In order to modulate the reference signal in to the signal path of the test setup, we connect the noise diode through a Hittie HMC547LP3 switch to the reference signal input of the test setup. The switch is shown in Figure 6.18b and supports signals from DC up to 20 GHz as well as a maximum switching frequency of 150 MHz. The schematic of the implemented

(a) Noise Diode

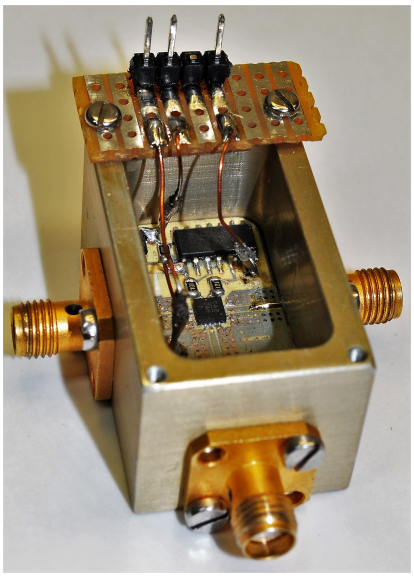

(b) RF Switch

Figure 6.18: The two components used to generate the reference signal. (a) shows the noise diode module used to generate the reference signal. (b) shows the RF switch which is used to modulate the reference signal.

switch is shown in Figure 6.19. The chip consists of two switches that alternate simultaneously, thereby connecting one of the two input ports to the common output and terminating the other input port with an internal resistor. For our experimental setup we connect the reference input of the test setup to the common port RFC, the noise diode to RF1, and a 50 Ω termination to RF2. This configuration enables two possible signal states, one where the noise diode signal is connected to the output of the switch (RFC) and the other where the external 50 Ω termination is connected to the output of the switch, hence allowing us to modulate a reference signal that consists

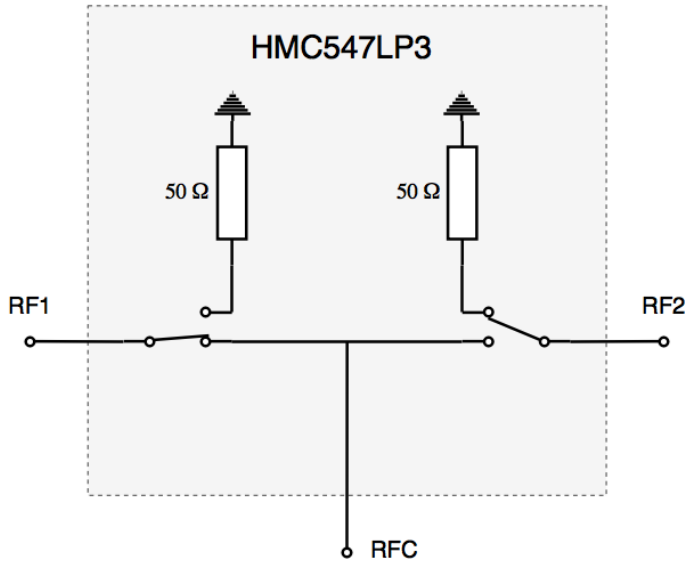

Figure 6.19: Schematic of the Hittie HMC547LP3 switch. RFC is the common port which alters between RF1 and RF2. Note, that the switch includes internal 50 Ω resistors to terminate the input not used.

of two signal states which are defined by the noise diode power P_{ON} or the thermal noise power of the termination resistor P_{OFF}. This means that even in the signal state where we do not add the noise diode power in to the test setup, we still add the thermal noise power P_{OFF} of the termination resistor, which leads to an increase in the overall system temperature of the receiver system. However, the value of the added noise power depends on the physical temperature of the termination resistor and the attenuation of the coupler used to add the reference signal into the signal path. For example, if the switch and the termination resistor is located at room temperature and we employ a 30 dB coupler to add the reference signal in to the signal path,

the contribution would be 0.3 K. But if we mount the switch and the termination resistor on to the first stage of the cryostat, which has a physical temperature of approximately 50 K, the contribution would be reduced to approximately 0.05 K.

6.4.2 Verification of the White Noise Stabilisation Method

The white noise stabilisation method is tested using the reference signal configuration described above and the ROACH based DSP power meter firmware implementation described in Section 6.1.2.1, allowing us to measure the total signal power of the test setup with an effective sample frequency of approximately 24 kHz. The reference signal employs a modulation frequency of 200 Hz for all measurements carried out to validate this stabilisation approach.

The modulation frequency is a compromise between two considerations. First, the modulation frequency must be above twice the $1/f$ knee frequency in order to Nyquist sample the gain fluctuations. Second, the modulation frequency must be low enough that we have sufficient samples for each signal state to determine the signal power. This is particular important for measurements that employ a short duty-cycle where the reference signal is only present for a short fraction within a modulation period. In addition to that, a modulated reference signal with a frequency of 200 Hz is not shown in the power spectrum plot which displays frequencies up to 100 Hz. This has the advantage that the reference signal does not affect the correct fit of the noise model.

The performance of this stabilisation technique is verified in the same way as for the CW stabilisation technique by fitting the noise model to the unstabilised and stabilised power spectrum. The reduction in pink noise level is also compared at 0.01 Hz. We performed two sets of measurement showing the effect of this stabilisation technique when varying the duty-cycle and power level of the modulated reference signal. The duty-cycle defines the percentage of which the reference signal is present within each modulation period, sensible values for the duty-cycle lie between $50\,\% \geq d > 0\,\%$. In general, a smaller duty-cycle is preferred as this reduces the time spent looking at the reference signal. The power level of the reference signal is limited by the dynamic

range of the receiving hardware, in our test setup the limiting component is the ADC. The ADC input range lies between 0 dBm and −41 dBm. However, as mentioned before in Section 6.1.3 the recommended input power level when sampling noise like signals is approximately −22 dBm. As we do not want to get close to the top end of the dynamic range, we define the maximum input power for a noise-like signal to be −12 dBm, which gives us a usable dynamic range for the reference modulation of approximately 10 dB.

6.4.2.1 Varying the Duty-Cycle

The first set of measurements employ a constant modulation power level of 9 dB while varying the duty-cycle from 30 % to 5 %. The unstabilised and stabilised power spectra for a duty-cycle of 30 %, 20 %, 10 %, and 5 % are shown in Figure 6.20 and the corresponding results of the fitted noise model are shown in Table 6.4. Note, that both spectra, the unstabilised and the stabilised spectra are based on the same measured data set.

The stabilised spectra for the first two measurements shown in Figure 6.20b and 6.20d employ a duty-cycle of 30 % and 20 %. Both spectra show that the gain fluctuations are corrected entirely down to a frequency of approximately 10^{-2} Hz. After that we can see that the pink noise starts to dominate the spectrum again. The fitted noise model states a reduction of the pink noise level at 10^{-2} Hz of more than 10 dB, which is a significant improvement. We assume that the remaining fluctuations responsible for the increase in the pink noise level for frequencies below 10^{-2} Hz are due to temperature changes in the cables and other components that connect the stabilised reference source with the coupler of the test setup signal chain.

The stabilised spectra for the measurements employing a duty-cycle of 10 % and 5 % are shown in Figure 6.20f and 6.20h, respectively. Both stabilised spectra show an increase in amplitude around 1 Hz, which correspond to the increase seen in the unstabilised spectra shown in Figure 6.20e and 6.20g. For frequencies below that we can see that the stabilised spectrum flattens. The spectrum remains flat down to approximately 10^{-2} Hz after which the pink noise level increases again. When looking

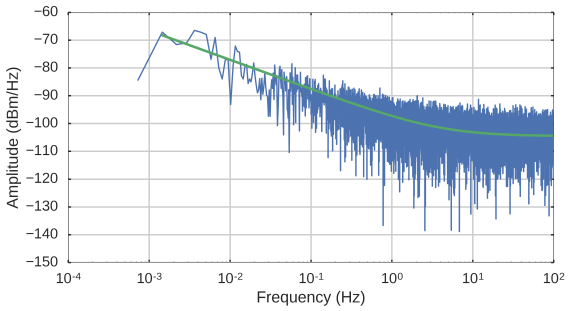

(a) Duty–Cycle 30 % unstabilised.

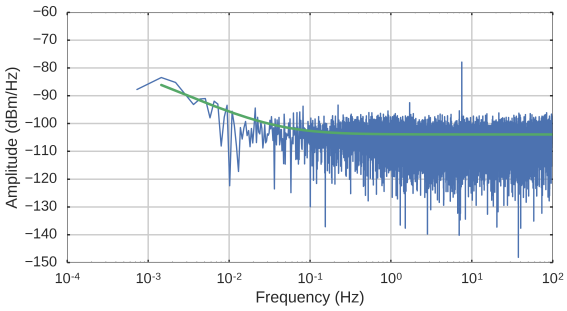

(b) Duty–Cycle 30 % stabilised.

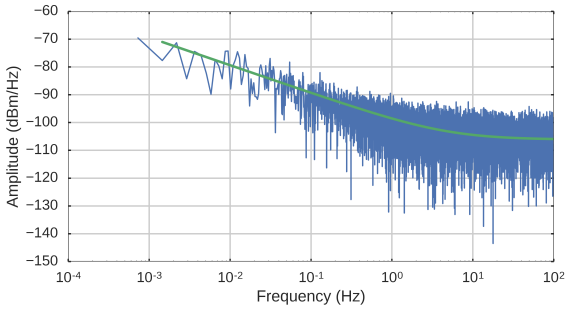

(c) Duty–Cycle 20 % unstabilised.

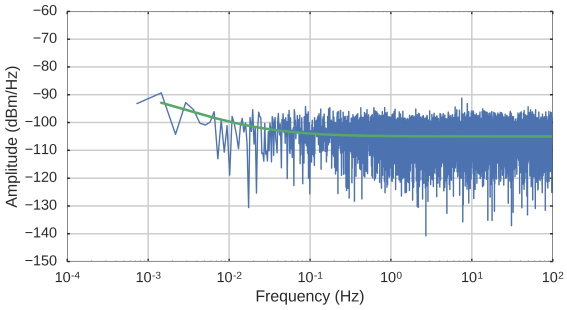

(d) Duty–Cycle 20 % stabilised.

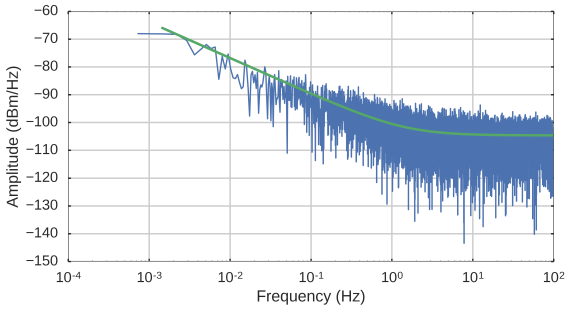

(e) Duty–Cycle 10 % unstabilised.

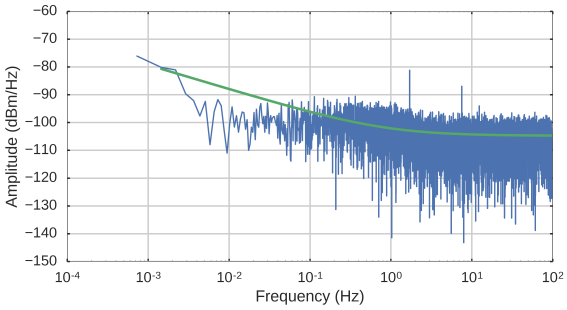

(f) Duty–Cycle 10 % stabilised.

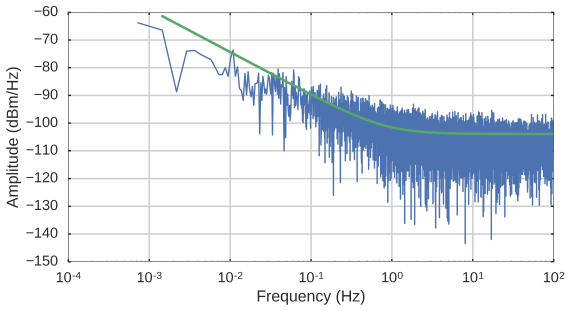

(g) Duty–Cycle 5 % unstabilised.

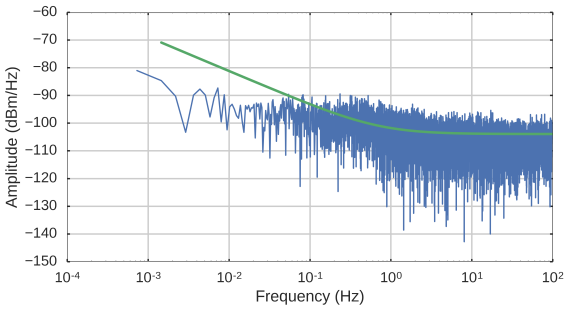

(h) Duty–Cycle 5 % stabilised.

Figure 6.20: Measured power spectra for four different duty-cycles. The plots on the left-hand side show the unstabilised spectra and the plots on the right-hand side show the stabilised spectra. The green line represents the fitted noise model to each power spectrum.

Table 6.4: Comparison of the unstabilised and stabilised power spectra.

Parameter		Unstabilised	Stabilised
Modulation Power 9 dBm, Duty–Cycle 30 %			
α		1.055	1.343
σ_w	$(\sqrt{\text{mW}})$	$5.91\,\text{x}10^{-6}$	$6.33\,\text{x}10^{-6}$
σ_c	$(\sqrt{\text{mW}})$	$1.23\,\text{x}10^{-5}$	$8.84\,\text{x}10^{-7}$
knee freq	(Hz)	4.06	0.04
σ_w^2	(dBm)	-104.6	-104.0
σ_c^2 at 10^{-2} Hz	(dBm)	-77.1	-94.2
Modulation Power 9 dBm, Duty–Cycle 20 %			
α		1.001	0.953
σ_w	$(\sqrt{\text{mW}})$	$4.92\,\text{x}10^{-6}$	$5.60\,\text{x}10^{-6}$
σ_c	$(\sqrt{\text{mW}})$	$1.08\,\text{x}10^{-5}$	$9.75\,\text{x}10^{-7}$
knee freq	(Hz)	1.30	0.02
σ_w^2	(dBm)	-106.2	-105.0
σ_c^2 at 10^{-2} Hz	(dBm)	-80.0	-101.2
Modulation Power 9 dBm, Duty–Cycle 10 %			
α		1.290	0.872
σ_w	$(\sqrt{\text{mW}})$	$5.85\,\text{x}10^{-6}$	$5.77\,\text{x}10^{-6}$
σ_c	$(\sqrt{\text{mW}})$	$7.40\,\text{x}10^{-6}$	$5.31\,\text{x}10^{-6}$
knee freq	(Hz)	1.40	0.83
σ_w^2	(dBm)	-104.7	-104.8
σ_c^2 at 10^{-2} Hz	(dBm)	-76.8	-88.1
Modulation Power 9 dBm, Duty–Cycle 5 %			
α		1.544	1.230
σ_w	$(\sqrt{\text{mW}})$	$6.35\,\text{x}10^{-6}$	$6.33\,\text{x}10^{-6}$
σ_c	$(\sqrt{\text{mW}})$	$5.48\,\text{x}10^{-6}$	$5.10\,\text{x}10^{-6}$
knee freq	(Hz)	0.83	0.71
σ_w^2	(dBm)	-104.0	-104.0
σ_c^2 at 10^{-2} Hz	(dBm)	-74.4	-81.3

at the fitted model we can see that the green line does overestimate the pink noise on these cases. This is due to the fact that the partly corrected spectrum does not have a clear $1/f$ knee frequency. Moreover, it consists of two knees, one around the original frequency at approximately 1 Hz and the other at lower frequency where the long term drift of the reference source limits the stabilisation. For these cases the performance of the gain stabilisation tends to be better than the parameter of the noise model represents. This means that in these cases the noise model used to fit the unstabilised spectrum is no longer adequate to describe the behaviour of the partly stabilised spectrum. Another example for this is shown in Figure 6.20h, where the noise level at 10^{-2} Hz is overestimated by at least 10 dB.

The appearance of a partly corrected gain drift has been seen before when we discussed the first measurement of the continuous-wave stabilisation approach where the signal-to-noise ratio was marginal. Hence, these two measurements show that for this setup a duty-cycle of 10 % and 5 % are not sufficient to entirely correct the gain drift. The reduction in duty-cycle leads to a decrease in the signal-to-noise of the reconstructed gain measurement which limits the ability to correct for small gain changes. One way of increasing the signal-to-noise on the reconstructed gain measurement would be to increase the power of the modulation signal. However, this is limited by the dynamic range of the signal chain, in our case this restricts the modulation power to 10 dB.

6.4.2.2 Varying the Reference Signal Power

This experiment shows the performance of the gain correction for a reference power level of 6 dB and 3 dB. To recall, the reference power level in the previous set of measurements shown in Section 6.4.2.1 was 9 dB. As we are going to reduce the reference power level for these measurements we expect that the uncertainty of the gain measurement increases. Therefore we only use a duty-cycle of 30 % and 20 %, both of which corrected the entire gain drift in the previous experiment. The unstabilised and stabilised power spectra are shown in Figure 6.21 and the corresponding results of the fitted noise model are shown in Table 6.5. Note, that both spectra, the unstabilised

and the stabilised spectra are based on the same measured data set.

The stabilised spectrum employing a duty-cycle of 30 % and a reference power level of 6 dB is shown in Figure 6.21b. We can see that the gain drift for this configuration is entirely corrected down to a frequency of approximately $4 \cdot 10^{-3}$ Hz. The fitted parameter of the noise model state a reduction of the pink noise level at 10^{-2} Hz of more than 19 dB. This shows that a duty-cycle of 30 % and a reference signal power level of 6 dB is sufficient to correct for the receiver gain fluctuations.

The unstabilised and stabilised spectra for the second measurement employing a duty-cycle of 20 % and a reference power level of 6 dB are shown in Figure 6.21c and 6.21d, respectively. The stabilised spectrum shows a small increase in amplitude around 1 Hz, which corresponds to the increase of the unstabilised spectrum. This feature indicates that for this configuration the uncertainty of the measured gain starts to limit the ability to correct all gain fluctuations. Although we can see that this configuration is not able to correct all gain fluctuations it still reduces the pink noise level at 10^{-2} Hz by more than 10 dB.

When further reducing the reference power level to 3 dB the gain correction becomes even less effective. This can be seen in particular in the stabilised spectra employing a duty-cycle of 30 % and 20 % which are shown in Figure 6.21f and 6.21h, respectively. Both plots show an increase in amplitude around 1 Hz which shows that the uncertainty on the measured gain is too high to correct for small gain drifts. Although we can see by the flattening of the spectra that some gain drifts are corrected, however this configuration of duty-cycle and reference power level is not sufficient to stabilise the test setup.

In summary we can say that this experiment demonstrated that the white-noise stabilisation approach can be applied to significantly improve the stability of a receiver system. This experiment also shows that the correct parameter settings for the reference signal power and duty-cycle are important to successful correct all gain drifts. In addition to that we experienced that the stabilised noise diode provides a very stable reference signal, which made it easier to perform these sets of measurement compared to the continuous-wave stabilisation experiments.

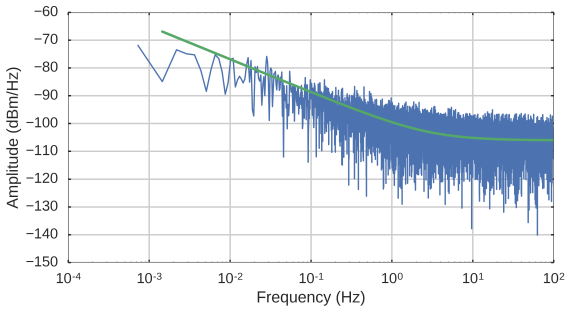

(a) Duty–cycle 30 % unstabilised (6 dB).

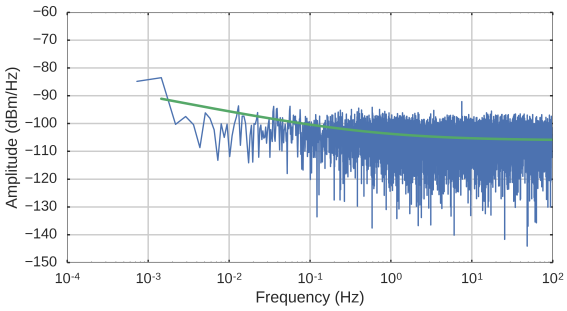

(b) Duty–cycle 30 % stabilised (6 dB).

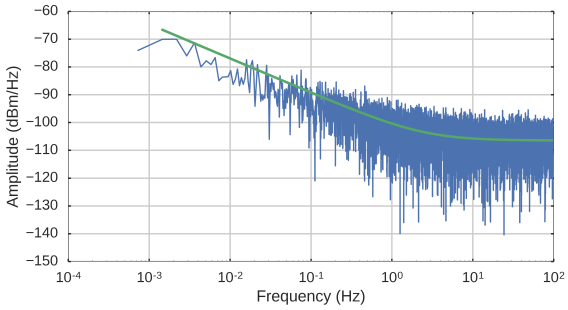

(c) Duty–cycle 20 % unstabilised (6 dB).

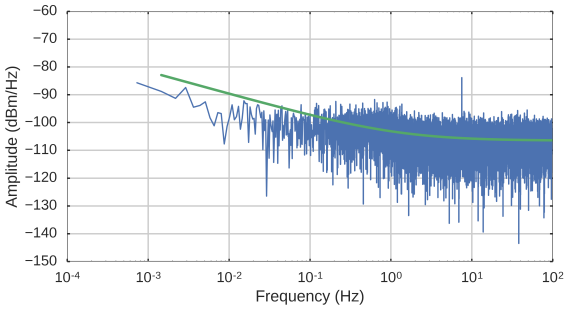

(d) Duty–cycle 20 % stabilised (6 dB).

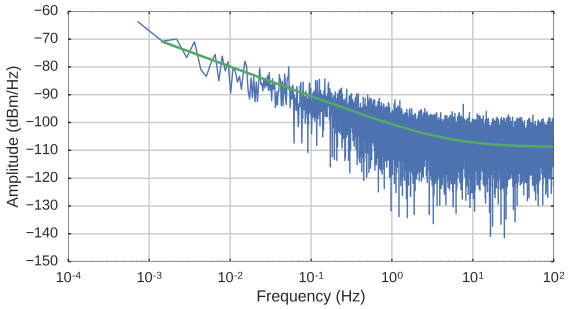

(e) Duty–cycle 30 % unstabilised (3 dB).

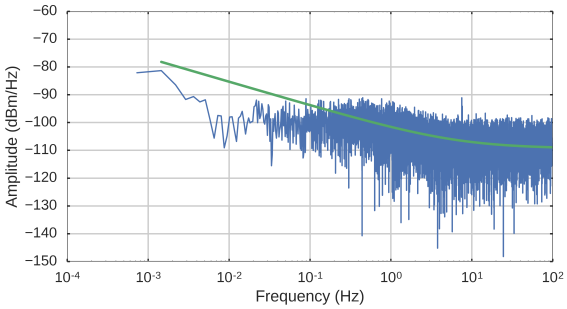

(f) Duty–cycle 30 % stabilised (3 dB).

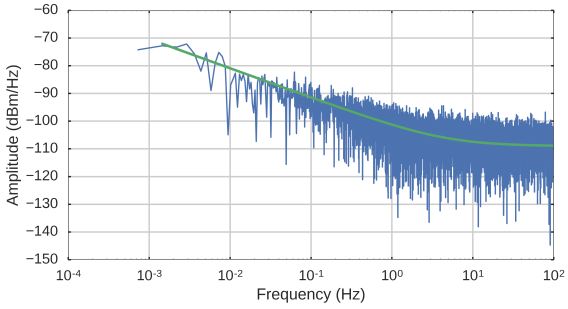

(g) Duty–cycle 20 % unstabilised (3 dB).

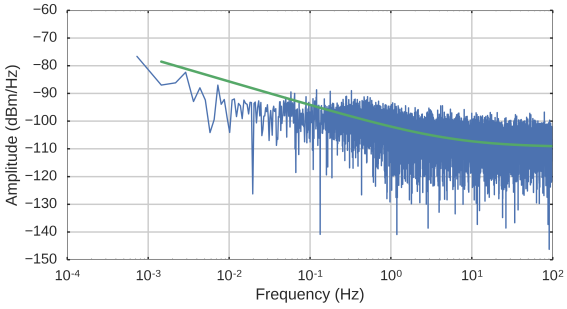

(h) Duty–cycle 20 % stabilised (3 dB).

Figure 6.21: Measured power spectra for two different duty-cycles and power levels. The plots on the left-hand side show the unstabilised spectra and the plots on the right-hand side show the stabilised spectra. The green line represents the fitted noise model to each power spectrum.

Table 6.5: Comparison of the unstabilised and stabilised power spectra.

Parameter		Unstabilised	Stabilised
Modulation Power 6 dBm, Duty–Cycle 30 %			
α		1.188	0.573
σ_w	$(\sqrt{\text{mW}})$	$4.97\,\text{x}10^{-6}$	$4.95\,\text{x}10^{-6}$
σ_c	$(\sqrt{\text{mW}})$	$9.31\,\text{x}10^{-6}$	$4.22\,\text{x}10^{-6}$
knee freq	(Hz)	2.89	0.59
σ_w^2	(dBm)	-106.1	-106.1
σ_c^2 at 10^{-2} Hz	(dBm)	-76.9	-96.0
Modulation Power 6 dBm, Duty–Cycle 20 %			
α		1.236	0.808
σ_w	$(\sqrt{\text{mW}})$	$4.74\,\text{x}10^{-6}$	$4.71\,\text{x}10^{-6}$
σ_c	$(\sqrt{\text{mW}})$	$8.33\,\text{x}10^{-6}$	$5.11\,\text{x}10^{-6}$
knee freq	(Hz)	2.49	1.24
σ_w^2	(dBm)	-106.5	-106.6
σ_c^2 at 10^{-2} Hz	(dBm)	-76.9	-89.7
Modulation Power 3 dBm, Duty–Cycle 30 %			
α		1.073	0.848
σ_w	$(\sqrt{\text{mW}})$	$3.59\,\text{x}10^{-6}$	$3.40\,\text{x}10^{-6}$
σ_c	$(\sqrt{\text{mW}})$	$8.65\,\text{x}10^{-6}$	$7.60\,\text{x}10^{-6}$
knee freq	(Hz)	5.18	6.75
σ_w^2	(dBm)	-108.9	-109.4
σ_c^2 at 10^{-2} Hz	(dBm)	-79.8	-85.4
Modulation Power 3 dBm, Duty–Cycle 20 %			
α		1.056	0.858
σ_w	$(\sqrt{\text{mW}})$	$3.54\,\text{x}10^{-6}$	$3.38\,\text{x}10^{-6}$
σ_c	$(\sqrt{\text{mW}})$	$7.87\,\text{x}10^{-6}$	$7.21\,\text{x}10^{-6}$
knee freq	(Hz)	4.58	5.91
σ_w^2	(dBm)	-109.0	-109.4
σ_c^2 at 10^{-2} Hz	(dBm)	-81.0	-85.7

6.4.3 Significance for the GHY-3 Receiver System

In Chapter 5 we discussed the fundamental theory of a radio receiver and how gain instabilities limit the sensitivity and integration time. This was followed in Section 5.3 by an estimate of the receiver system temperature and a calculation of the required gain stability for the GHY-3 receiver system. The required maximum integration time was set to be $\tau = 180\,\text{sec}$, which corresponds to the estimated time required by the telescope to operate a full turn in azimuth.

The experiments to validate the continuous-wave and white-noise stabilisation methods showed that both methods are able to stabilise the gain drift below frequencies of $10^{-2}\,\text{Hz}$ (100 sec), which provides sufficient gain stabilisation to integrate over times close to the required 180 sec. It is important to mention that in some configurations there is a small increase in pink noise for these integration times, however this increase is very small compared to a unstabilised system.

Furthermore, we should also mention that the long term gain drift is caused by the instabilities of the reference signal and can be further improved by providing a more stable reference source.

6.5 Comparison of both Stabilisation Methods

We showed in the previous sections that both stabilisation methods allow to remove the gain drift and therefore are suitable to be applied to the GHY-3 receiver system. In this section we want to discuss the advantages and disadvantages of each method and conclude which one is most suitable for our receiver system.

6.5.1 Advantages and Disadvantages of the CW Stabilisation Method

Using a continuous-wave as a reference signal to stabilise the gain drift has a number of advantages and disadvantages, which determine how suitable it is to be applied for a particular receiver system. The key advantages and disadvantages of the CW

stabilisation method are following.

- Advantages
  - Cost effective implementation compared with the Pseudo-Correlation architecture.
  - Allows to track the gain drift continuously by introducing a narrowband signal, thereby not affecting other frequency channels of the receiver system.
  - The receiver system using this method does not require a wide dynamic range, therefore it is suitable for systems employing wide band ADCs with a small number of bits.
- Disadvantages
  - The reference signal must be very stable and low-noise, up to the point that an Active-Level-Control located in the cryostat might be required.
  - Receiver systems that employ multiple parallel signal conditioning chains, like the multiple IF bands in the GHY-3 receiver system, require a reference signal in each signal chain.

6.5.2 Advantages and Disadvantages of the White-Noise Stabilisation Method

The stabilisation of the gain drift using a broadband noise signal has also its advantages and disadvantages, which determine how suitable such a stabilisation method is to be applied in a particular receiver system. The key advantages and disadvantages of the white noise stabilisation method are following.

- Advantages
  - Cost effective implementation compared with the Pseudo-Correlation architecture.

  - Receiver systems that employ multiple parallel signal conditioning chains, like the multiple IF bands in the GHY-3 receiver system, can be stabilised entirely as the reference signal is present in all frequencies.
  - The reference signal generation is straight forward using a standard noise diode module combined with a switch.

- Disadvantages
  - Reduction in observation time depending on the applied duty-cycle.
  - Requires a high dynamic range of the order of 5 dB to 10 dB.

6.5.3 Preferred Stabilisation Method for the GHY-3 Receiver System.

Part of the architecture of the GHY-3 receiver system is defined by the available GHY-3 digital signal processing hardware, which uses sixteen 1 Gsps analogue-to-digital converter. This means that the total receiver band is divided into sixteen 500 MHz sub-bands, each of which can have individual gain fluctuations. In order to correct the gain fluctuations in all sub-bands we need to ensure that each sub-band has a reference signal present which tracks the gain drift accurately.

For an implementation of the continuous-wave stabilisation method this would require eight individual tones each placed in one sub-band. Depending on the implementation we could also imagine a system which allows the reference signal to hop in frequency and track the gain of each sub-band for a fraction of the time. Note, that such an implementation must ensure that enough individual gain measurements are made in order to Nyquist sample the gain drift in all sub-bands. In addition to that it must be ensured that the noise contribution of the connected reference signal source does not significantly increase the system temperature of the receiver.

An implementation using a broad band white-noise signal intrinsically provides a reference signal in all present receiver sub-bands, which makes the implementation of this method straight forward. However, one must take into account that this

implementation reduces the observation time by the fraction of the duty-cycle, in case of GHY-3 receiver system we expect a duty-cycle of 20 %. On top of this decrease in observation time comes an increase in system temperature caused by the termination resistor of the switch. Nevertheless, the experiments performed in this chapter showed that for a successful implementation the available dynamic range of the receiver system should be greater than 6 dB. The GHY-3 digital signal processing hardware provides a dynamic range of up to 10 dB, which makes the white-noise stabilisation method suitable to implement.

In summary we can say that the receiver stabilisation using a continuous-wave method is more elegant, however it also requires more effort to be implemented in the GHY-3 receiver system. Whereas the white-noise stabilisation method is straight forward to implement and allows us to stabilise all sub-bands simultaneously

Chapter 7

GHY-3 Receiver System

In this chapter we present the design of receiver system for the GHY-3 telescope. In Section 7.1 we provide an overview and describe the system by dividing it into three parts, the cryostat, the signal conditioning, and the control and monitor system. After that in Section 7.2 we present the design work and verification for a number of components that we build for the GHY-3 receiver. The last Section 7.3 describes the digital signal processing hardware and the implementation of the Stokes spectrometer firmware.

7.1 System Overview

The GHY-3 receiver system can be divided into three functional areas: the cryostat, the signal conditioning, and the monitor and control system. Figure 7.1 shows the functional block diagram, which illustrates the connections between the individual blocks. On the top left one can see the cryostat, which houses the components that operate at low temperatures. The top right shows the signal conditioning, which consists of the room temperature analogue components and the digital signal processing. The control and monitor system, which monitors the status of each part of the receiver system and allows us to set certain parameters specific for an observation, e.g. the frequency of the local oscillator, and the applied FPGA firmware is located at the bottom. The receiver signal flow is indicated by the red arrows.

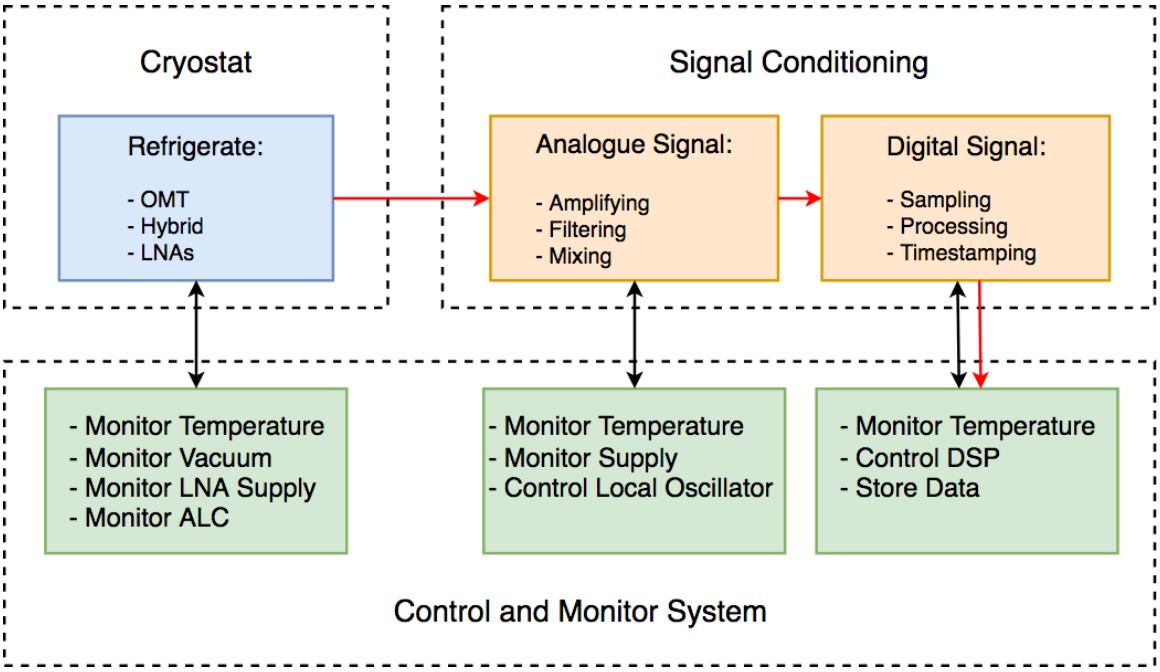

Figure 7.1: Simplified system diagram of the GHY-3 receiver. The cryostat houses the OMT, LNA's, and the ALC. The signal conditioning is divided into analogue and digital. The GHY-3 server that monitors and controls all receiver parameters is located at the bottom. The detected astronomical signal flow through the receiver system is indicated by the red arrows.

7.1.1 Cryostat

The cryostat refrigerates the first analogue signal components in the RF signal conditioning chain, by providing a vacuum environment in which a cryocooler is located. The reduced physical temperature of the OMT, hybrids, and low noise amplifiers reduces the thermal noise contribution in the receiver system, thereby increasing the sensitivity of the instrument. In Section 5.3.1 we showed that the system temperature of the receiver depends significantly on the loss and noise contribution of the first few components in the signal chain.

The cryostat is designed by Bob Watkins based on our requirements and the design of our signal components that needed to be integrated. A CAD model of the cryostat is shown in Figure 7.2, where (a) shows the assembly of the closed cryostat together with the feed horn and (b) shows the cryostat with the vacuum cylinder and heat

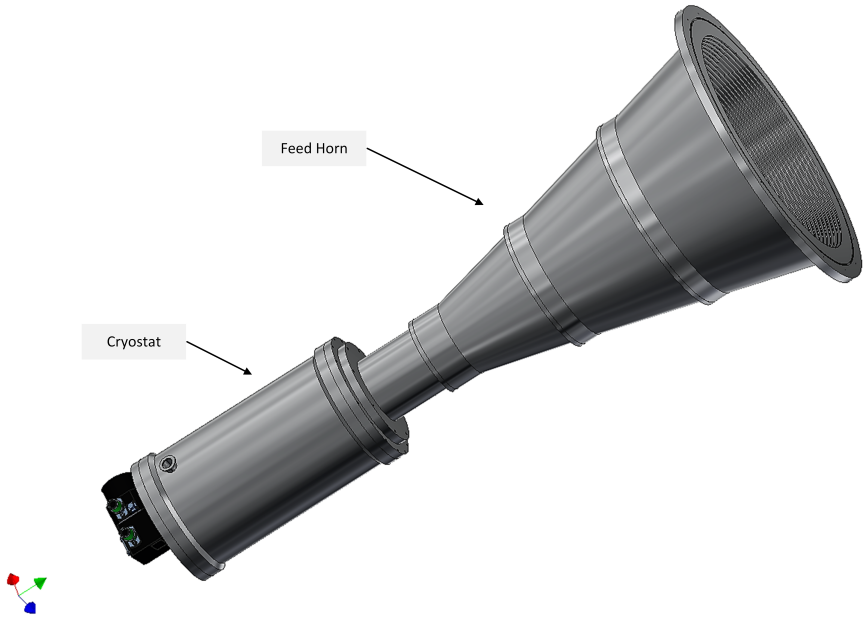

(a) Cryostat and Feed Horn Assembly

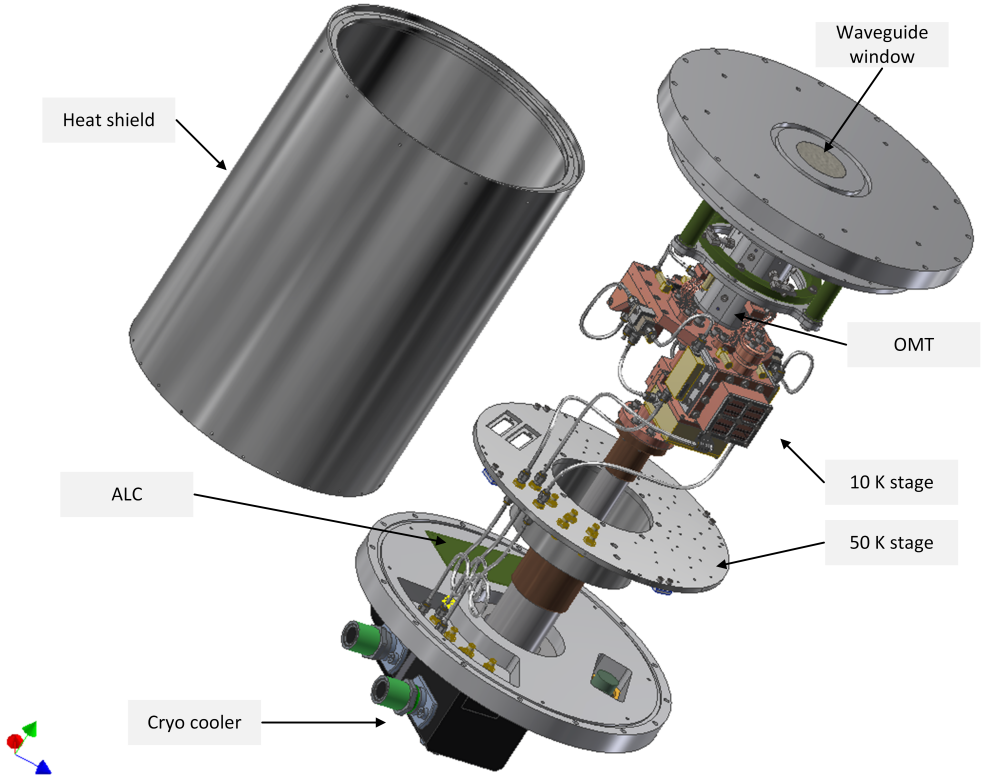

(b) Open Cryostat

Figure 7.2: CAD design of the GHY-3 cryostat. (a) shows the assembly of the cryostat and the feed horn. (b) shows the internal assembly of the cryostat with the outer vacuum cylinder removed.

shield removed. The GHY-3 cryostat uses a two-stage Gifford-McMahon cryocooler. The first stage refrigerates to approximately 50 K and the second stage to approximately 10 K. To be able to reach cryogenic temperatures the thermal isolation between the different temperature stages must be as high as possible, which means that the cryostat needs to maintain a vacuum. Hence, the dominating heat source for the cold stages are either radiative or through a thermal bridge between different temperature stages, e.g. cable connections. For the second stage to reach temperatures close to 10 K the radiative heat load emitted by the vacuum vessel must be shielded. This is done by installing a heat shield that is connected to the first stage of the cryocooler which remains at a physical temperature of approximately 50 K. The conductive heat load between the different stages is further minimized by the use of stainless steel RF cables and high thermal resistive wires like Constantan or Manganin.

The heat load on both stages can be estimated using the data sheet of the cryocooler, which includes a diagram illustrating the cooling power for both stages at different temperatures. The refrigeration capacity of the Coolsatar 6/30 cryocooler used in the GHY-3 cryostat is shown in Figure 7.3. This plot allows us to estimate the heat load based on the measured temperatures on both stages. The first and

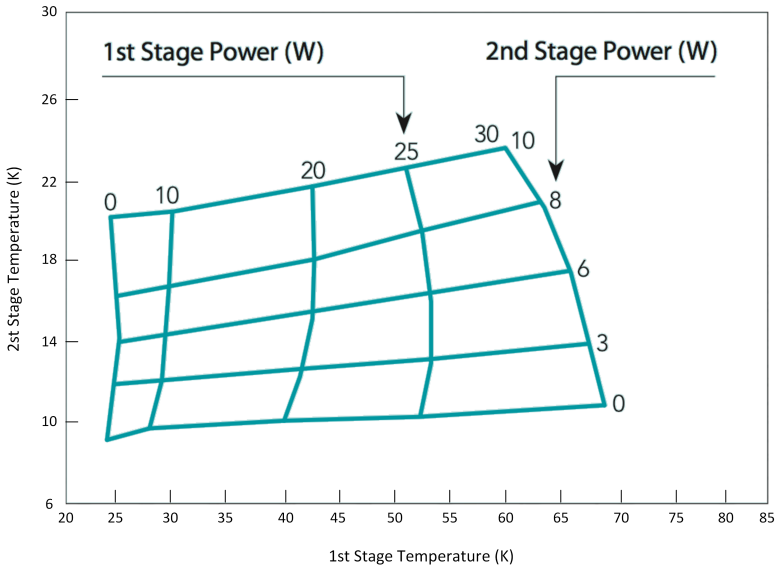

Figure 7.3: The refrigeration capacity of the Coolsatar 6/30 cryocooler used in the GHY-3 cryostat. The image has been taken from [80] and subsequently modified.

second stage reach a temperature of 51 K and 12 K, which corresponds to a heat load of 24 W and 3 W, respectively.

As the second stage of the cryocooler houses all RF components and operates them at approximately 10 K, it reduces the insertion loss and noise contribution of the OMT, hybrid, couplers, and low noise amplifiers.

7.1.2 Signal Conditioning

The signal chain processes the detected astronomical signal to a stage where it can be digitised by the analogue-to-digital converters. This process consists of amplifying, filtering and frequency mixing of the astronomical signal. The system diagram for the GHY-3 signal conditioning hardware is shown in Figure 7.4. The signal is detected by the feed horn on the left-hand side and digitised by the ADCs on the right-hand side. The first part of the signal conditioning chain amplifies and filters the entire receiver band which is defined by the passband of the applied filters, in our case of the $4 - 8.5$ GHz band-pass filter.

After the amplification and filter stages the signal needs to be downconverted to a lower frequency in order to be digitised by the ADCs. To do this, we split the passband into two channels using a power divider and connect the output channels to two in-phase/quadrature (IQ) frequency mixers. An IQ mixer has two output signals, one of which has a 90-degree phase shift (Q). As this channel has a phase shift of 90 deg it can be seen as the imaginary counter part of the real value in the in-phase channel. Hence, this setup allows us to complex sample the analogue IF band. The digital signal processing which will be described later in Section 7.3, uses both mixer outputs to digitise a complex sample of the analogue voltage signals. The complex voltage signal allows us to compute a complex frequency spectrum in which the positive and negative frequencies represent the frequencies above and below the local oscillator frequency.

The frequency conversion and the intermediate frequency sub-bands are shown in Figure 7.5. The receiver passband is downconverted with two local oscillators, at 5 GHz and 7 GHz, shown in yellow and green respectively. The intermediate frequency

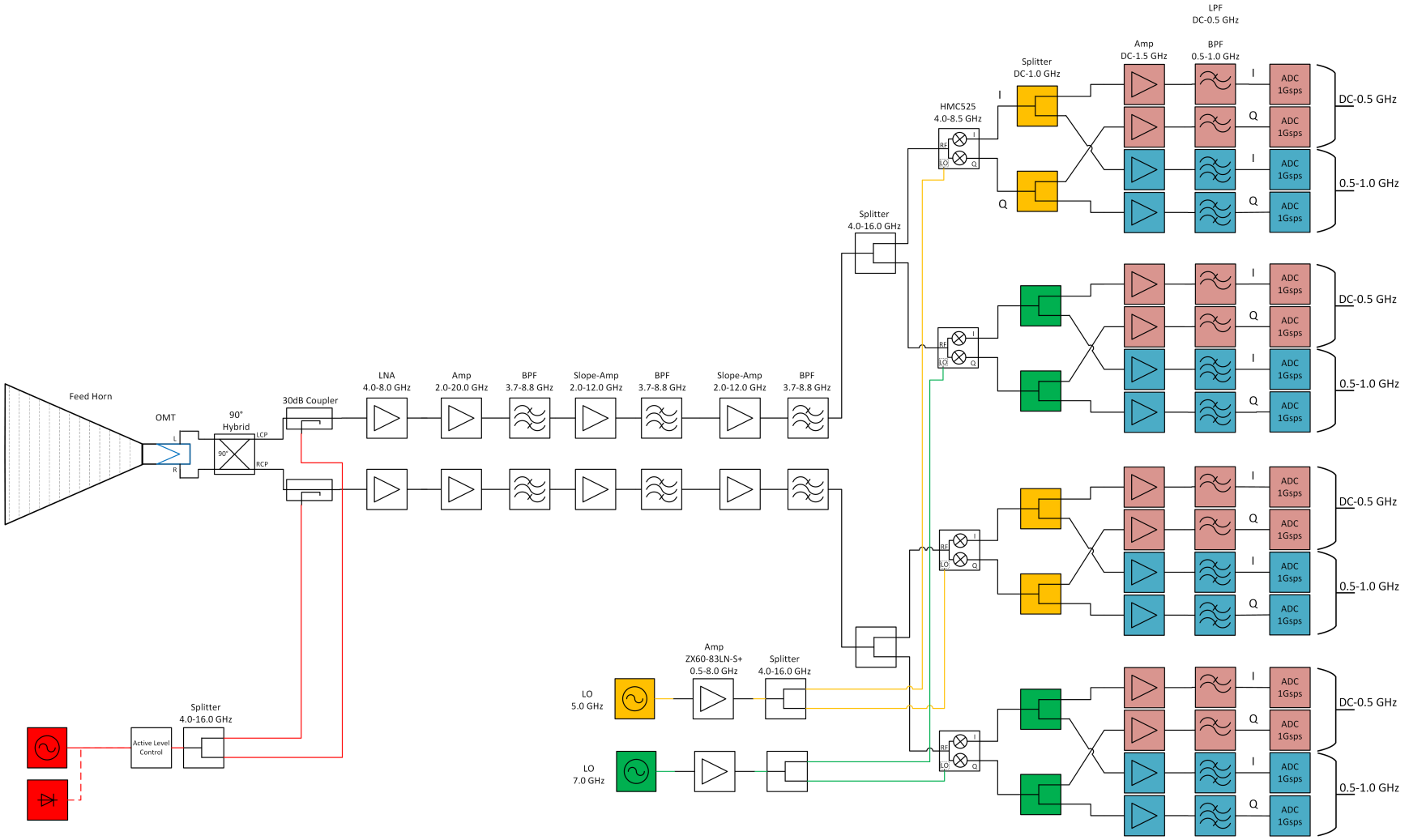

Figure 7.4: Analogue signal conditioning diagram of the GHY-3 receiver.

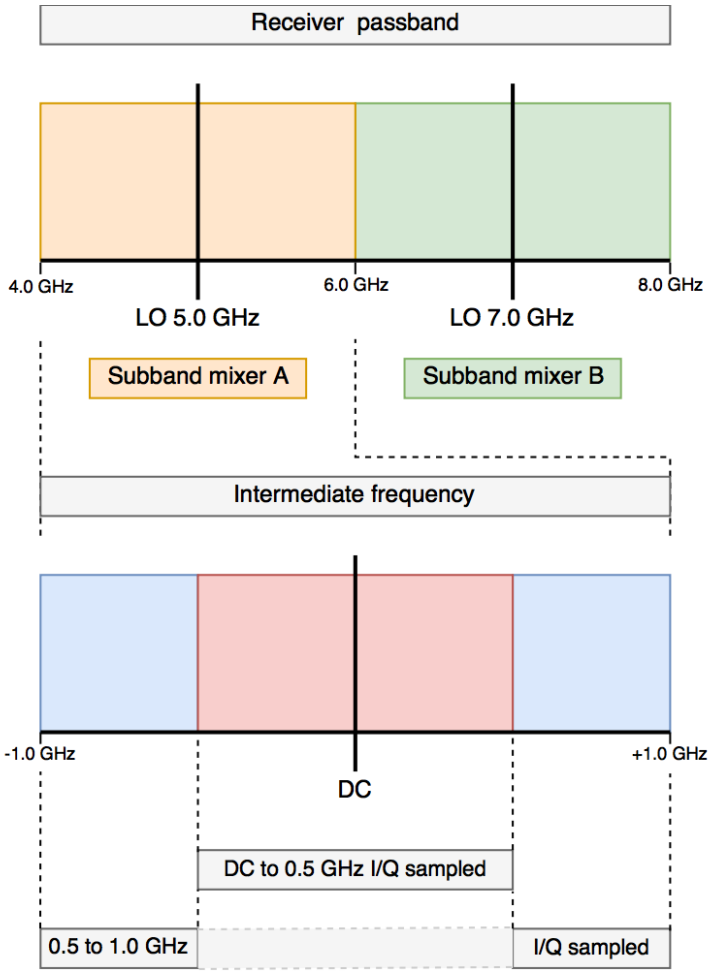

Figure 7.5: Illustrates the frequency conversion from the receiver passband to the intermediate frequency. The entire passband is converted using two IQ mixers with two local oscillators at 5.0 GHz and 7.0 GHz, coloured in yellow and green, respectively. The detailed intermediate frequency band of mixer A is shown at the lower part of the figure. The IF band is divided into two sub-bands by the anti-aliasing low-pass and band-pass filter, red and blue, respectively.

band for mixer A is illustrated in detail at the bottom of the figure. The red and blue sub-bands indicate the bands defined by the anti-aliasing lowpass and bandpass filter, respectively. Each sub-band represents a complex spectrum with positive and negative frequencies, which are digitised by sampling I and Q and processed by a complex Fourier transformation. Note, that the sub-band illustrated in red represents the receiver frequency band from $4.5 - 5.5$ GHz. In order to further visualise the hardware that is used to process the frequency bands shown in Figure 7.5 we applied the same colour code in Figure 7.4.

7.1.3 Control and Monitor System

The control and monitor system is of great importance when the receiver and the telescope is operated remotely. This has been demonstrated in experiments like the CBASS South project, where the antenna is located in the Karoo desert in South Africa [77]. Therefore, we put great effort into the design and software of the monitor and control system. To further ensure the reliability we used components which are used in industry and implemented standard communication protocols.

The system overview of the GHY-3 monitor and control system is shown in Figure 7.6. At the centre of the system is the GHY-3 server which connects to all sub systems. Its function is to provide the interface between the external connection and all sub systems. Essentially it monitors all receiver parameters, controls the digital signal

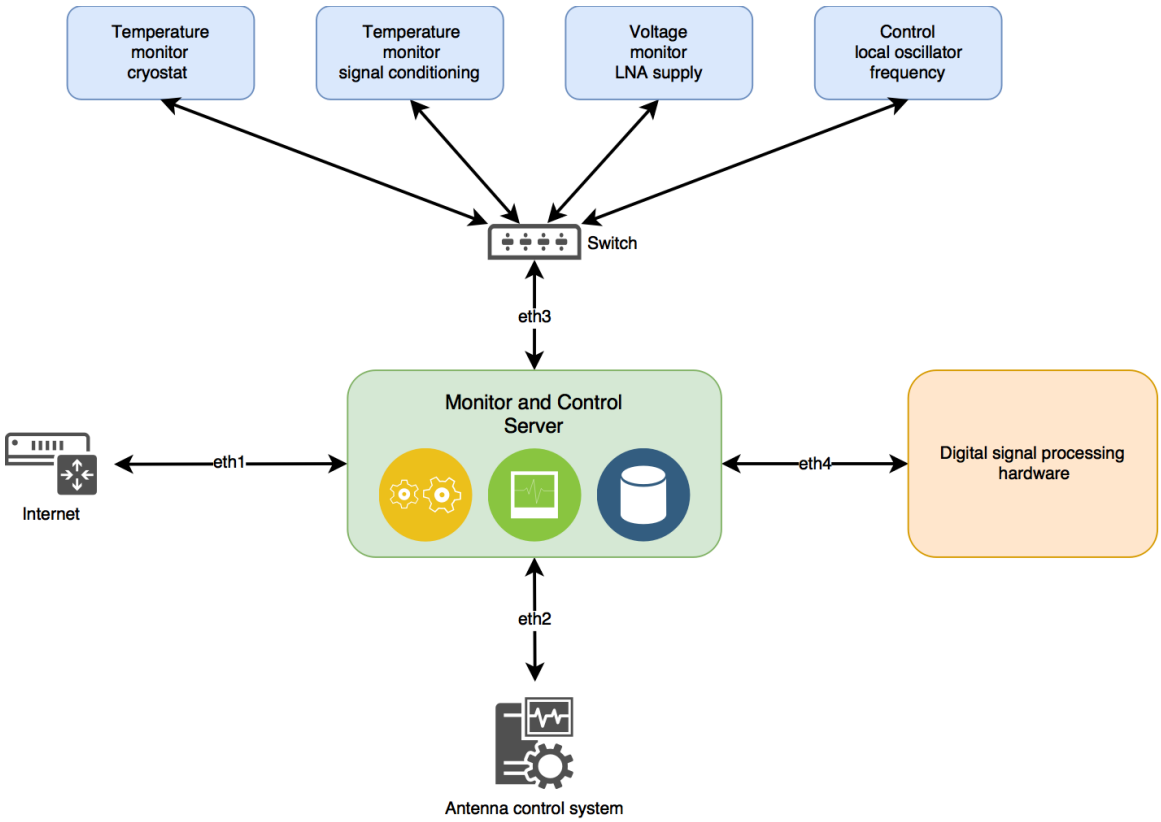

Figure 7.6: System diagram of the monitor and control architecture of the GHY-3 receiver. At the centre is the control and monitor server which is connected to the different areas of the receiver system via ethernet. Each sub system is independent and uses standardised communication protocols.

processing hardware, stores the observed data, and interfaces the antenna control system. The communication between the server and each sub-system is done via standard ethernet connections, each sub system connects to a separate network, which helps to isolate failures within a sub system. The control and monitor server together with parts of the monitor system is shown in Figure 7.7. At the top of the image one can see the GHY-3 server followed by the readout system for the cryostat temperature sensors, followed by the vacuum monitor and the LNA power supply.

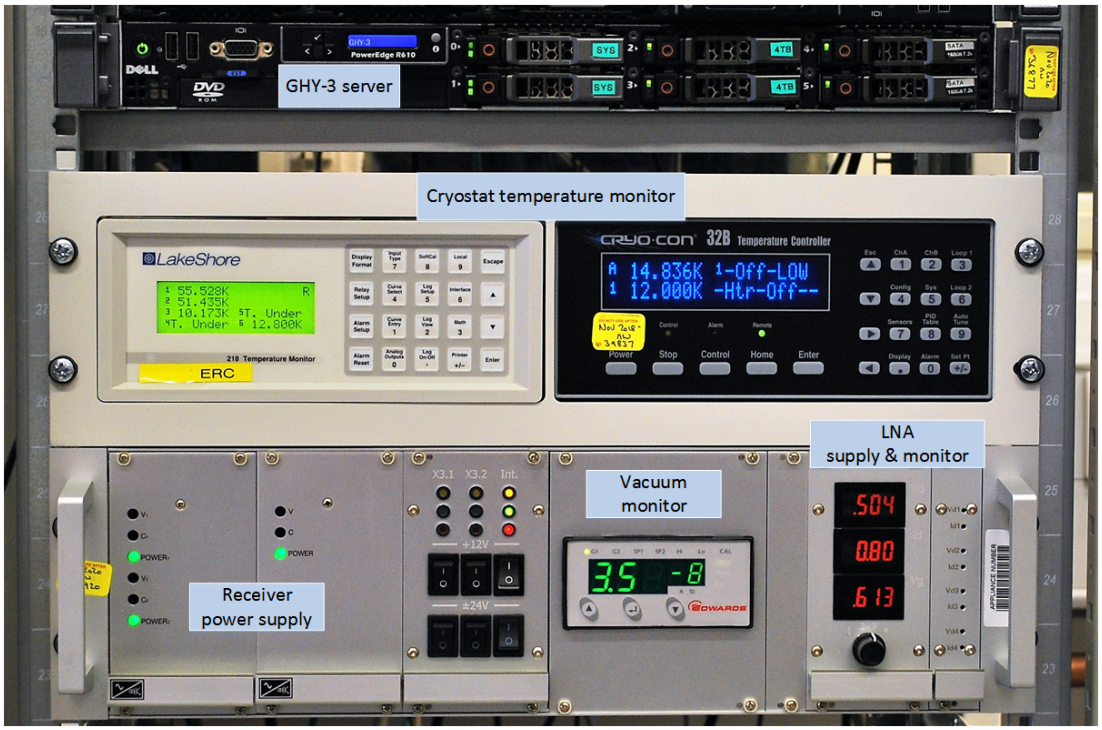

Figure 7.7: Part of the control and monitor hardware for the GHY-3 receiver system.

7.2 Component Designs

In this section we present a number of components and systems, which we designed especially for the GHY-3 receiver.

7.2.1 Analogue Signal Components

The analogue signal components were designed especially for the requirements of the GHY-3 receiver. All components except for the $4-8\,\mathrm{GHz}$ Active Level Control were designed using HFSS and measured using a four port Rohde & Schwarz ZNB20 Vector Network Analyser (VNA) which was calibrated to its coaxial ports.

7.2.1.1 4.0 – 8.5 GHz In Phase/Quadrature Mixer

The GHY-3 receiver is required to downconvert the receiver passband from $4-8.5\,\mathrm{GHz}$ to an intermediate frequency, which can be sampled by the ADCs. To implement the frequency conversion with as few components as possible, we decided to apply IQ mixers which allow us to down convert a $2\,\mathrm{GHz}$ band per mixer.

The mixer most suitable for our application is the HMC525LC4 from Analog Devices which supports a RF input range of $4-8.5\,\mathrm{GHz}$ and an IF output range of $\mathrm{DC}-3.5\,\mathrm{GHz}$. The mixer itself comes in a surface-mount package for which we designed a printed circuit board (PCB). In order to use standard box sizes throughout all our signal components we designed the mixer around pre-existing box dimensions. For the IQ mixer design we modified the number of SMA connectors on an existing box. The connection between the mixer chip and the SMA connectors are applied using a coplanar waveguide, which provides a broadband transmission for the IF and RF side of the mixer. The boxed mixer and its measured performance is shown in Figure 7.8. The mixer was measured using a local oscillator at $4.0\,\mathrm{GHz}$ with an output power of $14\,\mathrm{dBm}$. Hence, the plot in Figure 7.8b shows the conversion for I and Q from $4-8.5\,\mathrm{GHz}$ RF to $\mathrm{DC}-4.5\,\mathrm{GHz}$ IF. It can be seen that the conversion loss is around $-10\,\mathrm{dB}$ for both channels, which is consistent with the data sheet of the manufacturer and a typical value for those types of gallium arsenide mixers from

Analog Devices. Although the RF return loss also agrees with the value in the data sheet it is with approximately −6 dB very high, which in the worst case could lead to resonances in the signal chain. A way to reduce the effect of the mismatch at the RF input of the mixer would be to include some attenuation in the signal path.

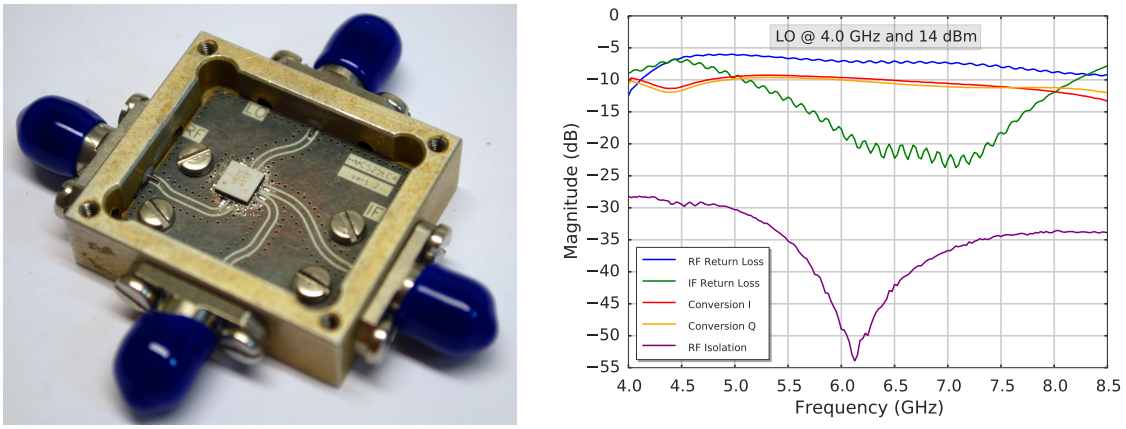

(a) Boxed mixer.

(b) Measured performance.

Figure 7.8: The GHY-3 IQ mixer. (a) The mixer PCB assembled in the box. (b) The measured performance of the boxed mixer, using a local oscillator at 4.0 GHz with an output power of 14 dBm.

7.2.1.2 4 – 16 GHz Wilkinson Divider

The GHY-3 power divider is required to split the RF signal after the amplification and filter stages. We designed the divider to operate over the receiver passband as well as to perform up to 16 GHz, making the design also useful for future projects. The divider implements a Wilkinson design [81], which has the advantage of being matched at all ports as well as having a high isolation between the two output ports. The GHY-3 Wilkinson divider was designed using the general design equations for a four section divider from [82], which allowed us to calculate the required impedance for the SMD resistors and the transmission line for each section of the divider. Using the calculated impedances, we then created a microstrip line model in HFSS and optimized the width of the microstrip to improve the return loss of all ports as well as to optimise the transmission from port one to port two and three. The HFSS model design layout and simulated performance is shown in Figure 7.9.

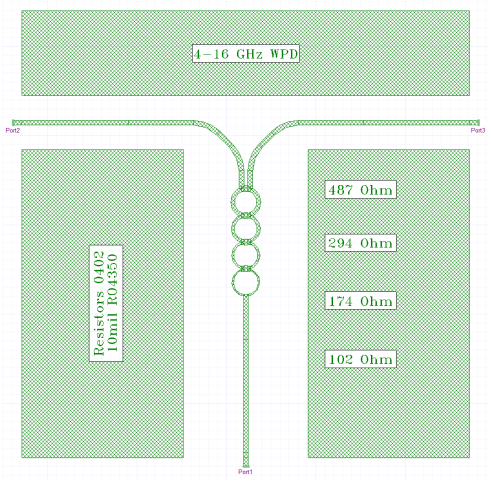

(a) HFSS design.

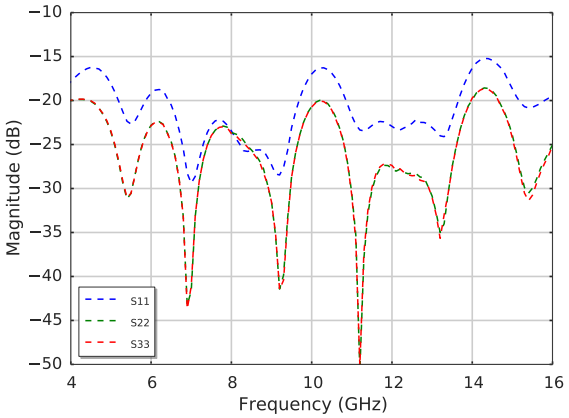

(b) Simulated return loss.

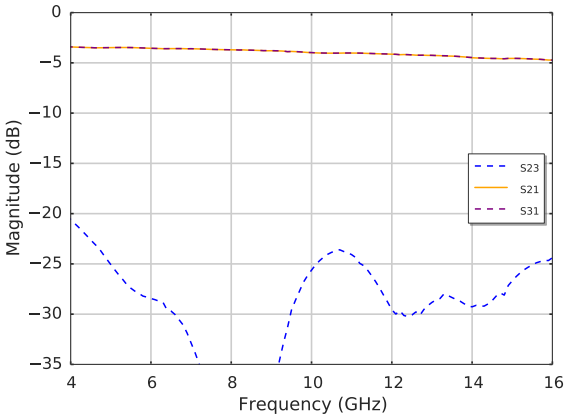

(c) Simulated insertion loss and isolation.

Figure 7.9: Simulated Wilkinson divider. (a) HFSS design, port one is at the bottom centre and port two and three are located on the left-hand and right-hand side, respectively. (b) Simulated return loss for all three ports. (c) Simulated transmission between port one and ports two and three, as well as the isolation between port two and three.

To measure the performance of the divider we manufactured a prototype on 10 mil Rogers 4350 substrate. The prototype is shown in Figure 7.10a and the measured response for the return loss and transmission is shown in Figure 7.10b and 7.10c, respectively. It can be seen that the measured performance of the splitter agrees very well with the simulated predictions in Figure 7.9b and 7.9c. The return loss for all three ports remains below −15 dB and the transmission is smooth over the entire operational bandwidth of the divider. It is worth pointing out that we do not see

any traces of a cavity resonance, that could be caused by the closed box assembly. Nevertheless, we apply a cavity absorber in each divider box consisting of a square of MR42-0007-20 material from Mast Technologies which is glued to the inside of the lid.

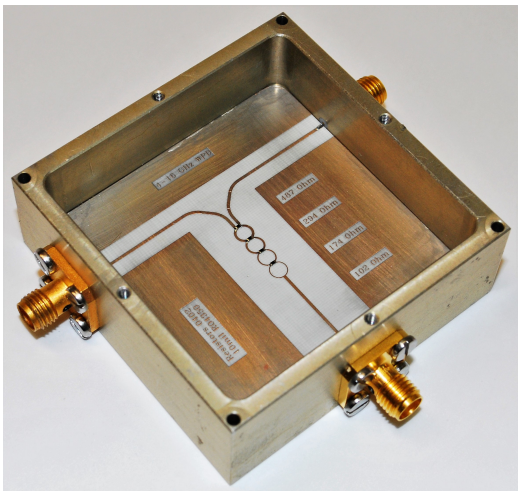

(a) Boxed divider.

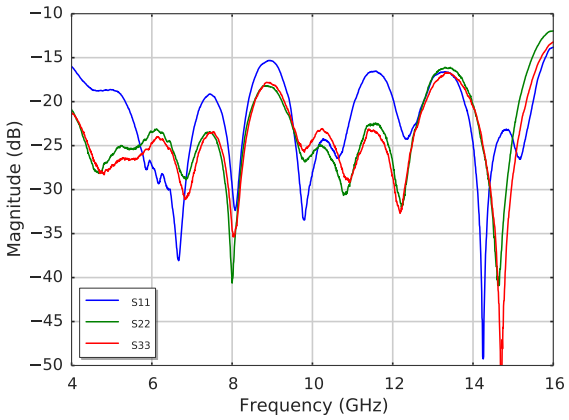

(b) Return loss.

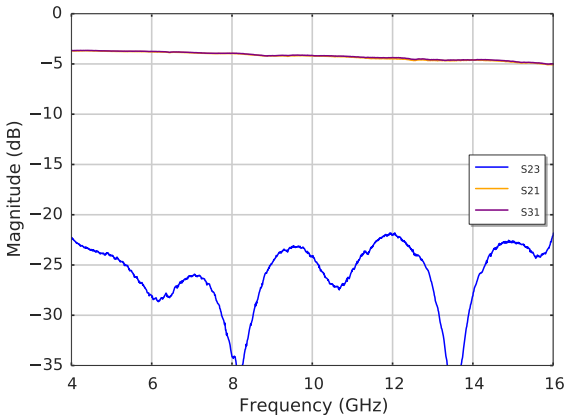

(c) Insertion loss and isolation.

Figure 7.10: Manufactured GHY-3 Wilkinson divider. (a) Assembled divider. (b) Measured return loss for all three ports. The common port is defined as port one. (c) Measured transmission between the common port and port two and three, as well as the isolation between port two and three.

7.2.1.3 4.0 – 8.5 GHz Bandpass Filter

The GHY-3 bandpass filter was designed to define the observational band of the receiver and to provide a sufficient out-of-band rejection to suppress RFI from satellite

communications at higher and lower frequencies. The filter is a concatenation of a band-pass and a low-pass filter. The band-pass filter defines the actual passband of the filter and the low-pass filter suppresses the reappearing of the passband at higher frequencies, where multiples of the design wavelength can transmit through the band-pass again. Both filters use different implementation techniques, which provide the best performance for their function. The band-pass filter is implemented as quarter-wave short-circuited stubs [83] and the low-pass filter is implemented using stepped impedances [54]. The HFSS design is shown in Figure 7.11a, where we can see the combined band-pass and low-pass filter in a standard box design layout. Each filter has been designed and simulated independently and was then connected to simulate the combined performance. The simulation of the quarter-wave short-circuited stubs band-pass filter is shown in Figure 7.11b, it can be seen that the passband is flat and the return loss is below $-20\,\mathrm{dB}$, we can also see that the passband reappears again at approximately 16 GHz. In order to suppress the reappearing of the passband we designed a stepped impedance low-pass filter which rejects the transmission above 12 GHz. The simulated performance of the low-pass filter is shown in Figure 7.11c. We can see that the passband of the low-pass is flat up to 11.5 GHz, which implies that the low-pass transmission should not affect the performance of the band-pass. This can be seen in Figure 7.11d, where we show the simulation of the combined low- and band-pass filter. The passband of the combined filter arrangement shows a similar performance, with respect to the location of the lower and higher cut-off frequencies, as the simulation of the band-pass alone. We can also see a slight increase in insertion loss across the passband, which is due to the combined insertion loss of both filters. Note that the simulation of the combined filter arrangement does not show a reappearing of the passband at higher frequencies.

To measure the performance of the GHY-3 band-pass filter, we manufactured a prototype on 10 mil Rogers 4350 substrate. A picture of the assembled prototype is shown in Figure 7.12a. When we measured the performance of the prototype, we discovered that the closed cavity of the box produces a resonance located within the passband, at 6.6 GHz. This can be seen as a narrowband dip in the insertion loss

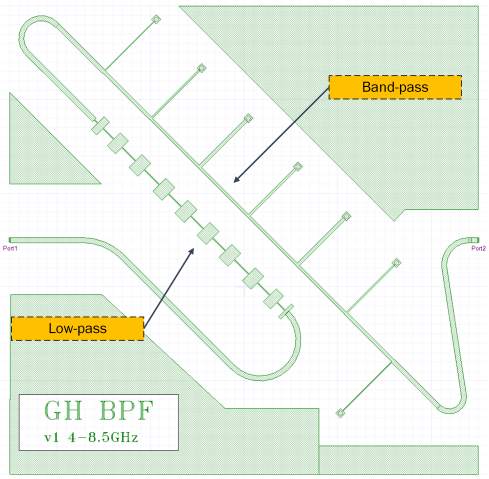

(a) HFSS design.

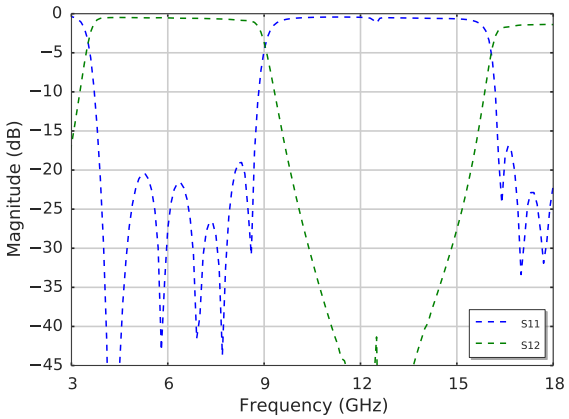

(b) Simulated band-pass.

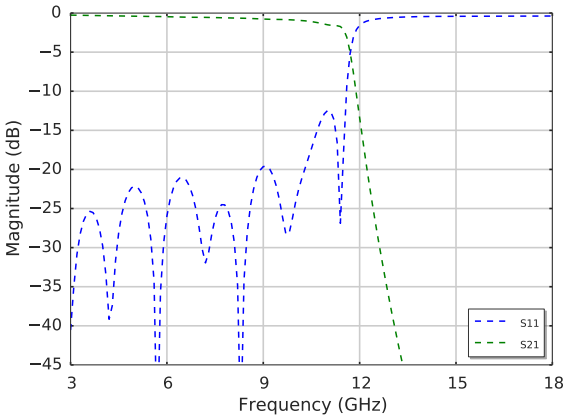

(c) Simulated low-pass.

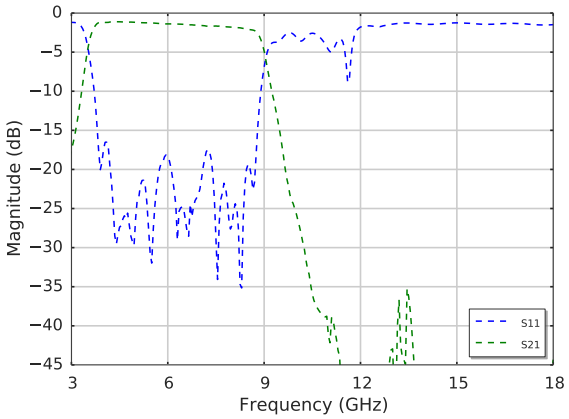

(d) Simulated band- and low-pass.

Figure 7.11: Simulated GHY-3 band-pass filter. (a) HFSS design of the combined low-pass and band-pass filter. (b) Simulated response of the quarter-wave short-circuited stubs band-pass filter. (c) Simulated response of the stepped impedances low-pass filter. (d) Simulated response of the combined band-pass and low-pass filter, as shown in (a).

and as a spike in the return loss in Figure 7.12b. In order to suppress the cavity resonance, we added the same absorber material as previous used in the design of the Wilkinson divider and glued it inside the lid of the box. After that we measured the passband of the filter again. Figure 7.12c shows that the resonance is diminished by the absorber and the passband is flat and the return loss remains below $-15\,\mathrm{dB}$.

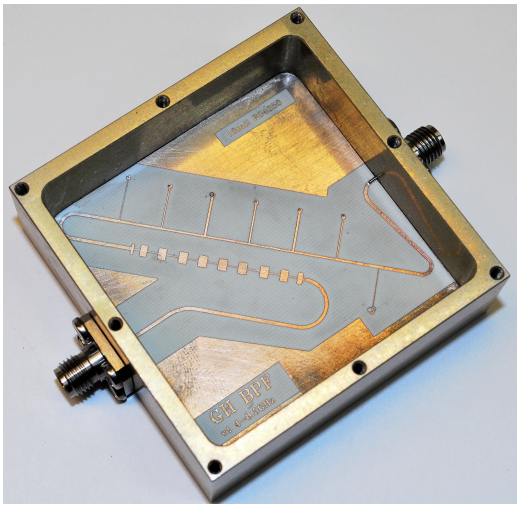

(a) Boxed filter.

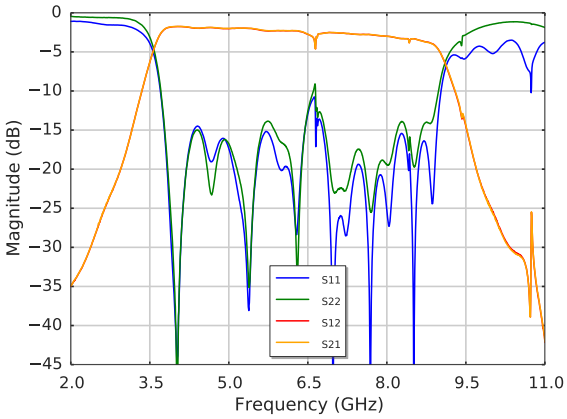

(b) Without a cavity absorber.

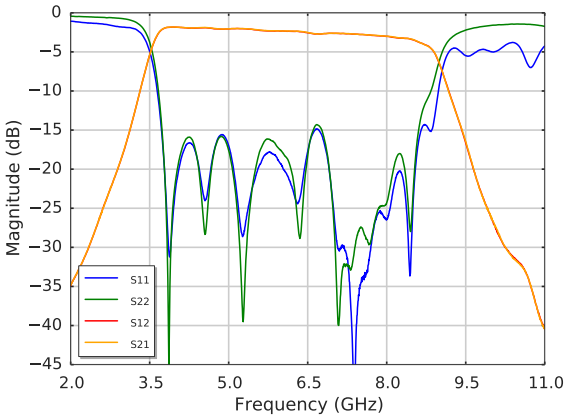

(c) With a cavity absorber.

Figure 7.12: Manufactured GHY-3 band-pass filter. (a) Assembled filter. (b) Measured return loss and transmission without a cavity absorber. (c) Measured return loss and transmission with a cavity absorber.

7.2.1.4 DC – 0.5 GHz and 0.5 – 1.0 GHz Anti Aliasing Filter

The GHY-3 anti-aliasing filters are designed to select a 500 MHz band within the downconverted ±1 GHz IF band. The filter bandwidth is specified by the 1 Gsps sampling rate of the ADCs that we use in our DSP hardware. As the ADCs support frequencies up to the second Nyquist zone, we designed two filters, one covering the band of the first Nyquist zone, from DC − 0.5 GHz, and one covering the second Nyquist zone from 0.5 − 1.0 GHz. Both filters require a sharp roll off and a high out-of-band rejection in order to prevent aliasing from other Nyquist zones.

Reference [77] presents the development of lumped element filters which were used for the same application in the C-BASS south receiver. However, the design files of those filters were not available and we decided to redesign both filters from scratch by only using the fundamental design idea, which is to implement the filter as a coplanar waveguide with surface mount devices (SMD) inductors and capacitors.

We first designed a mechanical housing for the filter, which allows us to mount a PCB with a coplanar waveguide and two standard SMA connectors. The physical length of the filter restricts the filter order as it limits the number of mountable components.

The filters were designed in two steps. First we defined the filter parameter in HFSS and calculated the ideal component values for each filter. The schematics used for the low-pass filter and band-pass filter implemented in the simulation are shown in Figure 7.13. It turned out that the impedance of the filters are matched well enough that we could design the band-pass filter by cascading a low-pass with a high-pass filter. After the ideal component values were determined, we investigated which components were available to purchase and then replaced component after component in the simulation model until the entire model consisted of purchasable components that still provided the required roll off and out-of-band rejection.

The first prototype is shown in Figure 7.14a and was build using 0402 inductors, which were picked to match the width of the 50 Ω coplanar waveguide.

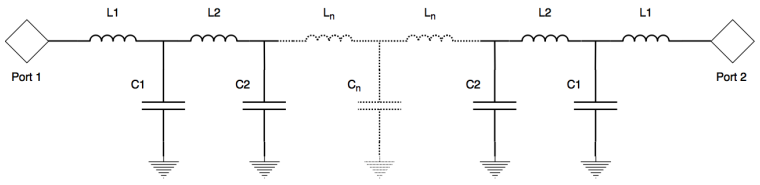

(a) Anti-aliasing low-pass filter schematic.

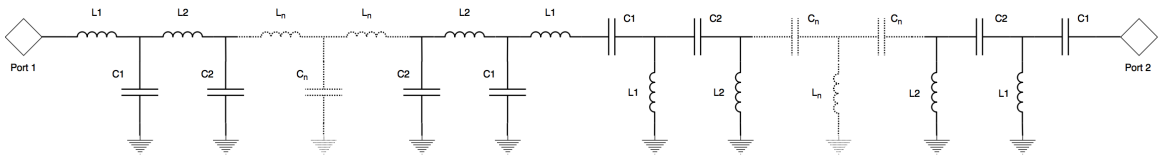

(b) Anti-aliasing band-pass filter schematic.

Figure 7.13: Schematic of the anti-aliasing lumped element filters.

The measured performance of this prototype showed a higher insertion loss and an earlier roll off than we expected based on our simulated predictions. As a reason for this deviation we suspected the ohmic resistance in the inductors. To test our theory we dipped the prototype filter in liquid nitrogen and measured its performance at 77 K. The comparison of the prototype filter at room temperature and at 77 K is

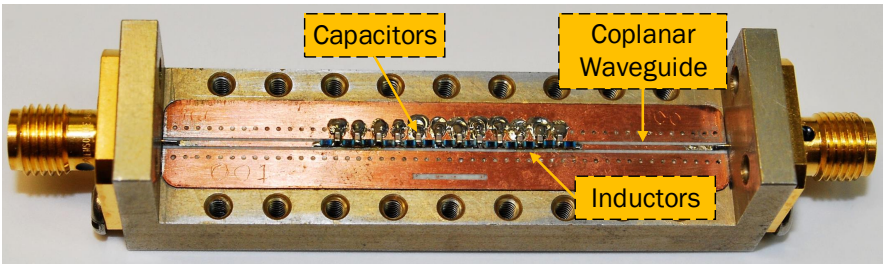

(a) Filter prototype.

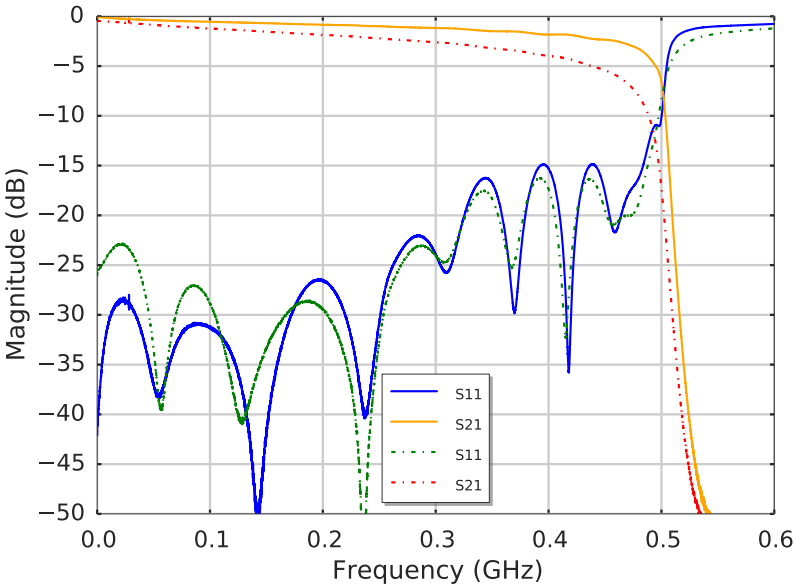

(b) Measured performance.

Figure 7.14: Manufactured filter prototype. (a) Filter prototype build from 0402 inductors. Not shown is the lid that encloses the filter, which is held down by the visible screw holes. (b) Measured performance of the filter at room temperature and at 77 K, dashed-dotted and solid line respectively.

shown in Figure 7.14b, where we can see that the insertion loss for the measurement at 77 K is much lower compared to the measured performance at room temperature. This experiment proved our initial suspicion and allowed us to redesign the filter with

inductors that have a lower internal resistance.

Based on this results we decided to replace the 0402 inductors with 0603, which is the next bigger package size. Due to the increase in package size the DC resistance of the inductors decreases approximately by a factor of five. As all component values required for the filter are also available in the 0603 package we just needed to redesign the PCB for the slightly bigger components and could build a second prototype based on the initial simulation model.

A picture of the second iteration anti-aliasing filters is shown in Figure 7.15. The upper filter is the $0.5-1.0\,\mathrm{GHz}$ band-pass and the lower filter is the $\mathrm{DC}-0.5\,\mathrm{GHz}$ low-pass. The comparison between the measured performance and simulated prediction

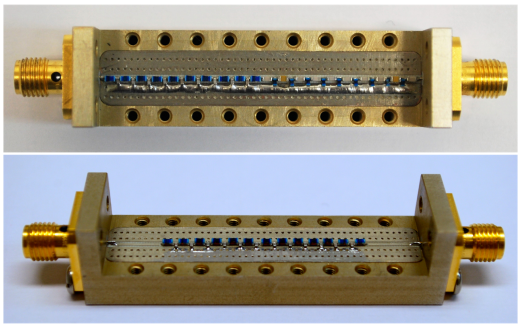

(a) Anti-aliasing filter.

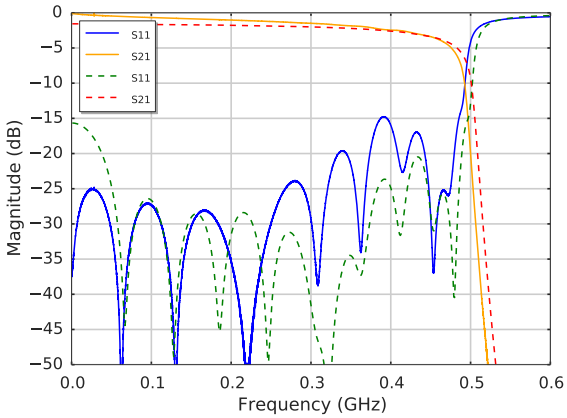

(b) Low-pass filter

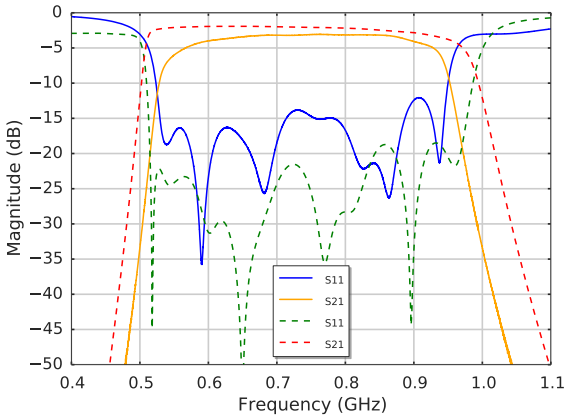

(c) Band-pass filter

Figure 7.15: Manufactured GHY-3 anti-aliasing filter. (a) The assembled filters; the upper one is the $0.5-1.0\,\mathrm{GHz}$ band-pass and the lower one is the $\mathrm{DC}-0.5\,\mathrm{GHz}$ low-pass filter. (b) Measured and simulated performance of the low-pass filter, solid and dashed line respectively. (c) Measured and simulated performance of the band-pass filter, solid and dashed line respectively.

for the low-pass and band-pass filter are shown in Figure 7.15b and 7.15c, respectively. One can see that the measured response of the low-pass filter agrees very well with the predicted response of the simulation. However, the measurement of the bandpass filter shows that the measured bandwidth of the filter is narrower than the simulation predicted, especially at the higher frequency end. We suspect that the insertion loss of the high-pass in the band-pass filter is significantly higher compared to the low-pass and therefore is the cause for the earlier roll off of the passband.

Nevertheless, the measured performance for both anti-aliasing filters is sufficient to be applied in the GHY-3 receiver system. For completeness and reusability we list the component values for the anti-aliasing low-pass and band-pass filter in Appendix A.

7.2.1.5 4 – 8 GHz Active Level Control

The active level control was designed after we tested the continuous wave gain-tracking method and discovered that the instability of the local oscillator reference source has the same order of magnitude as the gain instabilities in the receiver test setup (see Section 6.3.2). The aim of the ALC is to compensate the amplitude fluctuations of the reference signal and provides a stabilised output reference signal. As the output signal of the ALC still can be affected by temperature variations in cables and other hardware, we decided to integrate the entire unit inside the cryostat and temperature stabilise the control hardware.

The design of the ALC includes a number of specifications which define the required stability of the output signal, the noise performance, and the dynamic range. The requirement on the output stability states that the residual drift in the output power level must be less than 0.005 dB in order to be used as a reference signal for the receiver system. The noise performance requirement states that no additional noise to the receiver system must be introduced by the control loop. The dynamic range requirement states that the control loop must be able to correct for input power variations of 0.2 dB.

In order to meet these requirements we use a temperature stabilised proportional-

integral (PI) control loop that regulates the output power via a voltage-variable attenuator. The temperature stabilisation is essential because the power-voltage characteristic of the detector diode is temperature dependent. The block diagram of the control loop is shown in Figure 7.16. The setpoint value of the control loop is generated by a reference voltage source. This signal is then combined with the negative feedback voltage from the detector diode, after which we have the input signal to the PI controller. The output of the controller is then amplified to match the operational voltage range of the attenuator. Finally, the output reference signal is measured by the detector diode and fed back to the input of the control loop. The PI controller has the advantage that it has no permanent deviation between the set point and the measured output value. Any difference between the set point and the actual output power will be integrated in the controller and corrected until the difference is zero. The hardware implementation of the PI controller using an operational amplifier and a resistor-capacitor circuit is shown in Figure 7.17. The input signal x_e represents the error between the set point and the measured output value and x_a represents the control variable. The functional description of the PI controller in the time domain

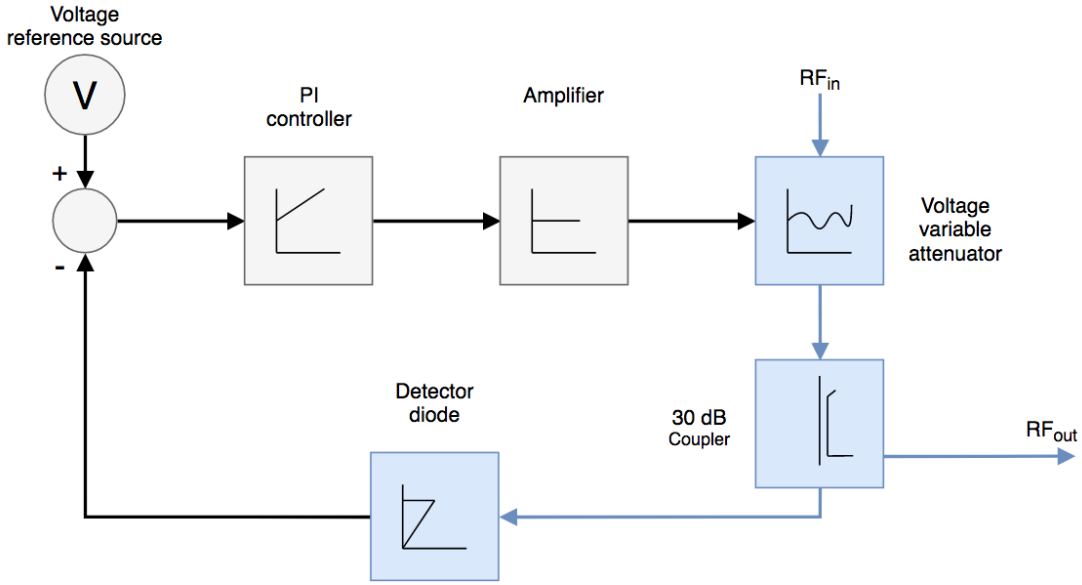

Figure 7.16: Schematic of the ALC control loop. The RF signal components and connections are illustrated in blue.

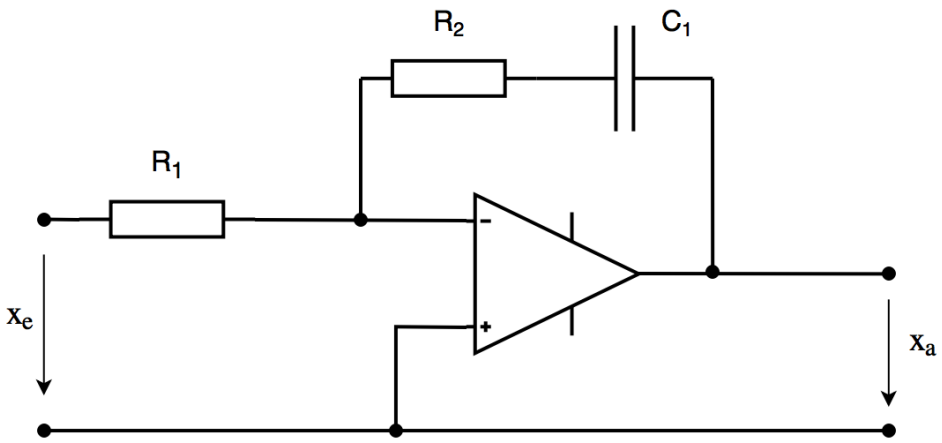

Figure 7.17: PI controller implementation.

is given by

$$h(t) = K_{\mathrm{R}} \left(1 + \frac{t}{T_1}\right) \sigma(t) \tag{7.1}$$

where

K_{R} : the gain of the controller,

T_1 : the integral time constant.

The gain and the integral time constant for the implementation shown in Figure 7.17 is given by

$$K_{\mathrm{R}} = \frac{\mathrm{R}_2}{\mathrm{R}_1}, \qquad T_1 = \mathrm{R}_2\mathrm{C}_1. \tag{7.2}$$

The GHY-3 ALC unit combines four individual circuits: power supply, monitor, temperature control, and level control circuit. A picture of the four layer PCB illustrating the location of the four circuits is shown in Figure 7.18a. The temperature control circuit also applies a PI control loop, which will be described in more detail in Section 7.2.2. The monitor system implements the readout for the actual temperature value and provides a 5 volt signal which indicates that the level control loop operates within its operational range. The top view of the ALC is shown in Figure 7.18b, we can see the arrangement of the RF components on the temperature-controlled aluminium plate. The local oscillator is connected to the input of the voltage variable attenuator, then the signal passes through a 30 dB coupler, which allows us to couple out the attenuated reference signal. The through path of the coupler is connected

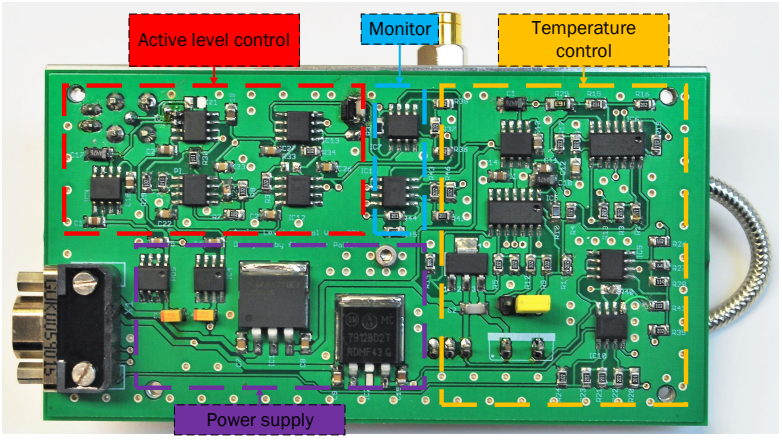

(a) Bottom view.

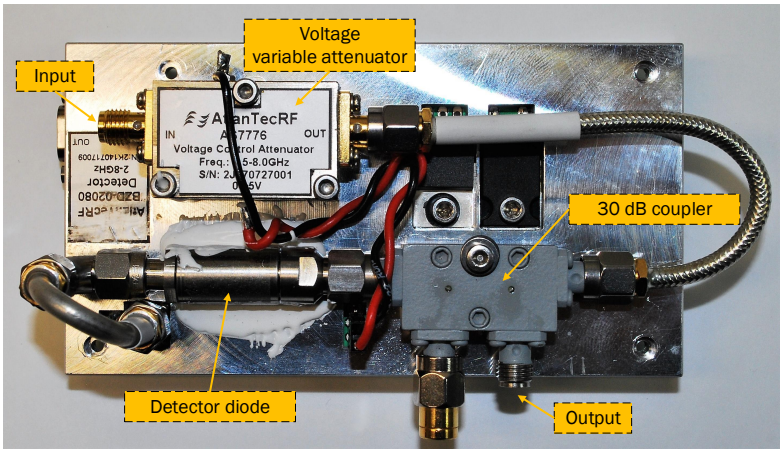

(b) Top view.

Figure 7.18: GHY-3 active level control. (a) Bottom view, showing the control PCB and the locations of the different circuits. (b) Top view, showing the arrangement of the attenuator, coupler, and detector diode.

to the detector diode which produces a voltage signal proportional to the detected power. The measured dynamic range of the ALC is shown in Figure 7.19. We swept the input power of the reference signal at a fixed frequency of 5.125 GHz and measured the output power after the 30 dB coupler. The measurement shows that the voltage variable attenuator has a dynamic range of approximately 1.7 dB, which is more than sufficient as we want to correct for very small amplitude changes of the order of 0.005 dB. The monitor system on the ALC provides a positive 5 volt output signal when the input signal power lies within the operational range of the ALC,

shown by the two dashed lines.

We could verify the functionality of the ALC with respect to its dynamic range and the output level stabilisation. However, to fully verify the design and the performance further measurements are required. The first measurement would be to compare the signal generator stability with and without the ALC present, similar to the measurements presented in Section 6.3.2. After that the ALC needs to be implemented into the test setup, so that we can verify the effect on the CW stabilisation method.

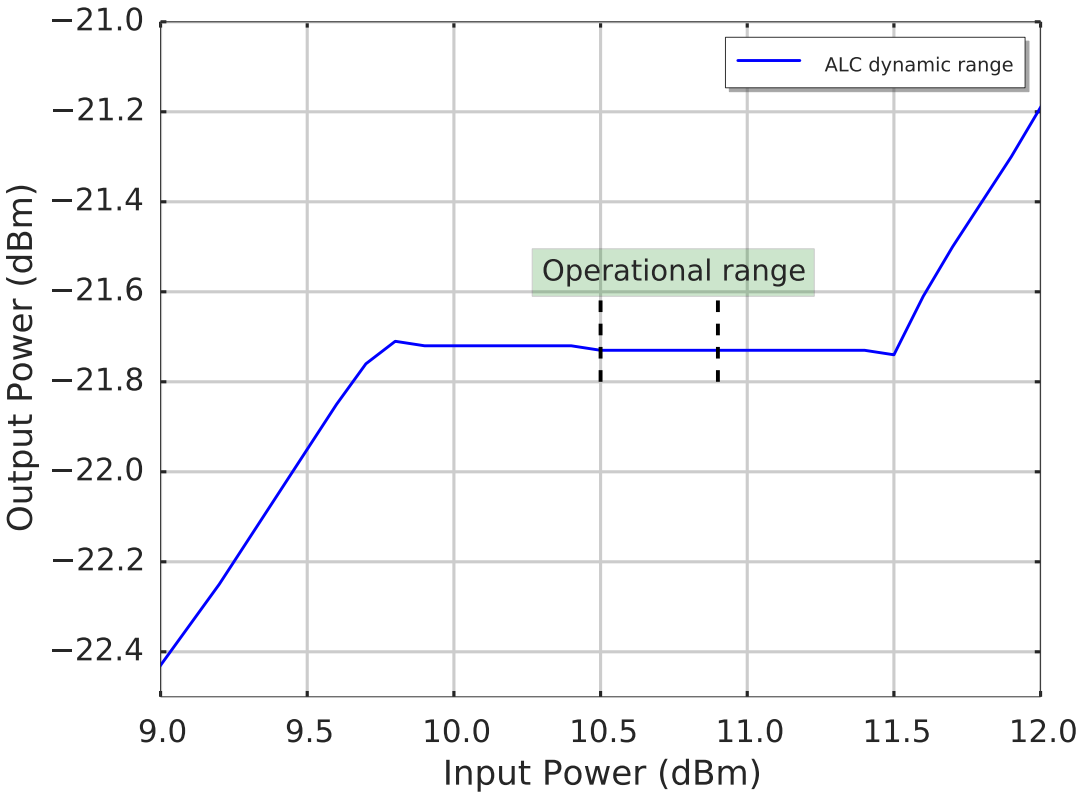

Figure 7.19: Measured dynamic range of the ALC.

7.2.2 Temperature Stabilised Modules

Any temperature changes of active and passive signal components have an effect on the overall gain of the signal chain. To minimize the influence of external temperature variation on the receiver gain we must decouple the signal components from those variations. This is done by operating the components at a stabilised tempera-

ture above the ambient temperature. This principle of operation has the advantages against a system that operates the components below the ambient temperature of being easier to implement.

The temperature-stabilised module platform was designed as a system that operates signal components in a controlled and monitored environment. Design inputs for the modules also came from the C-BASS South project, where we experienced that it is very difficult to locate and repair broken signal components in the field. Hence, we designed the modules to be replaced or interchanged by simply swapping an entire module. This has the advantage that maintenance work can also be performed by local personnel by swapping of field-replaceable modules. Broken modules can then be send to the lab where they can be debugged with the appropriate test equipment. In order to standardise the mechanical form factor of the modules we decided to use cases from the manufacturer Schroff [84] who has a range of 19" rack mount units that employ standard modules. The modules come in two different heights, a 3U and a 6U format with a variety of different widths. The most suitable case size for our application employs a height of 6U and a width of 35 mm. This form factor allows to mount a reasonable number of signal conditioning components into one module, while still being compact enough to have a sufficient number of modules per rack unit.

7.2.2.1 System Diagram

The system diagram for a module is shown in Figure 7.20. The control and monitor electronics on the top of the diagram serve three distinct tasks; first, to provide a clean and stable power supply for active signal components such as amplifiers and local oscillators. Second, to temperature stabilise the module to a selected set point temperature using an analogue PI controller. Third, to monitor the power supply, the actual temperature, and the difference between the set point temperature and the measured temperature. The bottom of the system diagram shows the space allocated for the signal components, which are specific for each module type as well as the temperature sensor and the heater. The LED bar allows to recognise the module status at a glance.

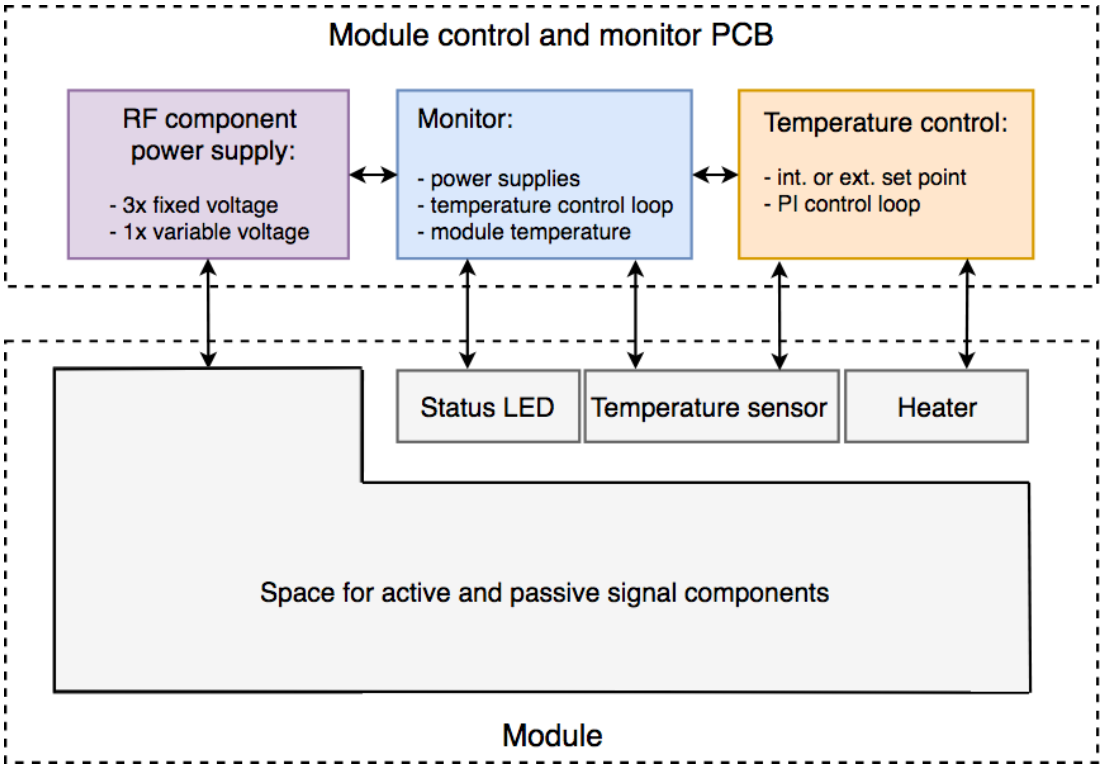

Figure 7.20: System diagram of a temperature stabilised module.

7.2.2.2 Temperature control loop

We took special care to design a temperature controller which does not produce any signals that could electromagnetically interfere with the components of the receiver signal conditioning. Therefore, we decided to only use analogue components for the temperature stabilisation control loop rather than a micro-controller or similar components that requires clock signals.

The analogue control loop shown in Figure 7.21 implements a PI controller similar to the one used in the ALC to stabilise the module temperature. Although the schematic of the control loop looks similar, the integral time constant in the controller is much higher. This is because of the increased reaction time of the output variable, which can be derived from the specific heat capacity of the module and the number of mounted components as well as the airflow through the rack.

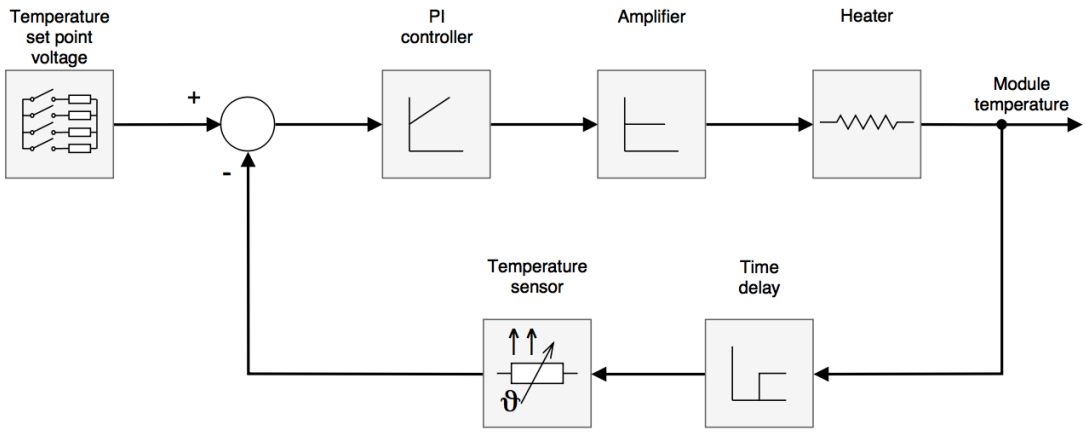

Figure 7.21: Module temperature stabilisation control loop.

Such a control loop becomes unstable when the time delay in the feedback loop causes a positive feedback signal to the input of the controller. There are two ways to avoid this problem. The first way is to reduce time delay in the feedback loop, which can be done by decreasing the heat capacity of the module or by mounting the temperature sensor close to the heater. The second way is to reduce the bandwidth of the controller by increasing the integral time constant and decreasing the controller gain. This has the effect that the controller reacts slower and allows for a greater time delay in the feedback loop. However, this also means that the controller takes longer to respond to abrupt temperature changes. Since for normal operation only slow ambient temperature changes are to be expected, we consider a reduction of the controller bandwidth to be justifiable.

The temperature control loop implemented in the GHY-3 modules uses a controller gain of $K_\mathrm{R} = 18$ and an integral time constant of $T_\mathrm{I} = 79\,\mathrm{ms}$.

7.2.2.3 Hardware implementation

The power supply, monitor, and control circuit is implemented on a two-layer PCB that sits at the rear end of the module. A picture of the PCB illustrating the position of the three different circuits is shown in Figure 7.22. The supply circuit uses linear voltage regulators to convert the 12 V module supply voltage to the voltage required by the active signal components, typically 5 V. The circuit supports up to

four separate outputs and has a current rating of maximal 600 mA per channel.

The monitor circuit applies comparators to check the output voltages of the power supply circuit. The red dip switch is used to select the channels which are monitored by the circuit, used for modules which employ less than 4 active components or none. The circuit also monitors the module temperature and provides an analogue output signal, which is sampled by the central ADC in the rack unit.

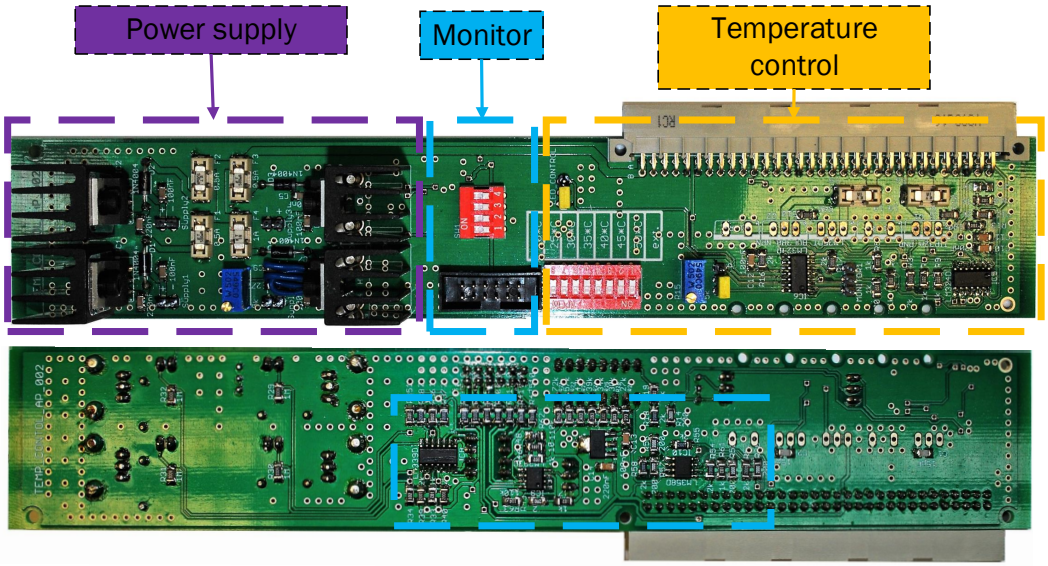

Figure 7.22: Top and bottom view of the control and monitor PCB.

The temperature control implementation allows for seven fixed temperature settings reaching from $20 - 50\,^{\circ}\mathrm{C}$ plus an external analogue reference input should a temperature set point be required to be controlled externally. The set point can be selected by the red dip switch in the temperature control area. Furthermore, the circuit also allows us to modify the controller gain K_{R} through the blue trim potentiometer, thereby allowing to tune the PI controller to different module characteristics. The default setting for the trim potentiometer is $3.6\,\mathrm{k}\Omega$ ($K_{\mathrm{R}} = 18$).

7.2.2.4 GHY-3 Signal Conditioning Modules

In this section we describe the four signal conditioning modules that we designed for the GHY-3 receiver system. The top view of the modules with the lid removed

is shown in Figure 7.23. The IF module shown in Figure 7.23a is used four times in the receiver system. Each module processes 2 GHz of bandwidth and consists of four amplifiers, four anti-aliasing filters, and two power dividers. The local oscillator module shown in Figure 7.23b is used twice in the receiver system and provides LO signals at 5 GHz and at 7 GHz. Both modules consists of the local oscillator module,

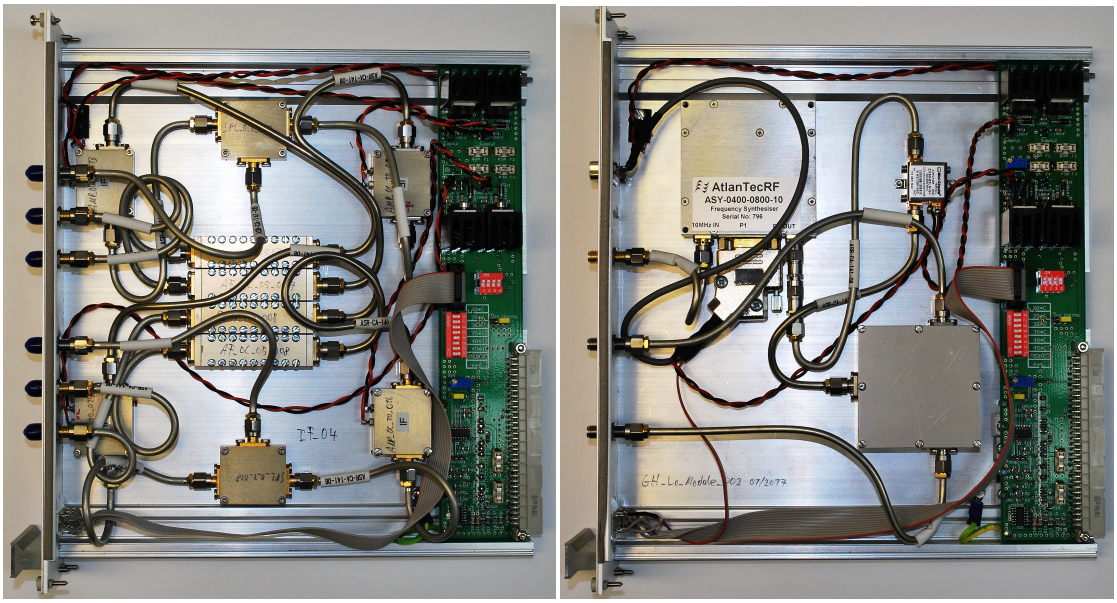

(a) IF module. (b) LO module

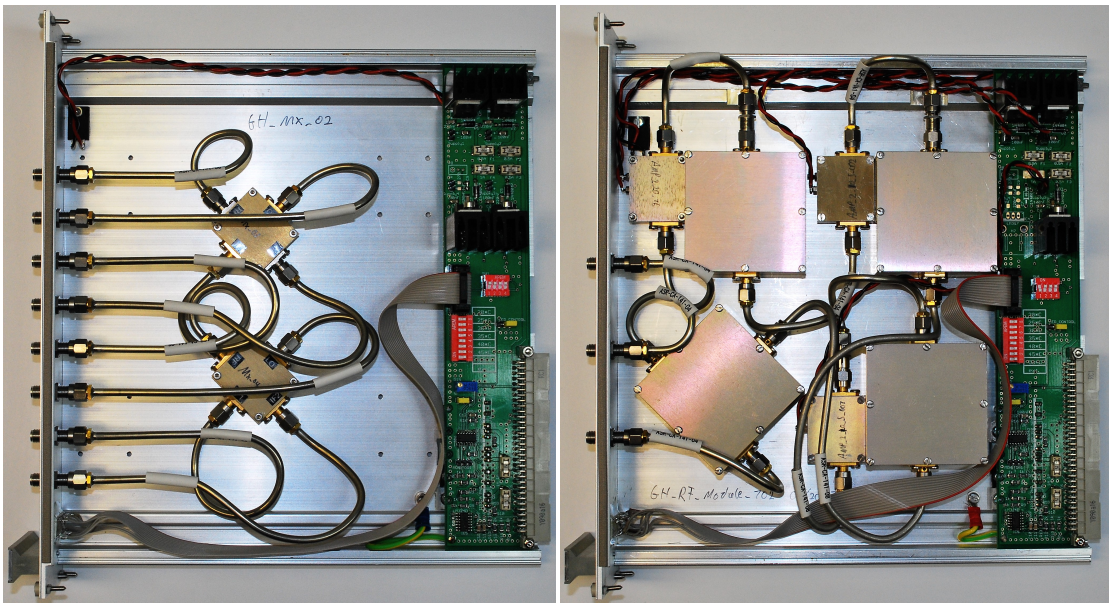

(c) MX module. (d) RF module.

Figure 7.23: GHY-3 signal conditioning modules.

an amplifier, and a power divider. The modules are controlled via an RS485 interface, which allows us to enable and disable the LO signal as well as set the LO frequency within the range of $4-8\,\mathrm{GHz}$. The mixer module shown in Figure 7.23c is used twice and houses two IQ mixers per module. The amplifier and filter module shown in Figure 7.23d covers a total bandwidth of $4.5\,\mathrm{GHz}$ and is used once per polarisation. It consists of three band-pass filters, a power divider, an amplifier, and two slope compensator amplifiers.

One of the two signal conditioning racks for the GHY-3 receiver system is shown in Figure 7.24. The rack houses two of the RF, MX, and LO modules, thereby implementing the first part of the room temperature signal conditioning chain shown earlier in the receiver system diagram in Figure 7.4. It is supplied by the two power supply units at the top right, both can be replaced by swapping an entire unit. On the bottom right, we can see an additional module that is not temperature stabilised, which houses and supplies the clock generator for the analogue-to-digital converters of the test setup.

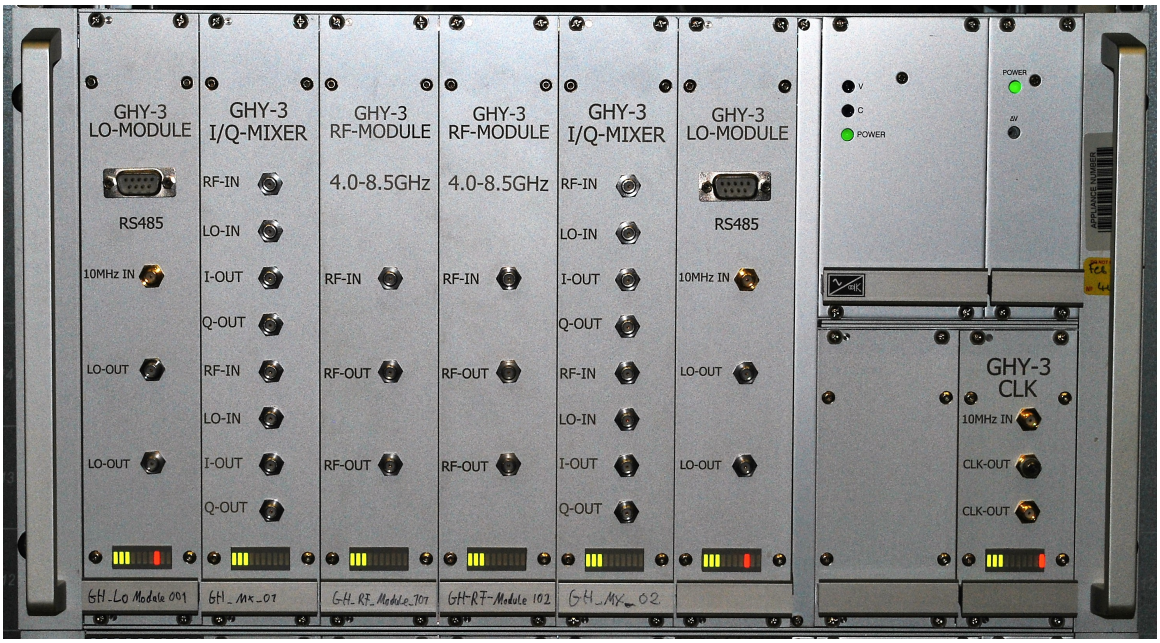

Figure 7.24: GHY-3 temperature stabilised signal conditioning rack.

7.2.2.5 Verification of the Temperature Stabilisation

We tested the stability of the temperature control loop by measuring the temperature of all modules in the signal conditioning rack as well as the room temperature. We then used the air-conditioning to vary the room temperature over a 24 hour time period. Figure 7.25 shows the measured module temperatures (top) and the measured room temperature (bottom) over the 24 hour period. We can see that the absolute module temperature can differ for individual modules, which is due to component tolerances that are used to create the set point temperature voltage. However, the temperature offset between the modules does not matter, as the important thing is the stability of the individual module temperature with respect to the ambient temperature change.

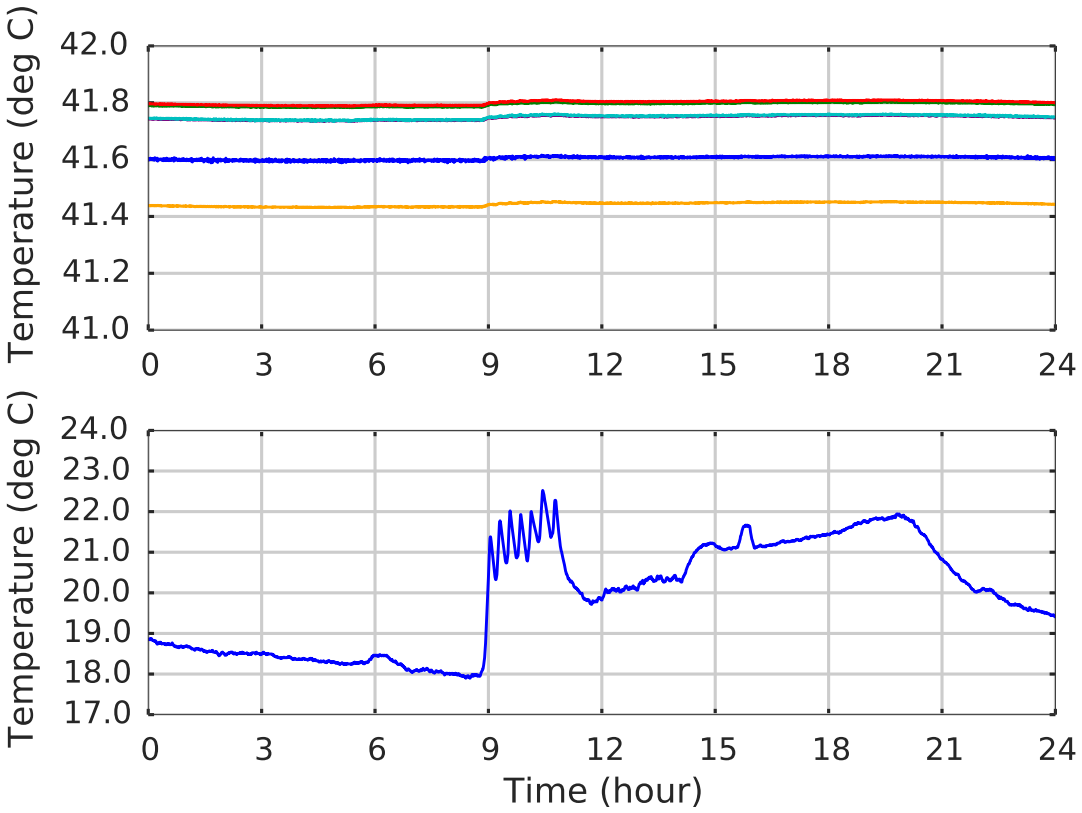

Figure 7.25: Measured temperatures over a period of 24 hours. The measured module temperatures (top) and the measured room temperature (bottom).

7.3 Digital Signal Processing

The GHY-3 receiver system uses the digital signal processing platform developed for the SKA low frequency aperture array which is described in detail in [85]. In this section we describe the hardware platform and the Stokes spectrometer implementation for the first light of the instrument. The other two operational modes of the receiver, interferometer mode and communication mode will be implemented after the commissioning phase of the telescope.

7.3.1 Digital Signal Processing Hardware

The digital signal processing board consists of three parts. First, the analogue to digital unit, which digitises the receiver signal in 500 MHz bandwidth sections. Second, the digital processing unit, which consists of two Xilinx® Kintex Ultrascale FPGAs. And third, the management and control unit, which allows us to monitor and control the hardware and software of the entire board. This includes tasks like initialising the firmware with the correct parameter settings, controlling the read out script, and applying calibration coefficients.

The functional block diagram of the DSP hardware alongside with an image of the board is shown in Figure 7.26. The analogue signals from the IF modules are connected to the input amplifiers of the board on the left-hand side. The gain of these amplifiers can be set through the python control interface thereby allowing us to individually level all signal channels of the receiver IF band. After that, all IF sub-bands are digitised by AD9680 dual input 14 bits ADCs from Analog Devices, which operate at 1 Gsps and support signals up to the second Nyquist zone. The eight most significant bits of each ADC are sent via high speed links to the FPGAs. The two FPGAs can either stream data via the 40 Gbit QSFP+ ethernet connections or, in case that the output rate is reduced enough, via the 1 Gbit management and control connection. The clock management system uses the 10 MHz reference signal to provide a number of clock signals that are distributed to the ADCs and FPGAs. The 1 PPS signal is connected to both FPGAs and allows them to time-stamp the

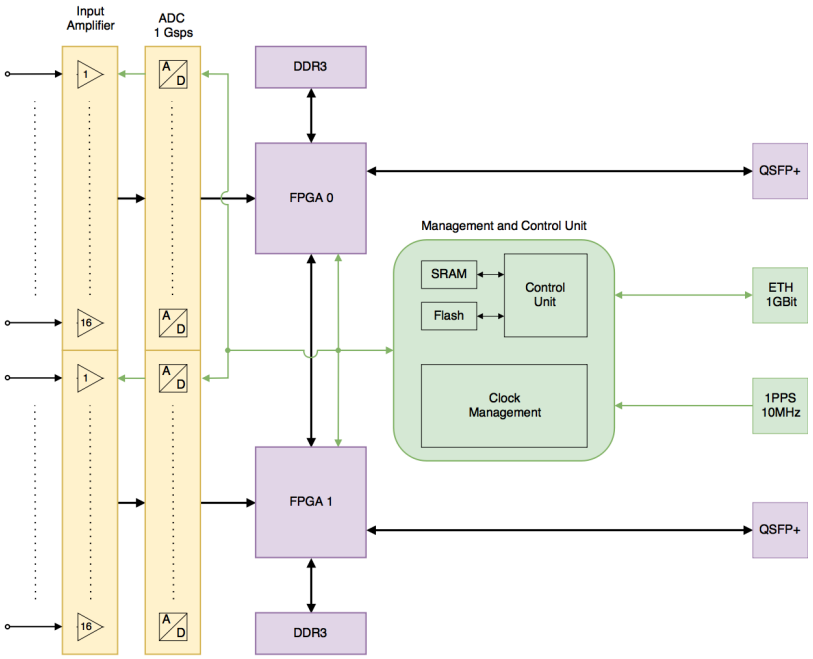

(a) Functional block diagram

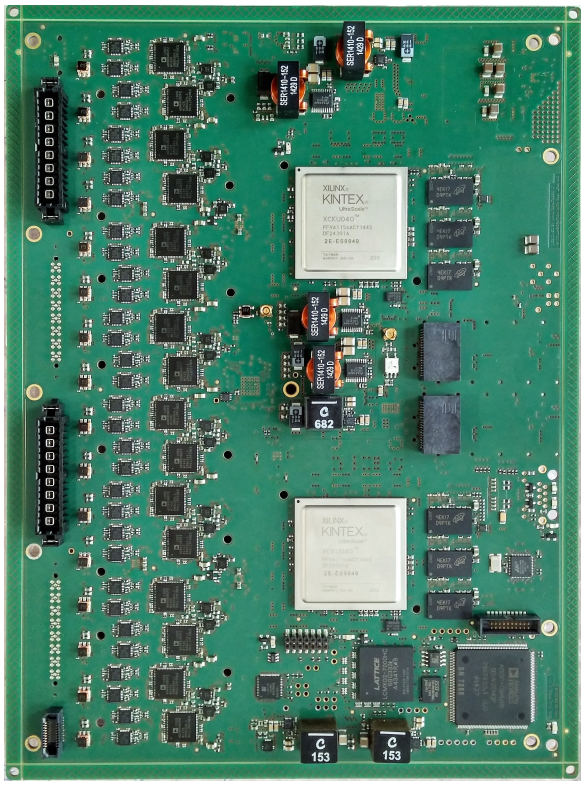

(b) Photo of the board

Figure 7.26: The digital signal processing unit. (a) The functional block diagram. (b) The top view of the board.

data together with the clock signal and the network time protocol.

To operate the SKA hardware as part of our receiver system we designed a rack unit, which supplies the board with 12 VDC and provides sufficient cooling to the DSP board. An image of the GHY-3 DSP unit is shown in Figure 7.27. Four complex I and Q input channels are located on either side of the unit and the network and clock connections are located at the centre.

Figure 7.27: GHY-3 Digital Signal Processing Unit.

7.3.2 Digital Signal Processing Firmware

The firmware for the single-dish operation mode, which is deployed for the first light of the receiver system, implements a full Stokes parameter spectrometer with a spectral resolution of 0.977 MHz. The FPGA firmware was designed by Riccardo Chiello based on our specifications and requirements. This section describes the implementation of the spectrometer followed by the calibration implementation and the readout configuration.

7.3.2.1 Stokes Detection

The Stokes parameter detection which is implemented in the firmware is based on the equations to determine Stokes I,V,Q, and U for circular polarized signals. The

equations are given by

$$I = |\mathrm{LCP}|^2 + |\mathrm{RCP}|^2 \,, \tag{7.3}$$

$$V = |\mathrm{LCP}|^2 - |\mathrm{RCP}|^2 \,, \tag{7.4}$$

$$Q = 2Re\left(\mathrm{LCP} \times \mathrm{RCP}^*\right), \tag{7.5}$$

$$U = -2Im\left(\mathrm{LCP} \times \mathrm{RCP}^*\right). \tag{7.6}$$

At this point it is important to distinguish between the complex sampled input values represented by I and Q, which are used to compute the complex frequency spectrum, and the Stokes parameter I and Q, which represents the total intensity and the real part of the cross-correlations between the two opposite circular polarized components.

7.3.2.2 Firmware System Diagram

A functional block diagram of the Stokes spectrometer is shown in Figure 7.28. Each of the two FPGAs process two polarisations and half of the receiver band (2 GHz). The firmware design can be divided into two processing tasks, first the computation of the complex spectrum and second the detection of the Stokes parameter $IVQU$.

To process 4 GHz of bandwidth per FPGA we implement four complex FFTs, which each use the 500 MHz I and Q input channels to compute one complex spectrum. The output channels represents the positive and negative complex frequencies, which are then rounded before the calibration is applied. The rounding is required to limit the number of bits in the FPGA firmware design to prevent overflow in the fixed-point-arithmetic, and provided the rounding is set up correctly it will only remove insignificant bits. The calibration is implemented by a complex multiplication of all frequency channels with calibration coefficients. The calibration process will be described in more detail in the next section.

The second part of the firmware calculates the Stokes parameters using the left circular polarized (LCP) and right circular polarized (RCP) signals. The output of

the Stokes parameter calculation is again rounded and then integrated in the accumulators (ACC) on the right-hand side of the functional block diagram. The integrated Stokes parameters are then streamed to the control and monitor server via the 1 Gbit interface.

7.3.2.3 Calibration Option

The signal calibration is implemented with a complex multiplication block that applies a complex coefficient to each frequency channel, thereby allowing us to correct for amplitude and phase errors. The calibration coefficients are stored in two random access memory (RAM) registers, labelled in Figure 7.28 as RAM0 and RAM1 which act as a double buffer. These registers can be accessed by both the FPGA and the management and control unit. The registers are linked to the calibration block through a MUX which allows toggling between both registers, thereby switching all coefficients at the same clock cycle. The management and control system can write new coefficients into the register which is not used to calibrate the signal, after updating the coefficients the MUX is then used to apply the new set of calibration coefficients.

7.3.2.4 Readout

The data readout is controlled by the management and control system. Its implementation allows us to read out the detected Stokes parameters as well as to read out the complex spectrum directly. It is set up to use the 1 Gbit link to send the data to the control and monitor server since the data rate after the accumulation does not justify the use of the 40 Gbit QSFP+ ethernet connection. The readout script running on the control and monitor server captures the timestamped data and stores it in two separate hdf5 files, one containing the Stokes parameters and the other one containing the complex frequency spectrum.

The readout system can be configured for different integration times, which are limited by either the bandwidth of the 1 Gbit link or the bit width of the accumulators on the FPGA.

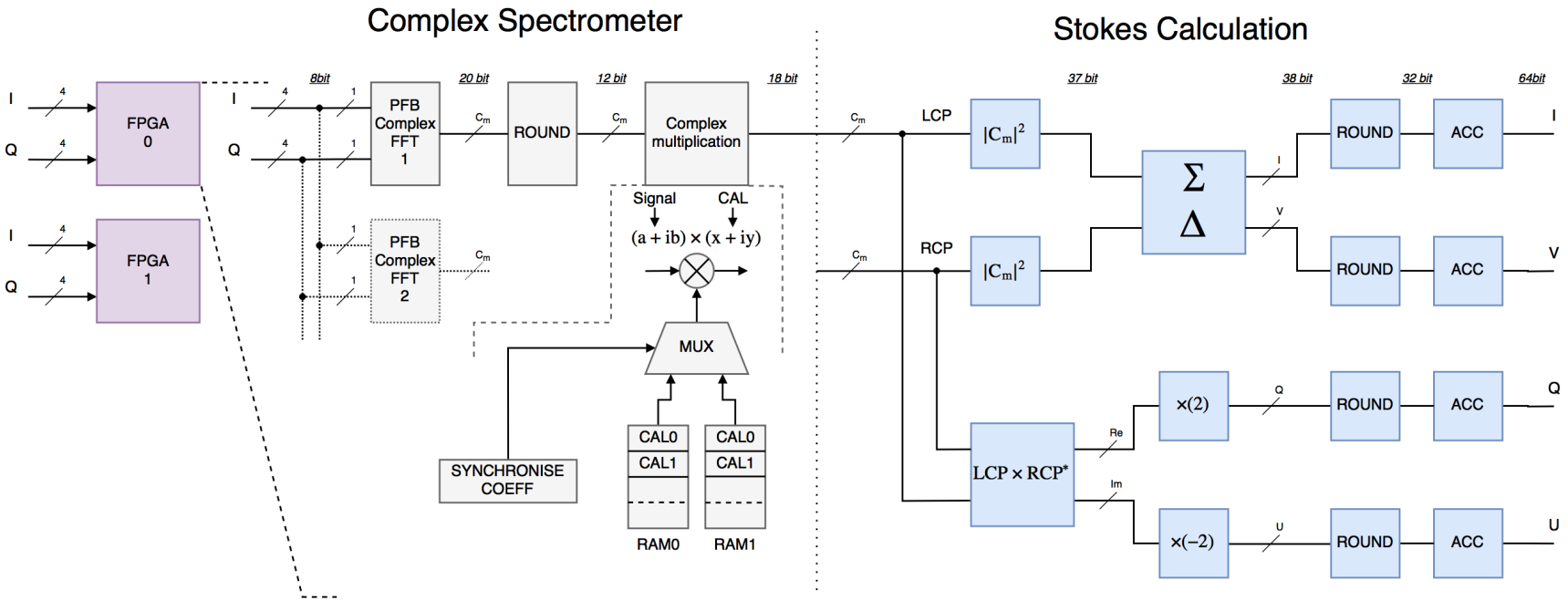

Figure 7.28: Functional block diagram of the GHY-3 DSP firmware.

Based on experimental results we determined that the lowest integration time which can still be read out by the system is approximately 3 mSec. The longest integration time is limited by the bit growth in the accumulator which can be calculated by subtracting the bit length of the input with the bit length of the accumulator. In our case this is 64 bit − 32 bit = 32 bit, which gives us a maximal number of integration cycles of 2^{32} before the accumulator overflows. By multiplying this number with the cycle time of approximately 864 nSec, we get a maximal integration time of approximately 1 hour on the DSP hardware, before we need to read out the integrated data. This is much longer than any realistic integration time, so an accumulator overflow is not a practical limitation.

7.4 Summary

In this chapter we presented the design and development of the GHY-3 receiver system. We started by providing a system overview of the three functional areas of the receiver system. These were the cryostat which provides the environment for the cryocooler to operate the front-end electronics at approximately 10 K, the signal conditioning which processes the received signals and stores it on a server, and the control and monitor system which allows us to operate the receiver and monitor its performance.

We then presented the design and verification of a number of individual components which were especially designed by us for the GHY-3 receiver. This includes the analogue signal components as well as the temperature stabilised module platform.

Finally, we presented the digital signal processing hardware and firmware, which implements a complex spectrometer and a Stokes parameter detection. This firmware implementation will be used for the first light of the receiver system during the commissioning phase of the telescope.

Chapter 8

Conclusions

The aim of my project was to design and build a radio astronomy receiver system for the GHY-3 antenna conversion project. In this chapter I conclude this thesis and the work which led to a complete receiver system. At the end of this conclusion I provide an outline of the next steps that will lead to the commissioning of the telescope.

8.1 Discussion

The receiver system presented in this thesis is a cryogenically cooled radio astronomy receiver that is designed to be integrated into the existing infrastructure of the GHY-3 antenna. The operational bandwidth meets the requirements of both the radio astronomy applications and the deep-space communication applications. The use of an FPGA based signal processing backend allows us to implement the different operational modes on the same hardware, which supports the synergy between radio astronomy and deep-space communications.

To integrate the new receiver system into the existing antenna infrastructure I analysed the optical configuration of the antenna and designed a wideband ring-loaded corrugated feed horn to efficiently illuminate the antenna optics. The transmission between the feed horn and the cryogenically cooled front-end electronics is done via the compact quad-ridged orthomode transducer. The novel design of this OMT has been successfully validated by measurements and the design and results have been

successfully published in [41].

The architecture of the receiver system includes a means to stabilise its gain fluctuations. As part of the design process I analysed and compared the performance of different stabilisation methods. Two of which were considered for the implementation into the GHY-3 receiver system. The white-noise and the continuous-wave stabilisation method have been analysed and tested in detail. The experimental results showed excellence performance in both cases, although it turned out that the continuous wave implementation will require an additional active level control located within the cryostat to achieve the required reference signal stability. As the GHY-3 digital signal processing hardware requires sixteen IF sub-bands to digitise the overall receiver band I decided to implement the white-noise stabilisation approach. The broadband reference signal in this case allows us to correct the gain drift in all parallel signal paths at once.

The receiver system comprises of several analogue signal conditioning components most of which had to be designed and developed especially. The components which I developed were the 4.0–8.5 GHz I/Q mixer, the 4.0–16 GHz Wilkinson divider, the 4.0–8.5 GHz bandpass filter, the DC–0.5 GHz and 0.5–1.0 GHz anti-aliasing filter, and the 4.0–8.0 GHz active level control. All these designs were individually tested and verified by measurements before being applied into the receiver signal conditioning chain. I also presented the first FPGA firmware design, which will be used for the single dish operational mode. The design implements a full stokes spectrometer with a total number of 4096 frequency channels over the observational band of 4–8 GHz. This firmware design is going to be used during the commissioning phase of the instrument.

To house the room temperature analogue signal components, I designed a modular rack-based system that temperature stabilises all mounted components, thereby reducing environmental effects on the receiver system. Special care was given to avoid any spurious signals close to the mounted analogue signal components. Therefore, I designed the entire temperature stabilisation control loop and monitor logic with analogue operational amplifiers and comparators. The first prototype of my tem-

perature stabilised modular rack-based system upgraded the existing analogue signal components of the C-BASS south experiment and was deployed in 2017.

In summary, I can say that I designed and built a complete receiver system during the last three years of my DPhil. I am confident, that this receiver system will enable the GHY-3 antenna to be used as a scientific instrument and contribute to the radio astronomy community in the United Kingdom.

8.2 Future Work

In this section I want to provide and outline of the next steps that will lead to the successful completion of the GHY-3 antenna conversion project.

8.2.1 Measurements of the Receiver System

The next step in the conversion project is to measure the performance of the complete receiver system. This can be done as soon as the manufactured GHY-3 feed horn is delivered.

The first task would be to verify the feed horn design by measuring its far field beam pattern. After that we can measure the receiver system temperature using the Y-Factor method [64]. This method is used to determine the effective noise temperature of the receiver system, by measuring the ratio in output power for two different input temperatures T_{hot} and T_{cold}. The equation to calculate the system temperature is given by

$$T_{\text{sys}} = \frac{T_{\text{hot}} - Y \cdot T_{\text{cold}}}{Y - 1}, \tag{8.1}$$

with

$$Y = \frac{P_{\text{hot}}}{P_{\text{cold}}}, \tag{8.2}$$

where P_{hot} and P_{cold} are the measured output power level of the receiver system and T_{hot} and T_{cold} are the corresponding temperature input in Kelvin.

8.2.2 Receiver Mount

To integrate the receiver system into the existing antenna, we asked our workshop to design a receiver mount that allows us to place the new receiver system at the focus point of the GHY-3 antenna. The receiver mount is designed by Joe Tacon based on our requirements and measured antenna dimensions.

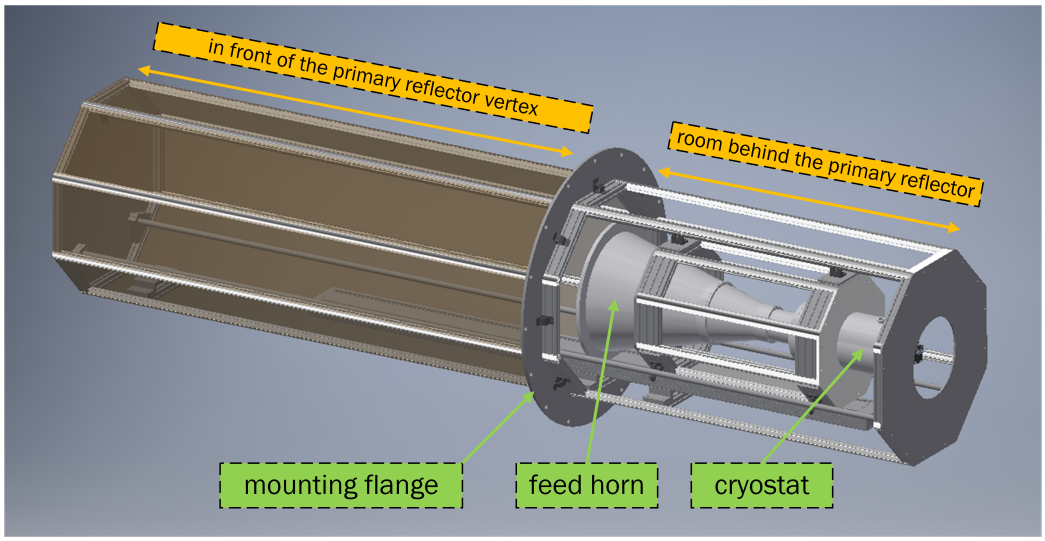

(a) CAD design.

(b) Assembled frame.

Figure 8.1: GHY-3 receiver mount.

As the new feed horn including the cryostat is shorter than the existing feed horn, the entire feed horn including the cryostat must be placed in front of the reflector in order to be located at the focus point of the antenna. The design of the receiver mount is based around a linear actuator, that allows us to position the receiver at the focus point and retract it into the room behind the primary reflector for maintenance. A CAD drawing of the receiver mount design is shown in Figure 8.1a and a picture of the assembled frame is shown in Figure 8.1b. The receiver system is mounted on a trolley inside the frame. The linear actuator on the bottom uses a stepper motor to position the feed horn and the cryostat at the focus point of the antenna. When the receiver mount is built, we will assemble the entire unit and verify the function and stability of the mount. After that it will be shipped to Goonhilly, where it will be lifted into the dish via a crane.

8.2.3 Antenna Control System

The antenna control system was originally designed to track geostationary satellites, which means it was designed to lock onto a satellite signal and correct only for small movements. Since the operation as a radio astronomy instrument requires accurate tracking of astronomical sources we must interface the existing control system in a way that it allows us to continuously track objects. In addition of the capabilities of tracking astronomical sources the instrument must also be able to superimpose certain patterns such as a cross or raster. The implementation of the antenna control is planned by setting up a computer which calculates azimuth and elevation positions at constant time intervals and updates the antenna control.

8.2.4 Commissioning of the Receiver System

The final step in the project is to commission the receiver system which includes a number of measurements validating its performance.

An appropriate way to measure the performance of the receiver system is to measure its System Equivalent Flux Density (SEFD). The SEFD uses both, the system

temperature $T_{\rm sys}$ and the effective aperture area $A_{\rm eff}$, thereby allowing us to compare system sensitivities between different instruments. It is defined as the unit of flux that doubles the system temperature and is given by

$$\mathrm{SEFD} = \frac{2\mathrm{k_b}\mathrm{T_{sys}}}{\mathrm{A_{eff}}} \tag{8.3}$$

The SEFD can be measured directly by observing sources with known flux $S(\nu)$. To do this we compare the detected power when observing the source $P_{\rm on}$ with the detected power when not observing the source $P_{\rm off}$. The SEFD for this case is calculated by

$$\mathrm{SEFD} = \frac{\mathrm{S}(\nu)}{\frac{\mathrm{P_{on}}}{\mathrm{P_{off}}} - 1} \tag{8.4}$$

Appendix A

Anti-Aliasing Filter Values

Table A.1: Component values for the anti-aliasing DC–0.5 GHz low-pass filter.

Low-pass filter, $n = 25$			
Component	Value	Package	Part number
L_1	13 nH	0603	LQW18AN13NG80D
L_2	30 nH	0603	LQW18AN30NG80D
L_3	33 nH	0603	LQW18AN33NG80D
L_4	33 nH	0603	LQW18AN33NG80D
L_5	33 nH	0603	LQW18AN33NG80D
L_6	33 nH	0603	LQW18AN33NG80D
L_7	33 nH	0603	LQW18AN33NG80D
C_1	9.5 pF	0402	GJM1555C1H9R5WB01D
C_2	11 pF	0402	GJM1555C1H110GB01D
C_3	12 pF	0402	GJM1555C1H120GB01D
C_4	12 pF	0402	GJM1555C1H120GB01D
C_5	12 pF	0402	GJM1555C1H120GB01D
C_6	12 pF	0402	GJM1555C1H120GB01D

Table A.2: Component values for the anti-aliasing 0.5–1.0 GHz band-pass filter.

Low-pass filter, $n = 19$			
Component	Value	Package	Part number
L_1	6.8 nH	0603	LQW18AN6N8G80D
L_2	15 nH	0603	LQW18AN15NG80D
L_3	16 nH	0603	LQW18AN16NG80D
L_4	17 nH	0603	LQW18AN17NG80D
L_5	17 nH	0603	LQW18AN17NG80D
C_1	4.8 pF	0402	GJM1555C1H4R8WB01D
C_2	5.8 pF	0402	GJM1555C1H5R8WB01D
C_3	6.0 pF	0402	GJM1555C1H6R0WB01D
C_4	6.0 pF	0402	GJM1555C1H6R0WB01D
C_5	6.1 pF	0402	GJM1555C1H6R1WB01D
High-pass filter, $n = 19$			
C_1	7.5 pF	0603	GQM1885C2A7R5WB01D
C_2	3.4 pF	0603	GQM1885C2A3R4WB01D
C_3	3.1 pF	0603	GQM1885C2A3R1WB01D
C_4	3.0 pF	0603	GQM1885C2A3R0WB01D
C_5	3.0 pF	0603	GQM1885C2A3R0WB01D
L_1	11 nH	0402	LQW15AN11NG80D
L_2	8.7 nH	0402	LQW15AN8N7G80D
L_3	8.5 nH	0402	LQW15AN8N5G80D
L_4	8.3 nH	0402	LQW15AN8N3G80D
L_5	8.3 nH	0402	LQW15AN8N3G80D

References

[1] M. J. Gaylard, M. F. Bietenholz, L. Combrinck, R. S. Booth, S. J. Buchner, B. L. Fanaroff, G. C. MacLeod, G. D. Nicolson, J. F. H. Quick, P. Stronkhorst, and T. L. Venkatasubramani. An African VLBI Network of radio telescopes. *ArXiv e-prints: 1405.7214*, 2011.

[2] L. Woodburn, T. Natusch, S. Weston, P. Thomasson, M. Godwin, C. Granet, and S. Gulyaev. Conversion of a New Zealand 30-Metre Telecommunications Antenna into a Radio Telescope. *Publications of the Astron. Soc. of Australia*, **32**(e017), May 2015.

[3] Peter M. McCulloch, Simon P. Ellingsen, David L. Jauncey, Steven J. B. Carter, Giuseppe Cimo, James E. J. Lovell, and Richard G. Dodson. Cosmic: Microarcsecond resolution with a 30 meter radio telescope. *The Astronomical Journal*, **129**(4):2034, 2005.

[4] K. Fujisawa, H. Mashiyama, T. Shimoikura, and N. Kawaguchi. The Yamaguchi 32-m Radio Telescope. In *8th Asian-Pacific Regional Meeting Volume II*, pages 3–4, 2002.

[5] J. Ishitsuka, M. Ishitsuka, N. Kaifu, S. Miyama, M. Inoue, M. Tsuboi, M. Ohishi, K. Fujisawa, T. Kasuga, K. Miyazawa, and S. Horiuchi. A 32 m Parabolic Antenna in Peru At 3,370m of Altitude. *ArXiv e-prints: 0501035*, January 2005.

[6] C. J. Copley, V. Thondikulam, A. Loots, S. Bangani, K. Cloete, L. Combrinck, S. Gioio, J. Ludick, G. Nicolson, A. W. Pollak, P. Pretorius, J. F. H. Quick, G. Taylor, F. Ebrahim, C. Humphreys, K. Maake, R. Maganane, R. Majinjiva,

A. Mapunda, M. Manzini, N. Mogakwe, A. Moseki, N. Qwabe, N. Royi, K. Rosie, J. Smith, S. Schietekat, O. Toruvanda, C. Tong, B. van Niekerk, W. Walbrugh, and W. Zeeman. The African Very Long Baseline Interferometry Network:The Ghana Antenna Conversion. *ArXiv e-prints: 1608.02187*, August 2016.

[7] Consortium of Universities for Goonhilly Astronomy. Repurposing of Communications Antennas for Radio Astronomy, 2017. URL https://www2.physics.ox.ac.uk/research/experimental-radio-cosmology/goonhilly.

[8] CSIRO Astronomy and Space Science. Canberra Deep Space Communication Complex, 2018. URL https://www.cdscc.nasa.gov.

[9] M. E. Jones, A. C. Taylor, M. Aich, C. J. Copley, H. C. Chiang, R. J. Davis, C. Dickinson, R. D. P. Grumitt, Y. Hafez, H. M. Heilgendorff, C. M. Holler, M. O. Irfan, L. R. P. Jew, J. J. John, J. Jonas, O. G. King, J. P. Leahy, J. Leech, E. M. Leitch, S. J. C. Muchovej, T. J. Pearson, M. W. Peel, A. C. S. Readhead, J. Sievers, M. A. Stevenson, and J. Zuntz. The C-Band All-Sky Survey (C-BASS): Design and capabilities. *ArXiv e-prints: 1805.04490*, May 2018.

[10] K. Liu, G. Desvignes, I. Cognard, B. W. Stappers, J. P. W. Verbiest, K. J. Lee, D. J. Champion, M. Kramer, P. C. C. Freire, and R. Karuppusamy. Measuring pulse times of arrival from broad-band pulsar observations. *Monthly Notices of the Royal Astronomical Society*, **443**:3752–3760, October 2014.

[11] S. Johnston, M. Kramer, D. R. Lorimer, A. G. Lyne, M. McLaughlin, B. Klein, and R. N. Manchester. Discovery of two pulsars towards the Galactic Centre. *Monthly Notices of the Royal Astronomical Society*, **373**:L6–L10, November 2006.

[12] W. Farah, C. Flynn, M. Bailes, A. Jameson, K. W. Bannister, E. D. Barr, T. Bateman, S. Bhandari, M. Caleb, D. Campbell-Wilson, S.-W. Chang, A. Deller, A. J. Green, R. Hunstead, F. Jankowski, E. Keane, J.-P. Macquart, A. Möller, C. A. Onken, S. Osłowski, A. Parthasarathy, K. Plant, V. Ravi, R. Shannon, B. E. Tucker, V. Venkatraman Krishnan, and C. Wolf. FRB mi-

crostructure revealed by the real-time detection of FRB170827. *ArXiv e-prints: 1803.05697*, May 2018.

[13] K. W. Bannister, R. M. Shannon, J.-P. Macquart, C. Flynn, P. G. Edwards, M. O'Neill, and et al. The Detection of an Extremely Bright Fast Radio Burst in a Phased Array Feed Survey. *Astrophysical Journal, Letters*, **841**:L12, May 2017.

[14] V. Gajjar, A. P. V. Siemion, D. C. Price, C. J. Law, D. Michilli, J. W. T. Hessels, S. Chatterjee, A. M. Archibald, G. C. Bower, C. Brinkman, S. Burke-Spolaor, J. M. Cordes, S. Croft, J. E. Enriquez, G. Foster, N. Gizani, G. Hellbourg, H. Isaacson, V. M. Kaspi, T. J. W. Lazio, M. Lebofsky, R. S. Lynch, D. MacMahon, M. A. McLaughlin, S. M. Ransom, P. Scholz, A. Seymour, L. G. Spitler, S. P. Tendulkar, D. Werthimer, and Y. G. Zhang. Highest-frequency detection of FRB 121102 at 4-8 GHz using the Breakthrough Listen Digital Backend at the Green Bank Telescope. *ArXiv e-prints: 1804.04101*, April 2018.

[15] University of Manchester Jodrell Bank Observatory. e-MERLIN / VLBI National Radio Astronomy Facility, 2018. URL http://www.e-merlin.ac.uk.

[16] The European VLBI Network, 2018. URL http://www.evlbi.org.

[17] I. Heywood, H. Kloeckner, R. Beswick, S. T. Garrington, J. Hatchell, M. G. Hoare, M. J. Jarvis, I. Jones, T. W. B. Muxlow, and S. Rawlings. Expanding e-MERLIN with the Goonhilly Earth Station. *ArXiv e-prints: 1103.1214*, March 2011.

[18] European Space Agency. The Exomars Programme 2016-2020, 2016. URL http://exploration.esa.int/jump.cfm?oid=46048.

[19] I. Zouganelis, D. Mueller, C. St. Cyr, and H. R. Gilbert. Solar Orbiter - Exploring the Sun-Heliosphere Connection. In *EGU General Assembly Conference Abstracts*, volume **18**, page 7994, April 2016.

[20] R. Laureijs, J. Amiaux, S. Arduini, J. . Augueres, J. Brinchmann, R. Cole, M. Cropper, C. Dabin, L. Duvet, A. Ealet, and et al. Euclid Definition Study Report. *ArXiv e-prints: 1110.3193*, October 2011.

[21] National Instruments. Introduction to FPGA Technology: Top 5 Benefits, 2018. URL http://www.ni.com/white-paper/6984/en/.

[22] Xilinx®. System Generator for DSP, 2018. URL https://www.xilinx.com/products/design-tools/vivado/integration/sysgen.html.

[23] Altera®. Automated Generation of Hardware Accelerators With Direct Memory Access From ANSI/ISO Standard C Functions, 2018. URL https://www.altera.com/content/dam/altera-www/global/en_US/pdfs/literature/wp/wp-aghrdwr.pdf.

[24] A. R. Foley, T. Alberts, R. P. Armstrong, A. Barta, E. F. Bauermeister, H. Bester, S. Blose, R. S. Booth, D. H. Botha, S. J. Buchner, and et al. Engineering and science highlights of the KAT-7 radio telescope. *Monthly Notices of the Royal Astronomical Society*, **460**(2):1664–1679, 2016.

[25] J. Chennamangalam, S. Scott, G. Jones, H. Chen, J. Ford, A. Kepley, D. R. Lorimer, J. Nie, R. Prestage, D. A. Roshi, M. Wagner, and D. Werthimer. A GPU-Based Wide-Band Radio Spectrometer. *ArXiv e-prints: 1411.0436*, December 2014.

[26] S. R. Meeker, B. A. Mazin, R. Jensen-Clem, A. B. Walter, P. Szypryt, M. J. Strader, and C. Bockstiegel. Design and Development Status of MKID Integral Field Spectrographs for High Contrast Imaging. In *Adaptive Optics for Extremely Large Telescopes IV*, page E75, December 2015.

[27] P. Benthem, M. Gerbers, J. G. B. de Vaate, S. Wynholds, J. Bast, T. Booler, and et al. The low frequency receivers for SKA 1-low: Design and verification. In *General Assembly and Scientific Symposium of the International Union of Radio Science*, pages 1–4, Aug 2017.

[28] SKA South Africa. MeerKAT radio telescope, 2018. URL http://www.ska.ac.za/gallery/meerkat/.

[29] Jack Hickish, Zuhra Abdurashidova, Zaki Ali, Kaushal D Buch, Sandeep C Chaudhari, Hong Chen, Matthew Dexter, Rachel Simone Domagalski, John Ford, Griffin Foster, et al. A Decade of Developing Radio-Astronomy Instrumentation using CASPER Open-Source Technology. *Journal of Astronomical Instrumentation*, **5**(04):1641001–12, 2016.

[30] Mike Wissolik, Darren Zacher, Anthony Torza, and Brandon Day. Virtex UltraScale+ HBM FPGA: A Revolutionary Increase in Memory Performance, 2017. URL https://www.xilinx.com/support/documentation/white_papers/wp485-hbm.pdf.

[31] Manish Deo, Jeffrey Schulz, and Lance Brown. Intel® Stratix® 10 MX Devices Solve the Memory Bandwidth Challange . 2017. URL https://www.altera.com/content/dam/altera-www/global/en_US/pdfs/literature/wp/wp-01264-stratix10mx-devices-solve-memory-bandwidth-challenge.pdf.

[32] L. Lin, T. C. Yeh, J. L. Wu, G. Lu, T. F. Tsai, L. Chen, and A. T. Xu. Reliability characterization of Chip-on-Wafer-on-Substrate (CoWoS) 3D IC integration technology. In *IEEE 63rd Electronic Components and Technology Conference*, pages 366–371, May 2013.

[33] Anthony Collins. All Programmable RF-Sampling Solutions. 2017. URL https://www.xilinx.com/support/documentation/white_papers/wp489-rfsampling-solutions.pdf.

[34] K. Rohlfs and T.L. Wilson. *Tools of Radio Astronomy*. Astronomy and Astrophysics Library. Springer Berlin Heidelberg, 2013. ISBN 9783662053942.

[35] C.A. Balanis. *Antenna Theory: Analysis and Design*. Wiley, 2012. ISBN 9780471714613.

[36] J.D. Kraus and R.J. Marhefka. *Antennas: For All Applications*. McGraw-Hill series in electrical engineering. McGraw-Hill, 2002. ISBN 9780071232012.

[37] Christian Matthias Holler. *Correlator and antenna design for the Arcminute Microkelvin Imager (AMI)*. PhD thesis, University of Cambridge, 2003.

[38] T. Luhmann. *Close Range Photogrammetry: Principles, Techniques and Applications*. Whittles, 2006. ISBN 9781870325509.

[39] TICRA. General Reflector Antenna Software Package GRASP, 2017. URL http://www.ticra.com/products/software/grasp.

[40] W.L. Stutzman and G.A. Thiele. *Antenna Theory and Design*. Antenna Theory and Design. Wiley, 2012. ISBN 9780470576649.

[41] A. W. Pollak and M. E. Jones. A Compact Quad-Ridge Orthogonal Mode Transducer With Wide Operational Bandwidth. *IEEE Antennas and Wireless Propagation Letters*, **17**(3):422–425, March 2018.

[42] P. K. Grimes, O. G. King, G. Yassin, and M. E. Jones. Compact broadband planar orthomode transducer. *Electronics Letters*, **43**(21):1146–1147, Oct 2007.

[43] A. Tribak, J. L. Cano, A. Mediavilla, and M. Boussouis. Octave bandwidth compact turnstile-based orthomode transducer. *IEEE Microwave and Wireless Components Letters*, **20**(10):539–541, Oct 2010.

[44] Y. Aramaki, N. Yoneda, M. Miyazaki, and T. Horie. Ultra-thin broadband OMT with turnstile junction. In *IEEE MTT-S International Microwave Symposium Digest, 2003*, volume **1**, pages 47–50, June 2003.

[45] J. A. Ruiz-Cruz, J. R. Montejo-Garai, J. M. Rebollar, and J. M. Montero. C-band orthomode transducer for compact and broadband antenna feeders. *IEEE Electronics Letters*, **45**(16):813–814, July 2009.

[46] Banham, R and Valsecchi, G and Lucci, L and Pelosi, G and Selleri, S and Natale, V and Nesti, R and Tofani, G. Electroformed Front-end at 100 GHz. 2005.

[47] A. Dunning. Double ridged orthogonal mode transducer for the 16-26 GHz microwave band. In *Workshop on the Applications of Radio Science*, Feb 2002.

[48] D. I. L. D. Villiers, P. Meyer, and K. D. Palmer. Broadband offset quad-ridged waveguide orthomode transducer. *IEEE Electronics Letters*, **45**(1):60–62, January 2009.

[49] E. J. Wollack, Wes Grammer, and Jessica M. Kingsley. The Bøifot Orthomode Junction, 2002. URL http://legacy.nrao.edu/alma/memos/html-memos/alma425/memo425.pdf.

[50] C. A. W. Vale and P. Meyer. Designing high-performance finline tapers with vector-based optimization. *IEEE Transactions on Microwave Theory and Techniques*, **47**(12):2467–2472, Dec 1999.

[51] The MathWorks, Inc. Matlab R2014b, 2018. URL https://uk.mathworks.com/products/matlab.html.

[52] ANSYS, Inc. High-Frequency Structure Simulator HFSS, 2017. URL http://www.ansys.com/Products/Electronics/ANSYS-HFSS.

[53] Vijay Ramasami. HFSS-MATLAB-SCRIPTING-API, 2017. URL https://github.com/yuip/hfss-api/.

[54] D.M. Pozar. *Microwave Engineering, 4th Edition*. Wiley, 2011. ISBN 9781118213636.

[55] G. M. Coutts. Wideband Diagonal Quadruple-Ridge Orthomode Transducer for Circular Polarization Detection. *IEEE Transactions on Antennas and Propagation*, **59**(6):1902–1909, June 2011.

[56] G. M. Coutts, H. Dinwiddie, and P. Lilie. S-band octave-bandwidth orthomode transducer for the Expanded Very Large Array. In *IEEE Antennas and Propagation Society International Symposium*, pages 1–4, June 2009.

[57] P.J.B. Clarricoats and A.D. Olver. *Corrugated Horns for Microwave Antennas*. Electromagnetics and Radar Series. P. Peregrinus, 1984. ISBN 9780863410031.

[58] Christophe Granet and Graeme L James. Design of corrugated horns: a primer. *IEEE Antennas and Propagation Magazine*, **47**(2):76–84, 2005.

[59] P.F. Goldsmith. *Quasioptical Systems: Gaussian Beam Quasioptical Propogation and Applications*. IEEE Press Series on RF and Microwave Technology. Wiley, 1998. ISBN 9780780334397.

[60] James, Graeme L and Thomas, Bruce M. TE_{11} to HE_{11} Cylindrical Waveguide Mode Converters Using Ring-Loaded Slots. *IEEE Transactions on Microwave Theory and Techniques*, **30**(3):278–285, 1982.

[61] A.D. Olver and Institution of Electrical Engineers. *Microwave Horns and Feeds*. Electromagnetics and Radar Series. IEE, 1994. ISBN 9780852968093.

[62] TICRA. Corrugated Horn Analysis by Modal Processing CHAMP, 2017. URL http://www.ticra.com/products/software/champ.

[63] B.F. Burke and F. Graham-Smith. *An Introduction to Radio Astronomy*. Cambridge University Press, 2010. ISBN 9780521878081.

[64] F.R. Connor. *Noise*. Introductory topics in electronics and telecommunication. Edward Arnold, 1982. ISBN 9780713134599.

[65] L. M. Ward and P. E Greenwood. $1/f$ noise. *Scholarpedia*, **2**(12):1537, 2007.

[66] Haartman, Martin von and Östling, Mikael. *1/F Noise in Mosfets*, pages 53–102. Springer Netherlands, Dordrecht, 2007. ISBN 978-1-4020-5910-0.

[67] Noise Figure of Passives, 2018. URL https://www.microwaves101.com/encyclopedias/noise-figure-of-passives.

[68] Noise Voltage and Power Distributions, 2018. URL https://www.cv.nrao.edu/course/astr534/NoiseRMS.html.

[69] National Radio Astronomy Observatory (NRAO). Radiometers, 2017. URL http://www.cv.nrao.edu/course/astr534/Radiometers.html.

[70] D. Sivia and J. Skilling. *Data Analysis: A Bayesian Tutorial*. Oxford science publications. OUP Oxford, 2006. ISBN 9780198568315.

[71] A.R. Thompson, J.M. Moran, and G.W. Swenson. *Interferometry and Synthesis in Radio Astronomy*. Astronomy and Astrophysics Library. Springer International Publishing, 2017. ISBN 9783319444314.

[72] University of California, Berkeley. Collaboration for Astronomy Signal Processing and Electronics Research CASPER, 2017. URL https://casper.berkeley.edu.

[73] A. W. Pollak. An example of using CASPER tutorials for teaching knowledge of firmware development for FPGAs. *Journal of Instrumentation*, **10**:C08012, August 2015.

[74] Francois Kapp. Roach on the test bench with two iadc's connected, 2009. URL https://casper.berkeley.edu/wiki/images/2/2c/Roach_with_iadcs_on_bench.jpg.

[75] D. C. Price. Spectrometers and Polyphase Filterbanks in Radio Astronomy. *ArXiv e-prints: 1607.03579*, July 2016.

[76] Luke Jew. *Measurements of diffuse galactic emission at 5 GHz with C-BASS*. PhD thesis, University of Oxford, 2017.

[77] Charles Judd Copley. *The C-Band All Sky Survey*. PhD thesis, University of Oxford, 2014.

[78] M. Pelgrom. *Analog-to-Digital Conversion*. Springer International Publishing, 2016. ISBN 9783319449715.

[79] J. Benesty, J. Chen, Y. Huang, and I. Cohen. *Noise Reduction in Speech Processing*. Springer Topics in Signal Processing. Springer Berlin Heidelberg, 2009. ISBN 9783642002960.

[80] Oxford Cryosystems. Coolstar Cryocoolers Manual, 2018. URL http://www.jcmueller.de/pdf/two-stage-coldheads.pdf.

[81] E. J. Wilkinson. An N-Way Hybrid Power Divider. *IRE Transactions on Microwave Theory and Techniques*, **8**(1):116–118, January 1960.

[82] S. B. Cohn. A Class of Broadband Three-Port TEM-Mode Hybrids. *IEEE Transactions on Microwave Theory and Techniques*, **16**(2):110–116, February 1968.

[83] M. Uhm, K. Kim, and D. S. Filipovic. Ultra-Wideband Bandpass Filters Using Quarter-Wave Short-Circuited Shunt Stubs and Quarter-Wave Series Transformers. *IEEE Microwave and Wireless Components Letters*, **18**(10):668–670, October 2008.

[84] Schroff. Pentair Technical Solutions GmbH, 2018. URL https://schroff.pentair.com.

[85] Giovanni Naldi, Andrea Mattana, Sandro Pastore, and et al. The Digital Signal Processing Platform for the Low Frequency Aperture Array: Preliminary Results on the Data Acquisition Unit. *Journal of Astronomical Instrumentation*, **06**(01): 1641014, March 2017.